ON THE VARIABILITY OF DOPPLER SPECTRA IN HF GROUNDWAVE RADAR REMOTE SENSING OVER THE OCEAN SURFACE: AN INVESTIGATION BASED ON PULSED AND FREQUENCY MODULATED SOURCES

JIANJUN ZHANG


CENTRE FOR NFLD. STUDIES
MEMORIAL UNIVERSITY
OF NEWFOUNDLAND

On the Variability of Doppler Spectra in HF Groundwave Radar Remote Sensing over the Ocean Surface: An Investigation Based on Pulsed and Frequency Modulated Sources

by

©Jianjun Zhang, B.Eng., M.Eng.

A thesis submitted to the School of Graduate Studies

in partial fulfillment of the requirements for the

degree of Doctor of Philosophy

Faculty of Engineering and Applied Science

Memorial University of Newfoundland

January, 2009

St. John's Newfoundland Canada

Abstract

An examination of the fluctuations of the Bragg peaks in high frequency (HF) radar received backscatter spectra from the ocean surface is considered in the light of recent cross section models. It is well known that there are likely several factors giving rise to this phenomenon. In the first part of the research work, the effect that is purely caused by the use of a pulsed Doppler radar waveform is examined. The radar received signal is assumed to be scattered from a time-varying random rough surface represented as a zero-mean, Gaussian random process. Numerical examinations of the existence and distribution of Bragg fluctuations are carried out first. Various radar operating frequencies and pulse widths are selected to simulate the time series for different conditions. Doppler spectra (power spectral density, PSD) are estimated as periodograms. The centroids of the Bragg peaks are obtained and compared with theoretical values and the Bragg fluctuations from time to time are observed. The statistical properties of the centroid positions are indicated and compared with resolutions of the fast Fourier transform (FFT) algorithm to reveal their significance. Then the physical processes which underlie the observed variability of the HF sea echo over short time periods are examined. It will be seen that, by implementing both numerical and analytical techniques, interrogation of such a surface via a pulsed signal inherently leads to temporal variation of echo power at every frequency position of the Doppler spectrum.

The second part of the research work is an investigation of the Bragg fluctuations when HF radar uses the frequency modulated waveforms, which include frequency modulated continuous wave (FMCW) and frequency modulated interrupted continuous wave (FMICW) sources. Such waveforms are often employed in practical radar systems. The mathematical expressions of the cross sections for the FMCW and FMICW waveforms are worked out and their properties are addressed. Then, similar to the previous analysis for the pulsed waveform, time series of the radar received electric field signals are simulated

and the PSDs are calculated. Centroid positions of the Bragg peak regions are located and compared to the theoretical values. Statistical properties of the Bragg fluctuations are investigated and comparison with respect to that for the pulsed waveform is carried out. Field data from the Wellen Radar (WERA) are used to verify the simulation results and the fluctuations of the Bragg peaks for the FMCW waveform.

Acknowledgments

The author wishes to express his sincerest thanks to the Faculty of Engineering and Applied Science, Memorial University of Newfoundland (MUN), for affording him the opportunity of conducting this work. Particularly, the suggestions and guidance of the author's supervisors, Dr. Eric Gill and Dr. John Walsh, Faculty of Engineering and Applied Science, MUN, are greatly appreciated.

The author wishes to express his appreciation to his supervisory committee member, Dr. Cecilia Moloney, Faculty of Engineering and Applied Science, MUN, for her advice and helpful discussion.

Dr. Klaus-Werner Gurgel, Institute of Oceanography, University of Hamburg, Germany, is highly appreciated for permitting access to the WERA field data from the European Radar Ocean Sensing (EuroROSE) experiment conducted in Lyngoy, Norway.

Special thanks are due to Dr. Weimin Huang, for his helpful discussion and suggestions in research and preparation of the proposal. Thanks are also owed to author's colleagues and friends, Pradeep Bobby and David Green, for their help and assistance on computer programming and other aspects at various stages of the work.

The work could not have been completed without the graduate student support from Natural Science and Engineering Research Council (NSERC) grants to Dr. Eric Gill and Dr. John Walsh.

The unfailing patience and support of the author's wife, Qiu Jin, and their lovely son, Zhipu Zhang, are deeply appreciated.

Contents

List of Figures

List of Tables

Table of Symbols

ω_B : Theoretical Bragg frequency for the pulsed waveform (p. 7).

g : Acceleration due to gravity ($= 9.8$ m/s^2) (p. 7).

k_0 : Radar radiation wavenumber (p. 7).

ω_0 : Angular frequency of the electric field (p. 7).

μ_0 : Electric permittivity of free space (p. 7).

ϵ_0 : Magnetic permeability of free space (p. 7).

K : Wavenumber of ocean wave (p. 9).

$\Delta\rho_s$: Radial width of the scattering patch (p. 9).

τ_0 : Radar transmitting pulse duration (p. 9).

λ : Wavelength of ocean wave (p. 11).

$\vec{K}$: Ocean wave vector (p. 22).

$S_1\left(\vec{K}\right)$: Directional ocean surface wave spectrum (p. 22).

$\theta_{\vec{K}}$: Direction of $\vec{K}$ (p. 22).

$D\left(\theta_{\vec{K}}\right)$: Directional characteristic of the ocean surface (p. 22).

S_{PM} : Pierson-Moskowitz non-directional spectrum (p. 22).

α_{PM} : An empirical constant of Pierson-Moskowitz spectrum, $\alpha_{\mathrm{PM}} = 0.0081$ (p. 22).

u_w : Wind speed measured at 19.5 m above the ocean surface (p. 22).

$s(K)$: Spread function for ocean wave directional characteristics (p. 22).

$\bar{\theta}(K)$: Dominant wave direction (p. 22).

θ_w : Wind direction (p. 23).

$S_1\left(m\vec{K}\right)$: Ocean wave directional spectrum (p. 23).

σ_{1p} : First-order cross section for the pulsed waveform (p. 24).

ω_d : Radar Doppler frequency (p. 24).

c : Light speed in free space (p. 25).

ρ_1 : Distance from radar transmitter to the scattering patch (p. 25).

ρ_2 : Distance from scattering patch to the radar receiver (p. 25).

$\mathrm{Sa}(\cdot)$: Sinc function, $\mathrm{Sa}(x) = \dfrac{\sin(x)}{x}$ (p. 26).

K_{B} : Wavenumber of the Bragg peak (p. 26).

$\vec{K}_1$, $\vec{K}_2$: Wave vectors of the ocean wave (p. 26).

θ_{N} : Direction of the radar beam (p. 26).

σ_{2p} : Second-order cross section for the pulsed waveform (p. 27).

$\delta(\cdot)$: Dirac delta function (p. 27).

${}_S\Gamma_P$: Coupling coefficient arising from the wave-wave interactions (p. 27).

${}_H\Gamma_P$: Hydrodynamic coupling coefficient (p. 28).

${}_E\Gamma_P$: Electromagnetic coupling coefficient (p. 28).

ω_1 : Wave frequency of ocean wave, $\omega_1 = \sqrt{gK_1}$ (p. 28).

ω_2 : Wave frequency of ocean wave, $\omega_2 = \sqrt{gK_2}$ (p. 28).

$\theta_{\vec{K}_1}$: Angle of $\vec{K}_1$ from the reference direction (p. 28).

$\left(E_0^+\right)_{12}(t)$: Radar received time series (p. 31).

$\epsilon(\omega)$: Ocean wave random phase (p. 31).

σ : Summary of the first- and second-order cross section (p. 31).

λ_0 : Radar transmitting wavelength (p. 31).

P_t : Average power of the transmitting source (p. 31).

G_t : Free space antenna gain of the transmitting source (p. 31).

G_r : Free space gain of the receiving antenna (p. 31).

$F(\cdot)$: Rough spherical earth attenuation function (p. 31).

A_p : Area of the scattering patch (p. 31).

ρ_s : Distance from radar transmitter and receiver to the middle of scattering patch (p. 31).

$\epsilon_R = 80$: Relative permittivity of ocean surface (p. 31).

$\sigma_R = 4\ S/m$: Average conductivity of ocean surface (p. 31).

f_0 : Radar operating frequency (p. 32).

N_a : Element number of linear array (p. 32).

d_s : Element spacing of linear array (p. 32).

$P(\omega)$: General expression of Doppler power spectral density (p. 34).

Δt : Time interval of periodogram (p. 34).

Δ_{FFT} : FFT resolution (p. 38).

STD : Standard deviation (p. 38).

V_{FFT} : Speed of ocean wave corresponding to FFT resolution (p. 38).

STDL : Standard deviation for the left-hand side Bragg region (p. 38).

STDR : Standard deviation for the right-hand side Bragg region (p. 38).

V_L : Speed associated with STDL (p. 38).

V_R : Speed associated with STDR (p. 38).

$E_{13}(t)$: Electric field with two adjacent frequencies ω_1 and ω_3 (p. 47).

ϵ_1 : Random variable associated with ω_1 (p. 47).

ϵ_3 : Random variable associated with ω_3 (p. 47).

α_1 : A phase term contains random variable ϵ_1 (p. 50).

α_3 : A phase term contains random variable ϵ_3 (p. 50).

$P_T(\omega)$: Total PSD for the field with two adjacent frequencies ω_1 and ω_3 (p. 50).

$P_1(\omega)$: PSD for the field with frequency ω_1 (p. 50).

$P_3(\omega)$: PSD for the field with frequency ω_3 (p. 50).

$P_{13}(\omega)$: PSD for the cross field (p. 50).

α_{13} : Phase factor associated with P_T (p. 50).

$P_T(\omega_n)$: Total PSD for the field at ω_n with N frequencies (p. 52).

$\Delta\omega$: Frequency resolution of the Doppler spectrum (p. 53).

P_{norm} : Normalized PSD (p. 57).

nSTD : Normalized standard deviation (p. 58).

R_k : Random variable at arbitrary position k (p. 58).

$\langle \cdot \rangle$: Ensemble average (p. 58).

$\Delta\omega_p$: Width of the Bragg region for the pulsed waveform (p. 61).

T_0 : Period of the radar frequency, $T_0 = \frac{1}{f_0}$ (p. 63).

N_p : Number of sinusoidal period within one transmitting pulse, $N_p = \frac{\tau_0}{T_0}$ (p. 63).

ξ : Factor with $\xi = \tau_0^{-1} f_0^{-\frac{1}{2}}$ (p. 64).

NSTD : Standard deviation normalized by the half Δ_{FFT} (p. 65).

N_e : Equivalent number of the frequency points within the Bragg region (p. 68).

P_n : Doppler spectrum value at frequency f_n within the Bragg region (p. 68).

P_{max} : Maximum Doppler spectrum value of P_n (p. 68).

N_{eL} : N_e for the left-hand Bragg region (p. 69).

N_{eR} : N_e for the right-hand Bragg region (p. 69).

ξ_c : Critical value of ξ (p. 72).

β_c : Critical width of the Bragg region (Hz) (p. 72).

N_c : Critical number of frequencies within the Bragg region (p. 72).

$c(t)$: Chirp signal (p. 81).

α : Frequency sweep rate (p. 81).

T_r : Frequency sweep interval (p. 81).

B : Frequency sweep bandwidth (p. 81).

$i(t)$: Frequency modulated continuous wave signal (p. 82).

I_0 : Amplitude of the current $i(t)$ (p. 82).

$g(t)$: Equally spaced gating sequence (p. 83).

Rect$(\cdot)$: Rectangular function (p. 83).

N : Number of gates within one sweep interval (p. 83).

T_g : Period of gating sequence (p. 83).

τ_g : Open time of the gate (p. 83).

d_c : Duty cycle of the gating sequence, $d_c = \frac{\tau_g}{T_g}$ (p. 83).

$i_g(t)$: Frequency modulated interrupted continuous wave signal (p. 84).

$\left(E_0^+\right)_1(\omega_0)$: Electric field equation in frequency domain (p. 86).

$P_{\vec{K},\omega}$: Fourier series coefficients of the surface (p. 86).

ρ_0 : Variable of distance from radar transmitter and receiver to the scattering patch (monostatic configuration) (p. 86).

$G(\theta)$: Receiving antenna directivity function (p. 86).

$C_0\left(=\frac{I\Delta l k_0^2}{j\omega_0\epsilon_0}\right)$: Dipole constant in the temporal Fourier transform domain (p. 86).

I : Current on the dipole (p. 86).

Δl : Length of dipole (p. 86).

$\mathcal{F}^{-1}[\cdot]$: Inverse Fourier transform function (p. 86).

η_0 : Impedance of the free space, $\eta_0 = \sqrt{\epsilon_0/\mu_0}$ (p. 87).

$i_c(t)$: A temporal current excitation on the dipole (p. 87).

$\left(E_0^+\right)_1(t)$: First-order electric field for the FMCW waveform (p. 88).

ρ_s' : Range variable from $-\frac{\Delta\rho_s}{2}$ to $\frac{\Delta\rho_s}{2}$, of the ocean surface (p. 90).

$\left(E_0^+\right)_{11}(t_r)$: First-order electric field scattered from the first-order ocean waves (FMCW waveform) (p. 92).

$\left(E_0^+\right)_{12}(t_r)$: First-order electric field scattered from the second-order ocean waves (FMCW waveform) (p. 92).

${}_1P_{\vec{K},\omega}$: Fourier series coefficients of the first-order wave (p. 92).

${}_2P_{\vec{K},\omega}$: Fourier series coefficients of the second-order wave (p. 92).

$\left(E_{0g}^+\right)_1(t)$: First-order electric field for the FMICW waveform (p. 93).

$\left(E_{0g}^+\right)_{11}(t_r)$: First-order electric field scattered from the first-order ocean waves (FMICW waveform) (p. 95).

$\left(E_{0g}^{+}\right)_{12}(t_r)$: First-order electric field scattered from the second-order ocean waves (FMICW waveform) (p. 95).

$\left(E_{0}^{+}\right)_{11}^{D}(t_r)$: Demodulation of the first-order electric field (FMCW waveform) (p. 96).

ω_r : Transform variable corresponding to t_r (p. 98).

$\Phi_1^r(\omega_r)$: First-order range spectrum for the FMCW waveform (p. 98).

Δf : Frequency offset to the carrier frequency f_0 (p. 100).

Δf_{max} : Maximum frequency offset to f_0 (p. 100).

ρ_{MAX} : Theoretical maximum range of measurement (p. 100).

f_s : Sampling frequency (p. 103).

N_T : Number of samples within a sweep interval T_r (p. 103).

ρ_{max} : Maximum range of radar detection (p. 103).

ρ_r : Range variable from 0 to ρ_{max} (p. 104).

n_f : Frequency number over the range spectrum (p. 104).

$\Phi_2^r(\omega_r)$: Second-order range spectrum for the FMCW waveform (p. 104).

$\left(E_{0g}^{+}\right)_{11}^{D}(t_r)$: Demodulation of the first-order electric field (FMICW waveform) (p. 105).

$\Phi_{1g}^r(\omega_r)$: First-order range spectrum for the FMICW waveform (p. 106).

$\Phi_{2g}^r(\omega_r)$: Second-order range spectrum for the FMICW waveform (p. 110).

$\Phi_1^r(\omega_r,\ t)$: First-order time-varying range spectrum for the FMICW waveform (p. 113).

$\Phi_2^r(\omega_r,\ t)$: Second-order time-varying range spectrum for the FMICW waveform (p. 114).

$\Phi_{1g}^r(\omega_r,\ t)$: First-order time-varying range spectrum for the FMICW waveform (p. 114).

$\Phi_{2g}^r(\omega_r,\ t)$: Second-order time-varying range spectrum for the FMICW waveform (p. 114).

τ : Time shift (p. 115).

$\mathcal{R}_1(\omega_r, \tau)$: Normalized autocorrelation for the first-order backscatter field for the FMCW waveform (p. 115).

A_r : Effective free space aperture of the receiving antenna (p. 115).

L_s : Fundamental wavelength of the surface (p. 116).

N_s : $N_s = \dfrac{2\pi}{L_s}$ (p. 116).

T_s : Fundamental period of the surface (p. 116).

W_s : $W_s = \dfrac{2\pi}{T_s}$ (p. 116).

K_x : x component of the ocean surface wave (p. 116).

K_y : y component of the ocean surface wave (p. 116).

$\mathcal{P}_1(\omega_r, \omega_d)$: First-order PSD for the FMCW waveform (p. 117).

$\sigma_1(\omega_r, \omega_d)$: Range dependent first-order cross section for the FMCW waveform (p. 119).

$\mathcal{R}_2(\omega_r, \tau)$: Normalized autocorrelation for the second-order backscatter field for the FMCW waveform (p. 119).

$\mathcal{P}_2(\omega_r, \omega_d)$: Second-order PSD for the FMCW waveform (p. 120).

$\sigma_2(\omega_r, \omega_d)$: Range dependent second-order cross section for the FMCW waveform (p. 121).

$\mathcal{R}_{1g}(\omega_r, \tau)$: Normalized autocorrelation for the first-order backscatter field for the FMICW waveform (p. 122).

$\mathcal{P}_{1g}(\omega_r, \omega_d)$: First-order PSD for the FMICW waveform (p. 122).

$\sigma_{1g}(\omega_r, \omega_d)$: Range dependent first-order cross section for the FMICW waveform (p. 123).

$\mathcal{R}_{2g}(\omega_r, \tau)$: Normalized autocorrelation for the second-order backscatter field for the FMICW waveform (p. 124).

$\mathcal{P}_{2g}(\omega_r, \omega_d)$: Second-order PSD for the FMICW waveform (p. 124).

$\sigma_{2g}(\omega_r, \omega_d)$: Range dependent second-order cross section for the FMICW waveform (p. 125).

$\sigma_1(\omega_d)$: Range independent first-order cross section for the FMCW waveform (p. 126).

$\sigma_2(\omega_d)$: Range independent second-order cross section for the FMCW waveform (p. 126).

$\sigma_{1g}(\omega_d)$: Range independent first-order cross section for the FMICW waveform (p. 126).

$\sigma_{2g}(\omega_d)$: Range independent second-order cross section for the FMICW waveform (p. 127).

ω_{B}^{m} : Theoretical Bragg frequency for the FM waveforms (p. 130).

F_{am} : *Median* value of external *noise figure* (p. 140).

$\mathrm{N_{event}}$: Number of statistical events for different FFT overlap percentages (p. 157).

$\Theta(t_r)$: Summation of all the phase terms added to the received signal (p. 176).

$E^D(t_r)$: Demodulation with respect to $E(t_r)$ (p. 176).

LPF : Operation of low-pass filtering (p. 176).

$\left(E_0^+\right)_{12}^{D}(t_r)$: Demodulation of $\left(E_0^+\right)_{12}(t_r)$ (p. 177).

$\left(E_{0g}^+\right)_{12}^{D}(t_r)$: Demodulation of $\left(E_{0g}^+\right)_{12}(t_r)$ (p. 179).

Chapter 1

Introduction

1.1 General Introduction

When high frequency (HF, 3-30 MHz) ground wave radar is employed as a remote sensing tool in a marine environment, the transmitted signals, which are guided by a good conducting medium like ocean water, travel along the earth's curvature, reach far beyond the line-of-sight horizon, and couple strongly with the ocean surface. The radar received signals contain a large amount of information about the ocean surface itself as well as about objects on or near the surface. Useful data products include surface current vectors, wind and wave speeds and directions, and velocity information for hard targets such as ships, low-flying aircraft, and icebergs.

Figure 1.1 is a typical example of the Doppler spectrum (power spectral density, (PSD)) simulated with the radar frequency of 25 MHz and the wind velocity of 15 m/s, perpendicular to the radar look direction. The most significant effect which the ocean has on the Doppler spectrum is the production of two large peaks on each side of the zero Doppler frequency. These peaks, which are denoted as the first-order peaks, or Bragg peaks, are surrounded by a continuum that contains higher-order interactions between the electromagnetic (e-m) waves and ocean waves (Hasselmann, [1]). In Figure 1.1, the simulated continuum contains only the second-order scattering effects.

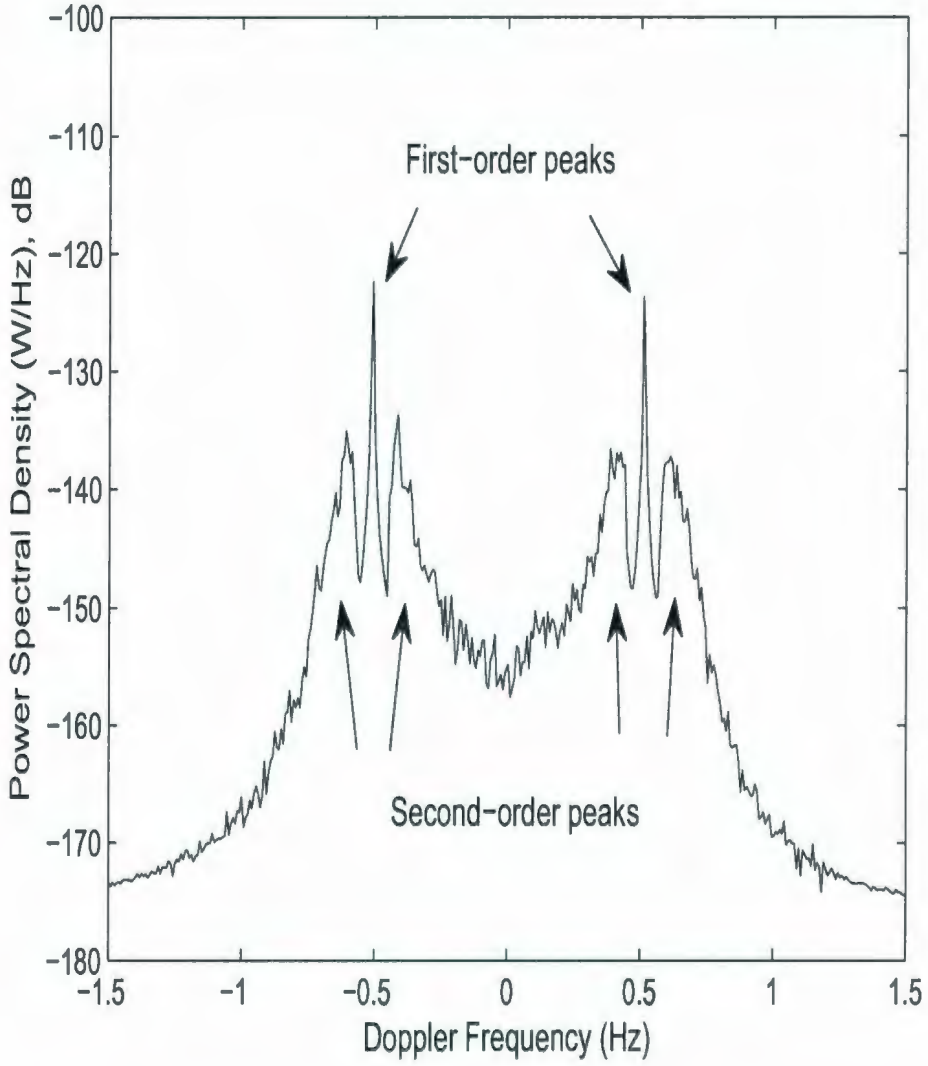

Figure 1.1: Simulated first- and second-order backscatter Doppler spectra with the operating frequency of 25 MHz and the wind velocity of 15 m/s, perpendicular to the radar look direction.

The fundamental mechanism of HF radar scatter over the ocean surface has been well accepted as Bragg scatter. Crombie [2] experimentally observed energy peaks at discrete frequency shifts above and below the carrier frequency in the radar spectrum. These peaks correspond uniquely to ocean waves which move directly toward and away from the radar (for positive and negative Doppler, respectively) and which for grazing incident angles have wavelengths exactly one-half the radar operating wavelength. Originally, ocean gravity waves of different wavelengths travel at different speeds as determined by the dispersion relationship for such waves. The occurrence of non-linear interaction among the ocean waves results in second-order and/or higher-order ocean waves with variable speeds. The signal backscattered from them will contain a range of Doppler frequencies as evidenced by the continuum in the received spectra.

The HF frequency band includes radiation of dekametric wavelengths, and the ocean surface waves responsible for the Bragg scatter in this context will have similar wavelengths. These waves, which are generated by wind and which are subject to a gravitational restoring force, are typically referred to as gravity waves. Gravity waves with various lengths (periods), heights, and directions disturb the ocean surface in four dimensions (three in space and one in time). The quantitative interpretation of the disturbed ocean surface requires the combination of deterministic and statistical analyses. Kinsman [3] summaries the various treatments in detail.

The similarity of wavelengths between e-m waves and ocean gravity waves causes a strong interaction between the two and provides the basis for HF radar to be a powerful oceanic remote sensing tool. Since the early 1970's, HF ground wave radar has proven useful in several important maritime applications. These include environmental assessment, fisheries management, offshore engineering and construction, search and rescue, national defense, and oceanographic research. In particular, HF radar ocean surface current measurement systems have been well developed and successfully operated throughout the world. The principle of these current measurement systems involves a frequency shift of the measured Bragg peaks from their theoretical positions in the Doppler spectra derived

from the Bragg scatter mechanism. This shift is primarily due to the motion of current beneath the water waves. The radial current speed along the radar look direction can be obtained from the magnitude of this shift. The current velocity can be extracted through vector summation if two separated radar receivers are employed and radial current speeds are measured individually and simultaneously.

Over the last three decades, several mathematical models have been developed to explain Crombie's experimental conclusions (e.g. Barrick [4], Srivastava [5], Walsh *et al.* [6]). All of these models successfully predict definite locations of the Bragg peaks. However, when comparing the theoretical result with practical measurement, fluctuations of the Bragg peaks and variations of the Doppler spectral magnitudes at every frequency point may be observed. These phenomena imply the existence of randomness in the radar received signal that needs further investigation, particularly since they influence the precision of the ocean surface current parameters deduced from the radar data. It is conjectured that the randomness of the ocean surface being interrogated by the radar is at least one of the reasons why the Bragg peaks fluctuate.

Initially in this thesis, the fluctuation of the Bragg peaks is considered under the assumption of a pulsed sinusoid being used as the transmitted waveform. In recent years, frequency modulated (FM) signals have been used extensively in HF radar remote sensing applications, and consequently will be considered here also. Of particular interest are the frequency modulated continuous wave (FMCW) and frequency modulated interrupted continuous wave (FMICW). The properties of the radar received signals from the ocean surface illuminated by such FM sources are highly desired in practice and will be carefully investigated in this study.

1.2 Objectives

The underlying mechanism of the fluctuations of the Bragg peaks will be examined based upon statistical analysis. The time series of radar return from the ocean surface will be

simulated using the radar cross section equations developed for the pulsed radar backscatter (see Walsh *et al.* [6]) and Pierson's model [7] of the ocean surface profile. Since in practice, measurements are always over finite space and finite time, it is desirable to find a way to describe the variability in the Doppler spectra, and thus the Bragg centroid randomness, from the finite length time series obtained from a finite width of the scattering patch over the ocean surface. This forms the primary objective of the first part of this research, which may be stated as the theoretical characterization of the Bragg fluctuations when the pulsed HF radar is used in ocean surface measurement.

The main differences between the proposed approach and earlier analyses (e.g. Barrick and Snider [8] and Barrick [9]) are that: (1) a pulsed source is assumed, corresponding to a finite radial width of the scattering patch, and (2) the dependence of the surface Fourier coefficients as functions of wave vectors with random phases is explicitly entered into the electric field equations before any other statistical averaging is carried out. Preliminary results for the pulsed signals appear in Zhang *et al.* [10] and further quantitative analysis forms a main portion in this thesis. It is expected that this analysis will help to determine appropriate error bounds for current measurement over the ocean surface.

In addition to the ordinary pulsed sinusoidal waveform, FM waveforms have become popular in HF radar systems. Consequently, it is desired to further check the feature of scatter and the Bragg fluctuation properties for these waveforms. As noted in Section 1.1, two linearly frequency modulated waveforms, namely FMCW and FMICW, will be considered. The first step of the second portion of the research is to evaluate the temporal electric field equations based on the general equations in Walsh *et al.* [6] (also appearing in the open literature in Walsh and Gill [11]). The PSD functions are obtained by calculating the Fourier transform of the autocorrelation function of the electric field equations. The radar cross sections will be obtained with the assumptions of a monostatic radar configuration (i.e. co-location of radar transmitter and receiver) and a time-varying Gaussian ocean surface profile. In the development of the second-order FMCW and FMICW cross sections, only the patch scatter from second-order waves resulting from hydrodynamic

coupling, which is dominant of all the second-order scatter cases, will be considered. The fluctuation properties of the Bragg peaks for the FM waveforms will be examined carefully following the process which is first developed for the pulsed radar waveform. The simulation results and the fluctuations of the Bragg peaks for the FMCW waveform will be compared with field data obtained from a Wellen Radar (WERA) (e.g. Wyatt *et al.* [12]).

1.3 Literature Review

1.3.1 Cross Section Development and Related Work

The phenomenon of scattering e-m waves from rough surfaces has been studied extensively as a classical problem in radio wave propagation, especially for surface wave communications. The analysis of developing a radar cross section model over the ocean surface finds its roots in the work of Lord Rayleigh on the scattering of acoustic waves from rough surfaces by a perturbation method (see Strutt [13]). The radar cross section is defined as "that area which, when multiplied by the power flux density of the incident wave, would yield sufficient power that could produce by isotropic radiation, the same radiation intensity as that in a given direction from the scattering surface" [14]. When the same method has been used by later investigators in analyzing e-m wave scatter from rough surfaces, the assumption of "slightly rough" is imposed. The term "slightly rough" is defined as that the product of the incident wavenumber and any surface deviation from the mean should be very much less than unity.

Following Rayleigh's perturbation method, Rice [15] investigated e-m wave scatter from a non-time-varying, two-dimensional "slightly rough" surface. Besides the slightly rough assumption, Rice chose the scattering surface to be a perfect conductor and the incident wave to be plane. It is through the boundary conditions that the surface parameters enter into the expression of the e-m field over the surface. In Rice's investigation, the

scattering field intensities were obtained up to second-order for both horizontal and vertical polarizations. Based upon Rice's perturbation approach, Peake [16] obtained the first-order backscatter cross section for a dielectric slightly rough surface for both polarizations. Rice's and Peake's analyses did not take the rough surface as a time-varying medium, however.

Valenzuela [17] developed the first- and second-order HF radar cross sections using a Neumann spectrum and cosine-squared directional distribution to describe the fully developed sea surface. A fully developed sea is one for which the wind blows over the surface sufficiently long from the same direction so that the created ocean waves will reach their saturation state. When the sea waves are fully developed, the wind will no longer be able to add net energy to them, and the sea state will have reached its maximum.

Barrick [18] extended Rayleigh's perturbation method to include a good conducting surface. He introduced the effective surface impedance when HF and very high frequency (VHF) e-m waves are incident on the ocean surface at grazing angles. He also found that the e-m wave propagation losses would increase according to the increased sea state. Barrick [4] then achieved an expression for the HF radar first-order cross section over a time-varying ocean surface, which gave Crombie's [2] experimental deductions a solid theoretical verification. In Barrick's first-order cross section expression, two symmetric Dirac delta functions are used to define the first-order Bragg "peaks" which appear at $\omega_B = \pm\sqrt{2gk_0}$, where ω_B is Doppler radian frequency of the Bragg peaks, g is acceleration due to gravity, and k_0 is wavenumber of the incident radiation, $k_0 = \omega_0\sqrt{\mu_0\epsilon_0}$, where ω_0 is the angular frequency of the electric field, while ϵ_0 and μ_0 are the electrical permittivity and magnetic permeability of free space, respectively. The Dirac delta functions in [4] result from the fact that the incident signal is chosen to be a plane wave.

In [19], Barrick developed the second-order backscatter cross section over the ocean surface. This is indicated by the continuum surrounding the Bragg peaks in Figure 1.1. He determined that the second-order cross section could be modeled as one scatter from a combination of two first-order ocean wave components or two successive scatters from

two first-order ocean waves. In keeping with the Bragg scatter mechanism, the wavelength of the combined components should match one-half the radar wavelength after vector addition and the direction of the combination should be along the radar beam. This cross section formulation is a nonlinear, two-dimensional, Fredholm-type integral equation, in which the integrand contains the hydrodynamic and e-m coupling coefficients corresponding to the different mechanisms of the second-order interactions between the radar signal and water waves as mentioned above. The nonlinearity of the second-order cross section arises from the product of two ocean wave directional spectra. A Dirac delta function in the integrand constrains the manner in which the wave vectors from the two spectra must be related to produce the continuum.

Other contributions to the topic of e-m fields scattering from rough surfaces include the methods of physical optics (Kodis [20], Barrick and Bahar [21]), the composite surface scattering approach (e.g. Brown [22, 23]), and the full-wave technique (e.g. Bahar [24], Bahar and Rajan [25]).

Largely based on Barrick's models, investigations were undertaken to obtain ocean surface information, including currents, directional wave spectra, and wind fields, from the HF radar received signals (e.g. Barrick *et al.* [26], Barrick [9], Lipa and Barrick [27, 28], Wyatt [29]). Lipa [30] reduced Barrick's [19] second-order cross section to a set of linear equations, which may be used to obtain the directional features of the ocean spectrum. Barrick and Lipa [31] discussed ocean current measurement from the first-order cross section of the radar received signal. They further derived a set of expressions [32] to account for shallow water. All of these models are for backscatter returns, and assumptions are made for grazing incidence and vertical polarization of the radar wave.

As noted above, Barrick's cross section methods [4, 19] (and those of several others), which are denoted as Barrick's method, are developed based on the assumption of a plane wave for the incident wave field. The Bragg scatter mechanism appearing in the cross section equations of Barrick's method is addressed by means of Dirac delta functions. This means that theoretically, the width of the Bragg peak is infinitesimal. In practice, however,

the Doppler spectra of the received signals exhibit finite-width Bragg peaks. These finite widths are commonly explained as a combined consequence of system timing limitations, external noise, such as noise from man-made sources and motion of the ionosphere, and surface current variability. Development of a cross section that better addresses at least the system timing issues is considered next.

Based on a generalized function method (e.g. Walsh [33]), Walsh and his colleagues (Srivastava, Dawe, Howell, and Gill) addressed the problem of e-m wave scatter from the ocean surface under the same assumptions as Barrick but with a pulsed radar waveform (see, for example [5, 6, 34, 35]). This approach, denoted as Walsh's method, leads to a squared sinc function in the cross section equations. In Walsh's method, it is the squared sinc function that models the connection between the radar radiation wavenumber k_0 and ocean wavenumber K through the Bragg scatter mechanism. In the spatial sense, the appearance of the squared sinc function in the cross section expression corresponds to the finite width of the scattering patch, which is determined by the duration of the transmitted pulse. With the squared sinc function, the positions of the Bragg peaks and the width of the Bragg region are sufficiently determined by k_0 and the radial extent $\Delta\rho_s$ of the scattering patch, or equivalently, by the pulse width τ_0. As the pulse duration tends to infinity, which it would for a plane wave, the scattering patch would be of infinite extent, the squared sinc function would be reduced to a Dirac delta function, and Walsh's results would reduce to those of Barrick's.

Walsh's method has been well developed over the last two decades and has gained extensive acceptance in the HF radar remote sensing community. The successful models include the first- and second-order cross sections developed by Srivastava and Walsh [5] for backscatter, higher-order backscatter cross sections by Walsh *et al.* [6], and bistatic radar cross sections by Walsh and Dawe [34], Gill and Walsh [35], and Gill *et al.* [36]. Based upon these cross sections, algorithms for extracting current velocity (e.g. Bobby [37], Jin [38]), wave height spectra (e.g. Gill and Walsh [39], Howell and Walsh [40], Zhang and Gill [41]), and HF radar received clutter and noise model [42] have been developed.

Several of these algorithms have been validated with field experiments.

In illustrating outcomes from Walsh's technique, the ocean surface profile has been typically described by Pierson's model [7], in which the time-varying ocean surface is a weighted combination of sinusoids with an infinite number of frequency and wavenumber components. The weighting factor contains a square-root of the wave directional spectrum which is a function of wind speed and direction. For each frequency or wavenumber component there is a time independent random phase factor which indicates its initial condition. The random phase variable is uniformly distributed from 0 to 2π. Pierson's model is a Gaussian interpretation of the ocean surface not only in space but also in time. While it is known the ocean surface is certainly not always Gaussian in nature, this description has been often successfully employed by both oceanographers (e.g. Kinsman [3]) and other researchers requiring a model for radar applications (e.g. Barrick and Snider [8]). Pierson's model has been successfully used in Walsh's radar cross sections for both monostatic and bistatic configurations, the latter referring to deployments for which the transmitter and receiver are widely separated from each other.

In much of the work by Walsh and his colleagues, the fact that the Fourier coefficients of the ocean surface are stationary time-varying random variables is implicit. Averaging over ideally long periods of time will remove any randomness and time dependency from the resulting Doppler spectra. However, if the power spectra are constructed from finite length time series, they will definitely exhibit a stochastic nature, which is an interesting problem of radar remote sensing that needs to be explored in depth.

1.3.2 HF Radar for Ocean Current Measurement

Conventional current measuring techniques may be distinguished by two types: Lagrangian and Eulerian [43]. Lagrangian type instruments, such as drifters, are deployed in a region where the current is to be measured. They will then drift following the motion of the water. Their positions must be tracked by ship, plane, or satellite. On the other hand, current

meters and acoustic Doppler current profilers (ADCP) are examples of Eulerian devices that are used to measure the velocity of water at a fixed position. An ADCP transmits and receives three to four acoustic beams and calculates the Doppler shifts in several directions. Each beam gives the radial current speed in the beam look direction, and the combination of several radial speeds will give the current velocity. Both Lagrangian and Eulerian methods are expensive for large-area monitoring, and, for the latter, since the acoustic frequencies are chosen typically from 0.25 MHz to 1 MHz, they are primarily useful for water depths from 3 m to over 100 m, i.e. the surface is excluded.

Crombie [44] first studied surface currents using HF ground wave radar. Subsequent experiments were carried out in 1972 at San Clemente Islands, USA, to investigate the resolution of current velocity (e.g. Stewart and Joy [45], Barrick *et al.* [26]). Results were compared with those obtained independently from drifters, and it was found that the resolution was better than 10 cm/s. It was also concluded that the current speed measured by HF radar is a mean value from sea surface to a depth of approximately $\lambda/8\pi$, where λ is the wavelength of the ocean wave from which the Bragg scatter will occur under grazing illumination by HF radar.

It may be pointed out that the nature of HF radar ocean current measurement may, in a sense, be considered from both the Lagrangian and Eulerian viewpoints (e.g. Fernandez [46]). From the Lagrangian perspective, the surface waves can be viewed as the drifters flowing with the current at the patch illuminated by the radar. Current speed along the radar look direction will cause additional Doppler shifts upon the theoretical Bragg frequency. Usually, these additional Doppler shifts have the same values and directions for left and right Bragg scatters. As a Eulerian type measurement, on the other hand, HF radar is considered to be used to measure the current within a specific region. This special characteristic of both Lagrangian and Eulerian types of HF radar measurements implies that the statistical averages are taken not only in a limited range but also in a limited duration.

There are many advantages in using HF radar for current measurement. Depending

on the operating frequency, it may routinely and economically provide over-the-horizon (OTH) coverage to more than 300 km in the radial direction over an area of a few thousand square kilometres. The ocean surface within the HF radar coverage is divided into many cells. The size of these cells depends upon the radar beam width and the width of the transmit pulse. Typically, a cell has a size scale from several hundred square metres to several square kilometres. HF radar ocean surface current measurement can be performed in near real time. A typical example of where such measurements would be highly beneficial is in the Grand Banks region, NL, Canada, where the offshore oil and gas industry is under active growth. The platformed structures may be hazarded by icebergs and bergy bits, which may attain significant velocities under the influence of surface currents. Therefore, detailed current records of this region may be helpful in the design and deployment of the offshore oil platforms.

In practical current measurements, radar Doppler spectra are calculated from the received time-varying field signals by means of spectral estimation. For the purpose of this work it includes three steps: The first step is to calculate the autocorrelation function of the time series. The second is to Fourier transform the autocorrelation function to obtain the Doppler PSD. The last is to locate the Bragg peak positions, positive and negative, and compare them to the theoretical Bragg frequencies. The Doppler difference of the Bragg lines from their theoretical positions is a clear indication of the underlying radial surface current. The product of the first and second steps is typically referred to as the periodogram, which may be equivalently calculated by the square of the magnitude of the Fourier transform of the radar received time series (Wiener-Khintchine theorem, see, for example, Proakis [47]).

Ideally, it would be desired that the positions of the Bragg peaks be stable over temporal periods associated with the radar measurements. However, fluctuations of the Bragg peaks have been observed when a specific ocean area is illuminated continuously and the Doppler spectra are calculated from consecutive time periods. Barrick and Snider [8] studied the statistical properties of the HF sea-echo signals received from the ocean

surface. Since the ocean surface height is recognized by oceanographers (e.g. Kinsman [3]) as a Gaussian random variable to first-order, Barrick and Snider asserted that the radar received sea echo signal is also Gaussian because: (1) it is synthesized as the sum of a large number of independent random events (Central Limit Theorem), (2) the expression of the backscattered electric field is essentially a linear operation upon a Gaussian random variable which gives another Gaussian random variable, and (3) real radar data are used to check the assumption and the results are positive.

Under the assumption of a Gaussian distribution of the sea echo signal, Barrick and Snider [8] pointed out that at each frequency position in the Doppler spectrum, the magnitude of the PSD will be a chi-square random variable with two degrees of freedom. Real data from HF radar located on the west coast of San Clemente Island were used to examine this deduction [8]. The normalized standard deviations of the power at specific spectral positions were calculated for 9×200 s time segments. Radar data of different operating frequencies, pulse widths, and different ranges were calculated to check the possible dependencies upon these parameters. Results indicated that no such dependencies were evident for all of them. Therefore, Barrick and Snider confirmed the Gaussian nature of the received scattering signal and gave a partial explanation to the Bragg fluctuations.

Based on the initial analysis, Barrick [48] derived an equation for the standard deviation of the Bragg fluctuations, which can be applied to bound the error of current measurement. The deduction of this equation applies under two conditions. The first is that the power at each frequency point is chi-square distribution with two degrees of freedom. The second is that the equivalent number of spectral points within the Bragg region be large. The latter condition ensures the distribution of the Bragg fluctuations is Gaussian and a closed form expression can be approximated. The influence of the shape of the Bragg region is also discussed. Because Barrick's equation for the standard deviation does not include a particular shape of the Bragg region, two models of shapes are checked: a rectangular shape and a Gaussian shape. The results show a very weak dependence upon shape.

Barrick's [48] standard deviation equation for the Bragg fluctuations does not specify

where the width of the Bragg region comes from. As mentioned earlier, Barrick's radar cross section method describes the Bragg scatter mechanism by a Dirac delta function, which dictates that the width of the Bragg region is infinitesimally narrow if other influences are absent. Therefore, the width of the Bragg region can only be considered to arise from some secondary sources, such as current variability and/or ionospheric motions.

In some HF radar field experiments a narrow Bragg peak can be achieved. For example, Barrick and Snider [8] used 20 μs and 100 μs pulse widths, corresponding to the range sizes (i.e. radial resolutions) of 3,000 m and 15,000 m, respectively. Within the operating frequency band, 3 MHz to 30 MHz, these pulse widths are large "enough" so that the incident radiation may be approximated as plane waves. However, 3 km and 15 km range resolutions are fairly coarse for ocean surface measurement. In fact, some modern HF radar systems have bandwidths large enough to give resolutions of 400 m or less (e.g. Hickey [49], Wyatt *et al.* [12]).

Since the width of the Bragg region likely results from multiple factors, it is important to investigate these factors. The Dirac delta function definition of the Bragg peak is not physically suited to such considerations.

As noted, in Walsh's formulations for the first-order field equation, the broadness of the Bragg region appears naturally from the analysis due to the specification of a pulsed source. In Walsh's Doppler spectrum, every frequency point within the Bragg region has a clear definition. That is, unlike the Dirac delta function that has value only at one point, the squared sinc function alluded to in Section 1.3.1 is, in fact, defined throughout the whole frequency domain.

As a further reason for the present investigation, it may be pointed out that modern HF radar systems are utilized not only for the remote sensing of ocean surface parameters, but may also be utilized for continuous over-the-horizon surveillance within a nation's 200 nautical mile exclusive economic zone (EEZ). This task includes detection of hard targets such as ships, missiles, and low-flying aircraft; and in these applications, the ocean clutter appearing in the Doppler spectrum will be viewed as the spectral background of the useful

information. In some cases the radial speed information of the target may be masked by the Bragg peaks, but clutter suppression techniques may be employed to uncover them. In view of these issues, a detailed knowledge of the Bragg scatter mechanism and its statistical properties will be vital in the development of such clutter suppression algorithms.

1.3.3 Transmitting Waveforms for HF Radar

It is known that the phenomenon of the Bragg fluctuations is evident no matter what radar waveform is employed. As noted previously, in the HF radar remote sensing community, frequency modulated waveforms, such as FMCW and FMICW, are widely used. Barrick [50] presented two fast Fourier transform (FFT) based techniques for processing FMCW radar signals. The first technique includes two consecutive FFT processes. Radar signals are first FFT transformed within a sweep interval to obtain the range information. Then the second FFT is carried out over several sweep intervals to give Doppler information. The second technique involves performing a single long FFT transform over several sweep intervals. Range and Doppler information can be derived simultaneously. Both techniques are shown to give identical results with the same FFT execution times.

Khan and Mitchell [51] presented a waveform analysis for a radar system with a design capability for over-the-horizon detection of ocean surface targets up to 400 km and a range resolution of 400 m. This analysis has been applied in the operation of a shore-based long range HF ground wave radar (HFGWR) system at Cape Race, Newfoundland, Canada. Several experiments have been conducted to verify the capabilities of the Cape Race HFGWR system using the FMICW waveform (e.g. Khan *et al.* [52]). In these experiments, a navy vessel, a helicopter, and three different icebergs were detected and encouraging results were obtained. In addition to the hard target detection and tracking over the ocean surface, Khan and Mitchell [51] suggest the possible capability of ocean surface parameter extraction by the radar system. However, there is no further report along this direction in that publication.

Both FMICW and FMCW radar transmitting waveforms can achieve good range and Doppler resolutions depending on bandwidth and sweep period. The FMCW waveform may be viewed as a special case of the FMICW waveform with duty cycle of the interrupt sequences equal to unity (see Khan and Mitchell [51]). Within a single frequency sweep, the use of the FMCW and FMICW waveforms ideally requires an instantaneous changing of radar transmitting frequencies. Even within a single pulse for the FMICW waveform, strictly speaking, the frequencies are changing from beginning to end. Recalling the mechanism for the Bragg scattering, the changing of operating frequency corresponds to different wavelengths of ocean waves for which Bragg scatter occurs. If the PSDs of the radar received sea echo signals within a finite time duration are examined, the Bragg fluctuations might be expected to exhibit some features which differ from those associated with the pulsed waveform. Therefore, derivation of the radar cross sections and examination of the Bragg fluctuations for the FM waveforms are of particular interest for ocean surface applications.

1.3.4 A Brief Consideration of HF Radar Systems Worldwide

Table 1.1 lists some of the major past and present HF radar ocean surface measurement systems around the world. In this table, the methods of range resolution include three sorts of waveforms: pulsed, FMCW and FMICW. Among them the FM waveforms are becoming more popular, especially in state-of-the-art systems. Direction finding and beamforming are two techniques of azimuthal resolution and are denoted in the table by D and B, respectively. Direction finding is based on the Fourier decomposition of the time series received by several (usually three or four) antennas [53]. Each Fourier component is attributed to a Doppler shift and in turn to a radial speed. Different radial speeds can be obtained by comparing the phases at the antenna receivers. The main advantages of the direction finding technique are that the compact phase-measuring arrays used may be quickly deployed and require little real estate.

Table 1.1: Past and Existing HF Radar Systems around the World. "D" represents direction finding and "B" represents beamforming.

System	Country	Waveform	D/B
CODAR (Barrick [53])	USA	pulsed	D
COSRAD (Heron *et al.* [54])	Australia	pulsed	B
HF ocean radar of CRL (Takeoka *et al.* [55])	Japan	FMICW	B
HFGWR (Hickey [49])	Canada	FMICW	B
OSMAR2000 (Yang *et al.* [56])	China	FMICW	B
OSCR (Prandle *et al.* [57])	UK	pulsed	B
PISCES (Shearman and Moorhead [58])	UK	FMICW	B
SeaSonde (Paduan and Rosenfeld [59])	USA	FMICW	D
WERA (Gurgel *et al.* [60])	Germany	FMCW	D/B

Another method to extract directional information is beamforming. In this method, large antenna arrays are used to generate a narrow radar beam. The radial speeds of targets (or ocean current) along the radar look direction can be measured. When two radar systems are deployed to cover the same area, the current velocity can be obtained through vector combination. The main advantage of beamforming, in general, is that in comparison to the compact systems used in direction-finding, large arrays allow for the extraction of higher-resolution information from the Doppler continuum and put less severe restrictions on signal quality. The information so obtained includes directional ocean-wave spectrum and surface wind velocity.

Other HF radar ocean remote sensing systems include multifrequency coastal radar, or the MCR system, which was originally designed by Stanford University in 1970's (e.g. Teague [61] and Fernandez [46]) and then developed jointly by the University of Michigan, the Environmental Research Institute of Michigan (ERIM), and Stanford University (e.g. Teague *et al.* [62]). This system can transmit signals at four different frequencies, simultaneously. Since different frequencies correspond to current speeds for different depths, the MCR system is able to measure the current speeds in different depths in the same scattering patch; i.e. the current shear in the vertical plane from the top to some maximum

depth, determined by the lowest of the multiple frequencies, may be estimated.

Ground wave propagation is not the only mode of operation which can be used to remotely sense the ocean surface. There are several HF radar systems that are designed to measure the ocean surface using the skywave mode (e.g. Six *et al.* [63]). In skywave mode, the transmitted signal will be first reflected by the ionosphere then scattered by the ocean surface. The scattered wave will also travel back to the radar receiver by means of ionospheric reflection. Of course, the fundamental principles on which the skywave systems operate are similar to those for HFGWR. One advantage is that this system is able to measure the ocean surface that is thousands of kilometres away from the radar location. However, this system is much more complicated and the received signal from the ocean surface is very much contaminated by the unstable motion of the ionospheric layers.

Of all the HF radar systems, an HFGWR system developed by researchers and engineers at Memorial University of Newfoundland, MUN, is of particular interest here because the simulated data in this research are largely based on the parameters of this radar (e.g. Hickey [49]). The HF radar research work was initiated by Dr. John Walsh in the Faculty of Engineering and Applied Science, in the early 1980's. Within an approximate ten years research period, several programs were conducted, including those which clearly established the feasibility of using HF radar for the over-the-horizon detection of ice, the measurement of the ocean surface parameters, such as currents and waves, and the detection of hard targets, such as ships and low-flying aircraft. Many successful experiments have been carried out, not only to legitimize HF radar as a powerful oceanic remote sensor but also to help validate Walsh's generalized function approach to e-m wave scattering (e.g. Walsh *et al.* [64], Gill and Walsh [39]). It was, in fact, the observation of data collected from the Cape Race system which suggested that the variability of the centroid positions of the Bragg regions in the Doppler spectra was a problem that needed further scrutiny.

1.4 Outline of the Thesis

This study begins with the e-m field equations describing the radiation received by HF radar when the target is the ocean surface. The main purpose of this study is to investigate the behavior of the randomness of the Bragg peaks when the PSDs of finite length time series are calculated as periodograms. The emphasis is upon the description of the significance of the Bragg fluctuations when pulsed and FM waveforms are used as radar transmitting waveforms.

In Chapter 2, the investigation is focused on the pulsed waveform. Long time series of radar received signals are simulated for various operating frequencies and pulse widths based on the HF radar received clutter model developed by Gill and Walsh [42] and the cross sections developed by previous investigators (e.g. Walsh *et al.* [6], Walsh and Dawe [34], Gill and Walsh [35], Gill *et al.* [36]). These long time series are segmented into equal length sequences and PSDs are calculated for each of them. The centroids of the Bragg peaks are located from the PSD plots and compared to the theoretical Bragg frequencies. The means and standard deviations of the Bragg fluctuations are tabulated and plotted. The significance of the Bragg fluctuations is discussed and the properties are explored numerically and theoretically.

In Chapter 3, radar backscatter cross sections for the FM waveforms are developed. This is a major new initiative based upon earlier work by Walsh *et al.* [6], Walsh and Dawe [34], and Gill and Walsh [35]. Since the fluctuation investigation is mainly in the vicinity of the Bragg regions, only the hydrodynamic coupling mechanism will be considered for the second-order scatter.

In Chapter 4, the first- and second-order cross sections for the FM waveforms are depicted and compared to those for the pulsed waveform. The Bragg fluctuation properties for the FM waveforms are investigated in a manner similar to that presented in Chapter 2 for the pulsed waveform. Field data for the FMCW waveform are used to examine the simulation results and the fluctuations of the Bragg peaks.

Chapter 5 provides an overall summary of the investigations and some suggestions for future research related to the findings here.

Chapter 2

Fluctuations of the Bragg Peaks for the Pulsed Radar Waveform

To illustrate the phenomenon of the fluctuations of the Bragg peaks, i.e. to verify that such a phenomenon indeed exists and to examine its properties, time series of the backscattered electric field over the ocean surface are simulated based on cross sections for the pulsed waveform. Radar operating frequencies from the upper, middle and lower HF band are chosen for investigation. Various radar pulse widths are selected in the time series simulation. The Doppler spectra are estimated as periodograms.

In this chapter, the statistical properties of the Bragg fluctuations will be analyzed. The significance of the Bragg fluctuations will be defined and conditions of the significance will be examined. A hybrid analytical and numerical scheme is used for investigation and interpretation.

2.1 Choice of the Ocean Spectral Model

Any description of the scattering of the radar signal from the ocean surface obviously must incorporate a model of that surface. This model will be addressed in advance, following the description of Gill and Walsh [42] (see also Gill [65]).

Typically, the ocean spectrum of wavevector $\vec{K}$, $S_1\left(\vec{K}\right)$, with its direction in $\theta_{\vec{K}}$ may be expressed as the product of a non-directional spectrum, $S_1(K)$ and a normalized directional factor, $D\left(\theta_{\vec{K}}\right)$ (e.g. Kinsman [3] and Tucker [66]):

$$S_1\left(\vec{K}\right) = S_1(K) D\left(\theta_{\vec{K}}\right) . \tag{2.1}$$

The normalization on $D\left(\theta_{\vec{K}}\right)$ is such that

$$\int_0^{2\pi} D\left(\theta_{\vec{K}}\right) d\theta_{\vec{K}} = 1 . \tag{2.2}$$

Clearly,

$$\int_0^{2\pi} S_1\left(\vec{K}\right) d\theta_{\vec{K}} = S_1(K) . \tag{2.3}$$

The Pierson-Moskowitz non-directional spectrum S_{PM} [67] is selected as the ocean wave spectrum with a modification of

$$S_1(K) = \frac{1}{2} S_{\mathrm{PM}}(K) \tag{2.4}$$

by Gill [65], where

$$S_{\mathrm{PM}}(K) = \frac{\alpha_{\mathrm{PM}}}{2K^4} e^{\left(\frac{-0.74 g^2}{K^2 u_w^4}\right)} . \tag{2.5}$$

In this equation, α_{PM} is a constant with value 0.0081 and u_w represents the wind speed measured at 19.5 m above the ocean surface.

The directional distribution $D\left(\theta_{\vec{K}}\right)$ in equation (2.1) is actually also a function of wavenumber K, which can be written as

$$D\left(\theta_{\vec{K}}, K\right) = F\left(s(K)\right) \cos^{2(s(K))}\left[\frac{\theta_{\vec{K}} - \bar{\theta}(K)}{2}\right] , \tag{2.6}$$

where $s(K)$ is referred to as the spread function and $\bar{\theta}(K)$ is the dominant direction of the waves (e.g. Tucker [66]). In simulations, $\bar{\theta}(K)$ is usually replaced by θ_w, the wind direction with respect to the radar look direction. When the dependence of frequency is removed from the spread function (e.g. Tucker [66]), the simplified directional distribution is written as,

$$D(\theta_{\vec{K}}) = F(s)\cos^{2s}\left[\frac{\theta_{\vec{K}} - \theta_w}{2}\right] . \tag{2.7}$$

A typical value of $s = 2$ is chosen following the suggestion of previous investigators (for example, Lipa and Barrick [28], Howell [68], Gill and Walsh [42]). For this case,

$$F(s=2) = \frac{4}{3\pi} , \tag{2.8}$$

and the directional ocean wave spectrum will be

$$S_1\left(m\vec{K}\right) = \left[\frac{\alpha_{\mathrm{PM}}}{4K^4}e^{\left(\frac{-0.74g^2}{K^2u_w^4}\right)}\right]\left[\frac{4}{3\pi}\cos^4\left(\frac{\theta_{\vec{K}} + \frac{(1-m)\pi}{2} - \theta_w}{2}\right)\right] . \tag{2.9}$$

Figure 2.1 is an illustration of Pierson-Moskowitz ocean wave spectra as a function of ocean wavenumber. The reference direction has been switched to the direction that is perpendicular to the radar look direction through a term of $\frac{(1-m)\pi}{2}$ with $m = \pm 1$. Wind speeds are chosen to be 10 m/s, 13 m/s, and 16 m/s, respectively for comparison purpose. It is noticed that the peak increases in amplitude and shifts to lower frequency as the wind speed increases. This has a significant effect on HF radar spectra, but does not affect the first-order cross section to any great extent. This is due to the fact that the ocean waves that produce the first-order peaks are generally in the high frequency end of the ocean spectrum, corresponding to the saturated region.

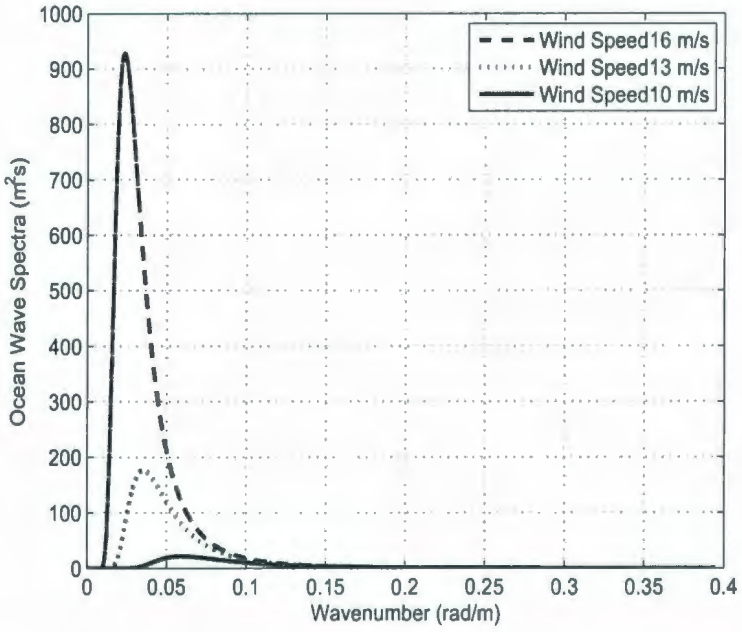

Figure 2.1: Pierson-Moskowitz ocean wave spectra as functions of wind speed and wavenumber.

2.2 First- and Second-order Backscatter Field Equations

2.2.1 First-order Cross Section

For the monostatic scattering configuration shown in Figure 2.2, the expression for the first-order cross section $\sigma_{1p}(\omega_d)$ may be obtained from Walsh *et al.* [6], or from Walsh and Gill [11] as a special case with the bistatic angle equal to zero. The result is

$$\sigma_{1p}(\omega_d) = 2^4 \pi k_0^2 \sum_{m=\pm 1} S_1(m\vec{K}) \frac{K^{\frac{5}{2}}}{\sqrt{g}} \Delta\rho_s \mathrm{Sa}^2 \left[\frac{\Delta\rho_s}{2} (K - 2k_0) \right] , \tag{2.10}$$

where the subscript p indicates that the radar transmitting waveform is a simple pulsed sinusoid. In this equation, ω_d is the radian Doppler frequency, $S_1(m\vec{K})$ is the ocean directional wave spectrum as in equation (2.9), and $\Delta\rho_s$ is the width of scattering patch,

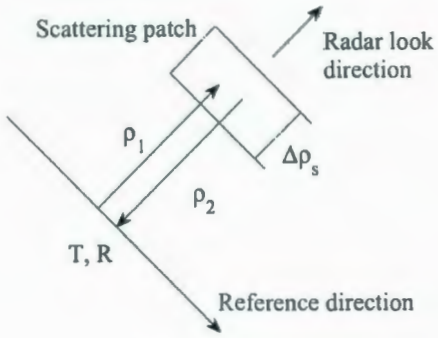

Figure 2.2: Monostatic radar configuration and the geometry of the scattering patch. The reference direction is fixed hereafter.

which is the smallest radial distance that can be unambiguously distinguished by the HF radar. Of course, $\Delta\rho_s$ depends on the pulse width τ_0 of the transmitted radar signal and is given by

$$\Delta\rho_s = \frac{c\tau_0}{2}\,, \tag{2.11}$$

where c is the vacuum speed of light (3×10^8 m/s). The $m=\pm1$ in equation (2.10) is used to distinguish the positive and negative portions of the Doppler shift, which arise from two sets of ocean waves, one with wave components moving along the radar look direction and another moving in the opposite direction; i.e.

$$m = 1 \quad \text{when } \omega_d < 0 \tag{2.12}$$

and

$$m = -1 \quad \text{when } \omega_d > 0\,. \tag{2.13}$$

The Doppler frequencies are related to the scattering wavenumber K by the dispersion relationship which is given by

$$\omega_d = -m\sqrt{gK}\ . \tag{2.14}$$

$\mathrm{Sa}(\cdot)$ is the sinc function $\left(\mathrm{Sa}(x) = \dfrac{\sin(x)}{x}\right)$. It may be noted from equation (2.10) that it is the squared sinc function that generates the first-order or Bragg peaks. This is the most significant difference between the Walsh's and Barrick's first-order cross section expression (e.g. Walsh *et al.* [6] and Barrick [4]); the latter contains a Dirac delta function as a result of using a plane wave as the transmitted signal. From equation (2.10), the magnitude K_{B} of the Bragg wavenumber responsible for the first-order scatter is specified as the value of K which maximizes $\mathrm{Sa}^2(\cdot)$. Clearly, then, for the monostatic radar configuration,

$$K_{\mathrm{B}} = 2k_0\ . \tag{2.15}$$

2.2.2 Second-order Cross Section

According to previous investigation (e.g. Hasselmann [1]), the second-order patch scatter consists of two types of interaction between the radar signal and ocean waves. One is due to the e-m signal interacting with a second-order ocean wave, which is denoted as the hydrodynamic coupling effect, while another is from the interaction between the radar wave and two first-order ocean waves, which is denoted as the electromagnetic coupling effect. If $\vec{K}_1$ and $\vec{K}_2$ are the wave vectors of the ocean waves, in order to generate the second-order scatter, $\vec{K}_1$ and $\vec{K}_2$ must satisfy the condition,

$$\vec{K}_1 + \vec{K}_2 = \vec{K}\ . \tag{2.16}$$

Here $\vec{K}$ is in the direction of the radar look direction θ_{N} and has a magnitude of $2k_0$.

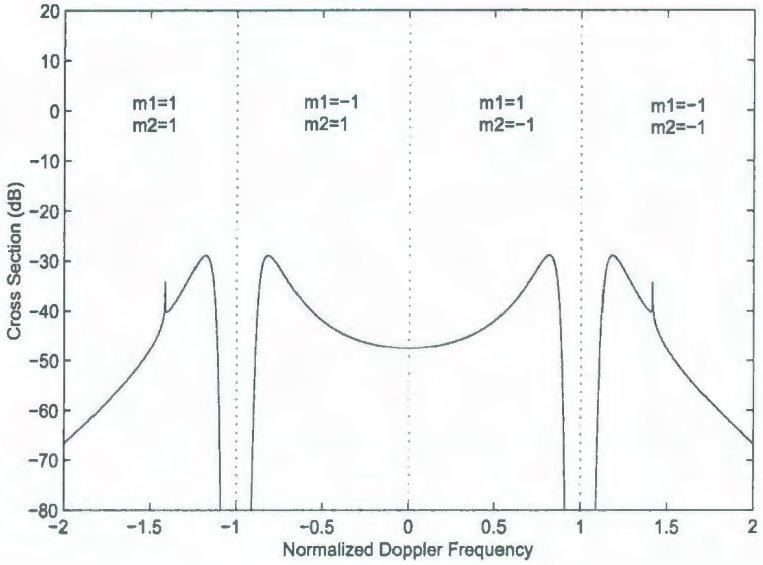

Figure 2.3: Four portions of the second-order cross section. The operating frequency is 25 MHz, the wind velocity is 15 m/s, 0° to the reference direction. Only the $K_1 < K_2$ case is simulated here.

The second-order cross section for patch scatter may be given as (e.g. Walsh *et al.* [6])

$$\sigma_{2p}(\omega_d) = 2^3\pi k_0^2 \Delta\rho_s \sum_{m_1=\pm1} \sum_{m_2=\pm1} \int_0^\infty \int_{-\pi}^{\pi} \int_0^\infty S_1\left(m_1\vec{K}_1\right) S_1\left(m_2\vec{K}_2\right) \left|{}_S\Gamma_P\right|^2 K^2$$
$$\mathrm{Sa}^2\left[\frac{\Delta\rho_s}{2}(K-2k_0)\right] \delta\left(\omega_d + m_1\sqrt{gK_1} + m_2\sqrt{gK_2}\right) K_1 dK_1 d\theta_{\vec{K}_1} dK \,, \qquad (2.17)$$

in which $\delta(\cdot)$ is the Dirac delta function. Figure 2.3 is a typical example of a second-order cross section of the patch being as depicted in Figure 2.2. Only the hydrodynamic coupling effect – i.e. the first of the two effects mentioned above – is plotted for the purpose of illustration. As shown in Figure 2.3, there are four portions corresponding to four possible combinations of m_1 and m_2, which represent four different Doppler frequency regions in the second-order cross section, respectively. If $m_1 = m_2$,

$$\left.\begin{array}{ll} \omega < -\omega_{\mathrm{B}}, & \text{when } m_1 = m_2 = 1 \\ \omega > \omega_{\mathrm{B}}, & \text{when } m_1 = m_2 = -1 \end{array}\right\} . \qquad (2.18)$$

If $m_1 \neq m_2$, $-\omega_B < \omega < \omega_B$, and

$$\left.\begin{array}{ll} -\omega_B < \omega < 0, & \begin{array}{l} m_1 = -1,\ m_2 = +1 \text{ if } K_1 < K_2 \text{ or} \\ m_1 = +1,\ m_2 = -1 \text{ if } K_1 > K_2 \end{array} \\ \text{and} & \\ 0 < \omega < \omega_B, & \begin{array}{l} m_1 = -1,\ m_2 = +1 \text{ if } K_1 > K_2 \text{ or} \\ m_1 = +1,\ m_2 = -1 \text{ if } K_1 < K_2 \end{array} \end{array}\right\} . \tag{2.19}$$

The parameter ${}_S\Gamma_P$ in equation (2.17) is referred to as the coupling coefficient. It is defined as

$${}_S\Gamma_P = \frac{1}{2}\left[\Gamma_P\left(\vec{K}_1, \vec{K}_2\right) + \Gamma_P\left(\vec{K}_2, \vec{K}_1\right)\right] , \tag{2.20}$$

with

$$\Gamma_P = {}_H\Gamma_P + {}_E\Gamma_P , \tag{2.21}$$

where ${}_H\Gamma_P$ is the hydrodynamic coupling coefficient and ${}_E\Gamma_P$ is the electromagnetic coupling coefficient. The hydrodynamic and electromagnetic coupling coefficients correspond, respectively, to the two scattering mechanisms referred to at the beginning of this subsection. The general expression of the hydrodynamic coupling coefficient is given by Walsh *et al.* [6], and for deep water, it can be simplified as

$${}_H\Gamma_P = \frac{1}{2}\left\{K_1 + K_2 + \frac{g}{\omega_1\omega_2}\left(K_1K_2 - \vec{K}_1 \cdot \vec{K}_2\right)\left[\frac{gK + (\omega_1 + \omega_2)^2}{gK - (\omega_1 + \omega_2)^2}\right]\right\} , \tag{2.22}$$

where ω_1 and ω_2 are frequencies of the ocean waves associated with the ocean wavenumbers K_1 and K_2, respectively, which have $\omega_1 = \sqrt{gK_1}$ and $\omega_2 = \sqrt{gK_2}$ according to the dispersion relationship. $\theta_{\vec{K}_1}$ is the angle of $\vec{K}_1$ from the reference direction. For the sake of completeness, we note that the electromagnetic coupling coefficient for the backscatter

is expressed as (e.g. Walsh *et al.* [6])

$$ {}_E\Gamma_P\left(\vec{K}_1, \vec{K}_2\right) = \frac{-j\left|\vec{K}_1 \times \vec{K}_2\right|^2}{2K^2\sqrt{\vec{K}_1 \cdot \vec{K}_2}} , \tag{2.23} $$

where $j = \sqrt{-1}$ and $K \approx 2k_0$. When simulating the second-order cross section, the hydrodynamic coupling coefficient is generally predominant (e.g. Gill [69]). An important issue associated with this research is the determination of the nulls which exist between the first- and second-order scatters (see Figure 1.1). Since the electromagnetic portion of ${}_S\Gamma_P$ is significantly smaller than the hydrodynamic portion in these regions, it will be ignored in the remainder of the analysis.

To calculate the second-order cross section of equation (2.17), the squared sinc function must be addressed (e.g. Walsh *et al.* [6]). From Lathi [70]

$$ \lim_{M\to\infty} M\mathrm{Sa}^2\left[Mx\right] = \pi\delta\left(x\right) , \tag{2.24} $$

and with the assumption that the scattering patch $\Delta\rho_s$ is large, we have

$$ \begin{aligned} & \lim_{\frac{\Delta\rho_s}{2}\to\infty} \mathrm{Sa}^2\left[\frac{\Delta\rho_s}{2}\left(K - 2k_0\right)\right] \\ = \; & \frac{2}{\Delta\rho_s} \lim_{\frac{\Delta\rho_s}{2}\to\infty} \frac{\Delta\rho_s}{2}\mathrm{Sa}^2\left[\frac{\Delta\rho_s}{2}\left(K - 2k_0\right)\right] \\ \approx \; & \frac{2\pi}{\Delta\rho_s}\delta\left(K - 2k_0\right) , \end{aligned} \tag{2.25} $$

and equation (2.17) becomes

$$ \begin{aligned} \sigma_{2p}\left(\omega_d\right) \approx \; & 2^6\pi^2k_0^4 \sum_{m_1=\pm1}\sum_{m_2=\pm1}\int_{-\pi}^{\pi}\int_0^{\infty} S_1\left(m_1\vec{K}_1\right) S_1\left(m_2\vec{K}_2\right) \\ & \left|{}_H\Gamma_P\right|^2 \delta\left(\omega_d + m_1\sqrt{gK_1} + m_2\sqrt{gK_2}\right) K_1 dK_1 d\theta_{\vec{K}_1} , \end{aligned} \tag{2.26} $$

The Dirac delta function in equation (2.26) can be evaluated using a technique presented

by Lipa and Barrick [27]. Letting

$$Y = \sqrt{K_1} \ , \tag{2.27}$$

we have

$$K_1 dK_1 = 2Y^3 dY \ . \tag{2.28}$$

Since $\vec{K_2} = \vec{K} - \vec{K_1}$, and the magnitude and direction of $\vec{K}$ is known, imposing the law of cosines, K_2 may be derived as

$$\begin{aligned} K_2^2 &= K_1^2 + 4k_0^2 - 4K_1 k_0 \cos\left(\theta_{\vec{K_1}} - \theta_{\rm N}\right) \\ &= Y^4 + 4k_0^2 - 4Y^2 k_0 \cos\left(\theta_{\vec{K_1}} - \theta_{\rm N}\right) \ . \end{aligned} \tag{2.29}$$

Letting

$$\begin{aligned} D_P\left(Y, \theta_{\vec{K_1}}\right) &= -\sqrt{g}\left(m_1\sqrt{K_1} + m_2\sqrt{K_2}\right) \\ &= -\sqrt{g}\left\{m_1 Y + m_2\left[Y^4 + 4k_0^2 - 4Y^2 k_0 \cos\left(\theta_{\vec{K_1}} - \theta_{\rm N}\right)\right]\right\} \ , \end{aligned} \tag{2.30}$$

the delta function constraint becomes

$$\delta\left(\omega_d + m_1\sqrt{gK_1} + m_2\sqrt{gK_2}\right) = \delta\left[\omega_d - D_P\left(Y, \theta_{\vec{K_1}}\right)\right] \ . \tag{2.31}$$

The Jacobian of the transformation will be

$$\left|\frac{\partial Y}{\partial D_P}\right|_{\theta_{K_1}} = g^{-\frac{1}{2}}\left|1 + \frac{m_1 m_2\left[Y^3 - 4Yk_0\cos\left(\theta_{\vec{K_1}} - \theta_{\rm N}\right)\right]}{\left[Y^4 + 4k_0^2 - 4Y^2 k_0\cos\left(\theta_{\vec{K_1}} - \theta_{\rm N}\right)\right]^{3/4}}\right|^{-1} \ . \tag{2.32}$$

After evaluating the delta function constraint by the Newton-Raphson method, equation

(2.26) becomes

$$\sigma_{2p}(\omega_d) \approx 128\pi^2 k_0^4 \sum_{m_1=\pm 1} \sum_{m_2=\pm 1} \int_{-\pi}^{\pi} \int_0^{\infty} S_1\left(m_1 \vec{K}_1\right) S_1\left(m_2 \vec{K}_2\right) \left|{}_H\Gamma_P\right|^2 \delta\left[\omega_d - D_P\left(Y, \theta_{\vec{K}_1}\right)\right] Y^3 \left|\frac{\partial Y}{\partial D_P}\right|_{\theta_{\vec{K}_1}} dD_P d\theta_{\vec{K}_1} , \tag{2.33}$$

or

$$\sigma_{2p}(\omega_d) \approx 128\pi^2 k_0^4 \sum_{m_1=\pm 1} \sum_{m_2=\pm 1} \int_{-\pi}^{\pi} S_1\left(m_1 \vec{K}_1\right) S_1\left(m_2 \vec{K}_2\right) \left|{}_H\Gamma_P\right|^2 Y^3 \left|\frac{\partial Y}{\partial D_P}\right|_{\theta_{\vec{K}_1}} d\theta_{\vec{K}_1} , \tag{2.34}$$

which can be calculated numerically.

2.2.3 Radar Received Time Series

The first- and second-order electric field equations may be simulated from the cross section equations (2.10) and (2.34) (e.g. Pierson [7], Walsh [71], and Gill and Walsh [42]) with

$$\left(E_0^+\right)_{12}(t) \approx C \int_{\omega} e^{j\omega t} e^{j\epsilon(\omega)} \sqrt{\sigma(\omega) \frac{d\omega}{2\pi}} , \tag{2.35}$$

where C is a collection of factors from the radar equation defined as (e.g. Barton [72])

$$C = \frac{\lambda_0^2 P_t G_t G_r \left|F\left(\rho_s\right)\right|^4 A_p}{(4\pi)^3 \rho_s^4} . \tag{2.36}$$

Here, P_t and G_t represent the peak power and free space antenna gain, respectively, of the transmitting source and G_r is receiver gain; $F(\rho_s)$, denoted as the rough spherical earth attenuation function, is a function of sea state, distance from radar transmitter to scattering patch and from scattering patch to receiver, constitutive parameters of the ocean surface (relative permittivity $\epsilon_R = 80$, average conductivity $\sigma_R = 4\ S/m$ are used for the ocean surface), and radio wave frequency. $F(\cdot)$ can be calculated from a FORTRAN

routine developed by Dawe [73]; A_p is the area of the scattering patch over the ocean surface; $A_p \approx \rho_s \Delta\rho_s \theta_{\mathrm{N}}$, where ρ_s is the range of the scattering patch; $\epsilon(\omega)$ in equation (2.35) is a random phase variable with a uniform distribution between 0 to 2π; and $\sigma(\omega)$ is the summation of the first- and second-order cross sections, $\sigma(\omega) = \sigma_{1p} + \sigma_{2p}$.

Equation (2.35) can be calculated by converting the integral equation to a summation equation (e.g. Pierson [7])

$$\left(E_0^+\right)_{12}(t) \approx C \lim_{\substack{\omega_{2p}\to\infty \\ (\omega_{2q+2}-\omega_{2q})\to 0}} \sum_{q=0}^{p} e^{j\omega_{2q+1}t} e^{\epsilon(\omega_{2q+1})} \sqrt{\sigma\left(\omega_{2q+1}\right) \frac{\omega_{2q+2}-\omega_{2q}}{2\pi}}\,, \quad (2.37)$$

where p and q are integers and $\omega_0, \omega_1, \omega_2, \cdots \omega_{2q+2}$ are net points over the ω-axis.

Figure 2.4 depicts a simulation of electric field time series using the model in equation (2.37). The parameters of the simulation include an operating frequency of $f_0 = 25$ MHz ($\lambda_0 = 12$ m), peak power $P_t = 16$ kW, transmitting antenna gain $G_t = 2$ dBi ≈ 1.585, scattering patch range of 50 km, receiving array gain

$$G_r = \frac{5.48\left(N_a + 1\right) d_s}{\lambda_0} = 65.76\,, \quad (2.38)$$

with linear array element number $N_a = 23$ and element spacing $d_s = 0.5\lambda_0$, a pulse width of 8 μs, corresponding to a patch width of $\Delta\rho_s = 1200$ m, a wind velocity of 15 m/s, 0° to the reference direction, and a sampling period of 0.25 s. Figure 2.5 is an expanded view of the first 512 points of the time series in Figure 2.4. From Figure 2.5 we can observe a periodic modulation of the e-m field indicating the existence of sinusoidal components. These sinusoidal components give rise to the Bragg peaks in the backscatter Doppler spectrum.

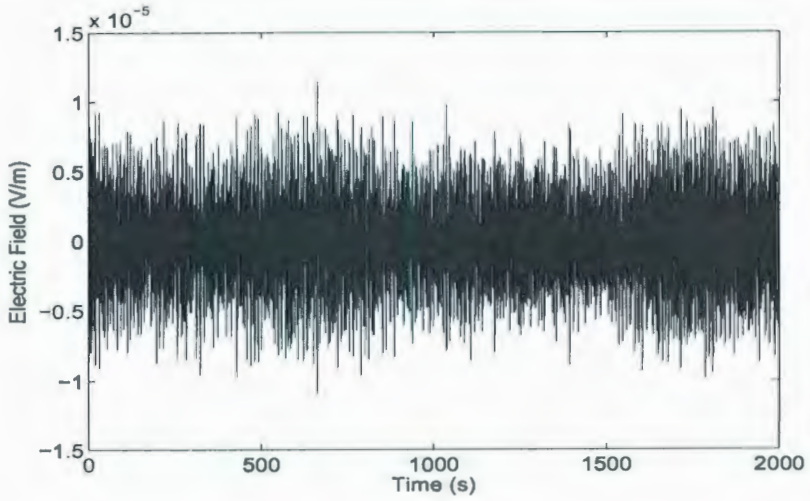

Figure 2.4: An 8192-point time series of the first- and second-order electric fields with the $f_0 = 25$ MHz, $\tau_0 = 8$ μs, a wind velocity of 15 m/s, 0° to the reference direction, and a sampling period of 0.25 s.

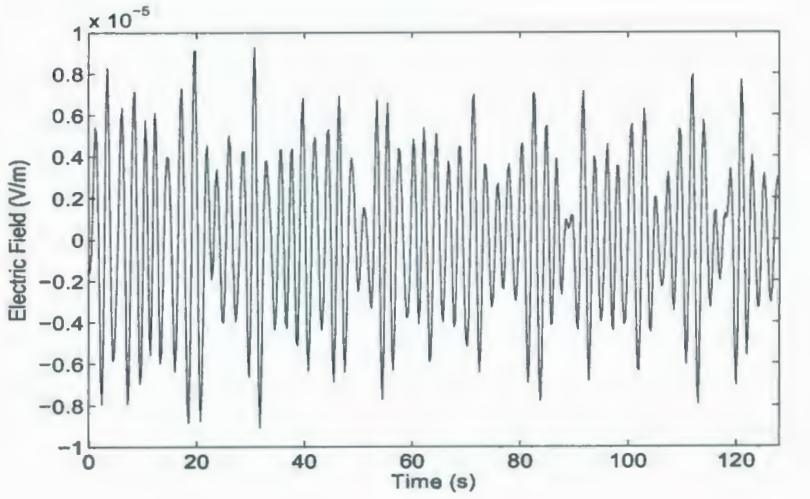

Figure 2.5: An expanded view of the first 512 points of the time series in Figure 2.4.

2.3 Doppler Spectra and Centroids of the Bragg Peak Regions

In the previous section, the algorithm for simulating the first- and second-order HF radar received time series has been described. Following this process the resulting electric field voltages will be stationary Gaussian random variables [8]. In this section, the Doppler spectra (PSD) of the time-varying electric fields are calculated as periodograms. The centroids of the Bragg peak regions are located and the distribution of the centroids is estimated numerically.

2.3.1 Calculation of the Doppler Spectra

If $x(t)$ is a time-varying random process, the Doppler spectra may be estimated [47] by

$$P(\omega) = \frac{1}{\Delta t}\left|\int_{t_1}^{t_2} x(t)e^{-j\omega t}dt\right|^2 , \tag{2.39}$$

where the time interval is from t_1 to t_2, i.e. $\Delta t = t_2 - t_1$. The quantity $P(\omega)$ is the so-called periodogram and is an estimate of the spectrum of $x(t)$. An alternate procedure to calculate the periodogram is to Fourier transform the autocorrelation of $x(t)$ within the same time interval (e.g. Proakis [47]).

2.3.2 Locations of the Centroids

The centroid of the Bragg peak is defined as the frequency position that separates the Bragg peak region into two portions with equal areas. A numerical procedure for locating the centroid is presented by Bobby [37]. The basic steps are:

1. Locate the positions of the maximum values of the positive and negative Doppler spectra, respectively, as the approximate peaks;

2. Find the average values of the spectra in the ranges $|1.8\omega_B| < \omega < |1.2\omega_B|$ and

$|0.8\omega_B| < \omega < |0.3\omega_B|$ of the Doppler spectrum;

3. For each peak, positive and negative, determine the first-order nulls on each side of the peak as those frequency values that fall underneath the corresponding average;

4. Locate the centroid frequency for each side of the Doppler spectrum as that frequency value at which half of the entire area of the peak is covered.

It is known that, in practice, ocean swell will cause narrow peaks in the second-order Doppler spectrum adjacent to the first-order lines. The presence of the swell peaks could potentially affect the identification of the null locations based on the algorithm above. However, for simplicity, the influence of swell is not considered in this analysis. Figure 2.6 depicts an example of the Doppler spectrum and centroid location of the time series in Figure 2.4. To see the variation of the Bragg peaks, we segment the time series into four equal-length consecutive parts, each having a length of 512 points. The Doppler spectrum is estimated and the position of the centroid is calculated for each segment. In Figure 2.6, a plot of the four Doppler spectra is depicted, and because of scaling, the variation of the centroid position indicated as dashed lines from top to bottom, are not immediately obvious. Figure 2.7 presents a closer look around the right-hand side peak of Figure 2.6. The variations of the magnitudes of the Bragg peaks can now be readily observed and these variations will obviously lead to fluctuations of the centroid positions. Similar results to those of Figures 2.6 and 2.7, but for an operating frequency of 5 MHz, are found in Figures 2.8 and 2.9, respectively.

2.4 Distribution of the Bragg Fluctuations

2.4.1 Numerical Calculation of the Standard Deviation

Since, as shall be seen, the distribution of the centroid positions is somewhat dependent on the width of the Bragg region, which is, in turn, dependent on the operating frequency

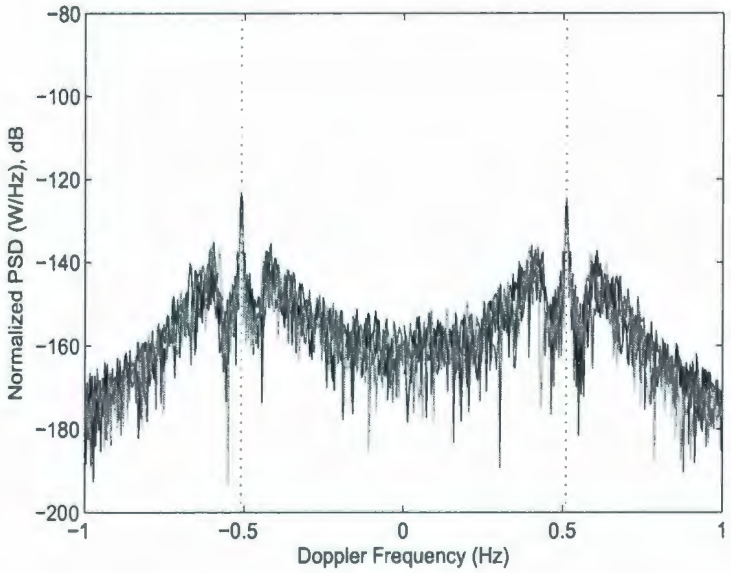

Figure 2.6: Fluctuations of the centroid positions for $f_0 = 25$ MHz. The centroid positions are indicated as dashed lines from top to bottom.

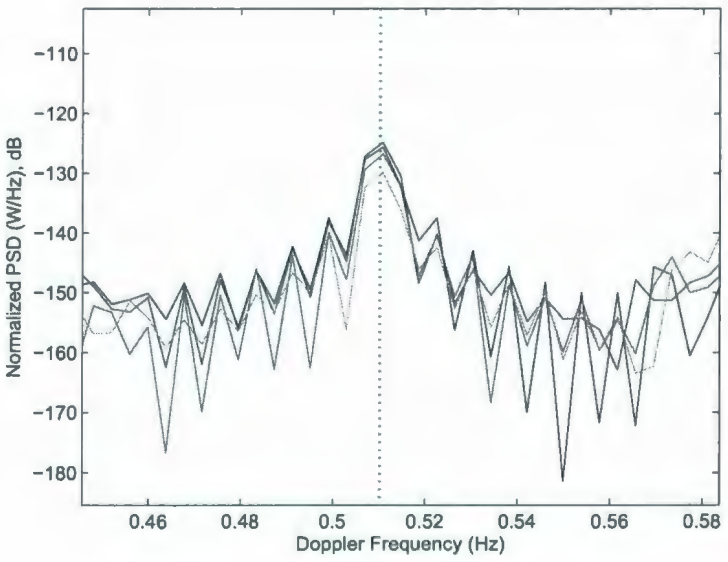

Figure 2.7: A closer look around the right-hand side peak of Figure 2.6.

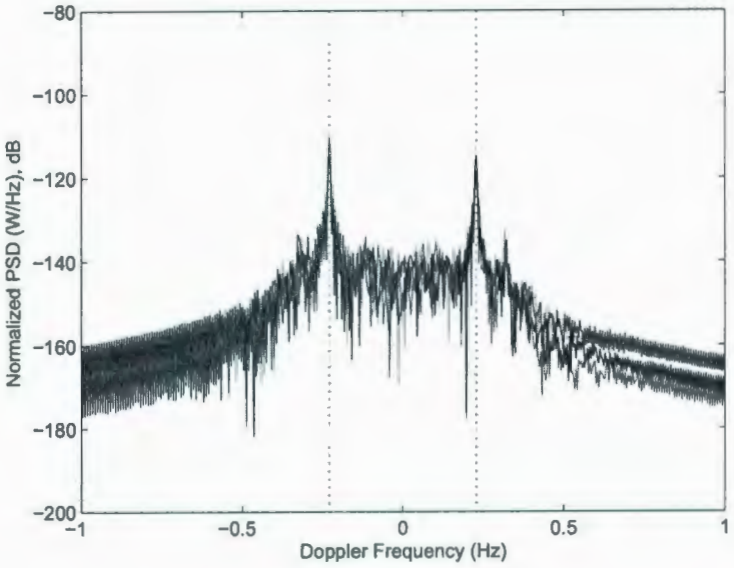

Figure 2.8: Fluctuations of the centroid positions for $f_0 = 5$ MHz. The centroid positions are indicated as dashed lines from top to bottom.

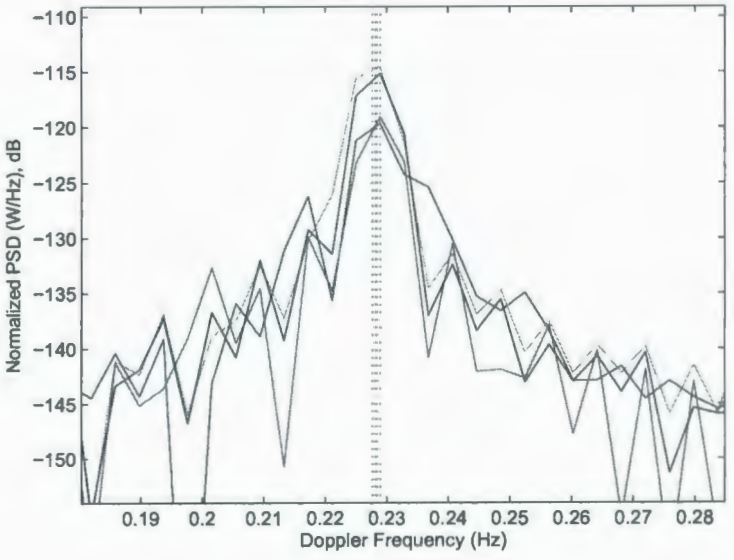

Figure 2.9: A closer look around the right-hand side peak of Figure 2.8.

and the pulse width, we attempt to determine the statistical properties of the distribution numerically. In this section, histogram plots of the centroid positions for both positive and negative Bragg regions are depicted.

Figures 2.10 to 2.12 are the investigation for the distributions of the centroid positions for different operating frequencies with a fixed pulse width of 4 μs. Radar operating frequencies of 25 MHz, 15 MHz, and 5 MHz, i.e. frequencies from the upper, middle, and lower portions of the HF band are selected. In order to calculate the Doppler spectra, fast Fourier transform (FFT) algorithm is used to implement the discrete Fourier transform (DFT). FFT resolution (Δ_{FFT}) and standard deviations (STDs) of the centroid positions with respect to the theoretical Bragg frequencies are plotted for comparisons. The condition of significant fluctuations of the Bragg peaks is defined as the STD exceeding the half Δ_{FFT}. In Figures 2.13 to 2.15, results for a fixed operating frequency of 5 MHz and pulse widths of 8 μs, 4 μs, and 2 μs, respectively, are shown.

Throughout the numerical estimations, the sea state is fixed by a steady wind velocity of 15 m/s, 0° to the reference direction. For each case, a time series of 65,536 points is generated from equation (2.37) with the sampling interval of 0.8 s. Then, the time series is segmented into 128 equal-length sequences with each containing 512 points. PSDs for these 512-point sequences are calculated and the centroid positions for both left and right sides of the Bragg regions are derived. The half Δ_{FFT} of each 512-point sequence is obtained as 0.0012 Hz. This Δ_{FFT} is fixed for various radar frequencies and pulse widths in our simulations in this section.

Table 2.1 summarizes the results of Figures 2.10 - 2.12 and also gives additional outcomes for other operating frequencies. In this table, V_{FFT} is ocean surface current resolution in speed (cm/s) corresponding to the half Δ_{FFT} of 0.0012 Hz. Since $V_{\mathrm{FFT}} = \dfrac{c\Delta_{\mathrm{FFT}}}{2f_0}$, V_{FFT} will take different values for different operating frequencies. "STDL" and "STDR" are the standard deviations for the left- and right-hand Bragg regions. V_L and V_R are speeds in cm/s associated with "STDL" and "STDR", respectively.

Table 2.2 summarizes the results of Figures 2.13 - 2.15 and includes outcomes for other

pulse width values. Half Δ_{FFT} is 0.0012 Hz, corresponding to a current resolution of 7.3 cm/s for $f_0 = 5$ MHz. "STDL" and "STDR", V_L and V_R have the same definitions as in Table 2.1.

Figures 2.16 and 2.17 are plots of the standard deviations as function of radar frequency and pulse width, respectively. In these figures, half of the Δ_{FFT} value is indicated as the bold solid line. Comparing with the half Δ_{FFT} the significance of the standard deviations will be identified.

The immediate conclusion from the previous simulation and estimation results is that the Bragg fluctuations do indeed exist and, under some circumstances, are significant. That is, under certain operating parameters, the standard deviation of the Bragg fluctuations lies outside the resolution imposed by the FFT. For example, as seen in Figure 2.12, when $f_0 = 5$ MHz and $\tau_0 = 4$ μs, the measured standard deviation of the left-hand peak position is 0.0016 Hz (Table 2.1), which exceeds half of the Δ_{FFT} of 0.0012 Hz. Since our purpose is to measure the ocean current speed, expressing these values in the units of speed, the half Δ_{FFT} corresponds to a speed of 7.3 cm/s while the standard deviation corresponds to 9.6 cm/s.

Because there is no noise or other contamination in the time series simulation at this stage, the only conclusion that must be drawn is that the source of the fluctuations with its standard deviation beyond the half Δ_{FFT} is the randomness of the ocean surface.

Since the width and position of the Bragg peak are determined by the operating frequency and pulse width, it is reasonable to investigate the dependence of the standard deviation of the Bragg fluctuations with respect to these two parameters, individually. Plots in Figures 2.16 and 2.17 show the existences of these dependencies. It may be observed that given a fixed pulse width, the standard deviation will, generally, decrease when the operating frequency is increased. On the other hand, given a fixed radar frequency, the standard deviation will also generally decrease when the radar pulse width is increased. However, when Figures 2.16 and 2.17 are examined carefully, it may be observed that the dependencies differ for the two general cases. Some of the details underlying these

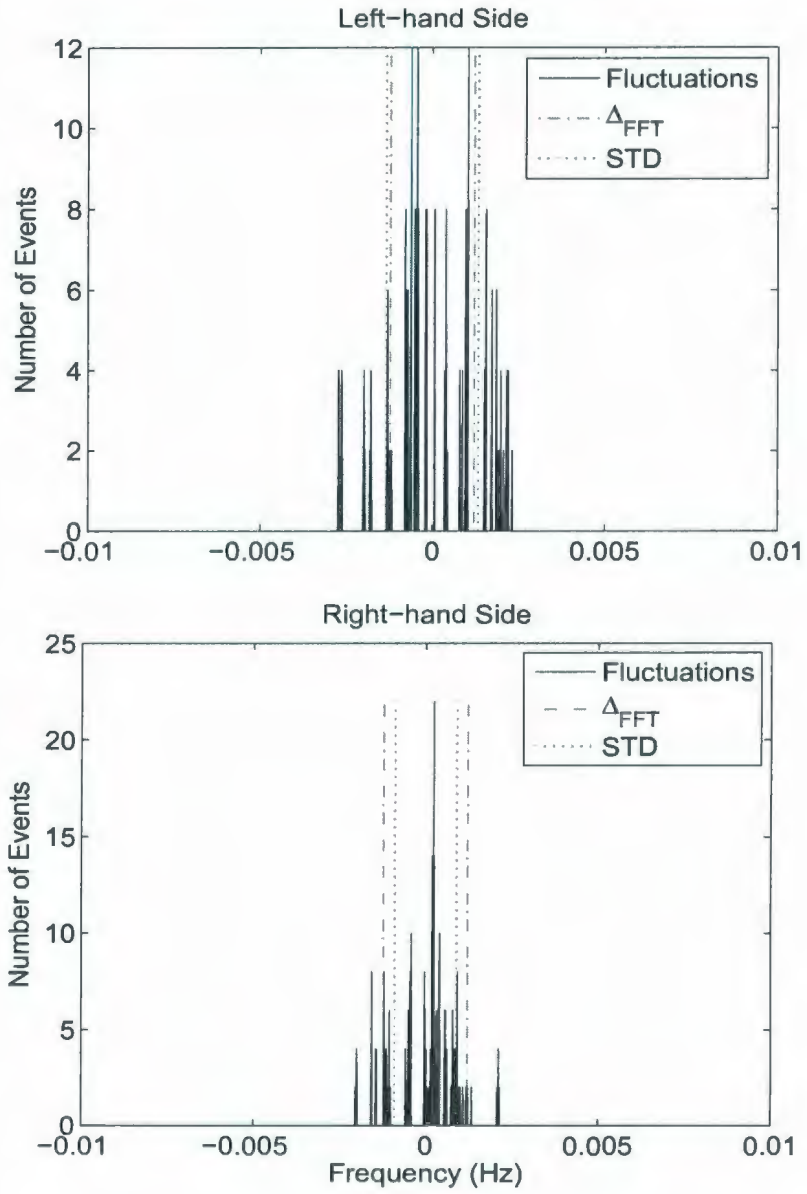

Figure 2.10: Distribution of the centroid positions with $f_0 = 25$ MHz and $\tau_0 = 4$ μs. The abscissa is the frequency difference between the measured centroid position and the theoretical Bragg frequency.

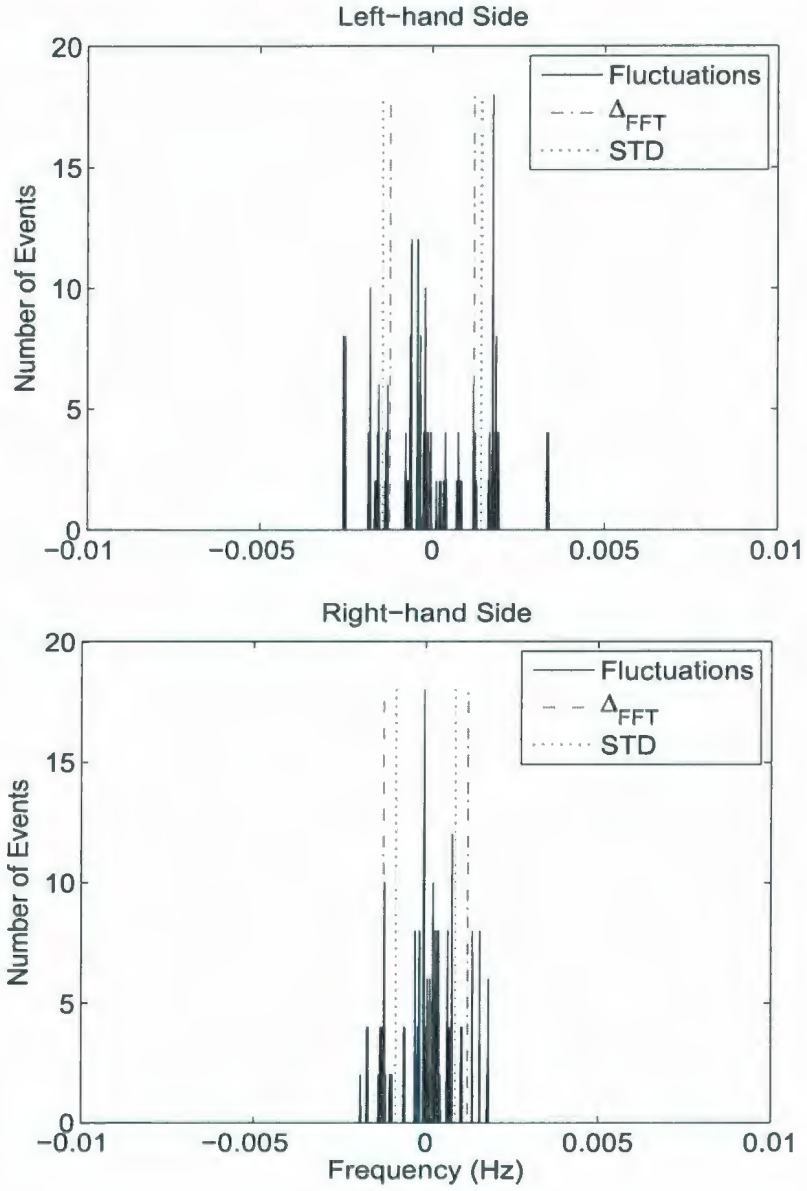

Figure 2.11: Distribution of the centroid positions with $f_0 = 15$ MHz and $\tau_0 = 4$ μs.

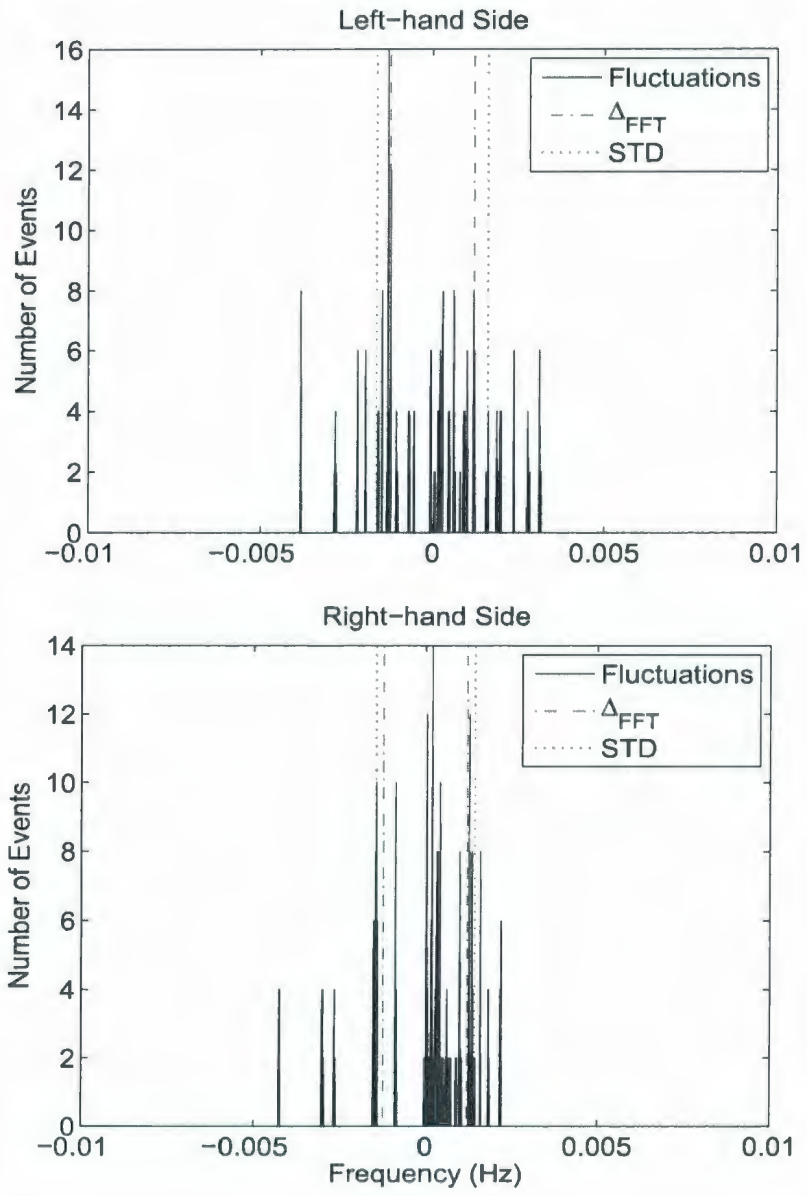

Figure 2.12: Distribution of the centroid positions with $f_0 = 5$ MHz and $\tau_0 = 4$ μs.

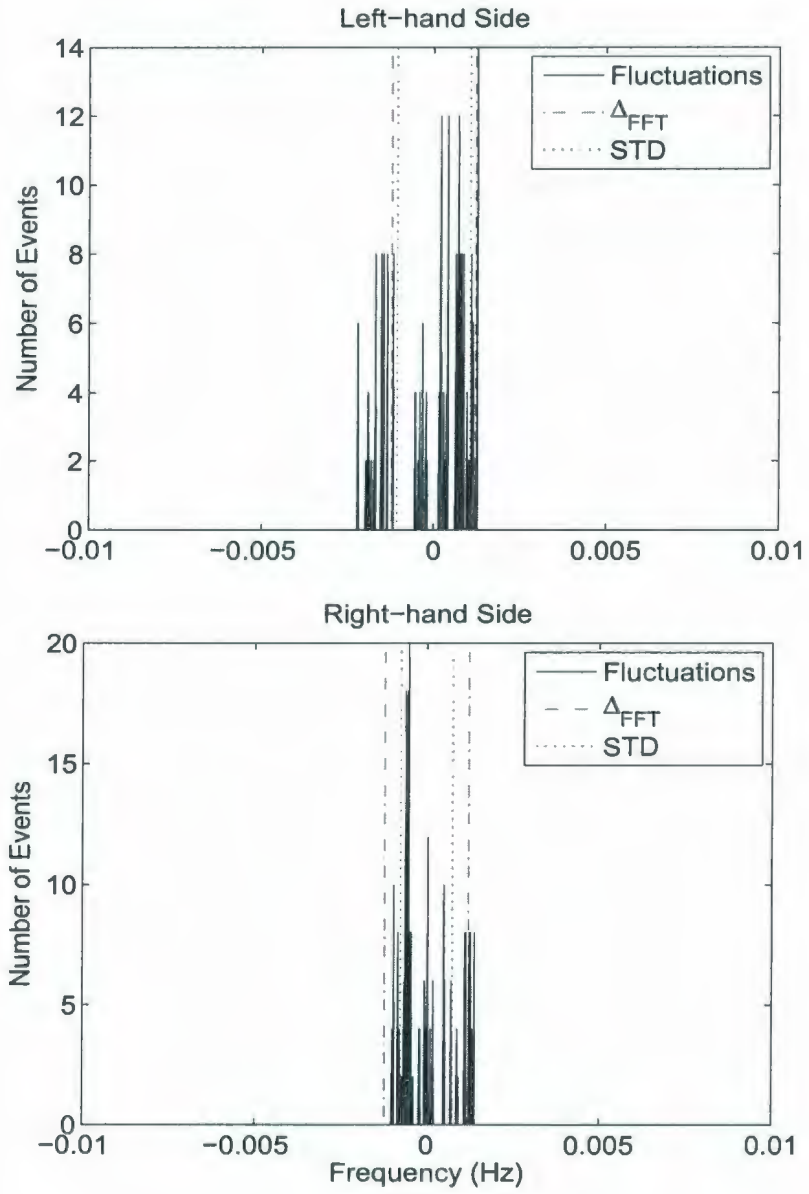

Figure 2.13: Distribution of the centroid positions with $\tau_0 = 8$ μs and $f_0 = 5$ MHz. The abscissa is the frequency difference between the measured centroid position and the theoretical Bragg frequency.

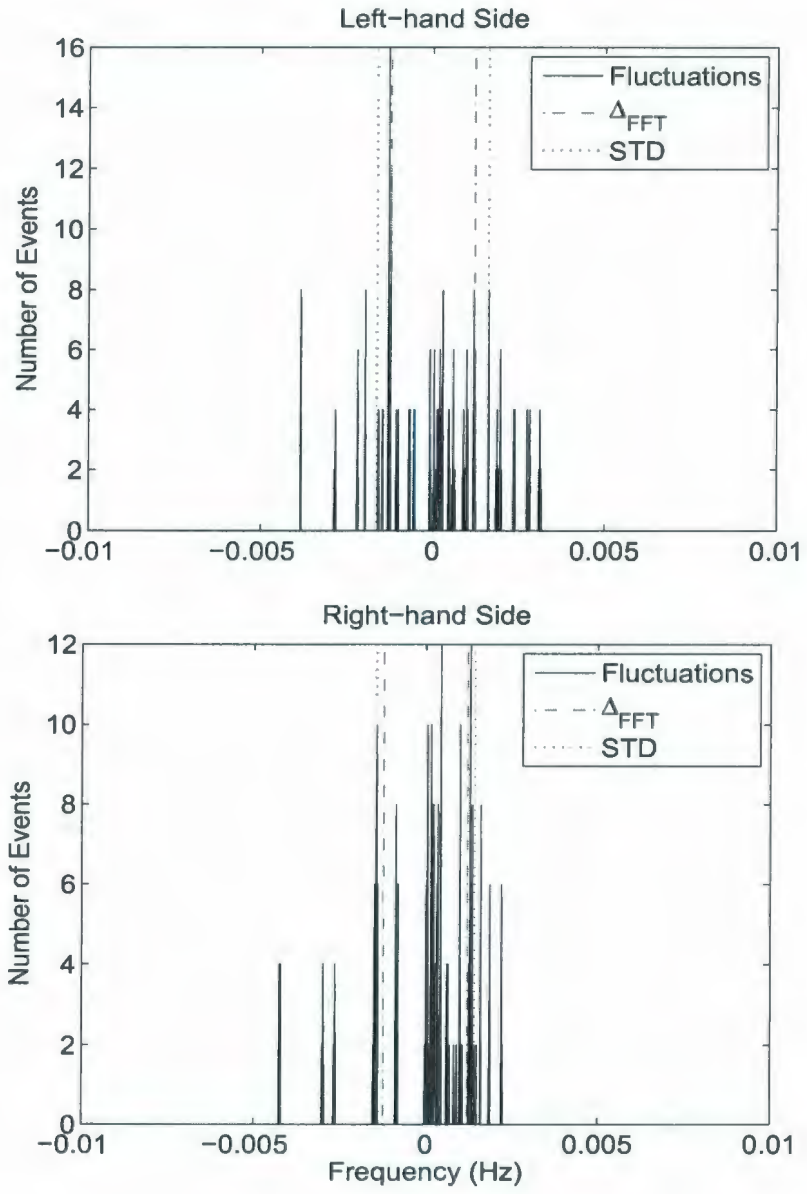

Figure 2.14: Distribution of the centroid positions with $\tau_0 = 4$ μs and $f_0 = 5$ MHz.

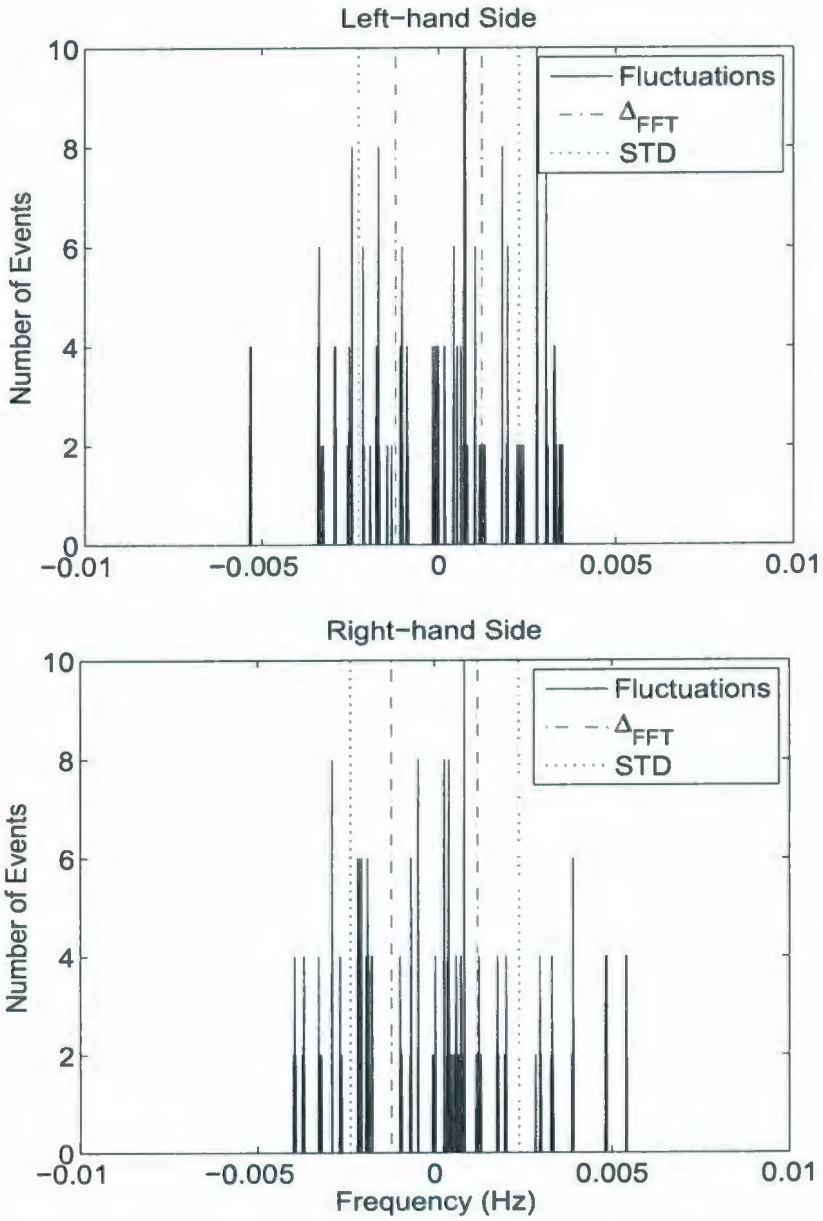

Figure 2.15: Distribution of the centroid positions with $\tau_0 = 2$ μs and $f_0 = 5$ MHz.

Table 2.1: Standard deviations for different operating frequencies when $\tau_0 = 4$ μs. The definitions of V_{FFT}, "STDL" and "STDR", and V_L and V_R are given in text.

f_0(MHz)	V_{FFT} (cm/s)	STDL (Hz)	V_L (cm/s)	STDR (Hz)	V_R (cm/s)
25	1.5	0.0011	1.2	0.0008	1.0
20	1.8	0.0012	1.8	0.0008	1.2
15	2.4	0.0014	2.8	0.0012	2.4
5	7.3	0.0016	9.6	0.0014	8.4
3	12.2	0.0045	45.0	0.0042	42.0

Table 2.2: Standard deviations for different pulse widths with $f_0 = 5$ MHz.

τ_0 (μs)	STDL (Hz)	V_L (cm/s)	STDR (Hz)	V_R (cm/s)
8	0.0011	6.6	0.0008	4.8
7	0.0012	7.2	0.0008	4.8
6	0.0014	8.4	0.0012	7.2
5	0.0012	7.2	0.0017	10.2
4	0.0016	9.6	0.0014	8.4
3	0.0021	12.6	0.0020	12.0
2	0.0023	13.8	0.0024	14.4
1	0.0045	27.0	0.0042	25.2

observations are considered in the following section.

2.5 Theoretical Analysis of the Bragg Fluctuations

In this section, the fundamental reason for the Bragg fluctuations found in the previous section will be examined. We will review the electric field equations and incorporate explicitly in them the randomness of the scattering surface. It is hoped that the final outcome will help to establish error estimation in ocean surface current measurement on a sound theoretical base.

2.5.1 Sources of the Bragg Fluctuations

In order to investigate the source of the Bragg fluctuations when Doppler spectra are calculated from finite time series received from HF radar, the electric field equation of Walsh *et al.* [6], Walsh and Dawe [34], or Gill and Walsh [35] should be examined carefully. The numerical version of the field equation (2.37) in Section 2.2.3 is rewritten here as

$$E(t) \approx C \lim_{\substack{\omega_{2p}\to\infty \\ (\omega_{2q+2}-\omega_{2q})\to 0}} \sum_{q=0}^{p} e^{j\omega_{2q+1}t} e^{\epsilon(\omega_{2q+1})} \sqrt{\sigma\left(\omega_{2q+1}\right) \frac{\omega_{2q+2}-\omega_{2q}}{2\pi}} \,. \tag{2.40}$$

Here, the $\left(E_0^+\right)_{12}(t)$ has been simplified as $E(t)$. All parameters have been defined in Section 2.2.3. To simplify the problem, along the frequency net points from ω_0 to ω_4, two arbitrary adjacent frequencies ω_1 and ω_3 are considered, with random phases of ϵ_1 and ϵ_3, respectively (e.g. Pierson [7]). The total field, $E_{13}(t)$, received from these two components becomes, from equation (2.40)

$$E_{13}(t) = C\left[e^{j\omega_1 t} e^{j\epsilon_1} \sqrt{\sigma(\omega_1)\frac{\omega_2-\omega_0}{2\pi}} + e^{j\omega_3 t} e^{j\epsilon_3} \sqrt{\sigma(\omega_3)\frac{\omega_4-\omega_2}{2\pi}}\right] . \tag{2.41}$$

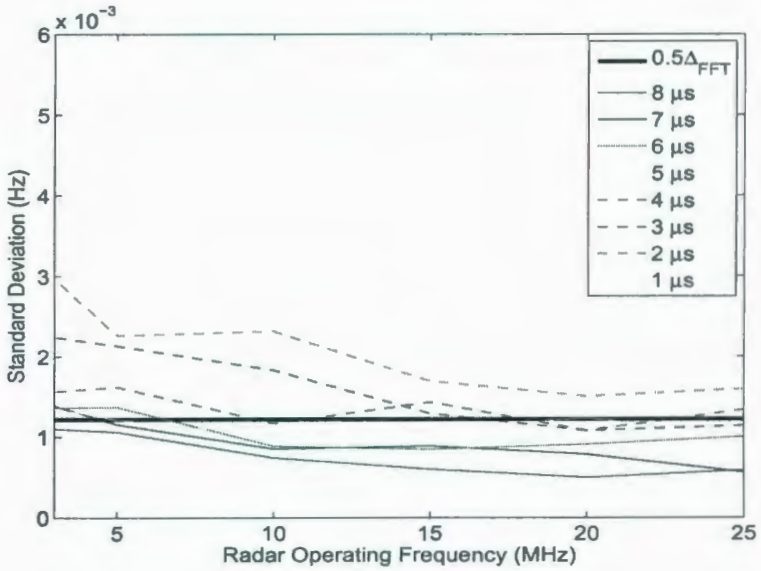

Figure 2.16: Plots of standard deviations of the centroid positions as a function of radar frequency for different pulse widths.

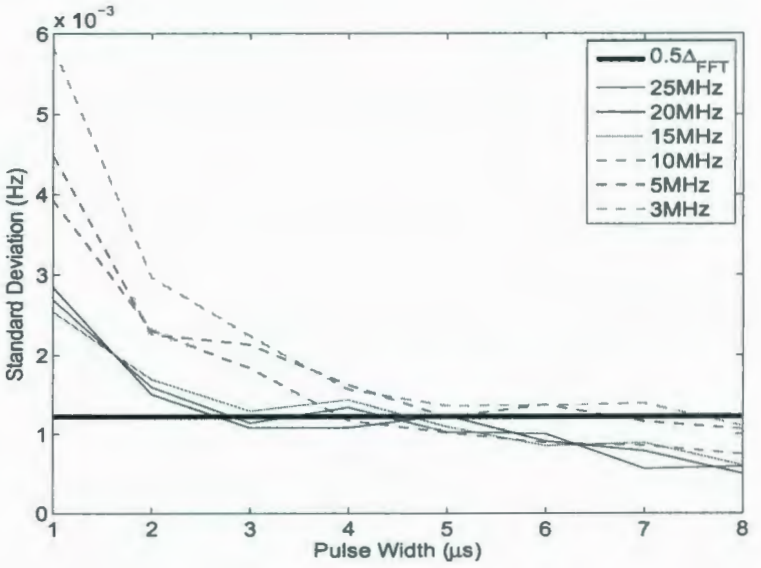

Figure 2.17: Plots of standard deviations of the centroid positions as a function of pulse width for different operating frequencies.

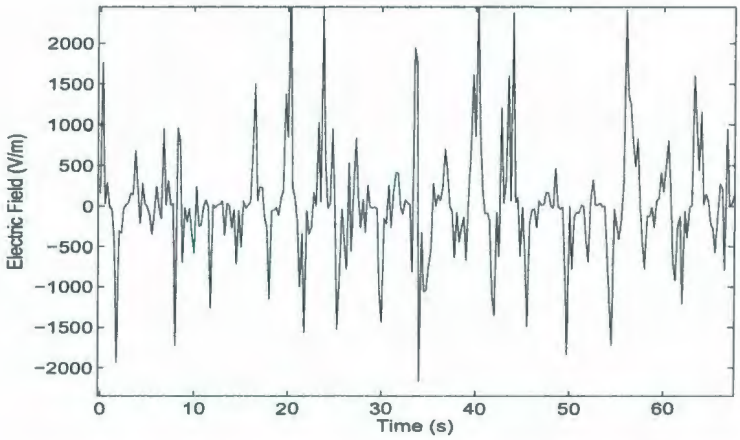

Figure 2.18: Simulation of radar time series. The signal contains two sinusoids with frequencies of 0.10 Hz and 0.13 Hz, respectively.

If $A_1(\omega_1)$ is defined as

$$A_1(\omega_1) = C\sqrt{\sigma(\omega_1)\frac{\omega_2 - \omega_0}{2\pi}}\,, \tag{2.42}$$

and $A_3(\omega_3)$ as

$$A_3(\omega_3) = C\sqrt{\sigma(\omega_3)\frac{\omega_4 - \omega_2}{2\pi}}\,, \tag{2.43}$$

and the exponential term $e^{j[\omega t+\epsilon(\omega)]}$ is written explicitly so as to show the behavior of the random phase term, equation (2.41) may be cast as .

$$\begin{aligned} E_{13}(t) &= A_1(\omega_1)e^{j(\omega_1 t+\epsilon_1)} + A_3(\omega_3)e^{j(\omega_3 t+\epsilon_3)} \\ &= E_1(t) + E_3(t)\,. \end{aligned} \tag{2.44}$$

Equation (2.44) may be viewed as the prototype of the e-m field time series received from the ocean surface; i.e. it represents the field which would be received if only two distinct wave frequencies with random phases were presented on the surface. Figure 2.18 provides a plot of this signal.

Fourier transforming the first term of equation (2.44) over an arbitrary finite time interval $[t_1, t_2]$ gives

$$\begin{aligned} E_1(\omega) &= \int_{t_1}^{t_2} A_1(\omega_1) e^{j(\omega_1 t + \epsilon_1)} e^{-j\omega t} dt \\ &= \frac{A_1 e^{j\epsilon_1}}{j(\omega_1 - \omega)} \left[e^{j(\omega_1 - \omega)t_2} - e^{j(\omega_1 - \omega)t_1} \right] \\ &= A_1 \Delta t e^{j\alpha_1} \mathrm{Sa}\left[\frac{\Delta t}{2} (\omega_1 - \omega) \right] , \end{aligned} \tag{2.45}$$

where $\Delta t = t_2 - t_1$ and $\alpha_1 = \epsilon_1 + \dfrac{t_1 + t_2}{2}(\omega_1 - \omega)$. Similarly, for the second term in equation (2.44)

$$E_3(\omega) = A_3 \Delta t e^{j\alpha_3} \mathrm{Sa}\left[\frac{\Delta t}{2} (\omega_3 - \omega) \right] , \tag{2.46}$$

where $\alpha_3 = \epsilon_3 + \dfrac{t_1 + t_2}{2}(\omega_3 - \omega)$. The total PSD, $P_T(\omega)$ is the square of the magnitude of the sum of $E_1(\omega)$ and $E_3(\omega)$ within the time interval Δt; i.e.

$$\begin{aligned} P_T(\omega) &= \frac{1}{\Delta t} |E_1(\omega) + E_3(\omega)|^2 \\ &= A_1^2 \Delta t \mathrm{Sa}^2 \left[\frac{\Delta t}{2} (\omega_1 - \omega) \right] + A_3^2 \Delta t \mathrm{Sa}^2 \left[\frac{\Delta t}{2} (\omega_3 - \omega) \right] \\ &+ A_1 A_3 \Delta t \mathrm{Sa}\left[\frac{\Delta t}{2} (\omega_1 - \omega) \right] \mathrm{Sa}\left[\frac{\Delta t}{2} (\omega_3 - \omega) \right] \cos(\alpha_{13}) \\ &= P_1(\omega) + P_3(\omega) + P_{13}(\omega) , \end{aligned} \tag{2.47}$$

where

$$\cos(\alpha_{13}) = \cos\left[(\epsilon_1 - \epsilon_3) + \frac{t_1 + t_2}{2} (\omega_1 - \omega_3) \right] . \tag{2.48}$$

In equation (2.47), it can be seen that the first and second terms, which are denoted as $P_1(\omega)$ and $P_3(\omega)$, respectively, are the PSDs of $E_1(t)$ and $E_3(t)$, individually. The third term, which is denoted as $P_{13}(\omega)$, is a cross term and represents the interaction between the two sinusoidal functions. The necessary and sufficient conditions that the cross term

exists are: (1) there is more than one frequency component and (2) the length of time series is finite.

In equation (2.47), $P_T(\omega)$ is defined across all possible frequencies. If the behavior of the PSD at frequency ω_1 is considered (i.e. by setting $\omega = \omega_1$), after absorbing Δt into the A's,

$$\begin{aligned} & P_T(\omega_1) = P_1(\omega_1) + P_3(\omega_1) + P_{13}(\omega_1) \\ = \; & A_1^2 + A_3^2 \mathrm{Sa}^2 \left[\frac{\Delta t}{2}(\omega_3 - \omega_1)\right] + A_1 A_3 \mathrm{Sa}\left[\frac{\Delta t}{2}(\omega_3 - \omega_1)\right] \cos(\alpha_{13}) \; . \end{aligned} \tag{2.49}$$

This equation also can be explained as the magnitude of the spectrum at frequency ω_1 influenced by the adjacent frequency component at ω_3. The first two terms of equation (2.49) on the right are deterministic terms no matter how the time series is segmented. They are actually the average value of the PSD estimate at frequency point ω_1. The last term on right side of equation (2.49) contains randomness and is of primary interest here. Several points are noteworthy. Firstly, in view of equation (2.48), this term contains the random phases ϵ_1 and ϵ_3. This means that the initial conditions of the two sinusoidal components will affect the result of the spectral estimate. Secondly, the spectral estimate results will be affected by the values of $\frac{t_1 + t_2}{2}$, which occur at the midpoints of the segmented time series. This means that we may not obtain the same PSD from time to time when the time series is divided into discrete sections. These properties are crucial since they imply that there exists a fundamental uncertainty in the magnitude of the PSD at each frequency point. Figure 2.19 shows that when equal length, consecutive time sequences are used to calculate PSDs from the time series of Figure 2.18, the resulting curves are similar but not coincident.

The previous analysis thus shows that there is randomness in the PSD when the finite length time series is calculated. While this example has been established using only two frequency components, the general idea must be applied to a continuum (in a discrete sense) of frequencies. This is true because, as is well known, the sea echo received by

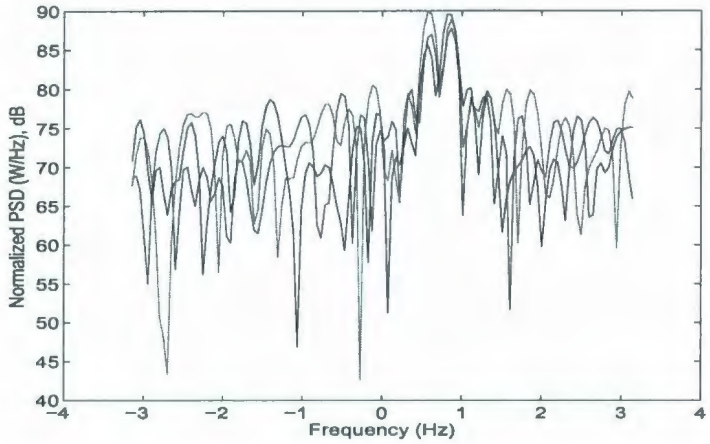

Figure 2.19: Fluctuations of PSDs. Each time sequence has a length of 128 points. Four consecutive time sequences are calculated and plotted together.

HF radar contains many frequency components corresponding to scatter from many ocean wavelengths. Therefore, there will be potentially a large number of cross terms that could introduce uncertainty to the power estimate at one frequency point.

2.5.2 Further Numerical Investigation of the Bragg Fluctuations

To numerically check the uncertainty of the power at each frequency point of the Doppler spectrum due to the influence from other frequencies, a finite but large number of frequencies will be examined. If N is the number of frequencies, equation (2.49) may be written in an expanded, more general, form with ω_n at the frequency position under the consideration as

$$\begin{aligned} P_T(\omega_n) &= P_1(\omega_n) + P_2(\omega_n) + \cdots + P_N(\omega_n) \\ &+ P_{12}(\omega_n) + P_{13}(\omega_n) + \cdots + P_{N-1,N}(\omega_n)\ . \end{aligned} \tag{2.50}$$

Clearly, equation (2.50) may be written more concisely as

$$P_T(\omega_n) = \sum_{i=1}^{N} P_i(\omega_n) + \sum_{i,j=1}^{N} P_{ij}(\omega_n) \,, \tag{2.51}$$

where the second term denotes the summation of the cross terms ($i \neq j$). These are, in fact, the terms where the randomness is contained. There are totally $1+2+3+\ldots+N-1 = \frac{N(N-1)}{2}$ cross terms. Each cross term can be represented as a weighting factor times a cosine function α_{ij} as in equation (2.49). The weighting factor is a function of frequency and time. The cosine function contains a random phase and a time dependency $\frac{t_i + t_j}{2}$. The distribution of the summation of these cross terms is to be estimated.

Figure 2.20 shows histogram results of the distribution of the summation of the cross term at several Doppler frequency positions when the operating frequency is $f_0 = 25$ MHz and a wind velocity is 15 m/s, 0° to the reference direction. Figure 2.21 is for $f_0 = 15$ MHz, and Figure 2.22 is for $f_0 = 5$ MHz. In these figures, the radar pulse width is fixed at 4 μs, corresponding to the size of the scattering patch of 600 m. The length of each time series is 512-point and the sampling interval is 0.5 s, corresponding to a frequency resolution of $\Delta\omega = \frac{4\pi}{512}$ rad/s and a frequency range from -2π to 2π in frequency domain. Since the absolute square of the variables with Gaussian distribution will result in a chi-square distribution with two degrees of freedom, the probability density function (PDF) of a chi-square distribution with two degrees of freedom is plotted for comparison. In Figures 2.20-2.22, the amplitudes have been normalized to the maximum value of 0.5.

In practice, those frequencies that are at and close to the Bragg peaks are of most concern. For illustration, the surrounding region of the positive Bragg peaks is examined. The frequency points of the Doppler spectrum being considered in each figure from top to the bottom, are at positions $-2\Delta\omega$, $-1\Delta\omega$, 0, $+1\Delta\omega$, and $+2\Delta\omega$, respectively, with respect to the theoretical Bragg peak. Each figure is a histogram plot of 4096 events, which represents the length of time series of 4096 × 512 points, or 4096 × 256 seconds in time. The reason for assuming such large numbers of events is that we want to clearly

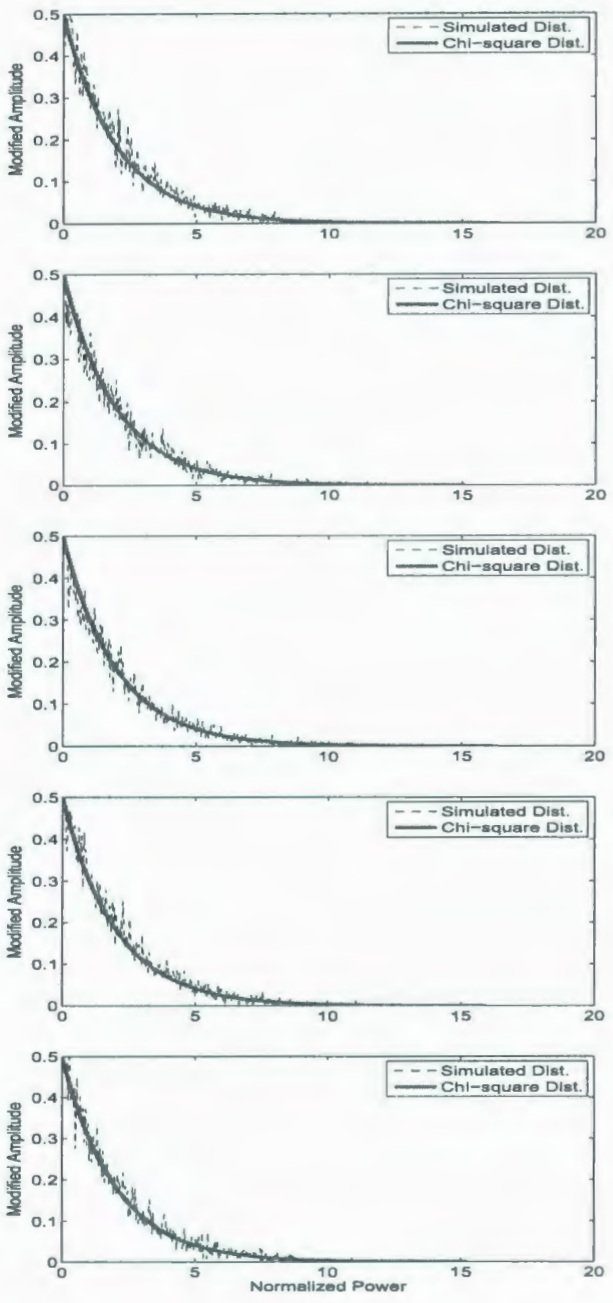

Figure 2.20: Histogram plots showing fluctuations of PSDs (dashed line) with f_0 = 25 MHz. From top to the bottom, the testing frequency points are $-2\Delta\omega$, $-1\Delta\omega$, 0, $+1\Delta\omega$, and $+2\Delta\omega$ with respect to the Bragg peak. A plot of a normalized chi-square distribution with two degrees of freedom (solid line) is for comparison.

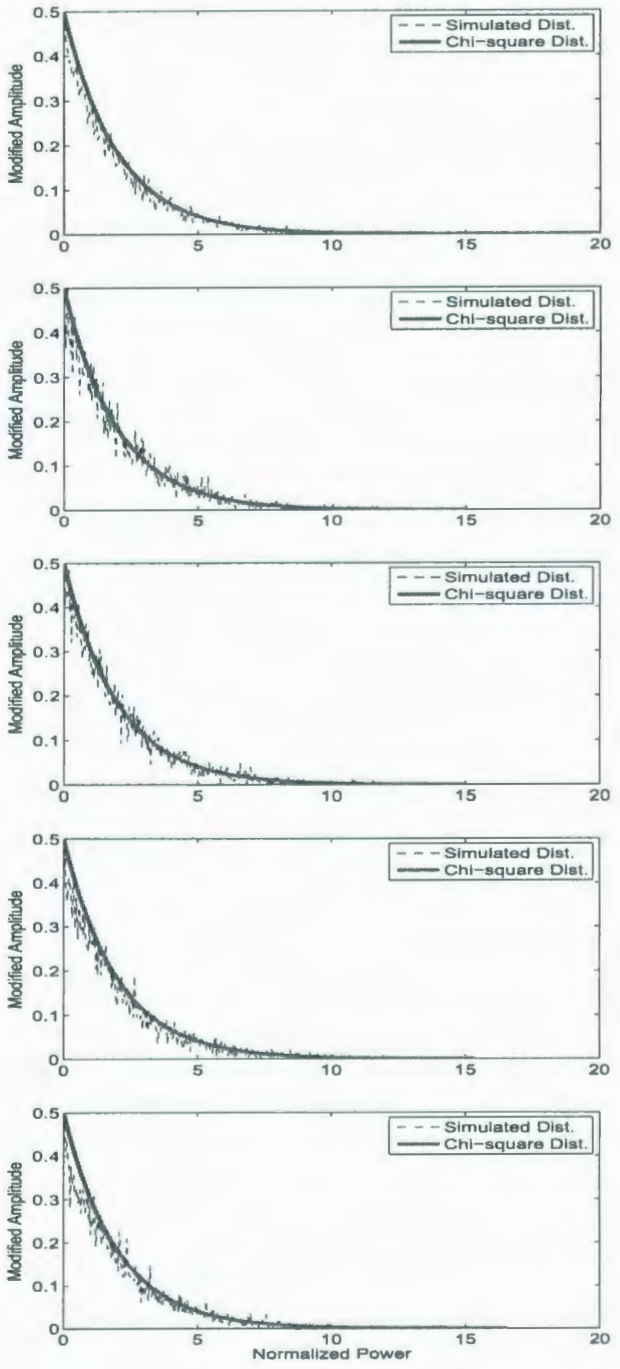

Figure 2.21: Histogram plots showing fluctuations of PSDs with $f_0 = 15$ MHz. The same test frequency points are chosen as in Figure 2.20.

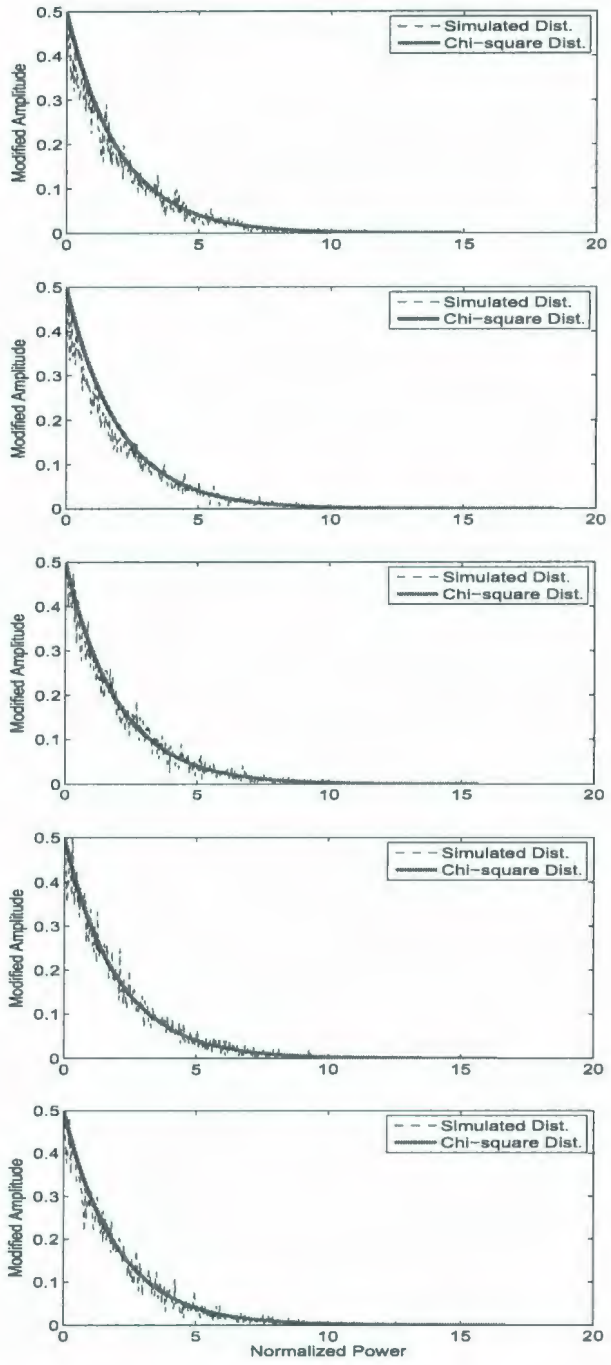

Figure 2.22: Histogram plots showing fluctuations of PSDs with $f_0 = 5$ MHz. The same test frequency points are chosen as in Figure 2.20.

observe the distribution of power at each frequency point. Of course, it is assumed that the radar parameters and sea state statistics are fixed within the whole time period. The solid line on each figure is a plot of a chi-square distribution with two degrees of freedom for comparison.

To investigate the relative magnitude of the fluctuations to the mean values, the magnitude of power is normalized by the corresponding mean; i.e. from equation (2.51) we have

$$\begin{aligned} P_{norm} &= \frac{\sum_{i=1}^{N} P_i(\omega_n) + \sum_{i,j=1}^{N} P_{ij}(\omega_n)}{\sum_{i=1}^{N} P_i(\omega_n)} \\ &= 1 + \frac{\sum_{i,j=1}^{N} P_{ij}(\omega_n)}{\sum_{i=1}^{N} P_i(\omega_n)} . \end{aligned} \tag{2.52}$$

Since

$$P_T(\omega_n) = \sum_{i=1}^{N} P_i(\omega_n) + \sum_{i,j=1}^{N} P_{ij}(\omega_n) \geq 0 , \tag{2.53}$$

we have

$$\sum_{i,j=1}^{N} P_{ij}(\omega_n) \geq -\sum_{i=1}^{N} P_i(\omega_n) , \tag{2.54}$$

and

$$\frac{\sum_{i,j=1}^{N} P_{ij}(\omega_n)}{\sum_{i=1}^{N} P_i(\omega_n)} \geq -1 , \tag{2.55}$$

and therefore, from equation (2.52)

$$P_{norm} = 1 + \frac{\sum_{i,j=1}^{N} P_{ij}(\omega_n)}{\sum_{i=1}^{N} P_i(\omega_n)} \geq 0 \,. \tag{2.56}$$

Equation (2.56) indicates that at each frequency position, the magnitude of the power may have opportunity to be zero due to the summation of the cross terms with randomness. This conclusion may be used to explain the phenomenon in practical experiment, that the Bragg region is sometimes split into two or more portions.

As another check for the distribution of the power at each frequency position, according to Barrick and Snider [8], the normalized standard deviations are examined for the previous simulation. The normalized standard deviation (nSTD) is defined as [8]

$$\text{nSTD} = \frac{\langle R_k^2 \rangle - \langle R_k \rangle^2}{\langle R_k \rangle^2} \,, \tag{2.57}$$

where R_k is a random variable at an arbitrary position k and $\langle \cdot \rangle$ is ensemble average. In these studies, R_k is the power of the Doppler spectrum at frequency position k. If R_k is chi-square distributed with two degrees of freedom, then the nSTD would be equal to unity.

Tables 2.3-2.5 list the means and nSTDs of the distributions corresponding to Figures 2.20 to 2.22. It can be seen that the means are all around zero. All nSTDs that are not at the Bragg frequencies are slightly less than unity. At the Bragg frequencies, however, the nSTD values are a little further less than unity. This phenomenon is in excellent agreement with Barrick and Snider's result [8] where real data were checked. This provides strong evidence that, at frequency points around the Bragg position, the distribution of the power spectrum is chi-squire with two degrees of freedom.

Table 2.3: Means and normalized standard deviations of the centroids at 25 MHz. This table is related to Figure 2.20, where "DF" indicates the Doppler frequency point and ω_B is the Bragg frequency of the Doppler spectrum. "Means" are mean values of the variables at each frequency point, "nSTD" is normalized standard deviations at each frequency point.

DF	$-2\Delta\omega$	$-1\Delta\omega$	ω_B	$+1\Delta\omega$	$+2\Delta\omega$
Means	0.0009	−0.0176	−0.0214	0.0102	−0.0179
nSTD	0.9268	0.9196	0.8315	0.9595	0.9181

Table 2.4: Means and nSTD of the centroids at 15 MHz. This table is related to Figure 2.21.

DF	$-2\Delta\omega$	$-1\Delta\omega$	ω_B	$+1\Delta\omega$	$+2\Delta\omega$
Means	−0.0054	0.0153	−0.0215	−0.0076	0.0084
nSTD	0.8901	0.9242	0.7349	0.9049	0.8951

Table 2.5: Means and nSTD of the centroids at 5 MHz. This table is related to Figure 2.22.

DF	$-2\Delta\omega$	$-1\Delta\omega$	ω_B	$+1\Delta\omega$	$+2\Delta\omega$
Means	−0.0279	−0.0258	−0.0202	0.0147	0.0128
nSTD	0.9589	0.9329	0.8930	0.9667	0.9476

2.6 Fluctuations as Functions of the Width of the Bragg Region and $\Delta_{\mathbf{FFT}}$

The previous section shows that the distribution of the power within the Bragg region of the Doppler spectrum seem to be chi-square. However, the distribution of the Bragg fluctuations may not be easily obtained analytically from the chi-square distribution. Barrick [48] achieves a closed form expression of the standard deviation of the fluctuations. His expression is under an assumption that there are large numbers of frequency points within the Bragg region. The "large numbers of frequency points" assumption ensures that the distribution of the centroid position can be reduced to be Gaussian distributed based on the Central Limit Theorem. To make the assumption valid, the Bragg region should be wide and the average of PSDs over several consecutive time segments should be carried out to include more frequency points. For example in Barrick's examination [48], at least 10 frequency points within the Bragg region are required if the rectangular spectral shape is considered.

In our study, Barrick's assumption does not apply for two reasons: First, the width of the Bragg region, which is explicitly defined by the squared sinc function, is relatively narrow. Second, the averaging process is not carried out since the time-varying behavior of the Bragg peaks is desired. Under this circumstance, a closed form expression of the standard deviation may not be obtained. However, numerical means may be used to investigate the problem. According to Walsh's method (e.g. Walsh *et al.* [6], Walsh and Dawe [34], Gill and Walsh [35]), for a known operating frequency and pulse width, the width of the Bragg region has been well defined. The analysis is therefore categorized as two cases: in the first instance, the standard deviations as a function of the width of the Bragg peaks for a fixed Δ_{FFT} is considered; secondly, the relationship between the standard deviations and Δ_{FFT} for a fixed width of the Bragg peak is examined. To achieve these aims, a large quantity of radar received time series will be simulated by: (1) varying the radar frequency and pulse width with fixed Δ_{FFT} and (2) varying Δ_{FFT} with fixed

radar frequency and pulse width. The Doppler spectra are calculated as periodograms and the standard deviations of the Bragg peaks associated with each time series are obtained.

2.6.1 Fluctuation as a Function of the Width of the Bragg Region

In this subsection an analytical expression for the width of the Bragg region will be deduced first, and then the detail of the dependence between the standard deviation of the Bragg peaks and the width of the Bragg region will be examined.

In the previous work shown in Figures 2.16 and 2.17, the standard deviations (in Hz) of the Bragg peaks are plotted against the operating frequency and pulse width, respectively for a fixed Δ_{FFT}. It is known that in each case the dependence is not linear. However, when the standard deviations are plotted with respect to the width of the Bragg region, the dependence is approximately linear. This can be seen in Figure 2.23 where the values of width of the Bragg region are obtained numerically from the PSD of the simulated electric field data. The Δ_{FFT} is fixed as 0.0012 Hz.

The linear relationship between the standard deviation and the width of the Bragg region, $\Delta\omega_p$, for the pulsed waveform, implies an equation of the form

$$\mathrm{STD} = b_1 \Delta\omega_p + b_2 \,, \tag{2.58}$$

where STD is standard deviation and b_1 and b_2 are constants which can be determined by the least square method (LSM) of fitting (Proakis [47]).

Theoretical Width of the Bragg Region

The width of the Bragg region $\Delta\omega_p$ is defined by the width of the main beam of the squared sinc function (e.g. equation(2.10)), which is calculated by the frequency difference between the first nulls adjacent to the principal maximum on left and right, i.e. the nulls of the

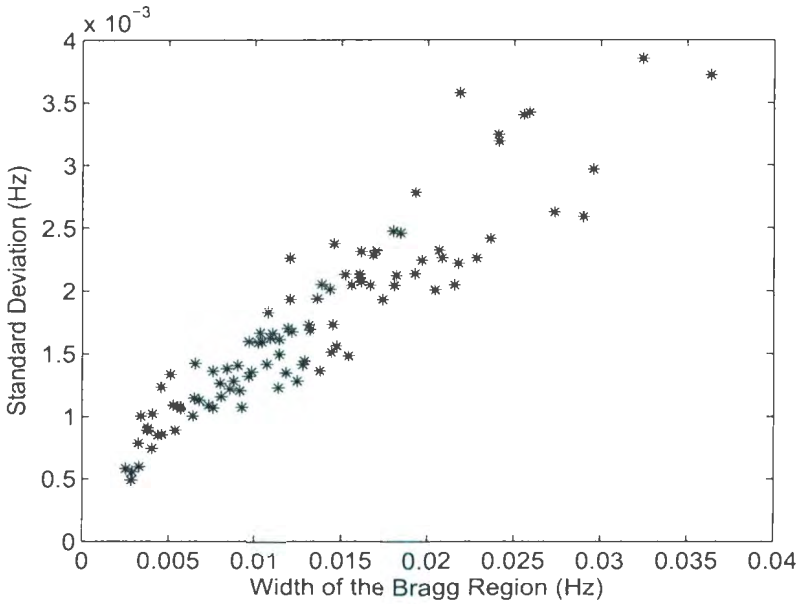

Figure 2.23: Standard deviations of the Bragg peaks as a function of the width of the Bragg region.

squared sinc function satisfies

$$\frac{\sin^2 x}{x^2} = 0\,, \quad \text{when} \quad x = \pm\pi\,. \tag{2.59}$$

The Bragg scatter associated with the monostatic radar cross section is

$$\mathrm{Sa}^2\left[\frac{\Delta\rho_s}{2}\left(K - 2k_0\right)\right]\,, \tag{2.60}$$

where the parameters are defined following equation (2.10). Substitution of equation (2.60) into equation (2.59) gives the first-order nulls adjacent to the theoretical Bragg frequencies, which is

$$\frac{\Delta\rho_s}{2}\left(K - 2k_0\right) = \frac{c\tau_0}{4}\left(K - 2k_0\right) = \pm\pi\,, \tag{2.61}$$

or

$$K = \frac{\omega^2}{g} = \pm\frac{4\pi}{c\tau_0} + 2k_0 \ . \tag{2.62}$$

Therefore, the total width of the Bragg region, from null to null, $\Delta\omega_p$ (left and right are equal) is

$$\Delta\omega_p = \sqrt{2gk_0}\left[\left(1+\frac{1}{f_0\tau_0}\right)^{\frac{1}{2}} - \left(1-\frac{1}{f_0\tau_0}\right)^{\frac{1}{2}}\right] \ . \tag{2.63}$$

Since for the HF frequency band, f_0 is from 3 MHz to 30 MHz and the radar pulse width τ_0 is generally larger than 2 μs, the value $(f_0\tau_0)^{-1}$ has a maximum of $\frac{1}{6}$, or in most cases of f_0 and τ_0 combinations, it is sufficient to assume that $(f_0\tau_0)^{-1} << 1$. Binomial expansion of the terms inside the rectangular brackets gives

$$\begin{aligned}&\left[\left(1+\frac{1}{f_0\tau_0}\right)^{\frac{1}{2}} - \left(1-\frac{1}{f_0\tau_0}\right)^{\frac{1}{2}}\right] \\ &\approx \left[\left(1+\frac{1}{2f_0\tau_0}\right) - \left(1-\frac{1}{2f_0\tau_0}\right)\right] = \frac{1}{f_0\tau_0} \ .\end{aligned} \tag{2.64}$$

Thus, equation (2.63) becomes

$$\Delta\omega_p \approx \sqrt{2gk_0}\,(f_0\tau_0)^{-1} \ . \tag{2.65}$$

In equation (2.65), $\omega_B = \sqrt{2gk_0}$ is the Bragg frequency for the monostatic radar configuration and $(f_0\tau_0)^{-1}$ may be written as $\frac{T_0}{\tau_0}$, where $T_0 = 1/f_0$ is the period of the radar wave. The reciprocal of $\frac{T_0}{\tau_0}$ is actually the number of the wave periods within one pulse width, i.e. $N_p = \frac{\tau_0}{T_0}$, so equation (2.65) can be rewritten as

$$\Delta\omega_p \approx \frac{\omega_B}{N_p} \ . \tag{2.66}$$

Equation (2.66) is the theoretical expression of the width of the Bragg region for the pulsed radar received Doppler spectrum. A comparison of equation (2.66) with the numerical calculation of the width of the Bragg region (after averaging) shows excellent agreement between them, and, therefore, $\Delta\omega_p$ in equation (2.58) can be replaced by equation (2.66).

Equation (2.66) may also be used to examine the dependence of the standard deviation of the Bragg fluctuations on either the radar frequency or the pulse width. In order to explicitly see these relationships, equation (2.65) may be cast as

$$\begin{aligned} \Delta\omega_p &\approx \sqrt{2gk_0}\,(f_0\tau_0)^{-1} \\ &= \sqrt{\frac{4\pi g}{c}}\tau_0^{-1} f_0^{-\frac{1}{2}} = \sqrt{\frac{4\pi g}{c}}\xi\,, \end{aligned} \tag{2.67}$$

where $\xi = \tau_0^{-1} f_0^{-\frac{1}{2}}$.

For a practical consideration, it is desired to know for what values of the radar frequency f_0 and pulse width τ_0 the standard deviation will be significant as compared to the Δ_{FFT}. In equation (2.67) the factor $\sqrt{\frac{4\pi g}{c}}$ is a constant, and in view of equation (2.58) it may be concluded that the standard deviation STD is linearly proportional to ξ. It is useful to plot the STD as a function of ξ (rather than $\Delta\omega_p$). From equation (2.58), the governing linear equation is

$$\mathrm{STD} = b_1\xi + b_2\,, \tag{2.68}$$

where b_1 and b_2 are re-defined as dictated by equation (2.67). Applying the LSM method [47] to fit the curve gives

$$b_1 = \frac{n\sum_{i=1}^{n} x_i y_i - \sum_{i=1}^{n} x_i \sum_{i=1}^{n} y_i}{n\sum_{i=1}^{n} x_i^2 - \left(\sum_{i=1}^{n} x_i\right)^2} \tag{2.69}$$

and

$$b_2 = \frac{1}{n}\left(\sum_{i=1}^{n} y_i - b_1 \sum_{i=1}^{n} x_i\right) . \tag{2.70}$$

Here, x_i and y_i corresponds to data arrays of ξ and STD, respectively, with n elements inside. Equation (2.68) is plotted in Figure 2.24 as compared to the simulated results.

In Figure 2.24, the STD is normalized by the half Δ_{FFT} (denoted as NSTD) to check its significance. If the value of the NSTD is larger than unity, the Bragg fluctuations are considered to be significant. The unity value of NSTD corresponds to the value $\xi = 79.39$ as indicated in Figure 2.24. This means that when the value ξ is equal to or larger than 79.39 the Bragg fluctuations will be significant. In Figure 2.25 the pulse width is plotted as a function of the radar frequency for those curves that have ξ values equal to or larger than 79.39. These curves show that for a required Δ_{FFT}, there is a trade-off between the pulse width and the radar frequency. When the values of ξ are inside the shadow region in Figure 2.25, the significant fluctuations are expected. As an example, from Figure 2.25, the standard deviations of the Bragg fluctuations for the operating frequencies of 25 MHz, 15 MHz, and 5 MHz are significant when the pulse widths are less than 2.8 μs, 3.4 μs, and 6.0 μs, respectively. On the other hand, the OSCR radar system referred to in Table 1.1 uses an operating frequency of 25 MHz and pulse width of 6.667 μs, which gives a value $\xi \approx 30$. According to Figure 2.25, this combination of operating parameters will not cause significant fluctuation of the Bragg peaks.

As another practical consideration, to ensure that the standard deviation of the Bragg fluctuations do not exceed a particular Δ_{FFT}, the previous results may be used to choose the proper combination of radar operating frequency and pulse width.

2.6.2 Standard Deviations for Different Δ_{FFT}s

As examined in Section 2.6.1, the Bragg fluctuations result from the randomness of the ocean surface waves when finite time series are used to estimate the Doppler spectra. For

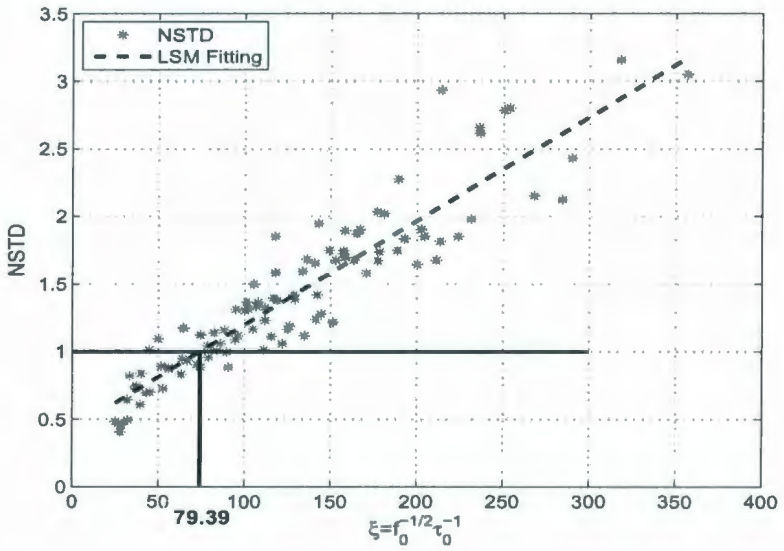

Figure 2.24: NSTD as a function of ξ (asterisk) and the LSM fitted line (dashed line). The horizontal solid line indicates the NSTD value equal to unity while the vertical solid line indicates the corresponding value of $\xi = 79.39$.

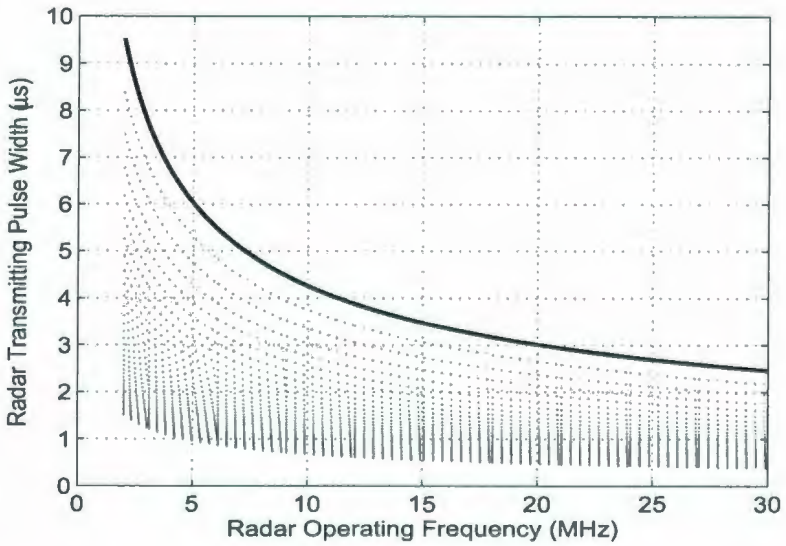

Figure 2.25: Radar pulse widths as a function of operating frequency for values of ξ equal to (solid line) and larger than (dashed lines) 79.39.

a fixed Δ_{FFT}, the standard deviation of the Bragg fluctuations is linearly proportional to the width of the Bragg region, which is sufficiently defined by a factor $\xi = \tau_0^{-1} f_0^{-\frac{1}{2}}$.

A subsequent logical question will be: Is there any explicit relationship between the standard deviation of the Bragg fluctuations and the Δ_{FFT} for a fixed value of ξ, or equivalently, for a fixed width of the Bragg region? A simple approach is to plot standard deviation against the Δ_{FFT}. Obviously, the increase of Δ_{FFT} will decrease the precision of the measurement. However, finer Δ_{FFT} will bring more frequency points to the Bragg region, which means more randomness will be added to the fixed region. As will be seen in the next subsection, there does not appear to be any simple linear relationship between the Bragg fluctuation and the Δ_{FFT}.

Standard Deviation as a Function of Δ_{FFT}

As a numerical examination, time series are simulated for a fixed ξ but processed with different Δ_{FFT}s. Two ways are used to alter the Δ_{FFT}s: one is to change the sampling interval, another is to change the number of samples (this number should be a power of two due to FFT algorithm). Here, the sampling intervals are chosen from 0.2 s to 0.8 s, while the number of samples are selected as 256, 512, 1024, and 2048. The data sets are simulated with a fixed pulse width of 4 μs and two operating frequencies of 5 MHz and 15 MHz. The standard deviations of the centroids for the left and right Bragg regions are obtained using the procedure described before. The Δ_{FFT}s and standard deviations of the left and right Bragg regions are tabulated in Table 2.6 for 5 MHz and Table 2.7 for 15 MHz. Examination of the values of standard deviations and Δ_{FFT}s shows that there is no obvious relationship between them.

Barrick [48] introduces the concept of equivalent number of frequency points within the Bragg region to analyze the Bragg fluctuations. In his analysis, with an assumption of many frequency points within the Bragg region, the distribution of the centroid position reduces to Gaussian according to the Central Limit Theorem. The standard deviation will be expressed as function of Δ_{FFT} and the square root of the equivalent number of the

frequency points within the Bragg region N_e,

$$\text{STD} \propto \Delta_{\text{FFT}}\sqrt{N_e}\,. \tag{2.71}$$

The equivalent number of the frequency points within the Bragg region is defined as

$$N_e = \frac{P_1 + P_2 + \cdots + P_N}{P_{max}} = \frac{\sum_{n=1}^{N} P_n}{P_{max}}\,, \tag{2.72}$$

where P_n is power of the Doppler spectrum at frequency f_n within the Bragg region, N is the number of the frequency positions within the Bragg region, and P_{max} is the maximum value in the set of $\{P_n, n = 1, 2, \cdots, n\}$.

In Table 2.6 for $f_0 = 5$ MHz and Table 2.7 for $f_0 = 15$ MHz, a set of values of N_e for different Δ_{FFT}s and standard deviations are listed. The standard deviations are plotted against $\Delta_{\text{FFT}}\sqrt{N_e}$ in Figures 2.26 and 2.27 with the operating frequencies of 5 MHz and 15 MHz. According to examination, there is no obvious relationship between the standard deviation of the centroid positions and the square root of N_e. This simulation result indicates that Barrick's result cannot be applied in the analysis. Another means of addressing the problem is required.

Determination of the Critical Value of ξ

In the last subsection we found a value of ξ for a specific Δ_{FFT} as the critical value say ξ_c, that, when a combination of f_0 and τ_0 makes the value ξ larger than ξ_c, significant Bragg fluctuations will occur. Implied in this statement is that for different Δ_{FFT}s, the critical value ξ_c will not be the same. If the relationship between the Δ_{FFT} and the ξ_c can be established in a simple, explicit manner, we may at least know how to choose the radar parameters and the Δ_{FFT} to avoid the significant Bragg fluctuations. Following this idea, large amounts of data have been simulated and processed using various Δ_{FFT}s.

Figures 2.28 and 2.29 are plots that can be used to estimate ξ_c by the least squares

Table 2.6: STD as a function of Δ_{FFT} (in Hz) for $f_0 = 5$ MHz and $\tau_0 = 4$ μs. STDL and STDR have been defined in Table 2.1, N_{eL} and N_{eR} are the equivalent numbers of the frequency points in the left- and right-hand Bragg regions, respectively.

$0.5\Delta_{\mathrm{FFT}}$ (Hz)	STDL (Hz)	STDR (Hz)	N_{eL}	N_{eR}
0.0098	0.0057	0.0053	1.6384	1.6705
0.0065	0.0041	0.0042	1.7760	1.7633
0.0049	0.0034	0.0030	1.7757	1.8405
0.0039	0.0026	0.0029	1.8891	1.8307
0.0033	0.0021	0.00255	2.0093	1.8747
0.0028	0.0025	0.0021	2.1307	2.0326
0.0026	0.0020	0.0021	2.0811	2.0982
0.0024	0.00197	0.00207	2.2186	2.1068
0.0020	0.0023	0.0015	2.3659	2.3791
0.0016	0.00165	0.00175	2.5094	2.2825
0.0014	0.0016	0.0019	2.8198	2.6962
0.0013	0.0014	0.0016	2.5980	2.4829
0.0012	0.00157	0.00147	2.6486	2.7259
9.77×10^{-4}	0.0016	8.203×10^{-4}	3.1992	3.2782
8.1380×10^{-4}	0.00096	0.0014	3.3018	3.2318
6.9754×10^{-4}	0.0013	0.0013	4.0929	3.2817
6.5104×10^{-4}	0.0013	0.0014	3.8401	3.8375
6.1035×10^{-4}	0.00115	0.00105	3.6087	3.9922
4.8828×10^{-4}	7.71×10^{-4}	5.57×10^{-4}	4.6574	4.4320
4.0690×10^{-4}	7.7786×10^{-4}	0.0011	4.8329	5.1852
3.4877×10^{-4}	9.1921×10^{-4}	7.6748×10^{-4}	5.2892	4.9578
3.2552×10^{-4}	5.9857×10^{-4}	0.0012	5.1319	4.8158
3.0518×10^{-4}	7.2033×10^{-4}	8.3782×10^{-4}	6.5789	6.7138

Table 2.7: STD as a function of Δ_{FFT} for $f_0 = 15$ MHz and $\tau_0 = 4$ μs. The symbols have the same definitions as in Table 2.6.

$0.5\Delta_{\mathrm{FFT}}$ (Hz)	STDL (Hz)	STDR (Hz)	N_{eL}	N_{eR}
0.0039	0.0027	0.0027	1.7899	1.7300
0.0033	0.0019	0.0022	1.7493	1.7438
0.0030	0.0016	0.0020	1.7531	1.8013
0.0028	0.0018	0.0018	1.7940	1.8554
0.0026	0.0016	0.0017	1.7817	1.8439
0.0024	0.0018	0.0012	1.7727	1.8654
0.0020	0.0013	0.0013	1.7538	1.9523
0.0016	0.0013	0.0012	1.9259	1.9919
0.0015	0.0010	0.0012	2.1428	2.1333
0.0014	0.0011	0.0012	1.9452	2.2745
0.0013	9.9672×10^{-4}	0.010	2.1645	2.1726
0.0012	0.0014	8.6551×10^{-4}	2.2913	2.2538
9.7656×10^{-4}	0.0010	7.2067×10^{-4}	2.1980	2.7378
8.1380×10^{-4}	8.2646×10^{-4}	9.1552×10^{-4}	2.9269	2.5963
7.5120×10^{-4}	9.2063×10^{-4}	0.0012	2.3202	2.8079
6.9754×10^{-4}	8.8607×10^{-4}	8.9518×10^{-4}	2.6479	2.7260
6.5104×10^{-4}	8.6104×10^{-4}	8.4710×10^{-4}	3.1920	2.7222
6.1035×10^{-4}	0.0011	8.1536×10^{-4}	2.9751	2.8635
4.8828×10^{-4}	9.4407×10^{-4}	4.8643×10^{-4}	2.6668	3.5461
4.0690×10^{-4}	5.8762×10^{-4}	6.0098×10^{-4}	3.1094	3.6339
3.7560×10^{-4}	5.9541×10^{-4}	7.3967×10^{-4}	3.2670	3.9474
3.4877×10^{-4}	7.1049×10^{-4}	5.0619×10^{-4}	4.1169	4.4781
3.2552×10^{-4}	6.7800×10^{-4}	8.2001×10^{-4}	4.1862	4.0625
3.0518×10^{-4}	6.1355×10^{-4}	5.1003×10^{-4}	4.4042	4.4838

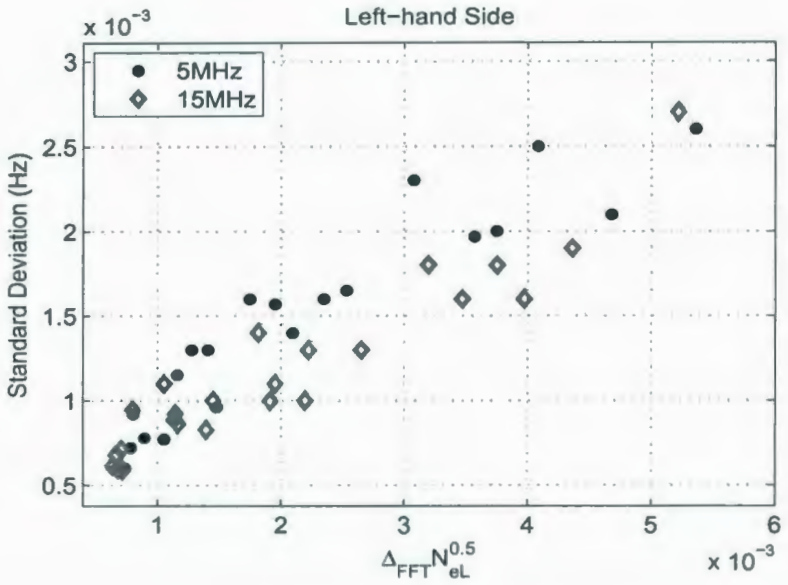

Figure 2.26: Standard deviation as a function of the product of the Δ_{FFT} and the square root of N_{eL}, $\Delta_{\mathrm{FFT}}\sqrt{N_{eL}}$. The radar $\tau_0 = 4$ μs, and $f_0 = 5$ MHz and $f_0 = 15$ MHz.

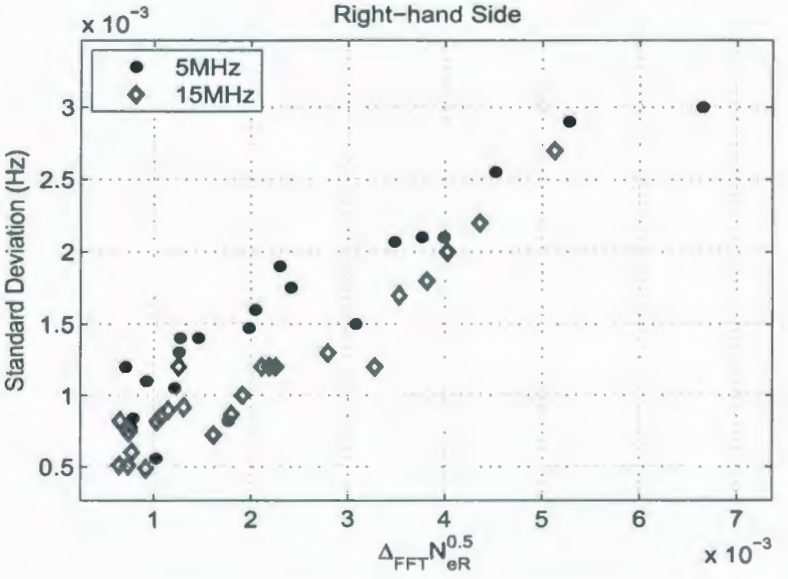

Figure 2.27: Same as in Figure 2.26 but for the right-hand side Bragg region.

Table 2.8: Estimation of the critical values for different Δ_{FFT}s. ξ_c is critical value, β_c is critical width of the Bragg region, and N_c is the critical number of frequency points within the Bragg region.

Δ_{FFT} (Hz)	ξ_c	β_c (Hz)	N_c
0.0130	381.77	0.0390	2.99
0.0078	220.80	0.0225	2.89
0.0066	192.40	0.0196	3.02
0.0048	147.88	0.0151	3.14
0.0040	126.27	0.0129	3.22
0.0032	101.76	0.0104	3.19
0.0024	79.39	0.0081	3.37
0.0020	71.40	0.0073	3.73
0.0012	39.80	0.0041	3.33

method (LSM) of fitting. These figures are plotted in the same manner as Figures 2.24 and 2.25 except the Δ_{FFT} is changed to be 0.0040 Hz. In Figure 2.28, the ξ_c value has been indicated in the x-axis as 126.27. Figure 2.29 depicts those f_0 and τ_0 combinations that make $\xi \geq \xi_c$.

Similarly, Figures 2.30 and 2.31 are for a $\Delta_{\mathrm{FFT}} = 0.0012$ Hz, Figures 2.32 and 2.33 are for a $\Delta_{\mathrm{FFT}} = 0.0020$ Hz. The corresponding ξ_c's are 39.80 and 71.40, respectively. More cases are studied and the results are listed in Table 2.8. In Figure 2.34, the ξ_c values are plotted against the corresponding Δ_{FFT}s. An approximately linear relation between them is observed.

Since for each ξ, there is a unique width of the Bragg region associated with it (equation (2.67)), the critical values ξ_c in Table 2.8 will define a set of "critical widths", β_c, of the Bragg region. The β_c will be linearly proportional to the Δ_{FFT}. If β_c is divided by the corresponding Δ_{FFT}, the result will be a constant and denoted as $N_c = \dfrac{\beta_c}{\Delta_{\mathrm{FFT}}}$. N_c is actually the "critical number" of frequency points within the Bragg region. β_c and N_c are also listed in Table 2.8. Since β_c is a linear function of Δ_{FFT}, N_c will be a constant for different Δ_{FFT}s. The physical meaning of this is that, when the number of frequency

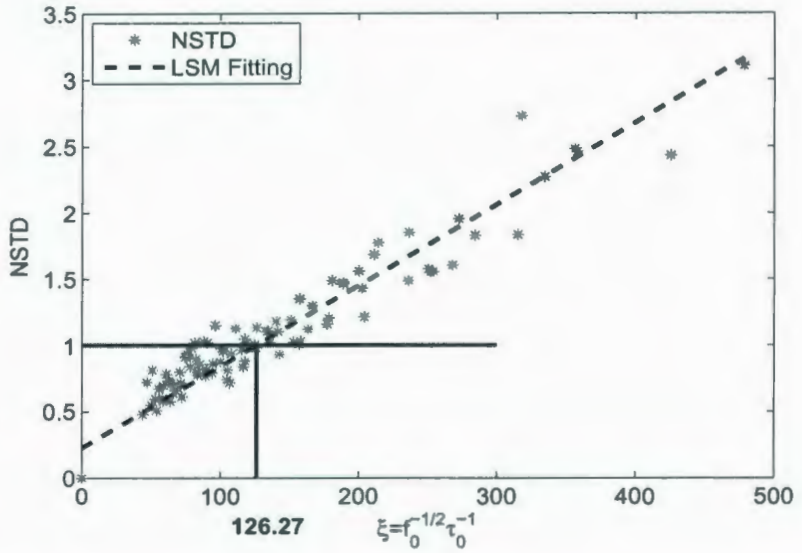

Figure 2.28: Plots of NSTD as function of ξ (asterisk) and the LSM fitted line (dashed line). The horizontal solid line indicates the NSTD value equal to unity while the vertical solid line indicates the corresponding value of $\xi_c = 126.27$. The Δ_{FFT} is 0.0040 Hz.

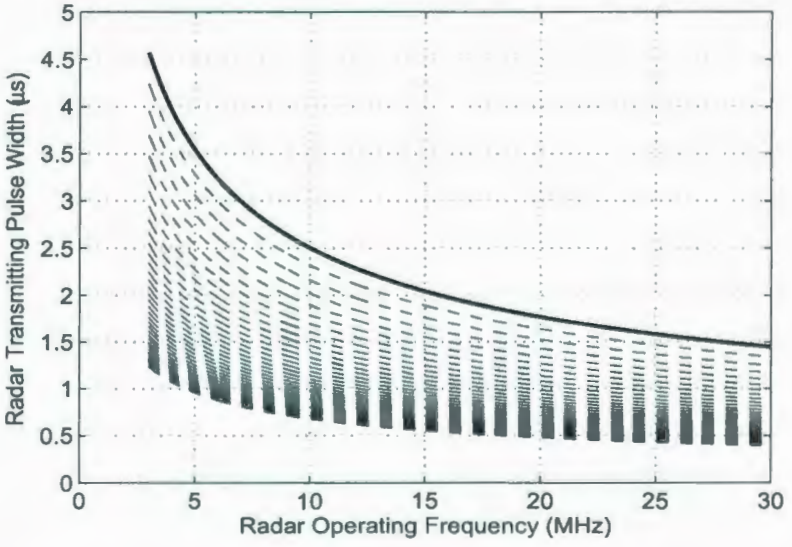

Figure 2.29: Plots of τ_0 as a function of f_0 for values of ξ equal to (solid line) and larger than (dashed lines) $\xi_c = 126.27$. The Δ_{FFT} is 0.0040 Hz.

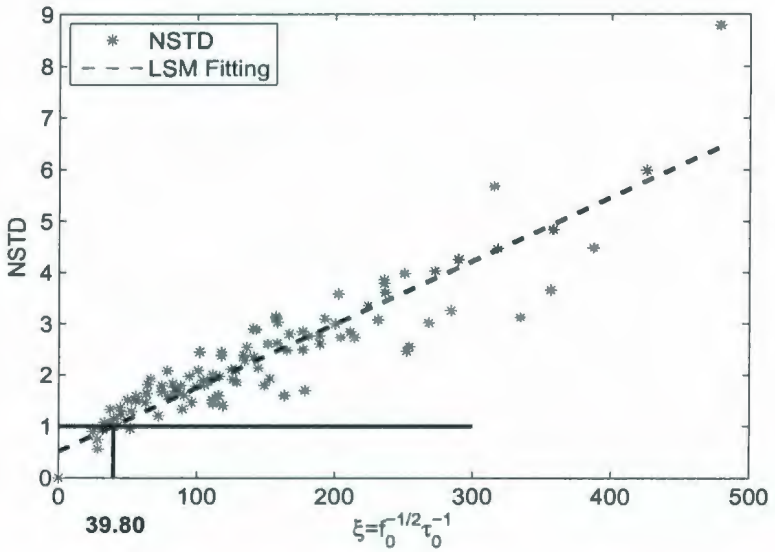

Figure 2.30: NSTD as a function of ξ. The dashed line is obtained by the LSM of fitting. This results $\xi_c = 39.80$ corresponding to $\Delta_{\mathrm{FFT}} = 0.0012$ Hz.

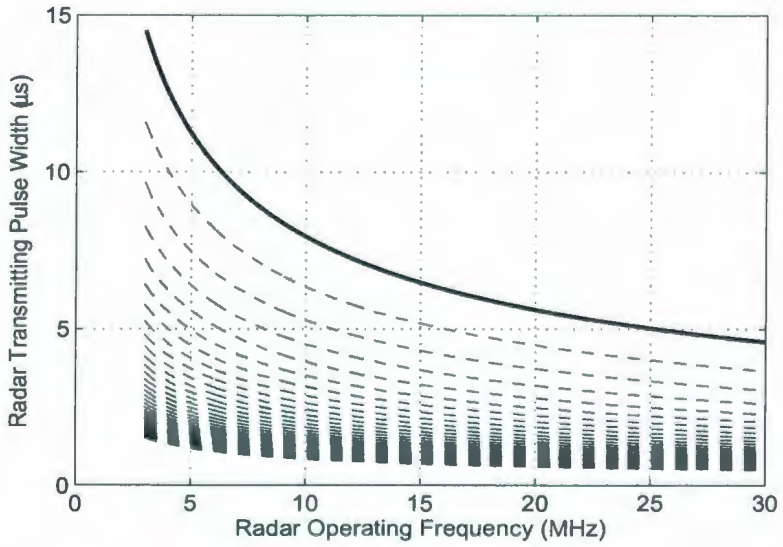

Figure 2.31: Same plots as in Figure 2.29 with $\xi_c = 39.80$ and $\Delta_{\mathrm{FFT}} = 0.0012$ Hz.

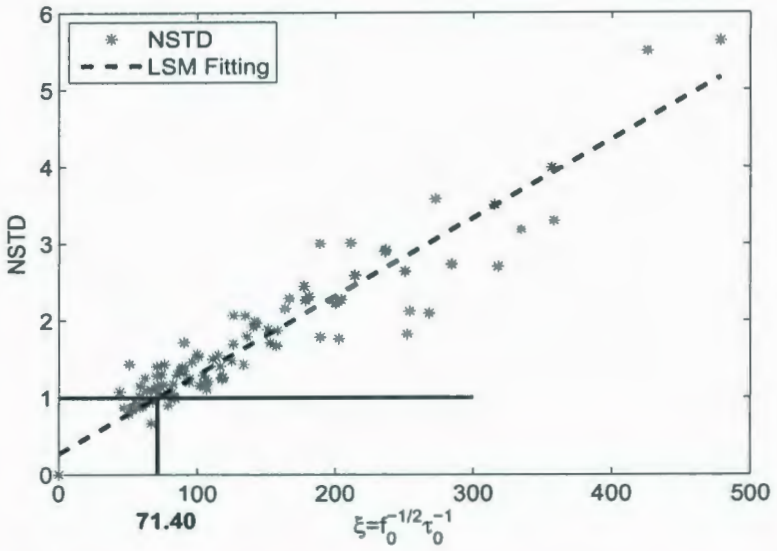

Figure 2.32: Same plots as in Figure 2.30 to determine the value of $\xi_c = 71.40$, corresponding to $\Delta_{\mathrm{FFT}} = 0.0020$ Hz.

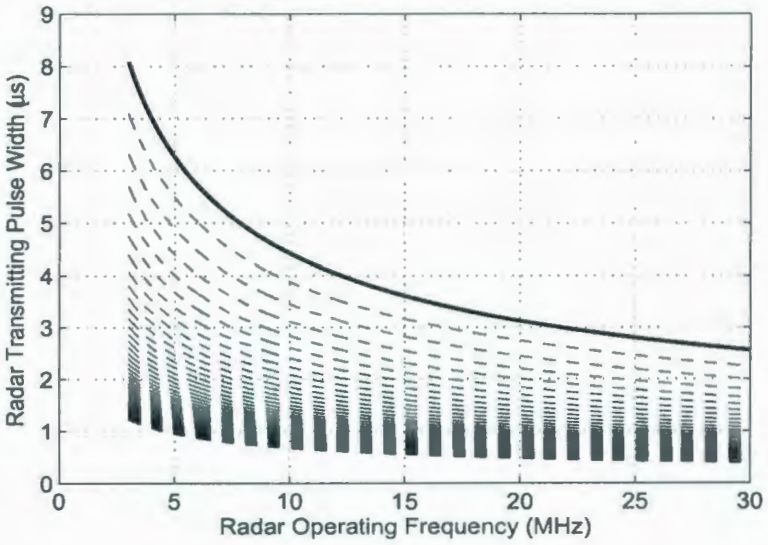

Figure 2.33: Same plots as in Figure 2.31 with $\xi_c = 71.40$ and $\Delta_{\mathrm{FFT}} = 0.0020$ Hz.

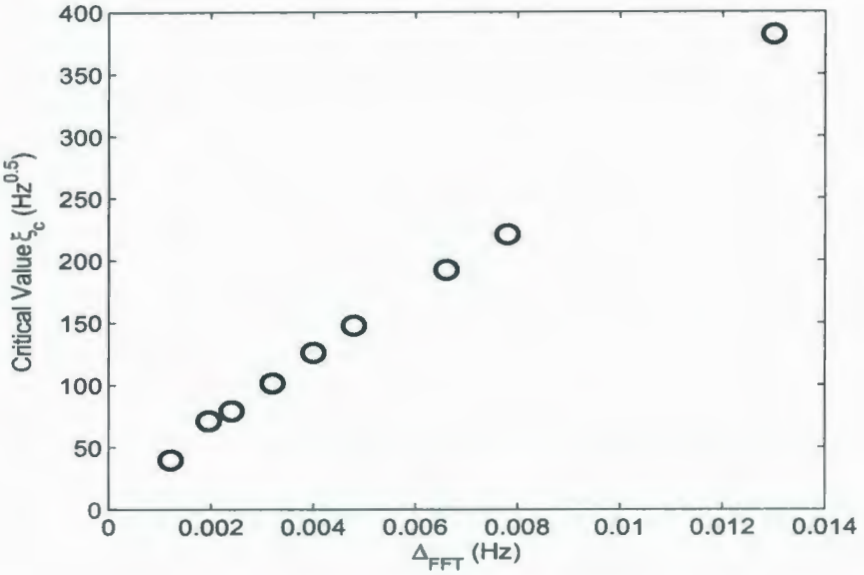

Figure 2.34: Critical value ξ_c as a function of Δ_{FFT}.

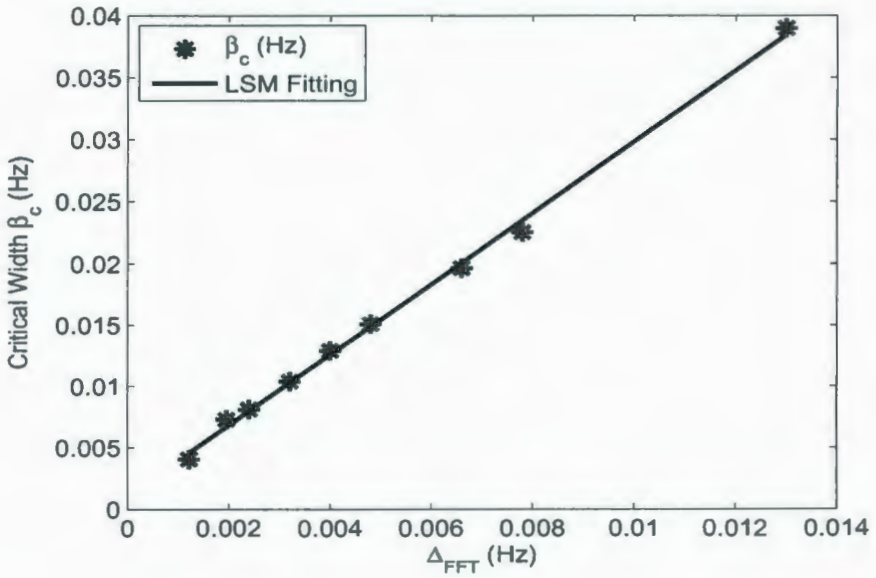

Figure 2.35: Plot of β_c as a function of Δ_{FFT} to determine N_c.

points within the Bragg region is larger than N_c, significant Bragg fluctuations will occur. In practice, however, N_c has variable values due to our numerical scheme. N_c may be determined by the LSM of fitting [47]. Similar to equation (2.69), we have

$$N_c = \frac{n\sum_{i=1}^{n}\Delta_{\mathrm{FFT}i}\beta_c^i - \sum_{i=1}^{n}\Delta_{\mathrm{FFT}i}\sum_{i=1}^{n}\beta_c^i}{n\sum_{i=1}^{n}\Delta_{\mathrm{FFT}i}^2 - \left(\sum_{i=1}^{n}\Delta_{\mathrm{FFT}i}\right)^2} \tag{2.73}$$

where n is the number of β_c obtained. N_c has an approximated value of 2.9 determined by equation (2.73) with simulated data. N_c should be positive but may not necessarily be an integer. More precise estimation of N_c may be obtained if more data sets are used. Figure 2.35 depicts a plot of β_c versus Δ_{FFT} to determine N_c by the LSM of fitting. As an example, the OSCR radar system has a $\Delta_{\mathrm{FFT}} \approx 0.0059$ Hz. According to Figures 2.34 and 2.35, the critical value ξ_c and critical width β_c can be approximately estimated as 180 and 0.0018 Hz, respectively.

2.7 Chapter Summary

According to Pierson [7], the ocean surface may be described by wave components with each component having a deterministic magnitude and a random initial phase term, which is uniformly distributed on the interval [0 2π). Under Pierson's model, the ocean surface fits the description of a Gaussian zero-mean process. While there are certainly instances in which the ocean does not exhibit this behavior, it has been shown to be a satisfactory model for many purposes. Since any linear operation on a Gaussian random variable produces another Gaussian random variable, the HF radar received signals will be Gaussian, as shown by Barrick and Snider [8].

If a pulsed source is used to illuminate the ocean surface, a finite scattering patch will be selected by the finite duration pulse (e.g. Walsh *et al.* [6], Walsh and Dawe [34], Gill and Walsh [35]). Since a pulse with finite duration in time domain corresponds to a

continuous spectrum in frequency domain, the transmitted signal is actually a combination of frequency components. According to the Bragg scatter mechanism these frequency components will strongly resonate with a set of ocean gravity wave components. The random phase associated with each ocean wave component will then explicitly enter into the scattered electric field equation. Expressing this in the frequency domain yields a squared sinc function [6, 35] when the PSD is calculated. This is in contrast to the Dirac delta function which results from the plane wave incidence used in earlier analyses [4]. The width of the main lobe of the squared sinc function gives at least one explicit reason for the finite width of the Bragg peak.

If infinite length time series were used to calculate the Doppler spectrum as assumed in Walsh *et al.* [6], Walsh and Dawe [34], and Gill and Walsh [35], the power of the Doppler spectrum at each frequency component would be precisely determined because it is described by a Dirac delta function and independent from the others. All the initial randomness terms would be averaged out eventually when the PSD is estimated. Since an infinitely long time series is not realistic, the behavior of the Doppler spectrum calculated from finite time series is investigated to determine the error bound on the measurement of the position of the centroid of the first-order return. A numerical investigation has shown that when the PSD is calculated at an arbitrary frequency point from a finite length time sequence, the true power at the frequency point will be modified by power leaked from surrounding frequency points. The resulting power at that frequency position will become a random variable because the random phases of the scattering waves appear in the final expression as a summation of the cross terms. It is these cross terms that introduce the Bragg fluctuations.

The distribution of these variations has been checked numerically. Several frequency points close to the Bragg peaks on both sides are chosen to ensure that only the first-order Doppler spectra are involved. The distributions of power have been depicted as histograms at several frequencies around the Bragg peak and plotted together with the normalized chi-square distributions for comparison. The means and normalized standard

deviations have been calculated and tabulated. All of these taken together confirm that the distribution of the power at each frequency point is chi-square.

Another conclusion drawn from the previous numerical examination is that the distribution of the fluctuations of the Bragg peaks is a function of the width of the Bragg region and the Δ_{FFT}. Theoretically speaking, the width of the Bragg region can be sufficiently described by the radar frequency and pulse width. An attempt to derive a theoretical expression of the standard deviation of the Bragg fluctuations following Barrick's idea [48] was unsuccessful because the assumption of many frequency points within the Bragg region is invalid.

A numerical examination shows that for a fixed Δ_{FFT}, the standard deviation of the Bragg peak is linearly proportional to the width of the Bragg region, or to a value $\xi = \tau_0^{-1} f_0^{-\frac{1}{2}}$. When ξ is larger than a critical value ξ_c, the Bragg fluctuations will be significant, which means that the standard deviation of the Bragg fluctuations will be larger than the corresponding half Δ_{FFT}. The values of ξ_c vary for different Δ_{FFT}s, but they are linearly related. That is, for data processed with finer Δ_{FFT}, the value of ξ_c will be lower, and *vice versa*. This observation has two consequences: first, for a fixed-width Bragg region, increasing Δ_{FFT} will cause a corresponding increase in Bragg fluctuations, and, secondly, for a fixed Δ_{FFT}, a wider Bragg region will cause more significant fluctuations. A careful check shows that when the width of the Bragg region is approximately 3.0 times larger than the Δ_{FFT}, the Bragg fluctuations will be significant.

Chapter 3

Radar Cross Sections for the FM Waveforms

In the second part of the research work, HF radar backscatter cross sections will be derived with FM sources being employed as the radar transmitted waveforms. Equations associated with FM waveforms will be presented and some of their properties will be discussed. Then, the electric field equations will be obtained based on Walsh's generalized function method [33]. The first- and second-order radar backscatter cross sections will be derived from the field equations and the results will be analyzed.

In pulsed radar systems, the range resolution is determined by the pulse width. Of course, narrower pulses result in higher range resolutions. For example, as may be seen from equation (2.11), a 300 m range resolution requires a pulse width of 2 μs. Additionally, HF surface wave radar is anticipated to cover ranges that are well beyond the line-of-sight horizon. This requires that the pulse repetition time (prt) be increased correspondingly to isolate the transmitter and receiver that are co-located. Increasing prt and decreasing pulse width will cause a decrease of the duty cycle, which means a reduction of the average power radiated to the ocean surface. Since it is the average power, rather than the peak power, that is the measure of the capability of radar's range estimation [74], radar systems with the pulsed waveform have a limitation in providing enough average power to achieve

long range.

It is well known that the pulse compression technique can be used to transmit higher average power with lower peak power. FMCW waveforms, incorporating compression techniques discussed in this chapter, have been widely used throughout the radar remote sensing community (e.g. Cook and Bernfeld [75]). However, the duty cycle of the FMCW waveform is 100%. As a consequence of this, when HF radar is operated in a high power monostatic case, it is difficult to effectively isolate the transmitter and receiver (e.g. Khan *et al.* [52]). This is the main reason that the FMICW waveform has emerged. The FMICW waveform may be viewed as a gated version of the FMCW waveform with the gate being turned on and off according to the operation periods of the transmitter and receiver, respectively. On the other hand, the FMCW waveform can be viewed as a FMICW waveform with 100% duty cycle.

3.1 Expressions of the FM Waveforms

The FMCW signal may be derived from the chirp signal $c(t)$, which is given by

$$c(t) = \cos\left[2\pi\left(f_0 \pm \frac{\alpha t}{2}\right)t\right] \ , \quad \text{for all } \ t \ , \tag{3.1}$$

where f_0 is radar operating frequency, t is time, α is the frequency sweep rate with a unit of Hz/s and $\pm$ corresponds to the up- and down-chirps, respectively. In this analysis, only the up-chirp is considered. The FMCW signal is a periodic repetition version of the chirp signal with finite frequency sweep interval T_r. The sweep rate of the FMCW waveform (as is also the case for the FMICW waveform) may be expressed as the ratio of the sweep bandwidth B and the sweep interval, i.e. $\alpha = B/T_r$. The FMCW waveform $x(t)$ in one period may be cast as

$$x(t) = \cos\left[2\pi\left(f_0 + \frac{\alpha t}{2}\right)t\right] \ , \quad -\frac{T_r}{2} \leq t < \frac{T_r}{2} \ . \tag{3.2}$$

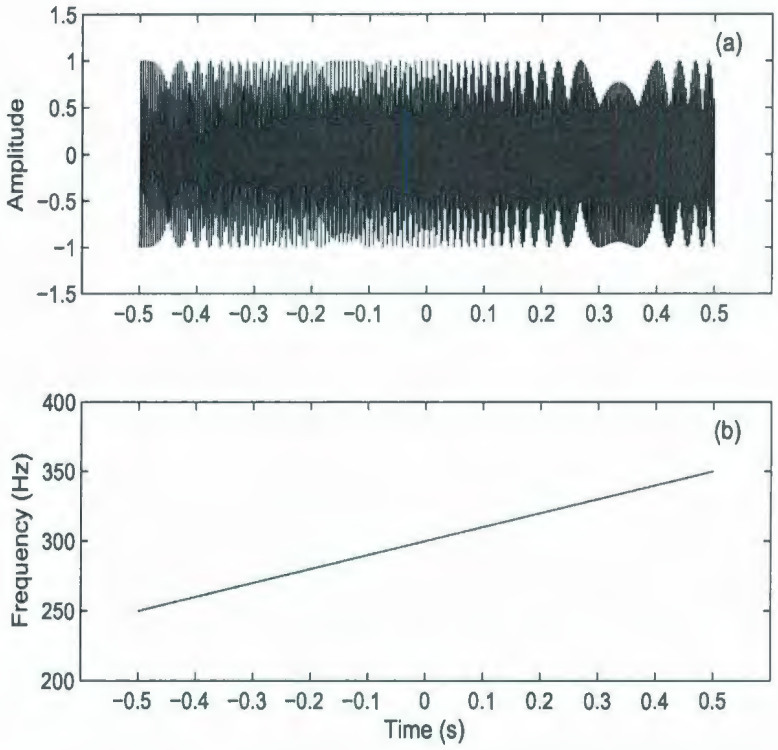

Figure 3.1: An example of FMCW signal (a) and its frequency-time plot (b). The radar parameters are $f_0 = 300$ Hz, $B = 100$ Hz, and $\alpha = 100$ Hz/s.

To be consistent with previous investigations (e.g. Walsh *et al.* [6], Walsh and Dawe [34], Gill and Walsh [35]), we use the exponential function to express the FMCW current waveform $i(t)$ as

$$i(t) = I_0 e^{j\left(\omega_0 t + \alpha \pi t^2\right)}, \quad -\frac{T_r}{2} \leq t < \frac{T_r}{2}, \tag{3.3}$$

where I_0 is the amplitude of the current and ω_0 is radian frequency of the signal with $\omega_0 = 2\pi f_0$. Figure 3.1 is an example of the FMCW waveform within one sweep interval with $f_0 = 300$ Hz, $T_r = 1$ s, and $B = 100$ Hz. The sweep rate is therefore $\alpha = 100$ Hz/s. In Figure 3.1, subplot (a) depicts a time sequence of the FMCW waveform and subplot (b) depicts the frequency sweep as a function of time.

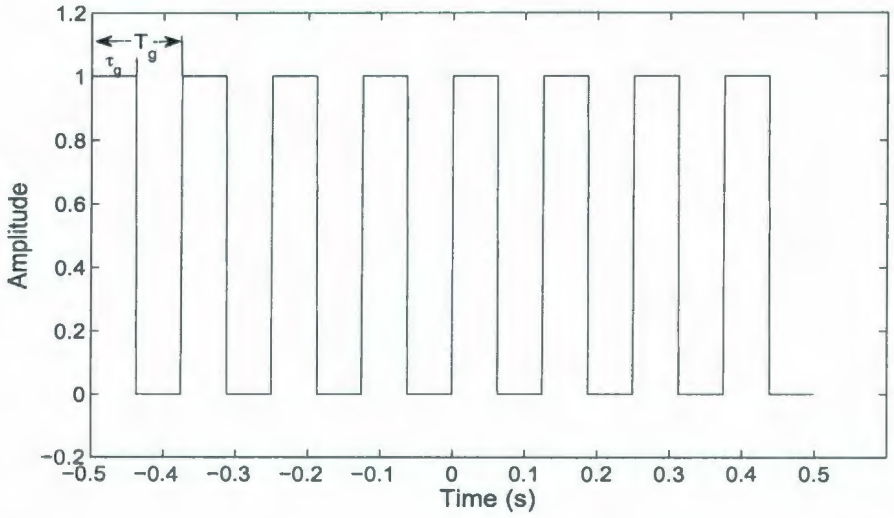

Figure 3.2: An example of a gating sequence within the sweep interval $T_r = 1$ s with $T_g = 0.125$ s, $\tau_g = 0.0625$ s, and $d_c = 50\%$.

In order to construct an FMICW waveform, an equally spaced gating sequence is defined as

$$g(t) = \sum_{n=0}^{N-1} \text{Rect}\left(\frac{t - nT_g - \frac{\tau_g}{2} + \frac{T_r}{2}}{\tau_g}\right), \tag{3.4}$$

where N is number of the gates within a sweep interval T_r, T_g is the period of the gate, and τ_g is the open time of the gate. Other gating sequences are found in the literature. However, only a linear equally spaced gating sequence is considered in our analysis. The ratio of τ_g to T_g is defined as the duty cycle d_c. Rect$(\cdot)$ is a rectangular function given by

$$\text{Rect}\,(x) = \begin{cases} 1, & |x| \leq \frac{1}{2} \\ 0, & \text{otherwise} \end{cases}. \tag{3.5}$$

Figure 3.2 is an example of a gating sequence with the gate period $T_g = 0.125$ s, the open time of the gate $\tau_g = 0.0625$ s, and the duty cycle $d_c = 50\%$.

According to the definition, the FMICW signal may be written as

$$i_g(t) = i(t)g(t) = I_0 e^{j(\omega_0 t + \alpha\pi t^2)} \sum_{n=0}^{N-1} \text{Rect}\left(\frac{t - nT_g - \frac{\tau_g}{2} + \frac{T_r}{2}}{\tau_g}\right). \tag{3.6}$$

Figure 3.3 depicts an example of an FMICW signal with $f_0 = 300$ Hz, $B = 100$ Hz, and $\alpha = 100$ Hz/s. The parameters of the gating sequence are the same as in Figure 3.2. Figure 3.4 depicts the PSDs of (a) the FMCW signal and (b) the FMICW signal. For

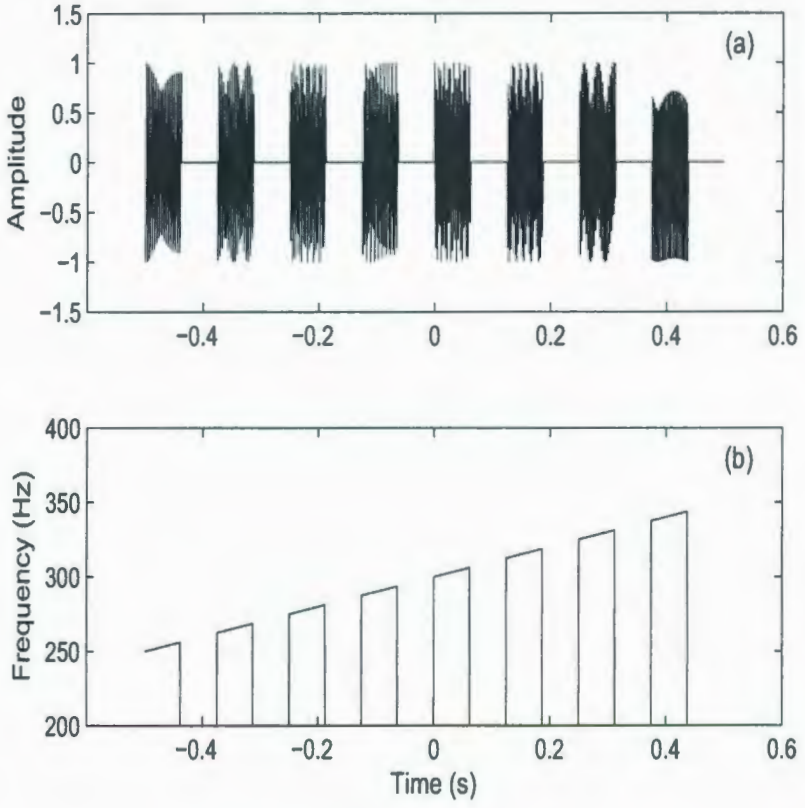

Figure 3.3: An example of FMICW signal (a) and its frequency-time plot (b). The radar parameters are $f_0 = 300$ Hz, $B = 100$ Hz, $\alpha = 100$ Hz/s. The gating parameters are $T_g = 0.125$ s, $\tau_g = 0.0625$ s, and $d_c = 50\%$.

the FMCW signal in Figure 3.4 (a), the plane spectrum has been shown for the carrier frequency $f_0 = 300$ Hz with $B = 100$ Hz. For the FMICW waveform in Figure 3.4

(b), however, the frequency band from 250 Hz to 350 Hz has been interrupted into eight portions. This corresponds to eight gates within the sweep interval.

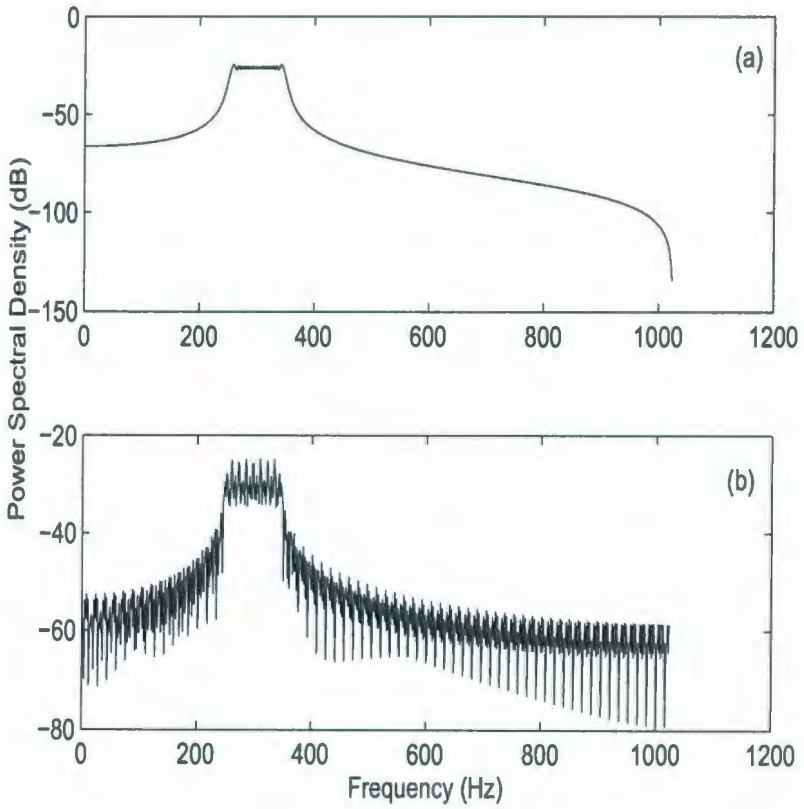

Figure 3.4: PSDs for (a) the FMCW signal and (b) the FMICW signal. The spectra are estimated as periodograms.

3.2 Radar Received Temporal Field Equations

According to previous investigations of HF radar scattering from rough surfaces (e.g. Walsh *et al.* [6], Walsh and Dawe [34], Gill and Walsh [35]), the radar received temporal field equation can be viewed as a convolution of two portions: one is a second-order derivative of the current signal excited on the antenna; another is a time-varying "system" that involves the description of the rough surface. Of course, in the frequency domain, the

field equation is a multiplication of the two portions. The general form of the first-order backscatter field equation in frequency domain has been given in Walsh *et al.* [6], Walsh and Dawe [34], and Gill and Walsh [35]. It is rewritten here as

$$\left(E_0^+\right)_1(\omega_0) = \frac{k_0 C_0}{(2\pi)^{3/2}} \sum_{\vec{K},\omega} P_{\vec{K},\omega} \sqrt{K} \int_{\rho_0} \frac{F^2(\rho_0)}{(\rho_0)^{3/2}} e^{jK\rho_0} e^{-j2k_0\rho_0} e^{-j\pi/4} G(\theta) d\rho_0 \,. \tag{3.7}$$

The radar backscattering configuration is depicted in Figure 2.2. In equation (3.7), C_0 is a dipole constant in the frequency domain with

$$C_0 = \frac{I\Delta l k_0^2}{j\omega_0 \epsilon_0} \,, \tag{3.8}$$

where I is a general current excitation on the dipole of length Δl. $G(\theta)$ is the receiving antenna "directivity" function, which in the narrow beam sense may be taken as approximately constant over the scattering patch. The scattering surface is specified as a Fourier series with coefficients $P_{\vec{K},\omega}$ for surface components whose wavenumbers and radian frequencies are $\vec{K}$ and ω, respectively. In our analysis, since a monostatic configuration is assumed so that the radar transmitter and receiver are co-located (Figure 2.2), the distances from the transmitter to the scattering patch ρ_1 and from patch to the receiver ρ_2 are identical, i.e. $\rho_1 = \rho_2 = \rho_0$. This yields the squared factor of $F^2(\rho_0)$ in equation (3.7). There also exists a parallel component of the field equation with complex conjugate exponential $e^{-jK\rho_0} e^{j2k_0\rho_0} e^{j\pi/4}$ and $G(\theta + \pi)$ (see Walsh *et al.* [6], Walsh and Dawe [34], Gill and Walsh [35]). However, this component is proven to be very small compared with equation (3.7), and we therefore ignore it in future development.

When equation (3.7) is inversely Fourier transformed to the time domain, according to the convolution theorem,

$$\mathcal{F}^{-1}\left[\left(E_0^+\right)_1(\omega_0)\right](t) = \frac{1}{(2\pi)^{3/2}} \mathcal{F}^{-1}\left[-j\frac{\eta_0 \Delta l}{c^2}\omega_0^2 I(\omega_0)\right] \overset{t}{*} \mathcal{F}^{-1}\left[\sum_{\vec{K},\omega} P_{\vec{K},\omega}\sqrt{K}\right.$$

$$\int_{\rho_0} \frac{F^2(\rho_0)}{(\rho_0)^{3/2}} e^{jK\rho_0} e^{-j2k_0\rho_0} e^{-j\pi/4} d\rho_0 \Bigg] , \tag{3.9}$$

where $\mathcal{F}^{-1}$ refers to the inverse Fourier transform, $\overset{t}{*}$ refers to a convolution in the time domain, and $\eta_0 = \sqrt{\epsilon_0/\mu_0}$ is the impedance of the free space. $G(\theta)$ may be taken as any appropriate constant and since it does not affect the outcome of the subsequent analysis it is here chosen as unity as in Walsh *et al.* [6]. Since the inverse Fourier transform is with respect to ω_0 or k_0, the second inverse Fourier transform on the right side of equation (3.9) is actually operated on the factor $e^{-j2k_0\rho_0}$. This may be cast explicitly as

$$\mathcal{F}^{-1}\left[-j\frac{\eta_0 \Delta l}{c^2}\omega_0^2 I(\omega_0)\right](t) \overset{t}{*} \mathcal{F}^{-1}\left[e^{-j2k_0\rho_0}\right](t) . \tag{3.10}$$

The first inverse Fourier transform of equation (3.10) can be evaluated as

$$\mathcal{F}^{-1}\left[-j\frac{\eta_0 \Delta l}{c^2}\omega_0^2 I(\omega_0)\right](t) = j\frac{\eta_0 \Delta l}{c^2}\frac{\partial^2 i_c(t)}{\partial t^2} , \tag{3.11}$$

where $i_c(t)$ is a general current excitation and will be replaced by equation (3.3) for the FMCW signal or equation (3.6) for the FMICW signal.

3.2.1 Field Equations for the FMCW Waveform

Having established the general procedure for developing the electric field equations, we now turn our attention to the FMCW waveform with the $i_c(t)$ in equation (3.11) being replaced by $i(t)$ of equation (3.3). The second-order derivative of $i(t)$ with respect to the time t is

$$\begin{aligned} \frac{\partial^2 i(t)}{\partial t^2} &= -I_0 e^{j(\omega_0 t + \alpha\pi t^2)}\left(\omega_0^2 + 4\pi\alpha\omega_0 t + 4\pi^2\alpha^2 t^2 - j2\pi\alpha\right) \\ &\approx -I_0\omega_0^2 e^{j(\omega_0 t + \alpha\pi t^2)} , \end{aligned} \tag{3.12}$$

where the approximation is due to the fact that $2\pi\alpha t \leq 2\pi B << \omega_0$ and $-j2\pi\alpha$ is neglected. Substitution from equation (3.12) into equation (3.11) gives

$$\mathcal{F}^{-1}\left[-j\frac{\eta_0\Delta l}{c^2}\omega_0^2 I\left(\omega_0\right)\right](t) = -jI_0\frac{\eta_0\Delta l\omega_0^2}{c^2}e^{j\left(\omega_0 t+\alpha\pi t^2\right)} . \tag{3.13}$$

The evaluation of the second inverse Fourier transform of equation (3.10) will give a Dirac delta function, which is

$$\mathcal{F}^{-1}\left[e^{-j2k_0\rho_0}\right] = \mathcal{F}^{-1}\left[e^{-j\frac{2\omega_0\rho_0}{c}}\right] \approx \delta\left(t-\frac{2\rho_0}{c}\right) . \tag{3.14}$$

The convolution of equation (3.13) with a Dirac delta function of equation (3.14) yields a time shift of term $\frac{2\rho_0}{c}$ to the time variable t. Equation (3.10) can be written as

$$\begin{aligned}&\left[-jI_0\eta_0\Delta lk_0^2 e^{j\left(\omega_0 t+\alpha\pi t^2\right)}\right] \overset{t}{*} \left[\delta\left(t-\frac{2\rho_0}{c}\right)\right] \\ &= -jI_0\eta_0\Delta lk_0^2 e^{j\left[\omega_0\left(t-\frac{2\rho_0}{c}\right)+\alpha\pi\left(t-\frac{2\rho_0}{c}\right)^2\right]} ,\end{aligned} \tag{3.15}$$

where $k_0 = \frac{\omega_0}{c}$ is invoked. Therefore, from equation (3.9), for the FMCW waveform, the first-order temporal electric field equation becomes

$$\begin{aligned}\left(E_0^+\right)_1(t) &= \frac{-jI_0\eta_0\Delta lk_0^2}{(2\pi)^{3/2}}\sum_{\vec{K},\omega} P_{\vec{K},\omega}\sqrt{K}e^{-j\pi/4} \\ &\quad \int_{\rho_0}\frac{F^2\left(\rho_0\right)}{\left(\rho_0\right)^{3/2}}e^{jK\rho_0}e^{j\left[\omega_0\left(t-\frac{2\rho_0}{c}\right)+\alpha\pi\left(t-\frac{2\rho_0}{c}\right)^2\right]}d\rho_0 .\end{aligned} \tag{3.16}$$

The integration range ρ_0 in equation (3.16) is defined as a scattering patch over the rough surface with its distance to the radar receiver from $\frac{ct}{2}$ to $\frac{c(t-\tau_0)}{2}$, where $\tau_0 = \frac{1}{B}$. Here, τ_0 is analogous to the pulse width for the pulsed waveform. Equation (3.16) then becomes

$$\left(E_0^+\right)_1(t) = \frac{-jI_0\eta_0\Delta lk_0^2}{(2\pi)^{3/2}}\sum_{\vec{K},\omega} P_{\vec{K},\omega}\sqrt{K}e^{-j\pi/4}$$

$$\int_{\frac{c(t-\tau_0)}{2}}^{\frac{ct}{2}} \frac{F^2(\rho_0)}{(\rho_0)^{3/2}} e^{jK\rho_0} e^{j\left[\omega_0\left(t-\frac{2\rho_0}{c}\right)+\alpha\pi\left(t-\frac{2\rho_0}{c}\right)^2\right]} d\rho_0 \,. \tag{3.17}$$

Equation (3.17) may be further simplified by expanding the phase term of the integrand as

$$\begin{aligned} \omega_0\left(t-\frac{2\rho_0}{c}\right)+\alpha\pi\left(t-\frac{2\rho_0}{c}\right)^2 &= \omega_0 t-\frac{2\omega_0\rho_0}{c}+\alpha\pi\left(t^2-\frac{4t\rho_0}{c}+\frac{4\rho_0^2}{c^2}\right) \\ &\approx \omega_0 t-\rho_0\left(2k_0+\frac{4\pi\alpha t}{c}\right)+\alpha\pi t^2 \,. \end{aligned} \tag{3.18}$$

The term $\frac{4\rho_0^2}{c^2}$ is dropped because it is not significant as compared to the other terms (ρ_0 is on the order of only a few hundreds of kilometres, maximally). After bringing the ρ_0 independent factors, $e^{j\omega_0 t}$ and $e^{j\alpha\pi t^2}$, outside the integral, equation (3.17) becomes

$$\begin{aligned} \left(E_0^+\right)_1(t) &= \frac{-jI_0\eta_0\Delta l k_0^2}{(2\pi)^{3/2}} \sum_{\vec{K},\omega} P_{\vec{K},\omega}\sqrt{K}e^{-j\pi/4}e^{j\left(\omega_0 t+\alpha\pi t^2\right)} \\ &\quad \int_{\frac{c(t-\tau_0)}{2}}^{\frac{ct}{2}} \frac{F^2(\rho_0)}{(\rho_0)^{3/2}} e^{j\rho_0\left(K-2k_0-\frac{4\pi\alpha t}{c}\right)} d\rho_0 \,. \end{aligned} \tag{3.19}$$

The integral in equation (3.19) will be reduced following the procedure of previous investigators (e.g. Walsh *et al.* [6]). The range information is replaced by some explicit distance expressions. Let

$$\rho_s = \frac{1}{2}\left[\frac{ct}{2}+\frac{c(t-\tau_0)}{2}\right] \tag{3.20}$$

and

$$\Delta\rho_s = \frac{c\tau_0}{2} \,, \tag{3.21}$$

where ρ_s is the distance from the radar transmitter and receiver to the middle of the scattering patch, and $\Delta\rho_s$ is width of the scattering patch. With the aid of equations

(3.20) and (3.21), the limits of integration may be written as

$$\frac{c\,(t-\tau_0)}{2} = \rho_s - \frac{\Delta\rho_s}{2} \tag{3.22}$$

and

$$\frac{ct}{2} = \rho_s + \frac{\Delta\rho_s}{2}\,. \tag{3.23}$$

The integration variable ρ_0 in equation (3.19) can be separated into two parts. One part is a constant distance ρ_s, another is a variable ρ_s' from $-\frac{\Delta\rho_s}{2}$ to $\frac{\Delta\rho_s}{2}$, i.e.

$$\rho_0 = \rho_s + \rho_s'\,. \tag{3.24}$$

Obviously, $d\rho_0 = d\rho_s'$, and the phase term of equation (3.19) will be

$$\begin{aligned}\rho_0\left(K - 2k_0 - \frac{4\pi\alpha t}{c}\right) &= (\rho_s + \rho_s')\left(K - 2k_0 - \frac{4\pi\alpha t}{c}\right)\\ &= \rho_s\left(K - 2k_0 - \frac{4\pi\alpha t}{c}\right) + \rho_s'\left(K - 2k_0 - \frac{4\pi\alpha t}{c}\right)\,.\end{aligned} \tag{3.25}$$

Since $\rho_0 \approx \rho_s >> \rho_s'$, we have the attenuation factor

$$\frac{F^2(\rho_0)}{(\rho_0)^{3/2}} \approx \frac{F^2(\rho_s)}{(\rho_s)^{3/2}}\,. \tag{3.26}$$

The ρ_s' independent factors can be brought outside the integral after changing the integral variable from ρ_0 to ρ_s' for equation (3.19). This gives

$$\begin{aligned}\left(E_0^+\right)_1(t) \;=\; & \frac{-jI_0\eta_0\Delta l k_0^2 F^2\left(\rho_s\right)}{(2\pi\rho_s)^{3/2}} \sum_{\vec{K},\omega} P_{\vec{K},\omega}\sqrt{K}e^{-j\pi/4}e^{j\left(\omega_0 t+\alpha\pi t^2\right)}\\ & e^{j\rho_s\left(K-2k_0-\frac{4\pi\alpha t}{c}\right)}\int_{-\frac{\Delta\rho_s}{2}}^{\frac{\Delta\rho_s}{2}} e^{j\rho_s'\left(K-2k_0-\frac{4\pi\alpha t}{c}\right)}d\rho_s'\,.\end{aligned} \tag{3.27}$$

Evaluation of the integral in equation (3.27) yields

$$\int_{-\frac{\Delta\rho_s}{2}}^{\frac{\Delta\rho_s}{2}} e^{j\rho_s'\left(K-2k_0-\frac{4\pi\alpha t}{c}\right)} d\rho_s' = \Delta\rho_s \mathrm{Sa}\left[\frac{\Delta\rho_s}{2}\left(K-2k_0-\frac{4\pi\alpha t}{c}\right)\right], \tag{3.28}$$

where $\mathrm{Sa}(x)$ has the usual form of $\dfrac{\sin x}{x}$. Then, the field equation (3.27) becomes

$$\left(E_0^+\right)_1(t) = \frac{-jI_0\eta_0\Delta l k_0^2 F^2(\rho_s)\Delta\rho_s}{(2\pi\rho_s)^{3/2}} \sum_{\vec{K},\omega} P_{\vec{K},\omega}\sqrt{K}e^{-j\pi/4}e^{j\left(\omega_0 t+\alpha\pi t^2\right)}$$
$$e^{j\rho_s\left(K-2k_0-\frac{4\pi\alpha t}{c}\right)}\mathrm{Sa}\left[\frac{\Delta\rho_s}{2}\left(K-2k_0-\frac{4\pi\alpha t}{c}\right)\right]. \tag{3.29}$$

Up to this point, the electric field equation has been developed for a fixed range ρ_s, a patch width $\Delta\rho_s$, and a sweep time t changing from $-\dfrac{T_r}{2}$ to time $\dfrac{T_r}{2}$. T_r is the time interval that the rough surface is illuminated by the radar and the surface is assumed to have no variability within that interval. Additionally, the time variable within a sweep interval T_r is redefined as t_r and time variable t will be retained when the time-varying ocean surface is introduced. After this modification, the first-order field equation over the rough surface becomes

$$\left(E_0^+\right)_1(t_r) = \frac{-jI_0\eta_0\Delta l k_0^2 F^2(\rho_s)\Delta\rho_s}{(2\pi\rho_s)^{3/2}} \sum_{\vec{K},\omega} P_{\vec{K},\omega}\sqrt{K}e^{-j\pi/4}$$
$$e^{j\left(\omega_0 t_r+\alpha\pi t_r^2\right)}e^{j\rho_s\left(K-2k_0-\frac{4\pi\alpha t_r}{c}\right)}\mathrm{Sa}\left[\frac{\Delta\rho_s}{2}\left(K-2k_0-\frac{4\pi\alpha t_r}{c}\right)\right]. \tag{3.30}$$

The "first-order scatter" described by equation (3.30) is more precisely interpreted as the field received after a single scatter from the rough surface. If we consider the ocean to consist of first and second-order waves, then this field actually consists of two distinct parts: one is a single scatter from the first-order surface waves, another is a single scatter from the second-order surface waves produced by the hydrodynamic coupling process referred to in Chapter 2. Using the same technique as found in Walsh *et al.* [6], Walsh and Dawe

[34], and Gill and Walsh [35], $\left(E_0^+\right)_1(t_r)$ can be expanded as

$$\left(E_0^+\right)_1(t_r) = \left(E_0^+\right)_{11}(t_r) + \left(E_0^+\right)_{12}(t_r) \ , \tag{3.31}$$

where $\left(E_0^+\right)_{11}(t_r)$ represents the received field due to a single scatter from first-order surface waves whose Fourier surface coefficients are symbolized as ${}_1P_{\vec{K},\omega}$. It can be expressed as

$$\left(E_0^+\right)_{11}(t_r) = \frac{-jI_0\eta_0\Delta l k_0^2 F^2(\rho_s)\Delta\rho_s}{(2\pi\rho_s)^{3/2}} \sum_{\vec{K},\omega} {}_1P_{\vec{K},\omega}\sqrt{K}e^{-j\pi/4}$$
$$e^{j\left(\omega_0 t_r + \alpha\pi t_r^2\right)} e^{j\rho_s\left(K-2k_0-\frac{4\pi\alpha t_r}{c}\right)} \mathrm{Sa}\left[\frac{\Delta\rho_s}{2}\left(K-2k_0-\frac{4\pi\alpha t_r}{c}\right)\right] \ . \tag{3.32}$$

The second term of equation (3.31), representing a single scatter from a second-order surface wave coupled from two first-order waves, takes the form

$$\left(E_0^+\right)_{12}(t_r) = \frac{-jI_0\eta_0\Delta l k_0^2 F^2(\rho_s)\Delta\rho_s}{(2\pi\rho_s)^{3/2}} \sum_{\vec{K}_1,\omega_1} \sum_{\vec{K}_2,\omega_2} {}_1P_{\vec{K}_1,\omega_1}\ {}_1P_{\vec{K}_2,\omega_2}\ {}_H\Gamma_P$$
$$\sqrt{K}e^{-j\pi/4} e^{j\left(\omega_0 t_r + \alpha\pi t_r^2\right)} e^{j\rho_s\left(K-2k_0-\frac{4\pi\alpha t_r}{c}\right)} \mathrm{Sa}\left[\frac{\Delta\rho_s}{2}\left(K-2k_0-\frac{4\pi\alpha t_r}{c}\right)\right] \ , \tag{3.33}$$

where the two Fourier surface coefficients ${}_1P_{\vec{K}_1,\omega_1}$ and ${}_1P_{\vec{K}_2,\omega_2}$ are associated with the interacting first-order waves which give rise to a second-order wave with coefficient ${}_2P_{\vec{K},\omega}$. According to the perturbational analyses, we have

$${}_2P_{\vec{K},\omega} = \sum_{\substack{\vec{K}_1+\vec{K}_2=\vec{K} \\ \omega=\omega_1+\omega_2}} {}_1P_{\vec{K}_1,\omega_1}\ {}_1P_{\vec{K}_2,\omega_2}\ {}_H\Gamma_P \ . \tag{3.34}$$

Here, the wave vector $\vec{K} = \vec{K}_1 + \vec{K}_2$ associated with the second-order surface wave does not satisfy the linear dispersion relationship (i.e. $\omega \neq \sqrt{gK}$). ${}_H\Gamma_P$ is the hydrodynamic coupling coefficient for the patch scatter (e.g. Hasselmann [1]).

3.2.2 Field Equations for the FMICW Waveform

Following the previous procedure for the FMCW waveform, the derivation of the field equation for the FMICW waveform involves a second-order derivative of the radar transmitted signal with respect to time t. From the current waveform equation (3.6) we have

$$\begin{aligned}\frac{\partial^2 i_g(t)}{\partial t^2} &= -I_0 e^{j\left(\omega_0 t+\alpha\pi t^2\right)}\left(\omega_0^2+4\pi\alpha\omega_0 t+4\pi^2\alpha^2t^2-j2\pi\alpha\right)\\ &\quad \sum_{n=0}^{N-1}\text{Rect}\left(\frac{t-nT_g-\frac{\tau_g}{2}+\frac{T_r}{2}}{\tau_g}\right)\\ &\approx -I_0\omega_0^2 e^{j\left(\omega_0 t+\alpha\pi t^2\right)}\sum_{n=0}^{N-1}\text{Rect}\left(\frac{t-nT_g-\frac{\tau_g}{2}+\frac{T_r}{2}}{\tau_g}\right), \end{aligned} \tag{3.35}$$

where the approximation $2\pi B << \omega_0$ is invoked, and the leading and trailing edge impulse terms are neglected in the derivation. The convolution with the delta function $\delta\left(t-\frac{2\rho_0}{c}\right)$ as in equation (3.15) gives

$$\begin{aligned}&\left[-jI_0\eta_0\Delta l k_0^2 e^{j\left(\omega_0 t+\alpha\pi t^2\right)}\sum_{n=0}^{N-1}\text{Rect}\left(\frac{t-nT_g-\frac{\tau_g}{2}+\frac{T_r}{2}}{\tau_g}\right)\right]\overset{t}{*}\left[\delta\left(t-\frac{2\rho_0}{c}\right)\right]\\ &= -jI_0\eta_0\Delta l k_0^2 e^{j\left[\omega_0\left(t-\frac{2\rho_0}{c}\right)+\alpha\pi\left(t-\frac{2\rho_0}{c}\right)^2\right]}\sum_{n=0}^{N-1}\text{Rect}\left(\frac{t-\frac{2\rho_0}{c}-nT_g-\frac{\tau_g}{2}+\frac{T_r}{2}}{\tau_g}\right).\end{aligned} \tag{3.36}$$

Therefore, the first-order temporal electric field equation can be cast as

$$\begin{aligned}\left(E_{0g}^{+}\right)_1(t) &= \frac{-jI_0\eta_0\Delta l k_0^2}{(2\pi)^{3/2}}\sum_{\vec{K},\omega}P_{\vec{K},\omega}\sqrt{K}e^{-j\pi/4}e^{j\left(\omega_0 t+\alpha\pi t^2\right)}\int_{\frac{c(t-\tau_0)}{2}}^{\frac{ct}{2}}\frac{F^2(\rho_0)}{(\rho_0)^{3/2}}\\ &\quad e^{j\rho_0\left(K-2k_0-\frac{4\pi\alpha t}{c}\right)}\sum_{n=0}^{N-1}\text{Rect}\left(\frac{t-\frac{2\rho_0}{c}-nT_g-\frac{\tau_g}{2}+\frac{T_r}{2}}{\tau_g}\right)d\rho_0,\end{aligned} \tag{3.37}$$

where the subscript g for "gates"' on $\left(E_{0g}^{+}\right)_1(t)$ indicates the use of the FMICW waveform. Using the same ρ_s and $\Delta\rho_s$ as previously defined in equations (3.20) to (3.21), respectively, and again following the same procedure as for the derivation of the field equation with the FMCW waveform, equation (3.37) becomes

$$\left(E_{0g}^{+}\right)_1(t) = \frac{-jI_0\eta_0\Delta l k_0^2 F^2(\rho_s)}{(2\pi\rho_s)^{3/2}} \sum_{n=0}^{N-1} \text{Rect}\left(\frac{t - \frac{2\rho_s}{c} - nT_g - \frac{\tau_g}{2} + \frac{T_r}{2}}{\tau_g}\right)$$
$$\sum_{\vec{K},\omega} P_{\vec{K},\omega}\sqrt{K}e^{-j\pi/4}e^{j\left(\omega_0 t + \alpha\pi t^2\right)}e^{j\rho_s\left(K - 2k_0 - \frac{4\pi\alpha t}{c}\right)} \int_{-\frac{\Delta\rho_s}{2}}^{\frac{\Delta\rho_s}{2}} e^{j\rho_s'\left(K - 2k_0 - \frac{4\pi\alpha t}{c}\right)} d\rho_s' \,, \quad (3.38)$$

where, as before, the approximation $\rho_0 \approx \rho_s >> \rho_s'$ gives

$$\frac{F^2(\rho_0)}{(\rho_0)^{3/2}} \approx \frac{F^2(\rho_s)}{(\rho_s)^{3/2}} \quad (3.39)$$

and

$$\sum_{n=0}^{N-1} \text{Rect}\left(\frac{t - \frac{2\rho_0}{c} - nT_g - \frac{\tau_g}{2} + \frac{T_r}{2}}{\tau_g}\right) \approx \sum_{n=0}^{N-1} \text{Rect}\left(\frac{t - \frac{2\rho_s}{c} - nT_g - \frac{\tau_g}{2} + \frac{T_r}{2}}{\tau_g}\right) . \quad (3.40)$$

The integration in equation (3.38) gives a sinc function and the expression of the first-order scattering field becomes

$$\left(E_{0g}^{+}\right)_1(t) = \frac{-jI_0\eta_0\Delta l k_0^2 F^2(\rho_s)\,\Delta\rho_s}{(2\pi\rho_s)^{3/2}} \sum_{n=0}^{N-1} \text{Rect}\left(\frac{t - \frac{2\rho_s}{c} - nT_g - \frac{\tau_g}{2} + \frac{T_r}{2}}{\tau_g}\right)$$
$$\sum_{\vec{K},\omega} P_{\vec{K},\omega}\sqrt{K}e^{-j\pi/4}e^{j\left(\omega_0 t + \alpha\pi t^2\right)}e^{j\rho_s\left(K - 2k_0 - \frac{4\pi\alpha t}{c}\right)}\text{Sa}\left[\frac{\Delta\rho_s}{2}\left(K - 2k_0 - \frac{4\pi\alpha t}{c}\right)\right] . \quad (3.41)$$

Comparison of equation (3.41) for the FMICW waveform with equation (3.30) for the FMCW waveform shows that the only difference between them is the multiplication of a delayed gating function. When changing the variable t to t_r and splitting the first-order

scattering into two distinct parts as was done for the FMCW waveform, the first-order scattering field for the FMICW waveform becomes

$$\left(E_{0g}^{+}\right)_{1}(t_r) = \left(E_{0g}^{+}\right)_{11}(t_r) + \left(E_{0g}^{+}\right)_{12}(t_r) \ . \tag{3.42}$$

The $\left(E_{0g}^{+}\right)_{11}(t_r)$ term represents the field for a single scatter from first-order surface waves, and it can be expressed as

$$\left(E_{0g}^{+}\right)_{11}(t_r) = \frac{-jI_0\eta_0\Delta l k_0^2 F^2(\rho_s)\,\Delta\rho_s}{(2\pi\rho_s)^{3/2}} \sum_{n=0}^{N-1} \mathrm{Rect}\left(\frac{t_r - \frac{2\rho_s}{c} - nT_g - \frac{\tau_g}{2} + \frac{T_r}{2}}{\tau_g}\right)$$
$$\sum_{\vec{K},\omega} {}_1P_{\vec{K},\omega}\sqrt{K}e^{-j\pi/4}e^{j\left(\omega_0 t_r + \alpha\pi t_r^2\right)}e^{j\rho_s\left(K - 2k_0 - \frac{4\pi\alpha t_r}{c}\right)}\mathrm{Sa}\left[\frac{\Delta\rho_s}{2}\left(K - 2k_0 - \frac{4\pi\alpha t_r}{c}\right)\right] \ . \tag{3.43}$$

The $\left(E_{0g}^{+}\right)_{12}(t_r)$ term represents a single scatter from the second-order surface waves produced by the hydrodynamic coupling process. It takes the form

$$\left(E_{0g}^{+}\right)_{12}(t_r) = \frac{-jI_0\eta_0\Delta l k_0^2 F^2(\rho_s)\,\Delta\rho_s}{(2\pi\rho_s)^{3/2}} \sum_{n=0}^{N-1} \mathrm{Rect}\left(\frac{t_r - \frac{2\rho_s}{c} - nT_g - \frac{\tau_g}{2} + \frac{T_r}{2}}{\tau_g}\right)$$
$$\sum_{\vec{K}_1,\omega_1}\sum_{\vec{K}_2,\omega_2} {}_H\Gamma_P\ {}_1P_{\vec{K}_1,\omega_1}\ {}_1P_{\vec{K}_2,\omega_2}\sqrt{K}e^{-j\pi/4}e^{j\left(\omega_0 t_r + \alpha\pi t_r^2\right)}$$
$$e^{j\rho_s\left(K - 2k_0 - \frac{4\pi\alpha t_r}{c}\right)}\mathrm{Sa}\left[\frac{\Delta\rho_s}{2}\left(K - 2k_0 - \frac{4\pi\alpha t_r}{c}\right)\right] \ , \tag{3.44}$$

where ${}_1P_{\vec{K}_1,\omega_1}$ and ${}_1P_{\vec{K}_2,\omega_2}$ are the Fourier surface coefficients associated with the interacting first-order waves and ${}_H\Gamma_P$ is the hydrodynamic coupling coefficient for the patch scatter as defined previously.

3.3 Range Estimation

The range information may be found by Fourier transforming the received signal within the sweep interval T_r. Before doing this, the received signal should be demodulated (see, for example [50, 52]). In the previous analysis, the first-order scatter has been separated into two components based on their different scattering principles: a single scatter from the first-order ocean waves and a single scatter from second-order hydrodynamically coupled ocean waves. The second component is hereafter denoted as the second-order scatter, while the first component is denoted as the first-order scatter. In the following subsections, the expressions of range estimation from the first- and second-order field equations are derived, first for the FMCW waveform, then for the FMICW waveform.

3.3.1 Range Estimation for the FMCW Waveform

Scattering from the First-order Waves

The derivation is from the first-order field equation (3.32). The demodulation is designed to approximate a matched filter. It is a "pre-process" which involves mixing the acquired signal with the original signal and low-pass filtering the outcome [50, 52]. The low-pass filtering removes the frequency component at twice the carrier frequency (details are included in Appendix A). As a result of the demodulation, the exponential factor $e^{j\left(\omega_0 t_r+\alpha\pi t_r^2\right)}$ will be eliminated, $e^{j\rho_s\left(K-2k_0-\frac{4\pi\alpha t_r}{c}\right)}$ will be replaced by its complex conjugation, and the sinc function will be unchanged. The resulting equation becomes

$$\left(E_0^+\right)_{11}^D(t_r)=E_0 e^{-j\rho_s\left(K-2k_0-\frac{4\pi\alpha t_r}{c}\right)}\mathrm{Sa}\left[\frac{\Delta\rho_s}{2}\left(K-2k_0-\frac{4\pi\alpha t_r}{c}\right)\right], \tag{3.45}$$

where the superscript D indicates the demodulation and E_0 is collection of factors in equation (3.32) with

$$E_0=\frac{-jI_0\eta_0\Delta l k_0^2F^2\left(\rho_s\right)\Delta\rho_s}{\left(2\pi\rho_s\right)^{3/2}}\sum_{\vec{K},\omega}{}_1P_{\vec{K},\omega}\sqrt{K}e^{-j\pi/4}. \tag{3.46}$$

The sinc function in equation (3.45) has a form of $\frac{\sin x}{x}$ and the $\sin x$ can be expressed in exponential form so that

$$\begin{aligned}\mathrm{Sa}\left[\frac{\Delta\rho_s}{2}\left(K-2k_0-\frac{4\pi\alpha t_r}{c}\right)\right] &= \left[2j\frac{\Delta\rho_s}{2}\left(K-2k_0-\frac{4\pi\alpha t_r}{c}\right)\right]^{-1} \\ &\left[e^{j\frac{\Delta\rho_s}{2}\left(K-2k_0-\frac{4\pi\alpha t_r}{c}\right)} - e^{-j\frac{\Delta\rho_s}{2}\left(K-2k_0-\frac{4\pi\alpha t_r}{c}\right)}\right] . \end{aligned} \tag{3.47}$$

The magnitude factor can be simplified by applying a binomial expansion to get

$$\left[2j\frac{\Delta\rho_s}{2}\left(K-2k_0-\frac{4\pi\alpha t_r}{c}\right)\right]^{-1} \approx \frac{1}{j\Delta\rho_s\left(K-2k_0\right)} , \tag{3.48}$$

since, compared with K and $2k_0$, the $\frac{4\pi\alpha t_r}{c}$ term is much smaller and can be neglected. A quick example is when $\alpha = 100$ kHz and $t_r \leq T_r = 0.25$ s, $\alpha t_r \leq 25$ kHz, which is much smaller than the radar frequencies within the HF band. Therefore, equation (3.45) becomes

$$\begin{aligned}\left(E_0^+\right)_{11}^D(t_r) &= \frac{E_0}{j\Delta\rho_s\left(K-2k_0\right)} \\ &\left[e^{-j(K-2k_0)\left(\rho_s-\frac{\Delta\rho_s}{2}\right)}e^{j\frac{4\pi\alpha}{c}\left(\rho_s-\frac{\Delta\rho_s}{2}\right)t_r} - e^{-j(K-2k_0)\left(\rho_s+\frac{\Delta\rho_s}{2}\right)}e^{j\frac{4\pi\alpha}{c}\left(\rho_s+\frac{\Delta\rho_s}{2}\right)t_r}\right] \\ &= E_0^A e^{j\frac{4\pi\alpha}{c}\left(\rho_s-\frac{\Delta\rho_s}{2}\right)t_r} - E_0^B e^{j\frac{4\pi\alpha}{c}\left(\rho_s+\frac{\Delta\rho_s}{2}\right)t_r} \\ &= E^A - E^B , \end{aligned} \tag{3.49}$$

where

$$E_0^A = \frac{E_0}{j\Delta\rho_s\left(K-2k_0\right)}e^{-j(K-2k_0)\left(\rho_s-\frac{\Delta\rho_s}{2}\right)} , \tag{3.50}$$

and

$$E_0^B = \frac{E_0}{j\Delta\rho_s\left(K-2k_0\right)}e^{-j(K-2k_0)\left(\rho_s+\frac{\Delta\rho_s}{2}\right)} . \tag{3.51}$$

The first-order range spectrum $\Phi_1^r(\omega_r)$ will be the Fourier transform of equation (3.49) with respect to t_r over the sweep interval T_r (e.g. Barrick [50]), with ω_r being the transform variable corresponding to t_r. The result may be symbolized as

$$\Phi_1^r(\omega_r) = \mathcal{F}\left[\left(E_0^+\right)_{11}^D(t_r)\right] = \mathcal{F}\left[E^A\right] - \mathcal{F}\left[E^B\right] , \tag{3.52}$$

where

$$\begin{aligned}\mathcal{F}\left[E^A\right] &= E_0^A \int_{-\frac{T_r}{2}}^{\frac{T_r}{2}} e^{j\frac{4\pi\alpha}{c}\left(\rho_s - \frac{\Delta\rho_s}{2}\right)t_r} e^{-j\omega_r t_r} dt_r \\ &= E_0^A T_r \mathrm{Sa}\left[\frac{T_r}{2}(\omega_a - \omega_r)\right]\end{aligned} \tag{3.53}$$

with $\omega_a = \dfrac{4\pi\alpha}{c}\left(\rho_s - \dfrac{\Delta\rho_s}{2}\right)$, and

$$\begin{aligned}\mathcal{F}\left[E^B\right] &= E_0^B \int_{-\frac{T_r}{2}}^{\frac{T_r}{2}} e^{j\frac{4\pi\alpha}{c}\left(\rho_s + \frac{\Delta\rho_s}{2}\right)t_r} e^{-j\omega_r t_r} dt_r \\ &= E_0^B T_r \mathrm{Sa}\left[\frac{T_r}{2}(\omega_b - \omega_r)\right]\end{aligned} \tag{3.54}$$

with $\omega_b = \dfrac{4\pi\alpha}{c}\left(\rho_s + \dfrac{\Delta\rho_s}{2}\right)$.

The arguments ω_a and ω_b in the sinc functions in equations (3.53) and (3.54) may be approximately equated as $\omega_a \approx \omega_b = \dfrac{4\pi\alpha}{c}\rho_s$ for $\rho_s >> \dfrac{\Delta\rho_s}{2}$, and then equation (3.52) becomes

$$\Phi_1^r(\omega_r) = T_r \mathrm{Sa}\left[\frac{T_r}{2}\left(\omega_r - \frac{4\pi\alpha}{c}\rho_s\right)\right]\left(E_0^A - E_0^B\right) . \tag{3.55}$$

It may be seen that the sinc function in equation (3.55) will generate a peak in the specific position of the spectrum, $\omega_r = \dfrac{4\pi\alpha}{c}\rho_s$, that indicates the range. This is the principle underlying range measurement for the HF radar when using FM waveforms. In view of

equations (3.50) and (3.51), equation (3.55) may be further manipulated to give

$$\begin{aligned}\Phi_1^r(\omega_r) &= \frac{E_0 T_r}{j\Delta\rho_s(K-2k_0)}\mathrm{Sa}\left[\frac{T_r}{2}\left(\omega_r-\frac{4\pi\alpha}{c}\rho_s\right)\right] \\ &\quad \left[e^{-j(K-2k_0)\left(\rho_s-\frac{\Delta\rho_s}{2}\right)}-e^{-j(K-2k_0)\left(\rho_s+\frac{\Delta\rho_s}{2}\right)}\right] \\ &= \frac{E_0 T_r}{j\Delta\rho_s(K-2k_0)}\mathrm{Sa}\left[\frac{T_r}{2}\left(\omega_r-\frac{4\pi\alpha}{c}\rho_s\right)\right]e^{-j\rho_s(K-2k_0)} \\ &\quad \left[e^{j\frac{\Delta\rho_s}{2}(K-2k_0)}-e^{-j\frac{\Delta\rho_s}{2}(K-2k_0)}\right], \end{aligned} \tag{3.56}$$

or

$$\begin{aligned}\Phi_1^r(\omega_r) &= \frac{E_0 T_r j\Delta\rho_s(K-2k_0)}{j\Delta\rho_s(K-2k_0)}\mathrm{Sa}\left[\frac{T_r}{2}\left(\omega_r-\frac{4\pi\alpha}{c}\rho_s\right)\right] \\ &e^{-j\rho_s(K-2k_0)}\mathrm{Sa}\left[\frac{\Delta\rho_s}{2}(K-2k_0)\right]. \end{aligned} \tag{3.57}$$

In the fraction portion of equation (3.57), the numerator factor can be obviously cancelled by the same factor in the denominator. By expanding the factor E_0 in equation (3.46), the range spectrum of the first-order scatter for the FMCW waveform will be

$$\begin{aligned}\Phi_1^r(\omega_r) &= \frac{-jI_0\eta_0\Delta l k_0^2 F^2(\rho_s)\Delta\rho_s T_r}{(2\pi\rho_s)^{3/2}}\sum_{\vec{K},\omega}{}_1P_{\vec{K},\omega}\sqrt{K}e^{-j\pi/4} \\ &\mathrm{Sa}\left[\frac{T_r}{2}\left(\omega_r-\frac{4\pi\alpha}{c}\rho_s\right)\right]e^{-j\rho_s(K-2k_0)}\mathrm{Sa}\left[\frac{\Delta\rho_s}{2}(K-2k_0)\right]. \end{aligned} \tag{3.58}$$

The power spectrum associated with equation (3.58) is the square of the absolute value of $\Phi_1^r(\omega_r)$. Figures 3.5 and 3.6 are examples of such power spectra. In these figures, a fixed scattering patch is selected 50 km away from the radar over the rough ocean surface. The ocean surface parameters are with a wind speed of 15 m/s, 0° to the reference direction, and a current of 1 m/s, 90° to the reference direction. To show the effect of changing the signal bandwidth, we consider two bandwidth values, $B = 100$ kHz and $B = 500$ kHz, in our illustration here and in the discussion of cross sections in the later sections. The reason for choosing these two bandwidths is that $B = 100$ kHz has been used elsewhere

(e.g. Barrick [50]) and the bandwidth $B = 500$ kHz will result in a range resolution of 300 m, which is among the finest resolutions found in HF radar literature (e.g. Gurgel *et al.* [60, 76]). In Figure 3.5, $f_0 = 10$ MHz, $T_r = 0.75$ s, and $B = 100$ kHz, corresponding to a sweep rate of $\alpha = 133.33$ kHz/s. In Figure 3.6, $f_0 = 25$ MHz and $B = 500$ kHz are used. The same sweep interval is applied as in Figure 3.5, resulting in a sweep rate of $\alpha = 666.67$ kHz/s. The sweep interval in each figure has been sampled 512 times, corresponding to a sampling rate of 682.67 Hz.

It is observed from Figures 3.5 and 3.6 that the maximum range estimations for the two cases are different. In Figure 3.5, the actual maximum range is 384 km, while in Figure 3.6, this value is 76.8 km. This difference is due to the different sweep bandwidths for a fixed number of samples within the sweep interval and is further addressed in what immediately follows.

When the FM signal is scattered over the patch and received, the range information will be brought back with a time delay $\Delta t = \frac{2\rho_s}{c}$. For each Δt, there will be a frequency offset Δf with respect to the carrier frequency f_0. This is given by

$$\Delta f = \alpha \Delta t = \frac{2\alpha}{c}\rho_s \,, \tag{3.59}$$

or

$$\Delta \omega = \frac{4\pi\alpha}{c}\rho_s \,. \tag{3.60}$$

Considering equation (3.58) in view of (3.60) it may be seen that when $\omega_r = \Delta\omega$, i.e. the frequency that the first sinc function takes its principal maximum, the range spectrum Φ_1^r achieves its maximum value. In fact, it is through examining Δf that radar systems with FM waveforms provide the range information. The frequency offset Δf has a maximum value of $\Delta f_{max} = \alpha T_r = B$. This maximum defines a theoretical maximum range $\rho_{MAX} = \frac{cT_r}{2}$, which is several hundred thousand kilometres and cannot be reached in practice. In

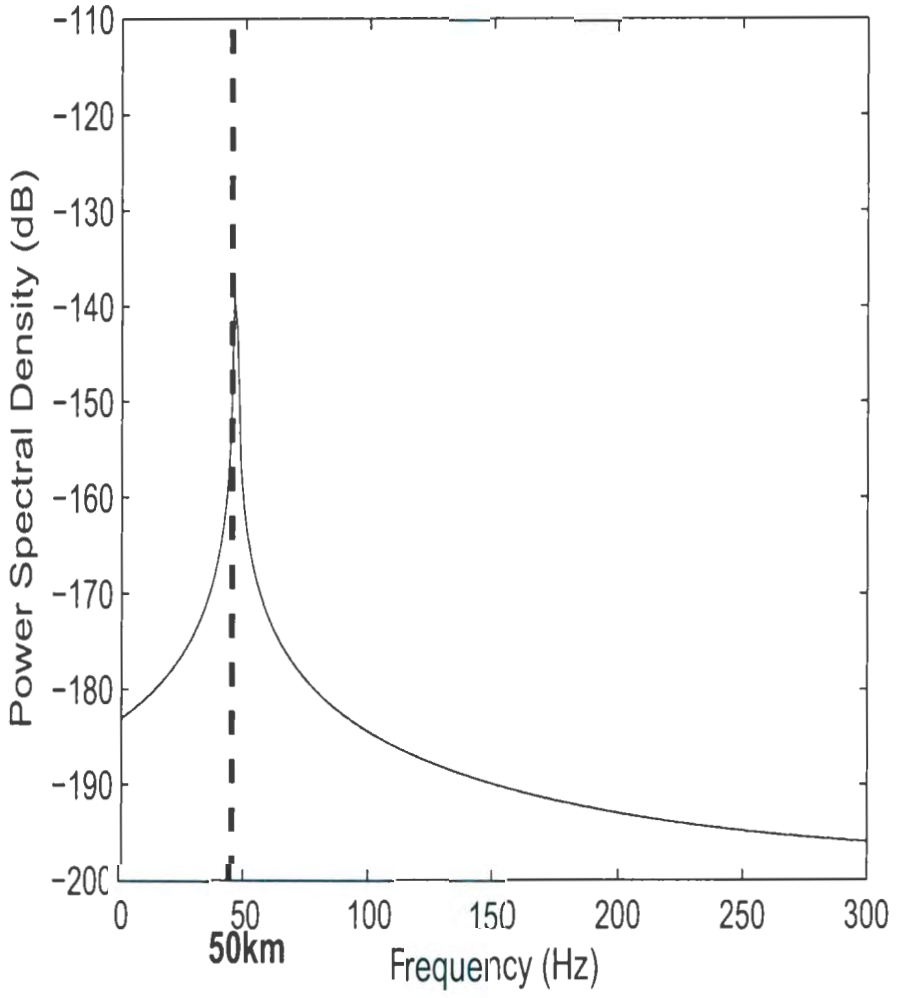

Figure 3.5: An example of range estimation for a fixed scattering patch 50 km from radar. The radar parameters are of $f_0 = 10$ MHz, $B = 100$ kHz, and T_r 0.75 s. The ocean surface wind speed is 15 m/s, 0° to the reference direction. A current of 1 m/s, 90° to the reference direction is simulated. The radar received signal is sampled with a sampling rate of 682.67 Hz.

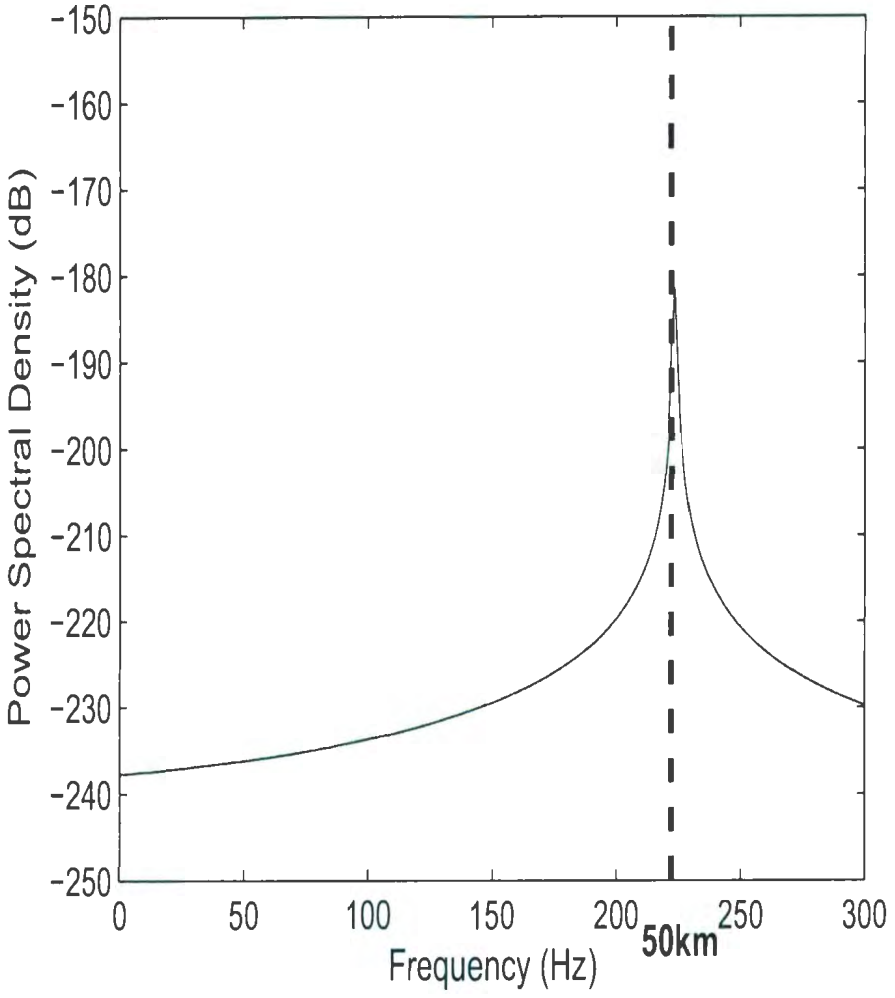

Figure 3.6: Estimate of the same range as Figure 3.5 with $f_0 = 25$ MHz and B - 500 kHz.

practice, the upper limit of the range estimation will be a few hundred kilometres at the most due to signal attenuation. When the sampling process is applied within the sweep interval, according to the sampling theorem, only those signals with frequencies that are equal to or less than one half the sampling frequency f_s will be reconstructed without distortion. This means that the sampling process will work as a low-pass filter that selects those signals with

$$\Delta f \leq \frac{1}{2} f_s = \frac{1}{2} \frac{N_T}{T_r} \ , \tag{3.61}$$

where N_T is the number of samples within a sweep interval T_r. Since $\Delta f = \alpha \Delta t = \frac{B \Delta t}{T_r}$ and $\Delta t = \frac{2\rho_s}{c}$, equation (3.61) becomes

$$\frac{B \Delta t}{T_r} \leq \frac{1}{2} f_s = \frac{1}{2} \frac{N_T}{T_r} \ , \tag{3.62}$$

or

$$\frac{2B\rho_s}{cT_r} \leq \frac{1}{2} \frac{N_T}{T_r} \ . \tag{3.63}$$

In this result, the maximum range ρ_{max} will occur for the case of equality, i.e. when

$$\rho_{max} = \frac{cN_T}{4B} \ . \tag{3.64}$$

Since $\frac{c}{2B} = \frac{c\tau_0}{2} = \Delta\rho_s$, equation (3.64) may also be written as

$$\rho_{max} = \frac{1}{2} \Delta\rho_s N_T \ . \tag{3.65}$$

Equation (3.64) or (3.65) is the governing equation for the maximum range estimation. Particularly, for a fixed sweep bandwidth, the range resolution $\Delta\rho_s$ will be fixed. Increasing the sampling number N_T within the sweep interval will increase the maximum detection

range.

Equation (3.64) may be rewritten to show the relationship between the range and the frequency number in the range spectrum. For a specific range, $\rho_r \leq \rho_{max}$,

$$\rho_r = \frac{cn_f}{4B}\ , \quad \text{or } n_f = \frac{4B\rho_r}{c}\ , \tag{3.66}$$

where n_f is the frequency number in the range spectrum. For example, in Figure 3.5, the scattering patch of 50 km corresponds to a frequency number of 66.7 (i.e. a frequency between number 66 and 67) in the range spectrum. In Figure 3.6, however, the same range corresponds to a frequency number of 44.4 (i.e. a frequency between number 44 and 45).

Scattering from the Second-order Waves

Starting from equation (3.33) and following the same process as for the scattering from the first-order surface waves, the range spectrum for a single scatter from the second-order waves can be obtained. Here we skip those intermediate steps and write the resulting range spectrum directly as

$$\Phi_2^r(\omega_r) = \frac{-jI_0\eta_0\Delta l k_0^2 F^2(\rho_s)\,\Delta\rho_s T_r}{(2\pi\rho_s)^{3/2}} \sum_{\vec{K}_1,\omega_1} \sum_{\vec{K}_2,\omega_2} {}_1P_{\vec{K}_1,\omega_1}\ {}_1P_{\vec{K}_2,\omega_2}\ {}_H\Gamma_P\sqrt{K}e^{-j\pi/4}$$
$$\mathrm{Sa}\left[\frac{T_r}{2}\left(\omega_r - \frac{4\pi\alpha}{c}\rho_s\right)\right] e^{-j\rho_s(K-2k_0)}\mathrm{Sa}\left[\frac{\Delta\rho_s}{2}(K-2k_0)\right]\ , \tag{3.67}$$

where all symbols have been previously defined. The detailed derivation can be found in Section 2 in Appendix A.

3.3.2 Range Estimation for the FMICW Waveform

The range estimation analysis for the FMICW waveform will follow the same procedure as that for the FMCW waveform. Among other features, it includes the signal demodulation

and Fourier transformation of the field equations with respect to the time variable t_r within the sweep interval T_r. In this section, we first deal with the electric field that scatters from the first-order waves. Then the scattering from the second-order waves will be written out directly analogous to the first-order case, just as was done for the FMCW waveform.

Scattering from the First-order Waves

For the field equation (3.43), as a result of the demodulation process, the exponential factor $e^{j\left(\omega_0 t_r + \alpha\pi t_r^2\right)}$ will be eliminated. The resulting equation is

$$\begin{aligned}\left(E_{0g}^{+}\right)_{11}^{D}(t_r) &= E_0 \sum_{n=0}^{N-1} \text{Rect}\left(\frac{t_r - \frac{2\rho_s}{c} - nT_g - \frac{\tau_g}{2} + \frac{T_r}{2}}{\tau_g}\right) e^{-j\rho_s\left(K - 2k_0 - \frac{4\pi\alpha t_r}{c}\right)} \\ &\quad \text{Sa}\left[\frac{\Delta\rho_s}{2}\left(K - 2k_0 - \frac{4\pi\alpha t_r}{c}\right)\right], \end{aligned} \tag{3.68}$$

where the subscript g indicates the application of the FMICW waveform and a collection of factor E_0 is

$$E_0 = \frac{-jI_0\eta_0\Delta l k_0^2 F^2(\rho_s)\,\Delta\rho_s}{(2\pi\rho_s)^{3/2}} \sum_{\vec{K},\omega} {}_1P_{\vec{K},\omega}\sqrt{K}e^{-j\pi/4}. \tag{3.69}$$

The sinc function in equation (3.68) may be simplified as was done in Section 3.3.1 and equation (3.68) will become

$$\begin{aligned}\left(E_{0g}^{+}\right)_{11}^{D}(t_r) &= E_g^A - E_g^B \\ &= E_{0g}^A \sum_{n=0}^{N-1} \text{Rect}\left(\frac{t_r - \frac{2\rho_s}{c} - nT_g - \frac{\tau_g}{2} + \frac{T_r}{2}}{\tau_g}\right) e^{j\frac{4\pi\alpha}{c}\left(\rho_s - \frac{\Delta\rho_s}{2}\right)t_r} \\ &\quad - E_{0g}^B \sum_{n=0}^{N-1} \text{Rect}\left(\frac{t_r - \frac{2\rho_s}{c} - nT_g - \frac{\tau_g}{2} + \frac{T_r}{2}}{\tau_g}\right) e^{j\frac{4\pi\alpha}{c}\left(\rho_s + \frac{\Delta\rho_s}{2}\right)t_r}, \end{aligned} \tag{3.70}$$

where

$$E_{0g}^{A} = \frac{E_0}{j\Delta\rho_s\left(K-2k_0\right)} e^{-j(K-2k_0)\left(\rho_s-\frac{\Delta\rho_s}{2}\right)} \tag{3.71}$$

and

$$E_{0g}^{B} = \frac{E_0}{j\Delta\rho_s\left(K-2k_0\right)} e^{-j(K-2k_0)\left(\rho_s+\frac{\Delta\rho_s}{2}\right)} . \tag{3.72}$$

Thus, the range spectrum $\Phi_{1g}^{r}\left(\omega_r\right)$ will be the Fourier transform of equation (3.70) with respect to t_r (e.g. Barrick [50]). That is

$$\Phi_{1g}^{r}\left(\omega_r\right) = \mathcal{F}\left[\left(E_{0g}^{+}\right)_{11}^{D}\left(t_r\right)\right] = \mathcal{F}\left[E_g^{A}\right] - \mathcal{F}\left[E_g^{B}\right] , \tag{3.73}$$

with

$$\mathcal{F}\left[E_g^{A}\right] = E_{0g}^{A}\int_{-\frac{T_r}{2}}^{\frac{T_r}{2}}\sum_{n=0}^{N-1}\mathrm{Rect}\left(\frac{t_r-\frac{2\rho_s}{c}-nT_g-\frac{\tau_g}{2}+\frac{T_r}{2}}{\tau_g}\right) e^{j\frac{4\pi\alpha}{c}\left(\rho_s-\frac{\Delta\rho_s}{2}\right)t_r} e^{-j\omega_r t_r} dt_r \tag{3.74}$$

and

$$\mathcal{F}\left[E_g^{B}\right] = E_{0g}^{B}\int_{-\frac{T_r}{2}}^{\frac{T_r}{2}}\sum_{n=0}^{N-1}\mathrm{Rect}\left(\frac{t_r-\frac{2\rho_s}{c}-nT_g-\frac{\tau_g}{2}+\frac{T_r}{2}}{\tau_g}\right) e^{j\frac{4\pi\alpha}{c}\left(\rho_s+\frac{\Delta\rho_s}{2}\right)t_r} e^{-j\omega_r t_r} dt_r . \tag{3.75}$$

In equations (3.74) and (3.75), the interval of integration over T_r is interrupted by the gating function so that t_r lies in the interval given typically by

$$\frac{2\rho_s}{c} + nT_g - \frac{T_r}{2} \le t_r \le \frac{2\rho_s}{c} + nT_g + \tau_g - \frac{T_r}{2} . \tag{3.76}$$

Therefore, the integration in equations (3.74) and (3.75) may be written as

$$\mathcal{F}\left[E_g^A\right] = E_{0g}^A \sum_{n=0}^{N-1} \int_{\frac{2\rho_s}{c}+nT_g-\frac{T_r}{2}}^{\frac{2\rho_s}{c}+nT_g+\tau_g-\frac{T_r}{2}} e^{j\frac{4\pi\alpha}{c}\left(\rho_s-\frac{\Delta\rho_s}{2}\right)t_r} e^{-j\omega_r t_r} dt_r \tag{3.77}$$

and

$$\mathcal{F}\left[E^B\right] = E_{0g}^B \sum_{n=0}^{N-1} \int_{\frac{2\rho_s}{c}+nT_g-\frac{T_r}{2}}^{\frac{2\rho_s}{c}+nT_g+\tau_g-\frac{T_r}{2}} e^{j\frac{4\pi\alpha}{c}\left(\rho_s+\frac{\Delta\rho_s}{2}\right)t_r} e^{-j\omega_r t_r} dt_r \ . \tag{3.78}$$

Equations (3.77) and (3.78) can be reduced to

$$\mathcal{F}\left[E_g^A\right] = E_{0g}^A \tau_g \mathrm{Sa}\left[\frac{\tau_g}{2}\left(\omega_a-\omega_r\right)\right] \sum_{n=0}^{N-1} e^{j\left(nT_g+\frac{2\rho_s}{c}+\frac{\tau_g}{2}-\frac{T_r}{2}\right)\left(\omega_a-\omega_r\right)} \tag{3.79}$$

and

$$\mathcal{F}\left[E_g^B\right] = E_{0g}^B \tau_g \mathrm{Sa}\left[\frac{\tau_g}{2}\left(\omega_b-\omega_r\right)\right] \sum_{n=0}^{N-1} e^{j\left(nT_g+\frac{2\rho_s}{c}+\frac{\tau_g}{2}-\frac{T_r}{2}\right)\left(\omega_b-\omega_r\right)} \ , \tag{3.80}$$

where $\omega_a = \dfrac{4\pi\alpha}{c}\left(\rho_s - \dfrac{\Delta\rho_s}{2}\right)$ and $\omega_b = \dfrac{4\pi\alpha}{c}\left(\rho_s + \dfrac{\Delta\rho_s}{2}\right)$, the same definitions as that in Section 3.3.2 for the FMCW waveform.

Equation (3.79) can be further manipulated by evaluating the summation of the exponential function to give

$$\begin{aligned}
\mathcal{F}\left[E_g^A\right] &= E_{0g}^A \tau_g \mathrm{Sa}\left[\frac{\tau_g}{2}\left(\omega_a-\omega_r\right)\right] e^{j\left(\frac{2\rho_s}{c}+\frac{\tau_g}{2}-\frac{T_r}{2}\right)\left(\omega_a-\omega_r\right)} \sum_{n=0}^{N-1} e^{jnT_g\left(\omega_a-\omega_r\right)} \\
&= E_{0g}^A \tau_g \mathrm{Sa}\left[\frac{\tau_g}{2}\left(\omega_a-\omega_r\right)\right] e^{j\left(\frac{2\rho_s}{c}+\frac{\tau_g}{2}-\frac{T_r}{2}\right)\left(\omega_a-\omega_r\right)} \left[\frac{1-e^{j(\omega_a-\omega_r)NT_g}}{1-e^{j(\omega_a-\omega_r)T_g}}\right] \\
&= E_{0g}^A \tau_g \mathrm{Sa}\left[\frac{\tau_g}{2}\left(\omega_a-\omega_r\right)\right] \frac{\sin\frac{NT_g}{2}\left(\omega_a-\omega_r\right)}{\sin\frac{T_g}{2}\left(\omega_a-\omega_r\right)} e^{j\left(\frac{2\rho_s}{c}+\frac{N-1}{2}T_g+\frac{\tau_g}{2}-\frac{T_r}{2}\right)\left(\omega_a-\omega_r\right)} \ .
\end{aligned} \tag{3.81}$$

Similarly, for equation (3.80)

$$\mathcal{F}\left[E_g^B\right] = E_{0g}^B \tau_g \mathrm{Sa}\left[\frac{\tau_g}{2}\left(\omega_b-\omega_r\right)\right] \frac{\sin\frac{NT_g}{2}\left(\omega_b-\omega_r\right)}{\sin\frac{T_g}{2}\left(\omega_b-\omega_r\right)} e^{j\left(\frac{2\rho_s}{c}+\frac{N-1}{2}T_g+\frac{\tau_g}{2}-\frac{T_r}{2}\right)\left(\omega_b-\omega_r\right)} \ .$$

(3.82)

Since $\frac{\Delta\rho_s}{2} << \rho_s$ in practice, we may assume $\omega_a = \omega_b \approx \frac{4\pi\alpha\rho_s}{c}$ in the $\mathrm{Sa}(\cdot)$ and $\frac{\sin}{\sin}$ arguments. Using these results, the range spectrum equation (3.73) becomes

$$\Phi_{1g}^{r}(\omega_r) = \frac{E_0\tau_g}{j\Delta\rho_s(K-2k_0)}\mathrm{Sa}\left[\frac{\tau_g}{2}\left(\omega_r - \frac{4\pi\alpha}{c}\rho_s\right)\right]\frac{\sin\frac{NT_g}{2}\left(\omega_r - \frac{4\pi\alpha}{c}\rho_s\right)}{\sin\frac{T_g}{2}\left(\omega_r - \frac{4\pi\alpha}{c}\rho_s\right)}$$
$$e^{-j\left(\frac{N-1}{2}T_g+\frac{\tau_g}{2}-\frac{T_r}{2}\right)\omega_r}e^{-j\rho_s\left(K-2k_0+\frac{2\omega_r}{c}-\frac{8\pi\alpha\rho_s}{c^2}-\frac{N-1}{2}T_g\frac{4\pi\alpha}{c}-\frac{2\pi\alpha\tau_g}{c}+\frac{2\pi\alpha T_r}{c}\right)}$$
$$\left[e^{j\frac{\Delta\rho_s}{2}\left(K-2k_0-\frac{8\pi\alpha\rho_s}{c^2}-\frac{N-1}{2}T_g\frac{4\pi\alpha}{c}-\frac{2\pi\alpha\tau_g}{c}+\frac{2\pi\alpha T_r}{c}\right)}\right.$$
$$\left.-e^{-j\frac{\Delta\rho_s}{2}\left(K-2k_0-\frac{8\pi\alpha\rho_s}{c^2}-\frac{N-1}{2}T_g\frac{4\pi\alpha}{c}-\frac{2\pi\alpha\tau_g}{c}+\frac{2\pi\alpha T_r}{c}\right)}\right] \tag{3.83}$$

or

$$\Phi_{1g}^{r}(\omega_r) = \frac{E_{0g}\tau_g j\Delta\rho_s\left(K-2k_0-\frac{8\pi\alpha\rho_s}{c^2}-\frac{N-1}{2}T_g\frac{4\pi\alpha}{c}-\frac{2\pi\alpha\tau_g}{c}+\frac{2\pi\alpha T_r}{c}\right)}{j\Delta\rho_s(K-2k_0)}$$
$$e^{-j\left(\frac{N-1}{2}T_g+\frac{\tau_g}{2}-\frac{T_r}{2}\right)\omega_r}\mathrm{Sa}\left[\frac{\tau_g}{2}\left(\omega_r - \frac{4\pi\alpha}{c}\rho_s\right)\right]\frac{\sin\frac{NT_g}{2}\left(\omega_r - \frac{4\pi\alpha}{c}\rho_s\right)}{\sin\frac{T_g}{2}\left(\omega_r - \frac{4\pi\alpha}{c}\rho_s\right)}$$
$$e^{-j\rho_s\left(K-2k_0+\frac{2\omega_r}{c}-\frac{8\pi\alpha\rho_s}{c^2}-\frac{N-1}{2}T_g\frac{4\pi\alpha}{c}-\frac{2\pi\alpha\tau_g}{c}+\frac{2\pi\alpha T_r}{c}\right)}$$
$$\mathrm{Sa}\left[\frac{\Delta\rho_s}{2}\left(K-2k_0-\frac{8\pi\alpha\rho_s}{c^2}-\frac{N-1}{2}T_g\frac{4\pi\alpha}{c}-\frac{2\pi\alpha\tau_g}{c}+\frac{2\pi\alpha T_r}{c}\right)\right]. \tag{3.84}$$

In the first fraction portion in equation (3.84), the factor

$$\left(K-2k_0-\frac{8\pi\alpha\rho_s}{c^2}-\frac{N-1}{2}T_g\frac{4\pi\alpha}{c}-\frac{2\pi\alpha\tau_g}{c}+\frac{2\pi\alpha T_r}{c}\right) \tag{3.85}$$

in the numerator can be approximated as $(K-2k_0)$ since the $\frac{8\pi\alpha\rho_s}{c^2}$, $\frac{N-1}{2}T_g\frac{4\pi\alpha}{c}$, $\frac{2\pi\alpha T_r}{c}$, and $\frac{2\pi\alpha\tau_g}{c}$ terms are all much smaller than $K-2k_0$. This approximation allows the entire equation (3.85) to be cancelled by $(K-2k_0)$ in the denominator to simplify equation (3.84). For the argument in the second sinc function in equation (3.84), the

approximation

$$\frac{\Delta\rho_s}{2}\left(K-2k_0-\frac{8\pi\alpha\rho_s}{c^2}-\frac{N-1}{2}T_g\frac{4\pi\alpha}{c}-\frac{2\pi\alpha\tau_g}{c}+\frac{2\pi\alpha T_r}{c}\right)\approx\frac{\Delta\rho_s}{2}\left(K-2k_0\right) \quad (3.86)$$

is applied since $8\pi\alpha\rho_s << c^2$, $2\pi\alpha\tau_g << c$, and

$$\frac{N-1}{2}T_g\frac{4\pi\alpha}{c}\approx\frac{NT_g}{2}\frac{4\pi\alpha}{c}=\frac{2\pi\alpha T_r}{c} \quad (3.87)$$

with $N >> 1$ and $NT_g = T_r$. The argument of the last exponential function in equation (3.84) may be manipulated as

$$\begin{aligned}&-j\rho_s\left(K-2k_0+\frac{2\omega_r}{c}-\frac{8\pi\alpha\rho_s}{c^2}-\frac{N-1}{2}T_g\frac{4\pi\alpha}{c}-\frac{2\pi\alpha\tau_g}{c}+\frac{2\pi\alpha T_r}{c}\right)\\&=-j\rho_s\left[K-2k_0+\frac{2\omega_r}{c}-\frac{8\pi\alpha\rho_s}{c^2}+\frac{2\pi\alpha}{c}\left(\tau_g-T_g\right)\right]\ .\end{aligned} \quad (3.88)$$

The approximations and manipulations of equations (3.85) to (3.88), taken together, provide a simplified version of equation (3.84), which is

$$\begin{aligned}\Phi_{1g}^r\left(\omega_r\right)=E_0\tau_g\mathrm{Sa}\left[\frac{\tau_g}{2}\left(\omega_r-\frac{4\pi\alpha}{c}\rho_s\right)\right]\frac{\sin\frac{T_r}{2}\left(\omega_r-\frac{4\pi\alpha}{c}\rho_s\right)}{\sin\frac{T_g}{2}\left(\omega_r-\frac{4\pi\alpha}{c}\rho_s\right)}e^{j\frac{T_g-\tau_g}{2}\omega_r}\\e^{-j\rho_s\left[K-2k_0+\frac{2\omega_r}{c}-\frac{8\pi\alpha\rho_s}{c^2}+\frac{2\pi\alpha}{c}\left(\tau_g-T_g\right)\right]}\mathrm{Sa}\left[\frac{\Delta\rho_s}{2}\left(K-2k_0\right)\right]\ ,\end{aligned} \quad (3.89)$$

or, with E_0 being written explicitly, as

$$\begin{aligned}\Phi_{1g}^r\left(\omega_r\right)=\frac{-jI_0\eta_0\Delta l k_0^2F^2\left(\rho_s\right)\Delta\rho_s\tau_g}{\left(2\pi\rho_s\right)^{3/2}}\sum_{\vec{K},\omega}{}_1P_{\vec{K},\omega}\sqrt{K}e^{-j\pi/4}\\\mathrm{Sa}\left[\frac{\tau_g}{2}\left(\omega_r-\frac{4\pi\alpha}{c}\rho_s\right)\right]\frac{\sin\frac{T_r}{2}\left(\omega_r-\frac{4\pi\alpha}{c}\rho_s\right)}{\sin\frac{T_g}{2}\left(\omega_r-\frac{4\pi\alpha}{c}\rho_s\right)}e^{j\frac{T_g-\tau_g}{2}\omega_r}\\e^{-j\rho_s\left[K-2k_0+\frac{2\omega_r}{c}-\frac{8\pi\alpha\rho_s}{c^2}+\frac{2\pi\alpha}{c}\left(\tau_g-T_g\right)\right]}\mathrm{Sa}\left[\frac{\Delta\rho_s}{2}\left(K-2k_0\right)\right]\ .\end{aligned} \quad (3.90)$$

The range spectrum has range related peaks defined by the sinc function $\left(\mathrm{Sa}(x)=\frac{\sin(x)}{x}\right)$

and the $\frac{\sin}{\sin}$ function. A careful check shows that it is the $\frac{\sin}{\sin}$ function that gives the dominant rise, and the sinc function $\mathrm{Sa}\left[\frac{\tau_g}{2}\left(\omega_r - \frac{4\pi\alpha}{c}\rho_s\right)\right]$ provides a magnitude floor of the spectrum. Comparison of this result with that obtained for the FMCW waveform in Section 3.3.2, where the range is indicated by the peak defined by a single sinc function, shows some interesting properties. The most significant difference is that the $\frac{\sin}{\sin}$ function has periodic peaks that will give ambiguity results for the range measurement. Figures 3.7 and 3.8 are examples of the range spectra (PSD) using the FMICW waveform. In these figures, all parameters are as given in Figures 3.5 and 3.6 except that the FMICW waveform is obtained by gating the respective FMCW waveform. The gating sequence includes 16 gates in a sweep interval with a duty cycle of 25%.

The periodic peaks appearing in Figures 3.7 and 3.8 are analogous to phenomena which arise in hard target detection such as discussed by Khan and Mitchell [51]. This is the main drawback when the FMICW waveform is used in the detection of discrete targets. Khan and Mitchell [51] point out that the frequency positions of those ambiguous peaks are well defined and a careful selection of the gating sequence will limit or even suppress their appearance. However, for the measurement of the ocean surface, the target of detection is continuous in range and the target ambiguity will not be observed in practice.

Scattering from the Second-order Waves

Starting from equation (3.44) for the FMICW waveform and following the same process as for the scattering from the first-order waves, the range spectrum for the second-order waves can be obtained. Appendix A gives the detailed derivation. The resulting equation is

$$\Phi_{2g}^{r}(\omega_r) = \frac{-jI_0\eta_0\Delta l k_0^2 F^2(\rho_s)\Delta\rho_s\tau_g}{(2\pi\rho_s)^{3/2}} \sum_{\vec{K}_{1},\omega_1} \sum_{\vec{K}_{2},\omega_2} {}_1P_{\vec{K}_{1},\omega_1}\, {}_1P_{\vec{K}_{2},\omega_2}\, {}_H\Gamma_P$$
$$\sqrt{K}e^{-j\pi/4}\mathrm{Sa}\left[\frac{\tau_g}{2}\left(\omega_r - \frac{4\pi\alpha}{c}\rho_s\right)\right] \frac{\sin\frac{T_r}{2}\left(\omega_r - \frac{4\pi\alpha}{c}\rho_s\right)}{\sin\frac{T_g}{2}\left(\omega_r - \frac{4\pi\alpha}{c}\rho_s\right)} e^{j\frac{T_g-\tau_g}{2}\omega_r}$$

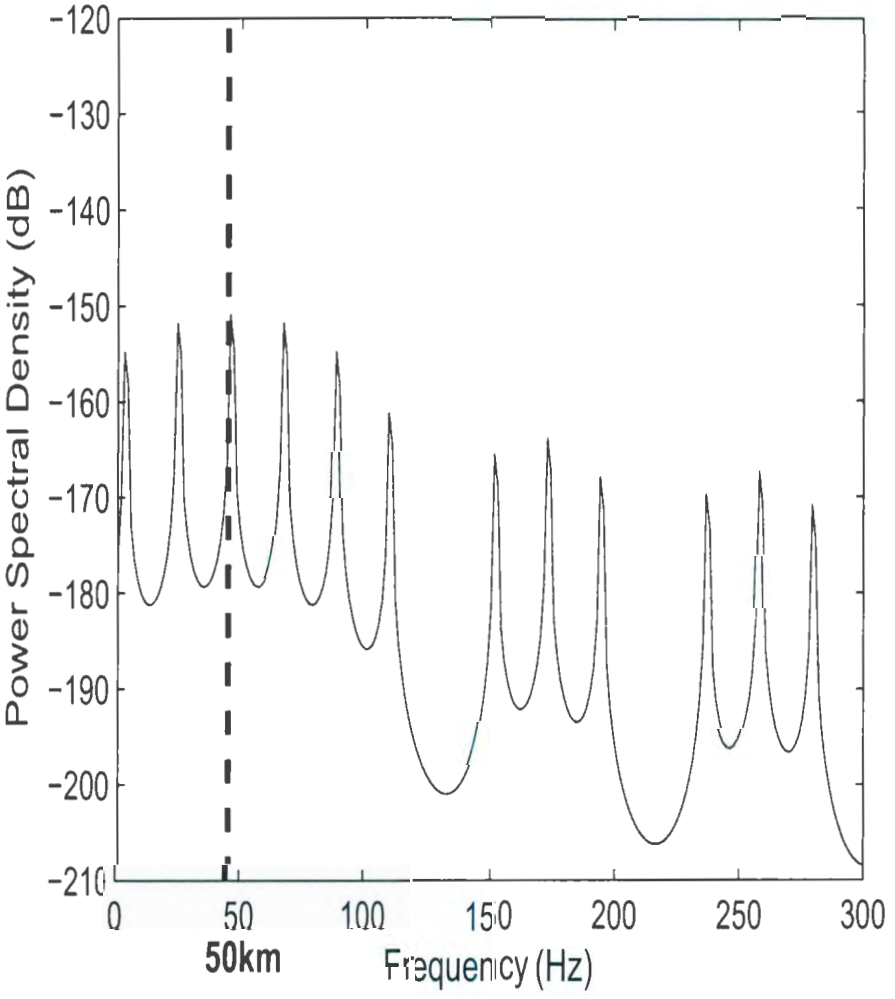

Figure 3.7: An example of range spectrum for the FMICW waveform. All parameters are the same as in Figure 3.5. There are 16 gates within a sweep interval with duty cycle of 25%.

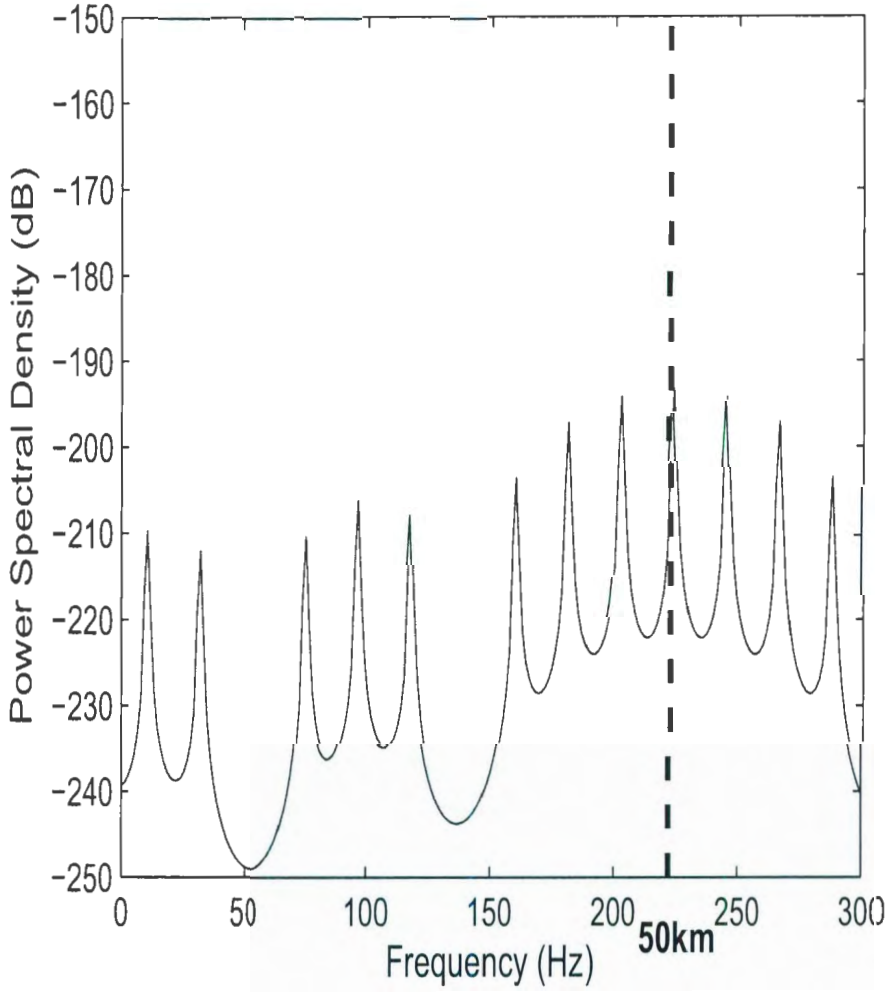

Figure 3.8: Estimation of the same range as in Figure 3.7 over the same rough surface with $f_0 = 25$ MHz and $B = 500$ kHz.

$$e^{-j\rho_s\left[K-2k_0+\frac{2\omega_r}{c}-\frac{8\pi a\rho_s}{c^2}+\frac{2\pi a}{c}(\tau_g-T_g)\right]}\mathrm{Sa}\left[\frac{\Delta\rho_s}{2}\left(K-2k_0\right)\right] . \tag{3.91}$$

Just as for the first-order case, the main difference between equations (3.91) and (3.67) is that there is a $\frac{\sin}{\sin}$ factor involved in the range spectrum.

3.4 Evaluation of Radar Cross Sections

At this stage, the first- and second-order range spectra for the FM waveforms have been obtained from the respective field equations. This work has been done by Fourier transforming the electric field equation over a sweep interval T_r. For the development of the radar cross section, the analysis will include many sweep periods to examine the Doppler shift effect. To be consistent with modeling scatter from the ocean surface, a time-variation must be introduced into the Fourier surface coefficients appearing in the electric field equations, or equivalently in the range spectral equations (3.58) and (3.67) for the FMCW waveform, and equations (3.90) and (3.91) for the FMICW waveform, respectively. According to previous investigation (e.g. Walsh *et al.* [6]), a factor of $e^{j\omega t}$, where ω is the radian frequency of the ocean wave, is introduced into the surface coefficients to indicate the time-varying property of the ocean surface. Since the Doppler effect is examined for a specific scattering patch over the ocean surface, only those patches at the same range will be picked up from the range transforms. This process is implemented by passing the received signals through a window with frequency bandwidth $B_r = \frac{1}{T_r}$. If we agree to choose an ideal window for our analysis, the amplitude of the received field will be modified by a factor of B_r. After these modifications, the time-varying equations corresponding to equations (3.58), (3.67), (3.90), and (3.91) may be written as

$$\Phi_1^r\left(\omega_r,\ t\right) = \frac{1}{T_r}\Phi_1^r\left(\omega_r\right)e^{j\omega t} , \tag{3.92}$$

$$\Phi_2^r(\omega_r,\ t) = \frac{1}{T_r}\Phi_2^r(\omega_r)\, e^{j(\omega_1+\omega_2)t}\ , \tag{3.93}$$

$$\Phi_{1g}^r(\omega_r,\ t) = \frac{1}{T_r}\Phi_{1g}^r(\omega_r)\, e^{j\omega t}\ , \tag{3.94}$$

and

$$\Phi_{2g}^r(\omega_r,\ t) = \frac{1}{T_r}\Phi_{2g}^r(\omega_r)\, e^{j(\omega_1+\omega_2)t}\ , \tag{3.95}$$

respectively, where ω_1 and ω_2 in the second-order equations are two radian frequencies of ocean waves that are involved in the second-order scatter.

The next step is to derive the radar cross sections from the field equations (3.92) and (3.93) for the FMCW waveform, and equations (3.94) and (3.95) for the FMICW waveform. The general procedure involves an autocorrelation of the fields for a particular patch of ocean, a Fourier transformation of the resulting ensemble averages, and a comparison with the radar range equation to yield the cross sections (see, for example, Walsh *et al.* [6]). The cross section results so obtained are idealized in that they assume the existence of infinitely many oceans with the same statistical features.

Obviously, any given radar time series can be received from only a single ocean and, in fact, for a finite time and a finite ocean patch. To mimic this reality, time series, representing scatter from a specific range cell (patch), may be constructed using the idealized cross sections. The PSD may be estimated via the usual periodogram technique. In this section, the first step is to derive the first- and second-order cross sections for the FMCW waveform. Then the cross sections for the FMICW waveform will be obtained following the same process.

3.4.1 PSD of the First-order Scatter for the FMCW Waveform

Starting from equation (3.92), the autocorrelation function of the field equation will be calculated with an assumption of a stationary ocean surface profile, such as Pierson's model [7]. The assumption ensures that the autocorrelation will be a function only of the time shift, τ. The autocorrelation with respect to t for the first-order backscattered field is written as (Papoulis, [77])

$$\mathcal{R}_1(\omega_r,\ \tau) \ = \ \frac{A_r}{2\eta_0}\left\langle \Phi_1^r(\omega_r,\ t+\tau)\,\Phi_1^{r*}(\omega_r,\ t)\right\rangle \ , \tag{3.96}$$

where $\langle\cdot\rangle$ refers to the statistical or ensemble average, $*$ indicates complex conjugation, and A_r is the effective free space aperture of the receiving antenna, given by (see, for example, Collin [78])

$$A_r = \frac{\lambda_0^2}{4\pi}G_r \ . \tag{3.97}$$

Substitution of equation (3.92) into equation (3.96) gives

$$\begin{aligned}\mathcal{R}_1(\omega_r,\ \tau) = {} & \frac{A_r\eta_0\left|I_0\Delta l\right|^2 k_0^4 F^4(\rho_s)\Delta\rho_s^2}{2\left(2\pi\rho_s\right)^3}\sum_{\vec{K},\omega}\sum_{\vec{K}',\omega'}\left\langle {}_1P_{\vec{K},\omega}\ {}_1P^*_{\vec{K}',\omega'}\right\rangle e^{j\omega(t+\tau)}e^{-j\omega' t} \\ & e^{-j\rho_s(K-2k_0)}e^{j\rho_s(K'-2k_0)}\sqrt{K}\sqrt{K'}\mathrm{Sa}^2\left[\frac{T_r}{2}\left(\omega_r-\frac{4\pi\alpha}{c}\rho_s\right)\right] \\ & \mathrm{Sa}\left[\frac{\Delta\rho_s}{2}\left(K-2k_0\right)\right]\mathrm{Sa}\left[\frac{\Delta\rho_s}{2}\left(K'-2k_0\right)\right] \ ,\end{aligned} \tag{3.98}$$

where $\langle\cdot\rangle$ and the summation have been interchanged since the only randomness is in the first-order Fourier surface coefficients, ${}_1P_{\vec{K},\omega}$ and ${}_1P_{\vec{K}',\omega'}$. For a real, zero-mean surface, the Fourier coefficients have the properties that (Rice, [15])

$${}_1P_{-\vec{K},-\omega} = \ {}_1P^*_{\vec{K},\omega} \tag{3.99}$$

and (Barrick, [4])

$$\left\langle {}_1P_{\vec{K},\omega}\ {}_1P^*_{\vec{K}',\omega'} \right\rangle = \begin{cases} N_s^2 W_s S\left(\vec{K},\omega\right), & \vec{K}=\vec{K}', \omega=\omega' \\ 0, & \text{otherwise} \end{cases} , \tag{3.100}$$

where $N_s = \dfrac{2\pi}{L_s}$, L_s being the fundamental wavelength of the surface, $W_s = \dfrac{2\pi}{T_s}$, T_s being the fundamental period, and $S\left(\vec{K},\omega\right)$ being the PSD of the ocean surface. The first-order component of $S\left(\vec{K},\omega\right)$ will be (Barrick, [4])

$$S_1\left(\vec{K},\omega\right) = \frac{1}{2}\sum_{m=\pm 1} S_1\left(m\vec{K}\right)\delta\left(\omega + m\sqrt{gK}\right) , \tag{3.101}$$

where $\delta(\cdot)$ is the Dirac delta function.

For a very large region of ocean surface, the fundamental wavelength L_s and period T_s will be very large so that N_s and W_s become very small. Then we have $N_s^2 \to d^2\vec{K}$ where $d^2\vec{K} \equiv dK_x dK_y \equiv K dK d\theta_{\vec{K}}$, and $W_s \to d\omega$. Under these conditions, the summations in equation (3.98) may be cast as integrals with the result being

$$\begin{aligned} \mathcal{R}_1\left(\omega_r,\ \tau\right) = {} & \frac{A_r \eta_0 \left|I_0 \Delta l\right|^2 k_0^4 F^4(\rho_s) \Delta\rho_s^2}{4\left(2\pi\rho_s\right)^3} \sum_{m=\pm 1} \int_{-\infty}^{\infty}\int_{-\pi}^{\pi}\int_0^{\infty} S_1\left(m\vec{K}\right) e^{j\omega\tau} K^2 \\ & \delta\left(\omega + m\sqrt{gK}\right) \mathrm{Sa}^2\left[\frac{T_r}{2}\left(\omega_r - \frac{4\pi\alpha}{c}\rho_s\right)\right] \mathrm{Sa}^2\left[\frac{\Delta\rho_s}{2}\left(K - 2k_0\right)\right] dK d\theta_{\vec{K}} d\omega . \end{aligned} \tag{3.102}$$

The ω integral in equation (3.102) immediately yields

$$\begin{aligned} \mathcal{R}_1\left(\omega_r,\ \tau\right) = {} & \frac{A_r \eta_0 \left|I_0 \Delta l\right|^2 k_0^4 F^4(\rho_s) \Delta\rho_s^2}{4\left(2\pi\rho_s\right)^3} \sum_{m=\pm 1} \int_{-\pi}^{\pi}\int_0^{\infty} S_1\left(m\vec{K}\right) e^{j\omega\tau} K^2 \\ & \mathrm{Sa}^2\left[\frac{T_r}{2}\left(\omega_r - \frac{4\pi\alpha}{c}\rho_s\right)\right] \mathrm{Sa}^2\left[\frac{\Delta\rho_s}{2}\left(K - 2k_0\right)\right] dK d\theta_{\vec{K}} , \end{aligned} \tag{3.103}$$

with $\omega = -m\sqrt{gK}$. The first-order PSD, $\mathcal{P}_1(\omega_r,\ \omega_d)$, will be

$$\mathcal{P}_1(\omega_r,\ \omega_d) = \mathcal{F}\left[\mathcal{R}_1(\omega_r,\ \tau)\right] . \tag{3.104}$$

The Fourier transform operates on the factor $e^{j\omega\tau}$ appearing in equation (3.103). The result will be

$$\mathcal{F}\left[e^{j\omega\tau}\right] = \mathcal{F}\left[e^{j\left(-m\sqrt{gK}\right)\tau}\right] = 2\pi\delta\left(\omega_d + m\sqrt{gK}\right) . \tag{3.105}$$

Therefore, the PSD of the first-order scatter becomes

$$\begin{aligned}\mathcal{P}_1(\omega_r,\ \omega_d) = \frac{A_r\eta_0\left|I_0\Delta l\right|^2 k_0^4 F^4(\rho_s)\Delta\rho_s^2}{16\pi^2\rho_s^3}\sum_{m=\pm1}\int_{-\pi}^{\pi}\int_0^{\infty} S_1\left(m\vec{K}\right)\delta\left(\omega_d + m\sqrt{gK}\right) \\ K^2\mathrm{Sa}^2\left[\frac{T_r}{2}\left(\omega_r - \frac{4\pi\alpha}{c}\rho_s\right)\right]\mathrm{Sa}^2\left[\frac{\Delta\rho_s}{2}\left(K - 2k_0\right)\right] dK\, d\theta_{\vec{K}} .\end{aligned} \tag{3.106}$$

Evaluating the Dirac delta function with respect to K, we obtain

$$K = \frac{\omega_d^2}{g} , \tag{3.107}$$

so that

$$dK = \frac{2\omega_d d\omega_d}{g} = \frac{2\sqrt{K}}{\sqrt{g}} d\omega_d . \tag{3.108}$$

Solving the ω_d integral while considering equation (3.108), equation (3.106) becomes

$$\begin{aligned}\mathcal{P}_1(\omega_r,\ \omega_d) = \frac{A_r\eta_0\left|I_0\Delta l\right|^2 k_0^4 F^4(\rho_s)\Delta\rho_s^2}{8\pi^2\rho_s^3}\sum_{m=\pm1}\int_{-\pi}^{\pi} S_1\left(m\vec{K}\right) \\ \frac{K^{2.5}}{\sqrt{g}}\mathrm{Sa}^2\left[\frac{T_r}{2}\left(\omega_r - \frac{4\pi\alpha}{c}\rho_s\right)\right]\mathrm{Sa}^2\left[\frac{\Delta\rho_s}{2}\left(K - 2k_0\right)\right] d\theta_{\vec{K}} .\end{aligned} \tag{3.109}$$

Equation (3.109) is the PSD equation of the first-order field as a function of the Doppler

frequency ω_d.

3.4.2 First-order Cross Section for the FMCW Waveform

The incremental form of the radar range equation, in which $d\mathcal{P}$ is the average power spectrum of the backscatter received from an elemental scattering region dA_p over the ocean surface, with cross section $\sigma(\omega_d)$, is (see Walsh *et al.* [6])

$$d\mathcal{P}(\omega_d) = \lambda_0^2 P_t G_t G_r \frac{|F(\rho_s)|^4}{(4\pi)^3 \rho_s^4} dA_p \sigma(\omega_d) \ , \tag{3.110}$$

where P_t and G_t represent the average power and free space antenna gain of the transmitting source, respectively. For a vertical dipole source (see, for example, Collin [78]),

$$8\pi P_t G_t = \eta_0 k_0^2 |I_0 \Delta l|^2 \ , \tag{3.111}$$

and the receiver gain G_r is, from equation (3.97),

$$G_r = \frac{4\pi A_r}{\lambda_0^2} \ . \tag{3.112}$$

Using equations (3.111) and (3.112), equation (3.110) becomes

$$\frac{d\mathcal{P}(\omega_d)}{dA_p} = \eta_0 k_0^2 |I_0 \Delta l|^2 A_r \frac{|F(\rho_s)|^4}{2(4\pi)^3 \rho_s^4} \sigma(\omega_d) \ . \tag{3.113}$$

Equation (3.113) is a general form of the radar range equation for an elemental scattering region. The order of the cross section depends on the order of the PSD. In the later analysis for the first- and second-order cross sections for the FM waveforms, equation (3.113) will be applied successively.

For a scattering patch of width $\Delta\rho_s$ and annular arc of extent $d\theta_{\mathrm{N}}$ at range ρ_s, the

elemental scattering region is given by

$$dA_p = \rho_s \Delta\rho_s d\theta_{\mathrm{N}} \,. \tag{3.114}$$

Using equations (3.109) and (3.114) along with the fact that $d\theta_{\mathrm{N}}$ is identital to $d\theta_{\vec{K}}$ gives

$$\begin{aligned}\frac{d\mathcal{P}_1\left(\omega_r,\,\omega_d\right)}{dA_p} &= \frac{A_r\eta_0\left|I_0\Delta l\right|^2 k_0^4 F^4(\rho_s)\Delta\rho_s}{8\pi^2\rho_s^4}\sum_{m=\pm1} S_1\left(m\vec{K}\right) \\ &\frac{K^{2.5}}{\sqrt{g}}\mathrm{Sa}^2\left[\frac{T_r}{2}\left(\omega_r-\frac{4\pi\alpha}{c}\rho_s\right)\right]\mathrm{Sa}^2\left[\frac{\Delta\rho_s}{2}\left(K-2k_0\right)\right] \,.\end{aligned} \tag{3.115}$$

Comparison of equation (3.115) with equation (3.113) will give the first-order radar cross section $\sigma_1\left(\omega_r,\,\omega_d\right)$ as

$$\begin{aligned}\sigma_1\left(\omega_r,\,\omega_d\right) &= 16\pi k_0^2\Delta\rho_s\sum_{m=\pm1} S_1\left(m\vec{K}\right)\frac{K^{2.5}}{\sqrt{g}}\mathrm{Sa}^2\left[\frac{T_r}{2}\left(\omega_r-\frac{4\pi\alpha}{c}\rho_s\right)\right] \\ &\qquad \mathrm{Sa}^2\left[\frac{\Delta\rho_s}{2}\left(K-2k_0\right)\right] \,.\end{aligned} \tag{3.116}$$

Comparing equation (3.116) with its replica for the pulsed waveform in equation (2.10), we can see that the main difference is that there is a squared sinc function factor involving the range of the scattering patch.

3.4.3 Second-order Cross Section for the FMCW Waveform

Following the same process as for the first-order cross section, the second-order patch scattering cross section for the FMCW waveform can be obtained immediately. Starting from equation (3.93), the autocorrelation function will be

$$\begin{aligned}&\mathcal{R}_2\left(\omega_r,\,\tau\right) = \frac{A_r\eta_0\left|I_0\Delta l\right|^2 k_0^4 F^4(\rho_s)\Delta\rho_s^2}{4\left(2\pi\rho_s\right)^3}\sum_{m_1=\pm1}\sum_{m_2=\pm1}\int_{-\infty}^{\infty}\int_{-\pi}^{\pi}\int_{0}^{\infty}\int_{-\infty}^{\infty}\int_{-\pi}^{\pi}\int_{0}^{\infty} \\ &S_1\left(m_1\vec{K}_1\right)S_1\left(m_2\vec{K}_2\right)\;\left|_H\Gamma_P\right|^2\;Ke^{j(\omega_1+\omega_2)\tau}\delta\left(\omega_1+m_1\sqrt{gK_1}\right)\delta\left(\omega_2+m_2\sqrt{gK_2}\right) \\ &\mathrm{Sa}^2\left[\frac{T_r}{2}\left(\omega_r-\frac{4\pi\alpha}{c}\rho_s\right)\right]\mathrm{Sa}^2\left[\frac{\Delta\rho_s}{2}\left(K-2k_0\right)\right]K_1dK_1d\theta_{\vec{K_1}}d\omega_1K_2dK_2d\theta_{\vec{K_2}}d\omega_2 \,.\end{aligned}$$

(3.117)

Here, $\vec{K}_1$ and $\vec{K}_2$ are the wave vectors of the first-order ocean waves and $\vec{K} = \vec{K}_1 + \vec{K}_2$, or $\vec{K}_2 = \vec{K} - \vec{K}_1$. The integrals with respect to ω_1 and ω_2 lead to $\omega_1 = -m_1\sqrt{gK_1}$ and $\omega_2 = -m_2\sqrt{gK_2}$. Equation (3.117) will become

$$\mathcal{R}_2(\omega_r,\ \tau) = \frac{A_r\eta_0\left|I_0\Delta l\right|^2 k_0^4 F^4(\rho_s)\Delta\rho_s^2}{4\left(2\pi\rho_s\right)^3} \sum_{m_1=\pm1}\sum_{m_2=\pm1}\int_{-\pi}^{\pi}\int_0^{\infty}\int_{-\pi}^{\pi}\int_0^{\infty}$$
$$S_1\left(m_1\vec{K}_1\right) S_1\left(m_2\vec{K}_2\right)\ \left|{}_H\Gamma_P\right|^2\ K e^{j(\omega_1+\omega_2)\tau}\mathrm{Sa}^2\left[\frac{T_r}{2}\left(\omega_r - \frac{4\pi\alpha}{c}\rho_s\right)\right]$$
$$\mathrm{Sa}^2\left[\frac{\Delta\rho_s}{2}\left(K - 2k_0\right)\right] K_1 dK_1 d\theta_{\vec{K}_1} K dK d\theta_{\vec{K}}\ . \tag{3.118}$$

In equation (3.118), the integral with respect to $\vec{K}_2$ has been transformed to $\vec{K}$ with the Jacobian of the transformation being unity. Fourier transformation of equation (3.118) will give the PSD of the second-order scatter. This Fourier transformation operates on the factor $e^{j(\omega_1+\omega_2)\tau}$ to give

$$\begin{aligned}\mathcal{F}\left[e^{j(\omega_1+\omega_2)\tau}\right] &= \int_{-\infty}^{\infty} e^{j(\omega_1+\omega_2)\tau} e^{-j\omega_d\tau} d\tau \\ &= 2\pi\delta\left(\omega_d + m_1\sqrt{gK_1} + m_2\sqrt{gK_2}\right)\ .\end{aligned} \tag{3.119}$$

Therefore, the PSD of the second-order scatter is

$$\mathcal{P}_2(\omega_r,\ \omega_d) = \mathcal{F}\left[\mathcal{R}_2(\omega_r,\ \tau)\right]$$
$$= \frac{A_r\eta_0\left|I_0\Delta l\right|^2 k_0^4 F^4(\rho_s)\Delta\rho_s^2}{16\pi^2\rho_s^3} \sum_{m_1=\pm1}\sum_{m_2=\pm1}\int_{-\pi}^{\pi}\int_0^{\infty}\int_{-\pi}^{\pi}\int_0^{\infty} S_1\left(m_1\vec{K}_1\right) S_1\left(m_2\vec{K}_2\right)$$
$$\left|{}_H\Gamma_P\right|^2\ K^2\delta\left(\omega_d + m_1\sqrt{gK_1} + m_2\sqrt{gK_2}\right)\mathrm{Sa}^2\left[\frac{T_r}{2}\left(\omega_r - \frac{4\pi\alpha}{c}\rho_s\right)\right]$$
$$\mathrm{Sa}^2\left[\frac{\Delta\rho_s}{2}\left(K - 2k_0\right)\right] K_1 dK_1 d\theta_{\vec{K}_1} dK d\theta_{\vec{K}}\ . \tag{3.120}$$

When equation (3.120) is normalized with respect to an elemental scattering region dA_p over the ocean surface as given by equation (3.114), we have

$$\frac{d\mathcal{P}_2(\omega_d,\,\omega_r)}{dA_p} = \frac{A_r\eta_0\left|I_0\Delta l\right|^2 k_0^4 F^4(\rho_s)\Delta\rho_s}{16\pi^2\rho_s^4} \sum_{m_1=\pm1}\sum_{m_2=\pm1}\int_0^\infty\int_{-\pi}^{\pi}\int_0^\infty S_1\left(m_1\vec{K}_1\right)$$
$$S_1\left(m_2\vec{K}_2\right)\,\left|{}_H\Gamma_P\right|^2\,K^2\delta\left(\omega_d + m_1\sqrt{gK_1} + m_2\sqrt{gK_2}\right)\mathrm{Sa}^2\left[\frac{T_r}{2}\left(\omega_r - \frac{4\pi\alpha}{c}\rho_s\right)\right]$$
$$\mathrm{Sa}^2\left[\frac{\Delta\rho_s}{2}\left(K-2k_0\right)\right]K_1dK_1d\theta_{\vec{K_1}}dK\,. \tag{3.121}$$

Comparison of equation (3.121) with equation (3.113) gives the second-order cross section as

$$\sigma_2(\omega_d,\,\omega_r) = 8\pi k_0^2\Delta\rho_s \sum_{m_1=\pm1}\sum_{m_2=\pm1}\int_0^\infty\int_{-\pi}^{\pi}\int_0^\infty S_1\left(m_1\vec{K}_1\right)S_1\left(m_2\vec{K}_2\right)$$
$$\left|{}_H\Gamma_P\right|^2K^2\delta\left(\omega_d + m_1\sqrt{gK_1} + m_2\sqrt{gK_2}\right)\mathrm{Sa}^2\left[\frac{T_r}{2}\left(\omega_r - \frac{4\pi\alpha}{c}\rho_s\right)\right]$$
$$\mathrm{Sa}^2\left[\frac{\Delta\rho_s}{2}\left(K-2k_0\right)\right]K_1dK_1d\theta_{\vec{K_1}}dK\,. \tag{3.122}$$

In Chapter 4, equation (3.122) will be evaluated and the second-order cross section for the FMCW waveform will be plotted. Its properties will be addressed in association with the plot in Chapter 4.

3.4.4 First-order Cross Section for the FMICW Waveform

With the experience gained in developing the first- and second-order ocean surface cross sections for the FMCW waveform we may readily deduce the corresponding models when a FMICW source is used. In this subsection the first-order cross section is derived starting from equation (3.94), following the process of autocorrelation, PSD estimation, and normalization to a scattering patch. The second-order cross section is obtained in the next subsection.

The autocorrelation $\mathcal{R}_{1g}(\omega_r,\ \tau)$ with respect to t for equation (3.94) is

$$\mathcal{R}_{1g}(\omega_r,\ \tau) = \frac{A_r}{2\eta_0}\left\langle \Phi^r_{1g}(\omega_r,\ t+\tau)\,\Phi^{r*}_{1g}(\omega_r,\ t)\right\rangle$$
$$= \frac{A_r\eta_0\left|I_0\Delta l\right|^2 k_0^4 F^4(\rho_s)\Delta\rho_s^2\tau_g^2}{2\left(2\pi\rho_s\right)^3 T_r^2}\sum_{\vec{K},\omega}\sum_{\vec{K}',\omega'}\left\langle {}_1P_{\vec{K},\omega}\ {}_1P^*_{\vec{K}',\omega'}\right\rangle e^{j\omega(t+\tau)}e^{-j\omega' t}\sqrt{K}\sqrt{K'}$$
$$\mathrm{Sa}^2\left[\frac{\tau_g}{2}\left(\omega_r-\frac{4\pi\alpha}{c}\rho_s\right)\right]\frac{\sin^2\frac{T_r}{2}\left(\omega_r-\frac{4\pi\alpha}{c}\rho_s\right)}{\sin^2\frac{T_g}{2}\left(\omega_r-\frac{4\pi\alpha}{c}\rho_s\right)}e^{-j\rho_s\left[K-2k_0+\frac{2\omega_r}{c}-\frac{8\pi\alpha\rho_s}{c^2}+\frac{2\pi\alpha}{c}(\tau_g-T_g)\right]}$$
$$e^{j\rho_s\left[K'-2k_0+\frac{2\omega_r}{c}-\frac{8\pi\alpha\rho_s}{c^2}+\frac{2\pi\alpha}{c}(\tau_g-T_g)\right]}\mathrm{Sa}\left[\frac{\Delta\rho_s}{2}(K-2k_0)\right]\mathrm{Sa}\left[\frac{\Delta\rho_s}{2}\left(K'-2k_0\right)\right]\ , \quad (3.123)$$

where all the symbols and parameters have been defined in Section 3.4.1. For a real, zero-mean large surface, equation (3.123) becomes

$$\mathcal{R}_{1g}(\omega_r,\ \tau) = \frac{A_r\eta_0\left|I_0\Delta l\right|^2 k_0^4 F^4(\rho_s)\Delta\rho_s^2\tau_g^2}{4\left(2\pi\rho_s\right)^3 T_r^2}\sum_{m=\pm1}\int_{-\infty}^{\infty}\int_{-\pi}^{\pi}\int_0^{\infty} S_1\left(m\vec{K}\right)e^{j\omega\tau}K^2$$
$$\delta\left(\omega+m\sqrt{gK}\right)\mathrm{Sa}^2\left[\frac{\tau_g}{2}\left(\omega_r-\frac{4\pi\alpha}{c}\rho_s\right)\right]\frac{\sin^2\frac{T_r}{2}\left(\omega_r-\frac{4\pi\alpha}{c}\rho_s\right)}{\sin^2\frac{T_g}{2}\left(\omega_r-\frac{4\pi\alpha}{c}\rho_s\right)}$$
$$\mathrm{Sa}^2\left[\frac{\Delta\rho_s}{2}(K-2k_0)\right]dK\,d\theta_{\vec{K}}d\omega\ . \quad (3.124)$$

The ω integral in equation (3.124) immediately yields

$$\mathcal{R}_{1g}(\omega_r,\ \tau) = \frac{A_r\eta_0\left|I_0\Delta l\right|^2 k_0^4 F^4(\rho_s)\Delta\rho_s^2\tau_g^2}{4\left(2\pi\rho_s\right)^3 T_r^2}\sum_{m=\pm1}\int_{-\pi}^{\pi}\int_0^{\infty} S_1\left(m\vec{K}\right)e^{j\omega\tau}K^2$$
$$\mathrm{Sa}^2\left[\frac{\tau_g}{2}\left(\omega_r-\frac{4\pi\alpha}{c}\rho_s\right)\right]\frac{\sin^2\frac{T_r}{2}\left(\omega_r-\frac{4\pi\alpha}{c}\rho_s\right)}{\sin^2\frac{T_g}{2}\left(\omega_r-\frac{4\pi\alpha}{c}\rho_s\right)}\mathrm{Sa}^2\left[\frac{\Delta\rho_s}{2}(K-2k_0)\right]dK\,d\theta_{\vec{K}} \quad (3.125)$$

with $\omega=-m\sqrt{gK}$. The PSD, $\mathcal{P}_{1g}(\omega_r,\ \omega_d)$, will be

$$\mathcal{P}_{1g}(\omega_r,\ \omega_d) = \mathcal{F}\left[\mathcal{R}_{1g}(\omega_r,\ \tau)\right]\ . \quad (3.126)$$

The Fourier transform again operates on the factor $e^{j\omega\tau}$. The result will be a Dirac delta

function, as

$$\mathcal{F}\left[e^{j\omega\tau}\right] = \mathcal{F}\left[e^{j\left(-m\sqrt{gK}\right)\tau}\right] = 2\pi\delta\left(\omega_d + m\sqrt{gK}\right) . \tag{3.127}$$

Therefore, the Doppler PSD for the first-order scattering field becomes

$$\begin{aligned}\mathcal{P}_{1g}\left(\omega_r,\, \omega_d\right) = & \frac{A_r\eta_0\left|I_0\Delta l\right|^2 k_0^4 F^4(\rho_s)\Delta\rho_s^2\tau_g^2}{16\pi^2\rho_s^3 T_r^2}\sum_{m=\pm 1}\int_{-\pi}^{\pi}\int_0^{\infty} S_1\left(m\vec{K}\right) \\ & \delta\left(\omega_d + m\sqrt{gK}\right) K^2 \mathrm{Sa}^2\left[\frac{\tau_g}{2}\left(\omega_r - \frac{4\pi\alpha}{c}\rho_s\right)\right]\frac{\sin^2\frac{T_r}{2}\left(\omega_r - \frac{4\pi\alpha}{c}\rho_s\right)}{\sin^2\frac{T_g}{2}\left(\omega_r - \frac{4\pi\alpha}{c}\rho_s\right)} \\ & \mathrm{Sa}^2\left[\frac{\Delta\rho_s}{2}\left(K - 2k_0\right)\right] dK\, d\theta_{\vec{K}} .\end{aligned} \tag{3.128}$$

Using the Dirac delta function to carry out the K-integration, equation (3.128) becomes

$$\begin{aligned}\mathcal{P}_{1g}\left(\omega_r,\, \omega_d\right) = & \frac{A_r\eta_0\left|I_0\Delta l\right|^2 k_0^4 F^4(\rho_s)\Delta\rho_s^2\tau_g^2}{8\pi^2\rho_s^3 T_r^2}\mathrm{Sa}^2\left[\frac{\tau_g}{2}\left(\omega_r - \frac{4\pi\alpha}{c}\rho_s\right)\right] \\ & \frac{\sin^2\frac{T_r}{2}\left(\omega_r - \frac{4\pi\alpha}{c}\rho_s\right)}{\sin^2\frac{T_g}{2}\left(\omega_r - \frac{4\pi\alpha}{c}\rho_s\right)}\sum_{m=\pm 1}\int_{-\pi}^{\pi} S_1\left(m\vec{K}\right)\frac{K^{2.5}}{\sqrt{g}}\mathrm{Sa}^2\left[\frac{\Delta\rho_s}{2}\left(K - 2k_0\right)\right] d\theta_{\vec{K}} .\end{aligned} \tag{3.129}$$

For a scattering patch of width $\Delta\rho_s$ and annular arc $d\theta_{\mathrm{N}}$ at range ρ_s

$$\begin{aligned}\frac{d\mathcal{P}_{1g}\left(\omega_r,\, \omega_d\right)}{dA_p} = & \frac{A_r\eta_0\left|I_0\Delta l\right|^2 k_0^4 F^4(\rho_s)\Delta\rho_s\tau_g^2}{8\pi^2\rho_s^4 T_r^2}\mathrm{Sa}^2\left[\frac{\tau_g}{2}\left(\omega_r - \frac{4\pi\alpha}{c}\rho_s\right)\right] \\ & \frac{\sin^2\frac{T_r}{2}\left(\omega_r - \frac{4\pi\alpha}{c}\rho_s\right)}{\sin^2\frac{T_g}{2}\left(\omega_r - \frac{4\pi\alpha}{c}\rho_s\right)}\sum_{m=\pm 1} S_1\left(m\vec{K}\right)\frac{K^{2.5}}{\sqrt{g}}\mathrm{Sa}^2\left[\frac{\Delta\rho_s}{2}\left(K - 2k_0\right)\right] .\end{aligned} \tag{3.130}$$

Comparison of equation (3.130) with the radar range equation (3.113) gives the first-order cross section for the FMICW waveform as

$$\sigma_{1g}\left(\omega_r,\, \omega_d\right) = 16\pi k_0^2\Delta\rho_s\left(\frac{\tau_g}{T_r}\right)^2\mathrm{Sa}^2\left[\frac{\tau_g}{2}\left(\omega_r - \frac{4\pi\alpha}{c}\rho_s\right)\right]\frac{\sin^2\frac{T_r}{2}\left(\omega_r - \frac{4\pi\alpha}{c}\rho_s\right)}{\sin^2\frac{T_g}{2}\left(\omega_r - \frac{4\pi\alpha}{c}\rho_s\right)}$$

$$\sum_{m=\pm 1} S_1\left(m\vec{K}\right)\frac{K^{2.5}}{\sqrt{g}}\mathrm{Sa}^2\left[\frac{\Delta\rho_s}{2}\left(K-2k_0\right)\right]. \tag{3.131}$$

It may be readily observed that equation (3.131) exhibits Bragg peak positions but different amplitude modulation as compared to that for the FMCW waveform in equation (3.116).

3.4.5 Second-order Cross Section for the FMICW Waveform

Following the same process as the derivation of the first-order cross section, the second-order patch scattering cross section for the FMICW waveform can be obtained immediately. Starting from the electric field equation (3.95), the normalized autocorrelation function will be

$$\begin{aligned}
&\mathcal{R}_{2g}\left(\omega_r,\,\tau\right)=\frac{A_r\eta_0\left|I_0\Delta l\right|^2k_0^4F^4(\rho_s)\Delta\rho_s^2\tau_g^2}{4\left(2\pi\rho_s\right)^3T_r^2}\sum_{m_1=\pm1}\sum_{m_2=\pm1}\int_{-\infty}^{\infty}\int_{-\pi}^{\pi}\int_0^{\infty}\int_{-\infty}^{\infty}\int_{-\pi}^{\pi}\int_0^{\infty}\\
&S_1\left(m_1\vec{K}_1\right)S_1\left(m_2\vec{K}_2\right)\left|{}_H\Gamma_P\right|^2Ke^{j(\omega_1+\omega_2)\tau}\delta\left(\omega_1+m_1\sqrt{gK_1}\right)\\
&\delta\left(\omega_2+m_2\sqrt{gK_2}\right)\mathrm{Sa}^2\left[\frac{\tau_g}{2}\left(\omega_r-\frac{4\pi\alpha}{c}\rho_s\right)\right]\frac{\sin^2\frac{T_r}{2}\left(\omega_r-\frac{4\pi\alpha}{c}\rho_s\right)}{\sin^2\frac{T_g}{2}\left(\omega_r-\frac{4\pi\alpha}{c}\rho_s\right)}\\
&\mathrm{Sa}^2\left[\frac{\Delta\rho_s}{2}\left(K-2k_0\right)\right]K_1dK_1d\theta_{\vec{K_1}}d\omega_1K_2dK_2d\theta_{\vec{K_2}}d\omega_2\,.
\end{aligned}\tag{3.132}$$

The integrals with respect to ω_1 and ω_2 and transformation of the $\vec{K}_2$ integral to a $\vec{K}$ integral with the unity Jacobian gives

$$\begin{aligned}
&\mathcal{R}_{2g}\left(\omega_r,\,\tau\right)=\frac{A_r\eta_0\left|I_0\Delta l\right|^2k_0^4F^4(\rho_s)\Delta\rho_s^2}{4\left(2\pi\rho_s\right)^3}\left(\frac{\tau_g}{T_r}\right)^2\sum_{m_1=\pm1}\sum_{m_2=\pm1}\int_{-\pi}^{\pi}\int_0^{\infty}\int_{-\pi}^{\pi}\int_0^{\infty}\\
&S_1\left(m_1\vec{K}_1\right)S_1\left(m_2\vec{K}_2\right)\left|{}_H\Gamma_P\right|^2K^2e^{j(\omega_1+\omega_2)\tau}\mathrm{Sa}^2\left[\frac{\tau_g}{2}\left(\omega_r-\frac{4\pi\alpha}{c}\rho_s\right)\right]\\
&\frac{\sin^2\frac{T_r}{2}\left(\omega_r-\frac{4\pi\alpha}{c}\rho_s\right)}{\sin^2\frac{T_g}{2}\left(\omega_r-\frac{4\pi\alpha}{c}\rho_s\right)}\mathrm{Sa}^2\left[\frac{\Delta\rho_s}{2}\left(K-2k_0\right)\right]K_1dK_1d\theta_{\vec{K_1}}dKd\theta_{\vec{K}}
\end{aligned}\tag{3.133}$$

with $\omega_1=-m_1\sqrt{gK_1}$ and $\omega_2=-m_2\sqrt{gK_2}$. The PSD will be

$$\mathcal{P}_{2g}^r\left(\omega_r,\,\omega_d\right)=\mathcal{F}\left[\mathcal{R}_{2g}\left(\omega_r,\,\tau\right)\right]$$

$$= \frac{A_r \eta_0 \left|I_0 \Delta l\right|^2 k_0^4 F^4(\rho_s) \Delta \rho_s^2}{16\pi^2 \rho_s^3} \left(\frac{\tau_g}{T_r}\right)^2 \mathrm{Sa}^2\left[\frac{\tau_g}{2}\left(\omega_r - \frac{4\pi\alpha}{c}\rho_s\right)\right] \frac{\sin^2\frac{T_r}{2}\left(\omega_r - \frac{4\pi\alpha}{c}\rho_s\right)}{\sin^2\frac{T_g}{2}\left(\omega_r - \frac{4\pi\alpha}{c}\rho_s\right)}$$
$$\sum_{m_1=\pm 1}\sum_{m_2=\pm 1}\int_{-\pi}^{\pi}\int_{0}^{\infty}\int_{-\pi}^{\pi}\int_{0}^{\infty} S_1\left(m_1\vec{K}_1\right) S_1\left(m_2\vec{K}_2\right) \left|{}_H\Gamma_P\right|^2 K^2$$
$$\delta\left(\omega_d + m_1\sqrt{gK_1} + m_1\sqrt{gK_2}\right) \mathrm{Sa}^2\left[\frac{\Delta\rho_s}{2}\left(K - 2k_0\right)\right] K_1 dK_1 d\theta_{\vec{K}_1} dK d\theta_{\vec{K}} \,. \qquad (3.134)$$

When equation (3.134) is divided by an elemental scattering region dA_p over the ocean surface (equation (3.114)), we have

$$\frac{d\mathcal{P}_{2g}^r\left(\omega_r,\, \omega_d\right)}{dA_p} = \frac{A_r \eta_0 \left|I_0 \Delta l\right|^2 k_0^4 F^4(\rho_s) \Delta \rho_s}{16\pi^2 \rho_s^4} \left(\frac{\tau_g}{T_r}\right)^2 \mathrm{Sa}^2\left[\frac{\tau_g}{2}\left(\omega_r - \frac{4\pi\alpha}{c}\rho_s\right)\right]$$
$$\frac{\sin^2\frac{T_r}{2}\left(\omega_r - \frac{4\pi\alpha}{c}\rho_s\right)}{\sin^2\frac{T_g}{2}\left(\omega_r - \frac{4\pi\alpha}{c}\rho_s\right)} \sum_{m_1=\pm 1}\sum_{m_2=\pm 1}\int_{0}^{\infty}\int_{-\pi}^{\pi}\int_{0}^{\infty} S_1\left(m_1\vec{K}_1\right) S_1\left(m_2\vec{K}_2\right) \left|{}_H\Gamma_P\right|^2 K^2$$
$$\delta\left(\omega_d + m_1\sqrt{gK_1} + m_1\sqrt{gK_2}\right) \mathrm{Sa}^2\left[\frac{\Delta\rho_s}{2}\left(K - 2k_0\right)\right] K_1 dK_1 d\theta_{\vec{K}_1} dK \,. \qquad (3.135)$$

Comparison of equation (3.135) with the radar range equation (3.113) gives the second-order cross section for the FMICW waveform as

$$\sigma_{2g}^r\left(\omega_r,\, \omega_d\right) = 8\pi k_0^2 \Delta\rho_s \left(\frac{\tau_g}{T_r}\right)^2 \mathrm{Sa}^2\left[\frac{\tau_g}{2}\left(\omega_r - \frac{4\pi\alpha}{c}\rho_s\right)\right] \frac{\sin^2\frac{T_r}{2}\left(\omega_r - \frac{4\pi\alpha}{c}\rho_s\right)}{\sin^2\frac{T_g}{2}\left(\omega_r - \frac{4\pi\alpha}{c}\rho_s\right)}$$
$$\sum_{m_1=\pm 1}\sum_{m_2=\pm 1}\int_{0}^{\infty}\int_{-\pi}^{\pi}\int_{0}^{\infty} S_1\left(m_1\vec{K}_1\right) S_1\left(m_2\vec{K}_2\right) \left|{}_H\Gamma_P\right|^2 K^2$$
$$\delta\left(\omega_d + m_1\sqrt{gK_1} + m_2\sqrt{gK_2}\right) \mathrm{Sa}^2\left[\frac{\Delta\rho_s}{2}\left(K - 2k_0\right)\right] K_1 dK_1 d\theta_{\vec{K}_1} dK \,. \qquad (3.136)$$

A further discussion can be found in Chapter 4.

3.5 Range Independent Cross Sections

In a closer view of the first- and second-order cross sections for the FMCW waveforms as detailed by equations (3.116) and (3.122), we can see that the range dependent factor is a squared sinc function. The principal maximum of the squared sinc function will take a

value of unity when the argument of the sinc function is equal to zero. For an arbitrary range ρ_s within ρ_{max} there will be a specific ω_r corresponding to it, making the principal maximum equal to unity (see equation (3.60)). When investigating the properties of the cross sections from the ocean surface we are actually concerned with an arbitrary range. Therefore, it is reasonable to write out the range independent cross section equations incorporating the maximum value of the squared sinc function. For the FMCW case, this gives

$$\sigma_1(\omega_d) = 16\pi k_0^2 \Delta\rho_s \sum_{m=\pm 1} S_1\left(m\vec{K}\right) \frac{K^{2.5}}{\sqrt{g}} \mathrm{Sa}^2\left[\frac{\Delta\rho_s}{2}(K-2k_0)\right] \tag{3.137}$$

and

$$\sigma_2(\omega_d) = 8\pi k_0^2 \Delta\rho_s \sum_{m_1=\pm 1} \sum_{m_2=\pm 1} \int_0^{\infty} \int_{-\pi}^{\pi} \int_0^{\infty} S_1\left(m_1\vec{K}_1\right) S_1\left(m_2\vec{K}_2\right) |{}_H\Gamma_P|^2 K^2$$
$$\delta\left(\omega_d + m_1\sqrt{gK_1} + m_2\sqrt{gK_2}\right) \mathrm{Sa}^2\left[\frac{\Delta\rho_s}{2}(K-2k_0)\right] K_1 dK_1 d\theta_{\vec{K}_1} dK \tag{3.138}$$

for the first- and second-order, respectively. Comparison of equations (3.137) and (3.138) for the FMCW waveform with equations (2.10) and (2.17) for the pulsed waveform shows that, after appropriate approximation, they are totally identical to the cross sections when the transmit waveform is a simple pulsed sinusoid.

For the FMICW waveform, the cross section equations (3.131) and (3.136) have two factors which appear to indicate a range dependency. For a specific range, the squared sinc function will take the maximum value unity while the squared $\frac{\sin}{\sin}$ function will take the maximum value of N^2, where $N = \frac{T_r}{T_g}$. Under these conditions, those equations may be reduced to range independent forms to give first- and second-order cross sections for the FMICW case as

$$\sigma_{1g}(\omega_d) = 16\pi k_0^2 \Delta\rho_s \left(\frac{\tau_g}{T_g}\right)^2 \sum_{m=\pm 1} S_1\left(m\vec{K}\right) \frac{K^{2.5}}{\sqrt{g}} \mathrm{Sa}^2\left[\frac{\Delta\rho_s}{2}(K-2k_0)\right] \tag{3.139}$$

and

$$\sigma_{2g}(\omega_d) = 8\pi k_0^2 \Delta\rho_s \left(\frac{\tau_g}{T_g}\right)^2 \sum_{m_1=\pm 1} \sum_{m_2=\pm 1} \int_0^\infty \int_{-\pi}^{\pi} \int_0^\infty S_1\left(m_1\vec{K}_1\right) S_1\left(m_2\vec{K}_2\right) |_H\Gamma_P|^2 K^2$$
$$\delta\left(\omega_d + m_1\sqrt{gK_1} + m_2\sqrt{gK_2}\right) \mathrm{Sa}^2\left[\frac{\Delta\rho_s}{2}(K - 2k_0)\right] K_1 dK_1 d\theta_{\vec{K}_1} dK \ , \qquad (3.140)$$

respectively. The factor $\frac{\tau_g}{T_g}$ is actually the duty cycle (d_c) of the gating sequence. Comparison of cross sections for the FMICW waveform with those for the FMCW waveform and simple pulsed sinusoid shows that they are identical in style except for an amplitude modulation by the squared duty cycle for the FMICW waveform. This result is reasonable because the FMICW waveform inherently radiates less power to the scattering patch than FMCW waveform if other parameters are identical. With this in mind, when cross sections are plotted and their properties are discussed in Chapter 4, we will not specify the FMCW and FMICW waveforms, but generally refer simply to FM waveforms instead. We will also simulate the ocean clutter based on these range independent cross sections (3.137)-(3.140) and investigate the fluctuation behavior of the Bragg peaks including comparisons with FMCW field data in that chapter.

3.6 Chapter Summary

In this chapter, the first- and second-order backscatter cross sections for the FM waveforms have been derived based on Walsh's method. The second-order results contain only the case of a single scatter from hydrodynamically coupled ocean waves. The procedure of evaluation includes the development of the temporal field equations, calculation of the range spectra, estimation of the PSD functions, and finally, derivation of the cross section equations.

The range estimation spectrum is obtained from the temporal field equation by Fourier transforming the sampled time series within a sweep interval. For a discrete target such as a vessel or a low-flying aircraft at a specific range within the radar coverage, a radar with

the FMCW waveform will generate a single peak corresponding to that range. However, for the radar system with the FMICW waveform, range ambiguity will occur for the same discrete target. This is due to the fact that the predominant peaks appear in the range estimation spectrum as defined by a $\frac{\sin}{\sin}$ function for the FMICW waveform, rather than a sinc function for the FMCW waveform.

It has been shown that for the FMCW and FMICW waveforms, the first- and second-order cross sections are identical after reasonable approximation for a specific scattering patch over the ocean surface except for an amplitude modulation of squared duty cycle for the FMICW waveform. The cross sections for the FMCW waveform are equal to the cross sections when the same scattering patch is illuminated by a pulsed waveform.

Chapter 4

Interpretation of the Cross Sections and Fluctuations of the Bragg Peaks for the FM Waveforms

In Chapter 2, the Bragg fluctuations for the pulsed waveform have been analyzed. In Chapter 3, the radar backscatter cross sections for the FM waveforms have been derived. In this chapter, the cross sections obtained in Chapter 3 will be numerically evaluated and depicted. One thing should be pointed out in advance. Since the cross sections for the FMICW waveform have only differences in a squared duty-cycle factor, they will be several dBs lower in magnitude than those for the FMCW waveform. Therefore, in order to simplify the depictions, cross sections are plotted for the FMCW waveform only. Since to the orders of approximation used here the cross sections for the FMCW waveform are identical to those for the pulsed waveform, we may consider their properties very quickly. Then the Bragg fluctuations of the radar received Doppler spectrum for the FM waveforms will be investigated. At the end of the chapter, simulation results and fluctuations of the Bragg peaks will be examined using field data.

4.1 First-order Cross Sections for the FM Waveforms

The first-order cross section for the FM waveforms is expressed in equation (3.137) or (3.139). Figures 4.1 and 4.2 are plots of the cross sections for the FM waveforms with operating frequencies of 25 MHz and 5 MHz, respectively. The operating frequency for the FM waveforms is defined as the central frequency of the sweep bandwidth and denoted as f_0. In these figures, the directional ocean wave spectrum is from equation (2.9), which has been addressed in Section 2.1 and the ocean state is kept unchanged, i.e. the wind velocity is 15 m/s, 0° to the reference direction (defined as the direction that is perpendicular to the radar look direction – see Figure 2.2 in Chapter 2) and the ocean surface current speed is zero. The sweep interval is 0.25 s, and the sweep bandwidth in each case is 500 kHz, corresponding to a range resolution of 300 m. In both figures, the vertical dashed lines indicate the Bragg frequencies associated with the operating frequencies. From equation (3.137) or (3.139), the Bragg frequencies ω_B^m for the FM waveforms will be $\omega_B^m = \pm\sqrt{2gk_0}$, which, to the orders of approximation assumed in the intervening analysis, are identical to those for the pulsed waveform with the operating frequency f_0.

Figure 4.3 contains a set of plots of the cross sections for different wind directions. The radar parameters are $f_0 = 25$ MHz, $T_r = 0.25$ s, and $B = 500$ kHz. The wind speed is 15 m/s. Subfigures (a), (b) and (c) correspond to the wind directions of 30°, 60°, and 90° to the reference direction, respectively. The magnitudes of the right-hand side peaks decrease with increasing wind direction angles until the disappearance occurs at the angle of 90° to the reference direction – at an angle that is perpendicular to the radar beam.

4.2 Second-order Cross Sections for the FM Waveforms

The squared sinc function in equation (3.138) or (3.140) may be approximated by a Dirac delta function with the assumption of a large scattering patch $\Delta\rho_s$. Invoking equation

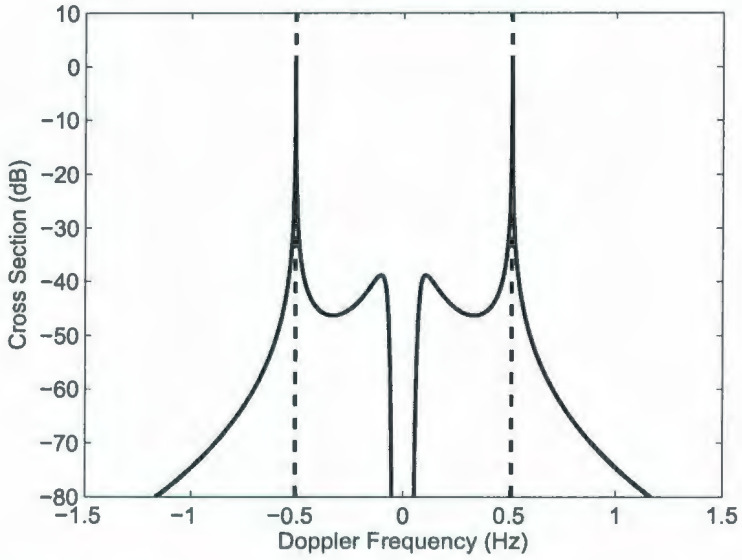

Figure 4.1: First-order cross section for the FM waveforms with $f_0 = 25$ MHz, $T_\tau = 0.25$ s, and $B = 500$ kHz. The wind velocity is 15 m/s, 0° to the reference direction and the ocean surface current speed is zero.

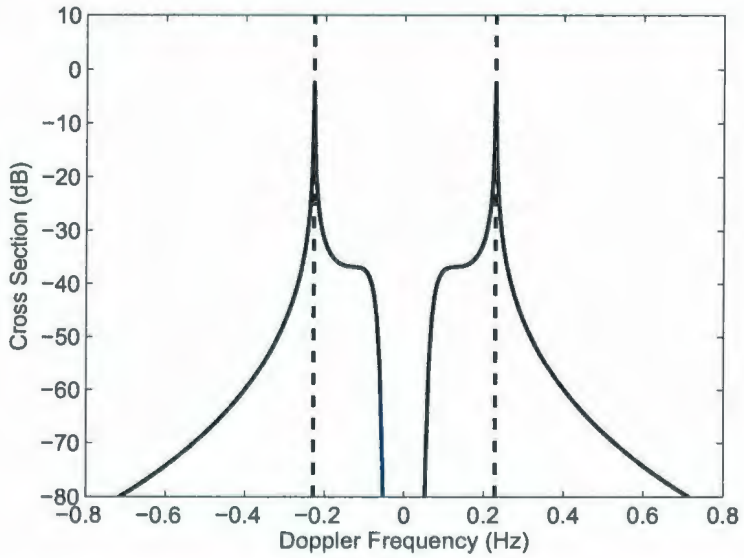

Figure 4.2: First-order cross section for the FM waveforms. All parameters are the same as in Figure 4.1 except $f_0 = 5$ MHz.

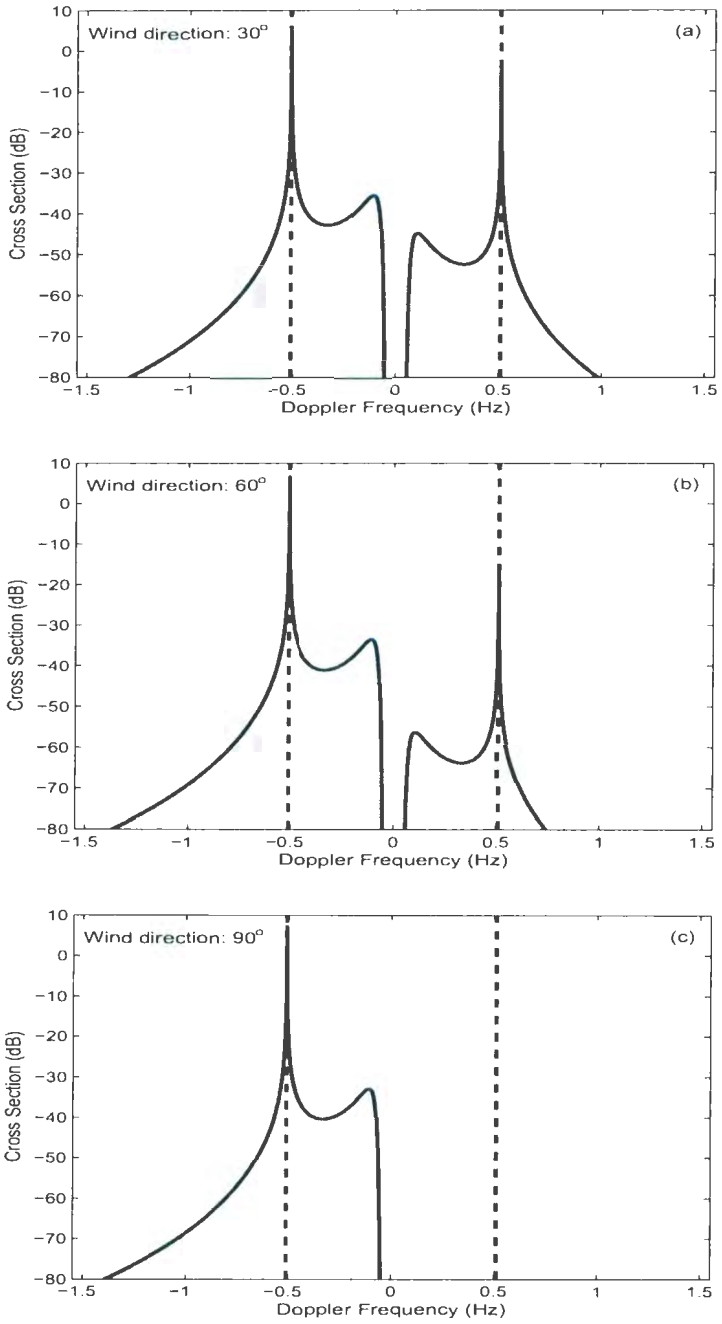

Figure 4.3: First-order cross sections for the FM waveforms with wind directions of (a) 30°, (b) 60°, and (c) 90°, respectively. All the other parameters are the same as in Figure 4.1.

(2.24) we have

$$\begin{aligned}
&\lim_{\frac{\Delta\rho_s}{2}\to\infty} \mathrm{Sa}^2\left[\frac{\Delta\rho_s}{2}(K-2k_0)\right] \\
&= \frac{2}{\Delta\rho_s}\lim_{\frac{\Delta\rho_s}{2}\to\infty}\frac{\Delta\rho_s}{2}\mathrm{Sa}^2\left[\frac{\Delta\rho_s}{2}(K-2k_0)\right] \\
&\approx \frac{2\pi}{\Delta\rho_s}\delta(K-2k_0)\ . \qquad (4.1)
\end{aligned}$$

Then, evaluating the integral with respect to K, equation (3.138) or (3.140) becomes

$$\begin{aligned}
\sigma_2(\omega_d) \approx\ & 64\pi^2 k_0^4 \sum_{m_1=\pm1}\sum_{m_2=\pm1}\int_{-\pi}^{\pi}\int_0^{\infty} S_1\left(m_1\vec{K}_1\right) S_1\left(m_2\vec{K}_2\right) \\
& |_H\Gamma_P|^2\,\delta\left(\omega_d + m_1\sqrt{gK_1} + m_2\sqrt{gK_2}\right) K_1 dK_1 d\theta_{\vec{K}_1}\ . \qquad (4.2)
\end{aligned}$$

The delta function constraint in equation (4.2) can be evaluated following the process in Chapter 2.2.2 for the pulsed waveform. The resulting equation will be

$$\begin{aligned}
\sigma_2(\omega_d) \approx\ & 128\pi^2 k_0^4 \sum_{m_1=\pm1}\sum_{m_2=\pm1}\int_{-\pi}^{\pi}\int_0^{\infty} S_1\left(m_1\vec{K}_1\right) S_1\left(m_2\vec{K}_2\right) \\
& |\ _H\Gamma_P|^2\,\delta\left[\omega_d - D_P\left(Y,\theta_{\vec{K}_1}\right)\right] Y^3\left|\frac{\partial Y}{\partial D_P}\right|_{\theta_{\vec{K}_1}} dD_P d\theta_{\vec{K}_1}\ , \qquad (4.3)
\end{aligned}$$

or

$$\begin{aligned}
\sigma_2(\omega_d) \approx\ & 128\pi^2 k_0^4 \sum_{m_1=\pm1}\sum_{m_2=\pm1}\int_{-\pi}^{\pi} S_1\left(m_1\vec{K}_1\right) S_1\left(m_2\vec{K}_2\right) \\
& |\ _H\Gamma_P|^2\, Y^3\left|\frac{\partial Y}{\partial D_P}\right|_{\theta_{\vec{K}_1}} d\theta_{\vec{K}_1}\ , \qquad (4.4)
\end{aligned}$$

where $\left|\frac{\partial Y}{\partial D_P}\right|_{\theta_{\vec{K}_1}}$ is the Jacobian of the transformation expressed in equation (2.32) in Section 2.2.2.

Just as there are singularities appearing in the second-order cross section for the pulsed waveform (e.g. Walsh and Dawe [34], Gill and Walsh [35]), there are also singularities in the

second-order cross sections for the FM waveforms. Since only the hydrodynamic coupling is considered, the singularities will only emerge in the Jacobian of the transformation.

In equation (2.32), when $\theta_{\vec{K}_1} = \theta_{\mathrm{N}}$, $Y = \sqrt{K_1} = \sqrt{k_0}$, and $m_1 m_2 = 1$, the factor $\left|\frac{\partial Y}{\partial D_P}\right|_{\theta_{\vec{K}_1}}$ will become infinite. This defines a pair of singularities with $\vec{K}_1 = \vec{K}_2 = (k_0, \theta_{\mathrm{N}})$, which implies

$$\omega_d = -m_1\sqrt{gk_0} - m_2\sqrt{gk_0} = \mp\sqrt{2}\sqrt{2gk_0}\,. \tag{4.5}$$

Here, $\sqrt{2gk_0}$ is actually the Bragg frequency ω_{B}^m. A similar discussion for the monostatic configuration with the pulsed waveform can be found in Barrick [19] and Srivastava [5], and for the bistatic radar configuration, in Walsh and Dawe [34] and Gill and Walsh [35].

4.2.1 Depictions of the Second-order Cross Sections

Figure 4.4 depicts the second-order cross sections for the FM waveforms with $f_0 = 25$ MHz, $T_r = 0.25$ s, and $B = 500$ kHz. The wind velocity is 15 m/s, 0° to the reference direction. In Figure 4.5, all the parameters are the same as in Figure 4.4 except the radar operating frequency is $f_0 = 5$ MHz.

Figures 4.6 and 4.7 depict the combinations of the first- and second-order cross sections for the FM waveforms with the operating frequencies of 25 MHz and 5 MHz, respectively. All the other parameters are the same as in Figures 4.4 and 4.5.

4.3 Fluctuation Properties of the Doppler Spectra for the FM Waveforms

4.3.1 Simulation of the Received Time Series

As in Chapter 2 for the pulse waveform, the simulation of the radar received time series from the ocean surface involves a transformation of the FM radar cross sections from the

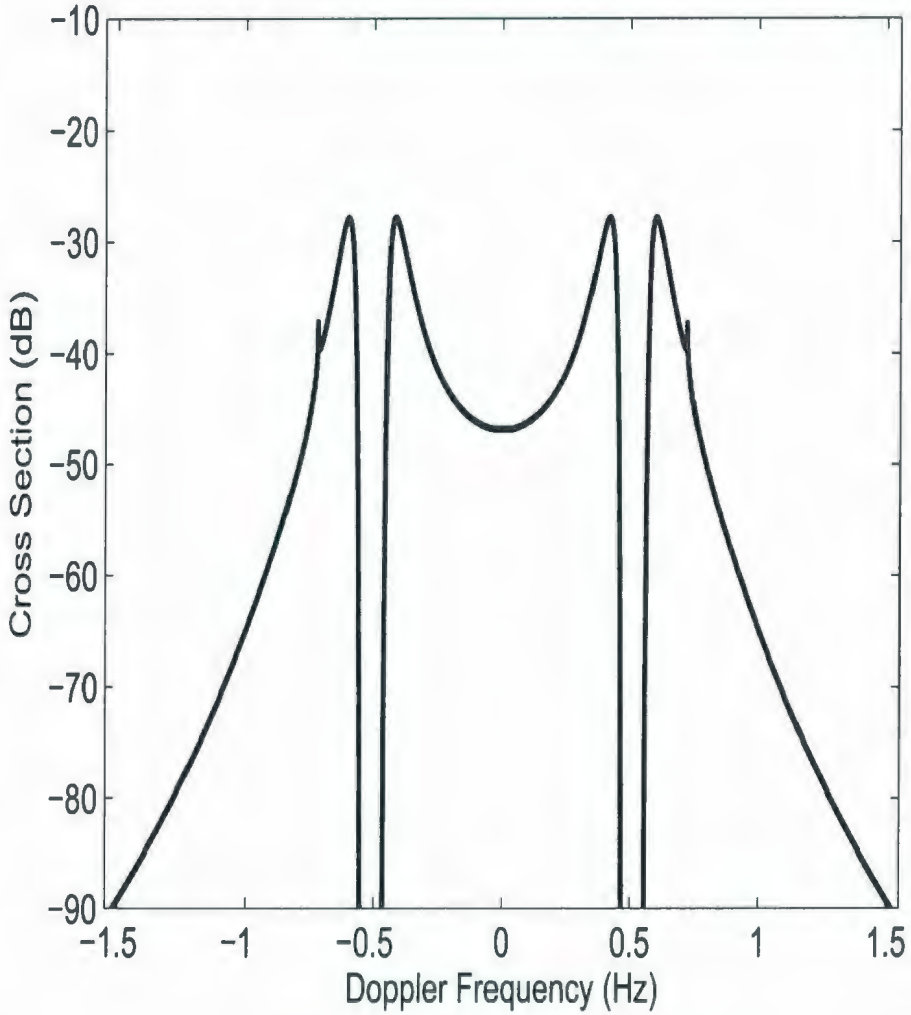

Figure 4.4: Second-order cross sections for the FM waveforms with $f_0 = 25$ MHz. The singularities are shown in frequency positions of $\mp\sqrt{2}\omega_{\mathrm{B}}^{m}$. The wind velocity is 15 m/s, 0° to the reference direction.

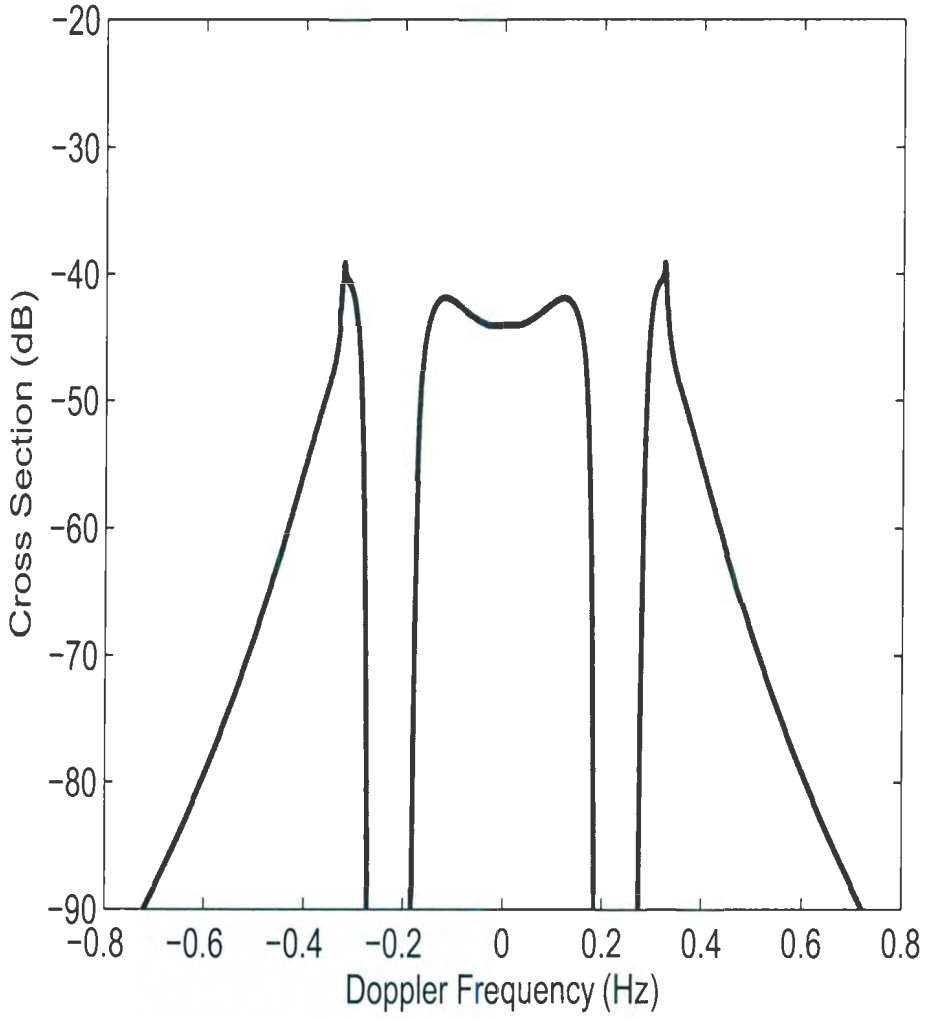

Figure 4.5: Second-order cross sections for the FM waveforms with $f_0 = 5$ MHz. Other parameters are as in Figure 4.4.

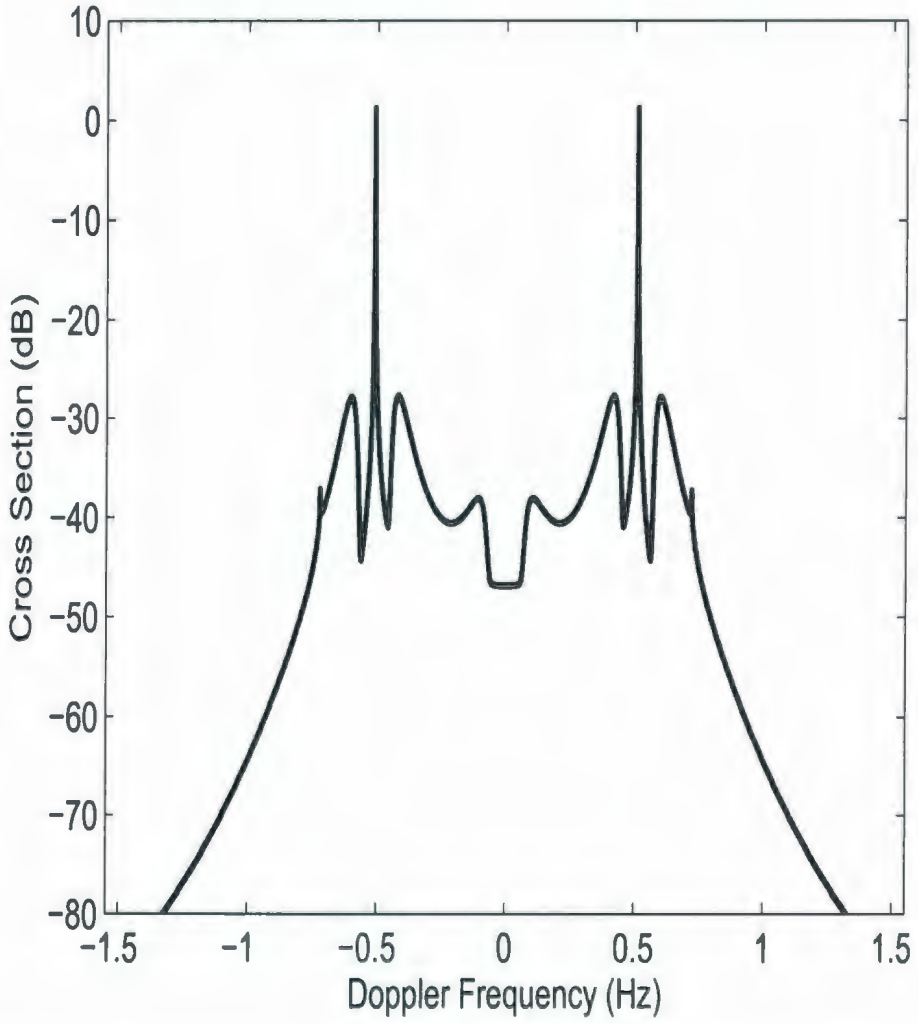

Figure 4.6: First- and second-order cross sections for the FM waveforms with $f_0 = 25$ MHz. Other parameters are as in Figure 4.4.

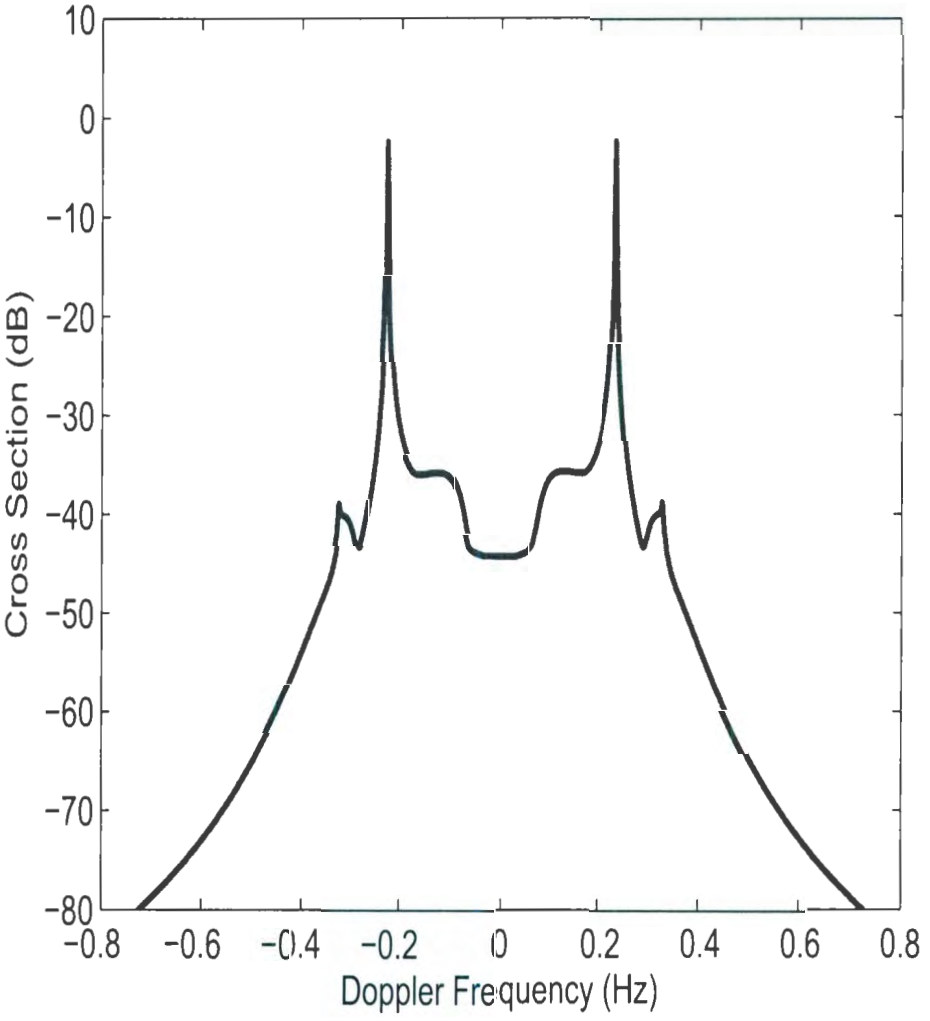

Figure 4.7: First- and second-order cross sections for the FM waveforms with $f_0 = 5$ MHz. Other parameters are as in Figure 4.4.

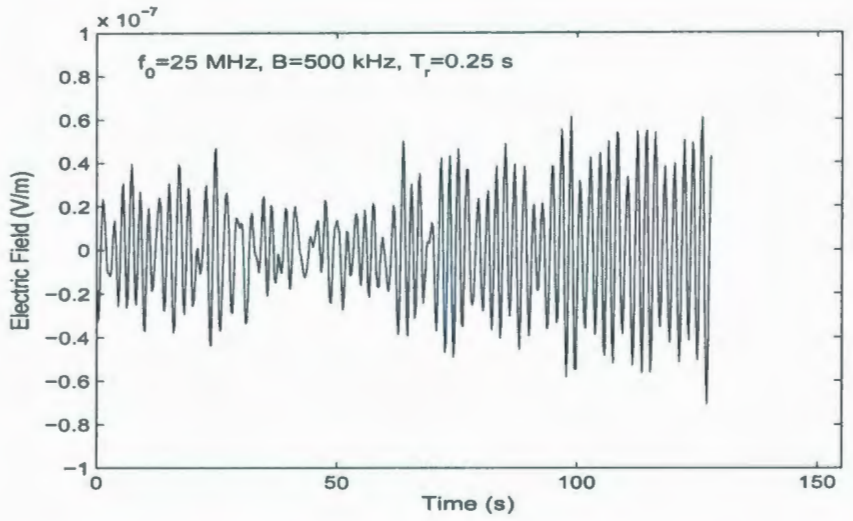

Figure 4.8: A 512-point time series for the FM waveforms with $f_0 = 25$ MHz, $T_r = 0.25$ s, and $B = 500$ kHz. The scattering patch is 50 km from the radar site (monostatic configuration). The wind velocity is 15 m/s, 0° to the reference direction.

frequency to the time domain by employing Pierson's model [7] for a one-dimensional stationary Gaussian process. Equation (2.37) again suggests a numerical scheme to accomplish this by replacing $\sigma_1 + \sigma_2$ with $\sigma(\omega_{2q+1})$ from equations (3.137) and (3.139) for the FMCW waveform (or $\sigma_{1g} + \sigma_{2g}$ for the FMICW). This model has been detailed in Gill and Walsh [42]. Figure 4.8 is an example of 512-point time series for the FM waveforms. In this figure, the radar parameters are $f_0 = 25$ MHz, $T_r = 0.25$ s, and $B = 500$ kHz. The scattering patch is 50 km from the radar transmitter and receiver (monostatic configuration), and the wind velocity is 15 m/s, 0° to the reference direction. It should be mentioned that initially external noise is not added when the radar received time series and the resulting PSDs are simulated here. The randomness of the simulated data is due to the random ocean surface only.

4.3.2 PSD of the Echo Signal from the Ocean Surface

The PSDs of the echo signals are calculated as periodograms. Figure 4.9 is an example of a PSD of the ocean clutter for the FM waveforms. The simulation parameters are the

same as for Figure 4.8. In (a) of Figure 4.9, the PSD is calculated from a 256-point time series. In (b) the time series is 512-point, and in (c) a 4096-point time series is used and 15 averages of 512-point FFTs are implemented with a 50% overlap. Parameters in Figure 4.10 are the same as those in Figure 4.9 except that $f_0 = 5$ MHz.

In practice, one of the major contaminations to the actual radar received signal is external noise. In Gill and Walsh [42] (see also [65]), a model of Gaussian white noise has been introduced for the HF radar received signals for the pulsed waveform. Using this model and keeping the same assumptions as in Gill and Walsh [42] and Gill [65] (*median* values of *noise figure* F_{am} = 22 dB and 42 dB [79] are used for the external noise for $f_0 = 25$ MHz and $f_0 = 5$ MHz, respectively), noisy radar received signals are simulated and the PSDs are calculated for the FM waveforms. Figures 4.11 and 4.12 are examples of the PSDs of the noisy signals for the FM waveforms with radar operating frequencies of $f_0 = 25$ MHz and $f_0 = 5$ MHz, respectively. Since the main purpose of the thesis is to investigate the fluctuations of the Bragg peaks due to the randomness of the ocean surface, noise will not be considered in the fluctuation analysis.

4.3.3 Determination of the Critical Values for the FM Waveforms

Using the same process as in Chapter 2, we first give two examples to show the fluctuations of the Bragg peak regions when the FM waveforms are used. Figures 4.13 and 4.14 are plots of four Doppler spectra for $f_0 = 25$ MHz and $f_0 = 5$ MHz, respectively. The sweep bandwidths for the two plots are fixed as $B = 500$ kHz. In order to see the variation of the Bragg peaks, we segment the time series into four consecutive parts, each having a length of 512 points. The Doppler spectrum is estimated and the position of the centroid is calculated for each segment. For each figure, the centroid positions are indicated by solid lines from top to bottom. This process is the same as in Figures 2.6 to 2.9 in Section 2.3.2 for the pulsed waveform. The variations of the magnitudes of the Bragg peaks can

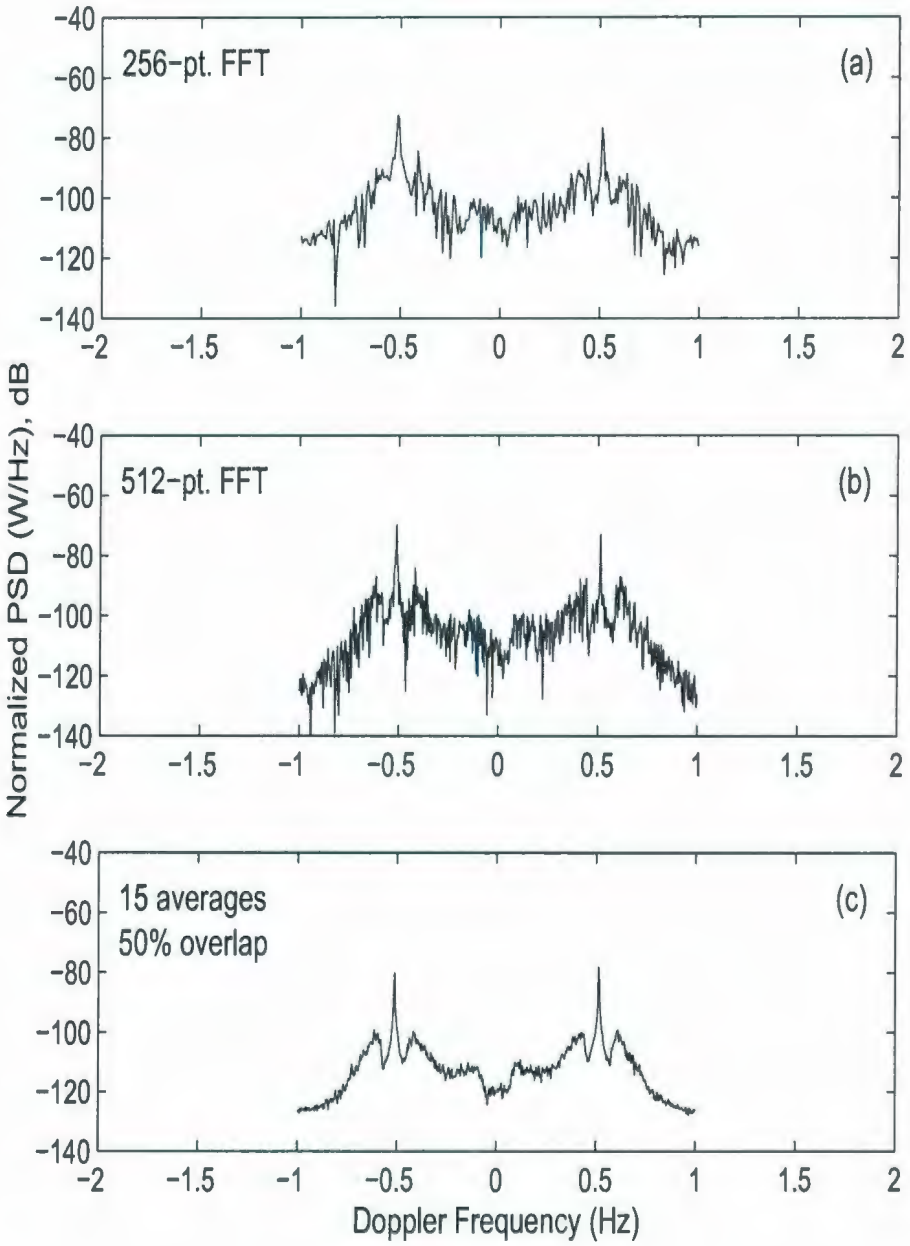

Figure 4.9: PSD of the clutter spectrum for the FM waveforms. All parameters are as in Figure 4.8.

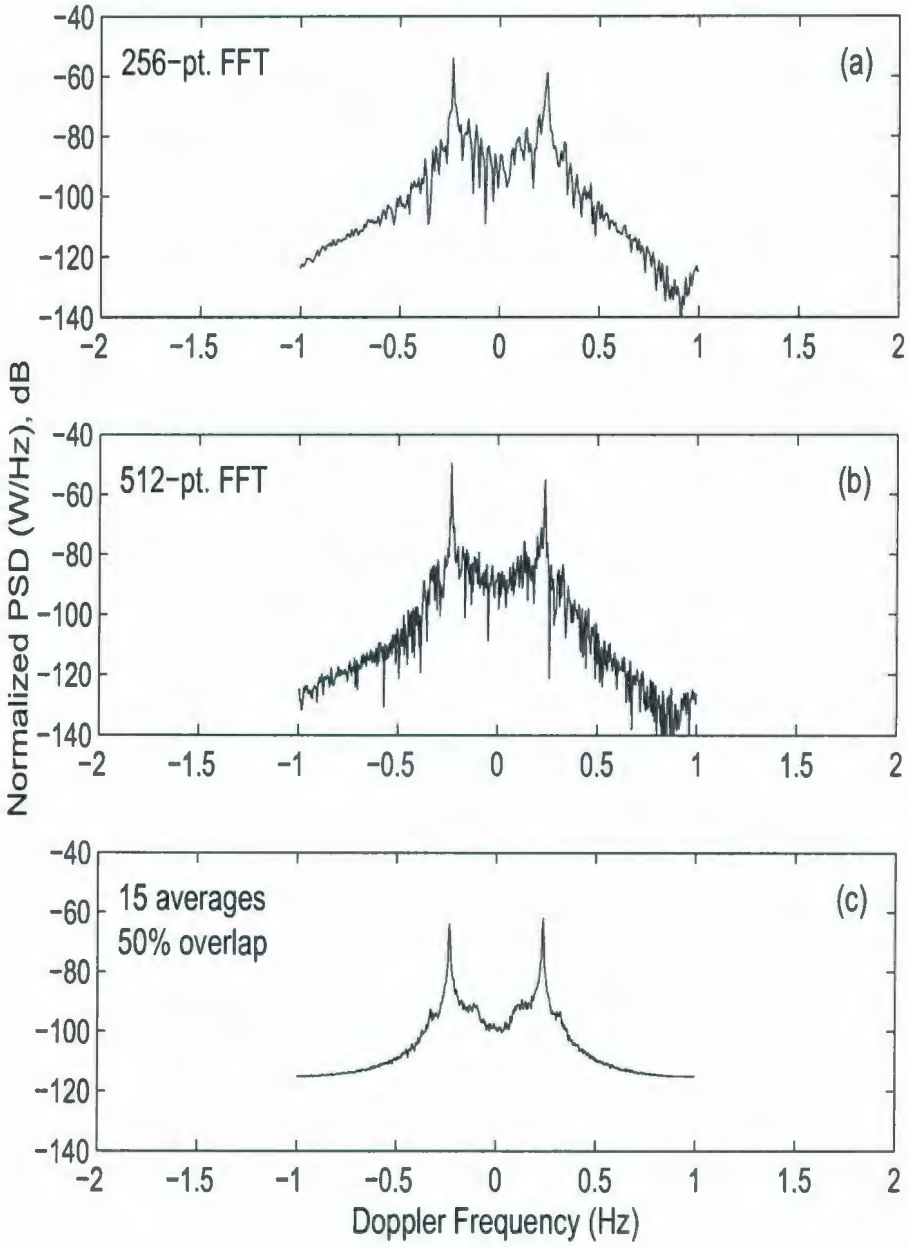

Figure 4.10: PSD of the clutter spectrum for the FM waveforms with $f_0 = 5$ MHz. Other parameters are as in Figure 4.9.

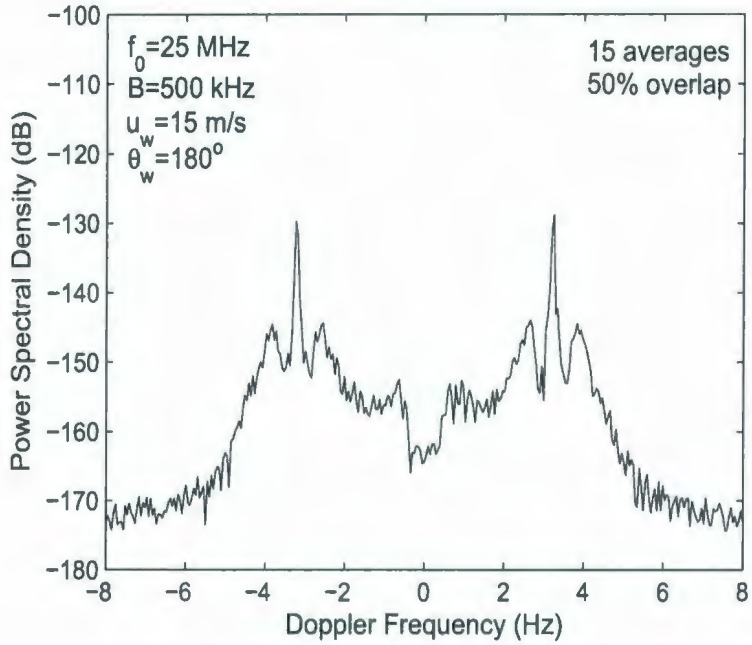

Figure 4.11: PSD of noisy signal for the FM waveforms with $f_0 = 25$ MHz.

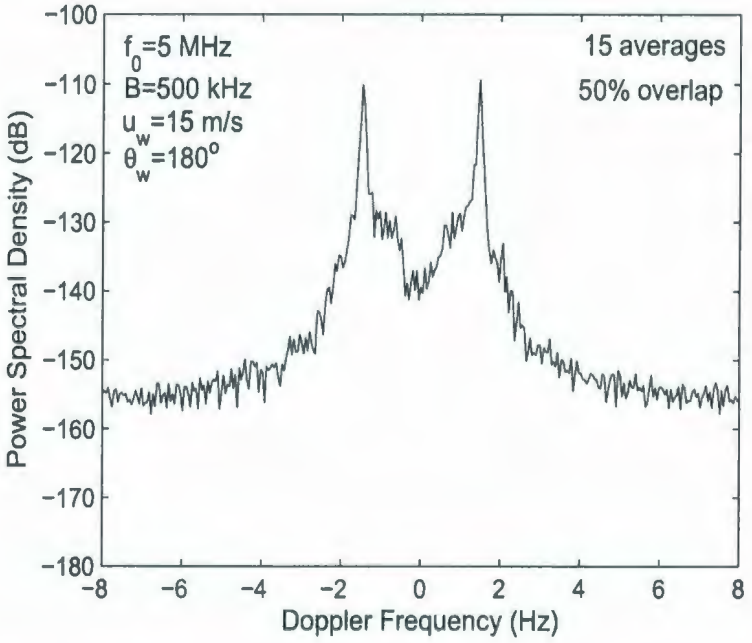

Figure 4.12: PSD of noisy signal for the FM waveforms with $f_0 = 5$ MHz.

be observed and these variations are at least one of the causes of the fluctuations of the centroid positions of the Bragg peaks. A numerical method should be invoked for detailed analysis as described in Chapter 2. Our goal is to determine the critical value ξ_c and critical number N_c for different Δ_{FFT}s as described in Section 2.6.2. For the FM waveform, the critical value ξ_c is defined the same as for the pulsed waveform because $\tau_0 = \frac{1}{B}$.

It may be recalled that the critical value ξ_c is a threshold for the fluctuations of the Bragg peaks being classed as significant. In Figure 4.15, the ξ_c values are plotted against the corresponding Δ_{FFT}s. The linear proportional relation between critical value and Δ_{FFT} is observed clearly. In Table 4.1, critical values are listed associated with Δ_{FFT}s. The definitions of the parameters in this table are the same as in Table 2.8. Detailed examples are given in Appendix B. Figure 4.16 is a plot of critical width of the Bragg region, β_c, as a function of Δ_{FFT}. As an example, in the European Radar Ocean Sensing (EuroROSE) experiment conducted in Lyngoy, Norway on April 3, 2000 (e.g., Wyatt *et al.* [12]), the WERA radar used an operating frequency of $f_0 = 27.65$ MHz and a sweep bandwidth of $B = 500$ kHz. The calculated ξ and β values are approximately 95.1 and 0.0097 Hz, respectively. According to Figures 4.15 and 4.16, theoretically speaking, if data are processed with a Δ_{FFT} finer than 0.0030 Hz, significant fluctuations of the Bragg peaks will occur. Figure 4.16 is used to calculate the N_c, the critical number of frequency points within the Bragg region, by the LSM fitting. The N_c is determined as 3.0, which is approximately equal to the value obtained for the pulsed waveform.

Figure 4.17 is a combined plot of Figures 2.35 and 4.16. This figure shows the similarity of the value N_c for the pulsed and FM waveforms.

4.4 Fluctuations of the Bragg Peaks for Field Data

Real HF radar data for the FMCW waveform have been obtained from the European Radar Ocean Sensing (EuroROSE) experiment conducted in Lyngoy, Norway on April 3, 2000 (e.g., Wyatt *et al.* [12]). The radar system was the Wellen Radar, or WERA developed at

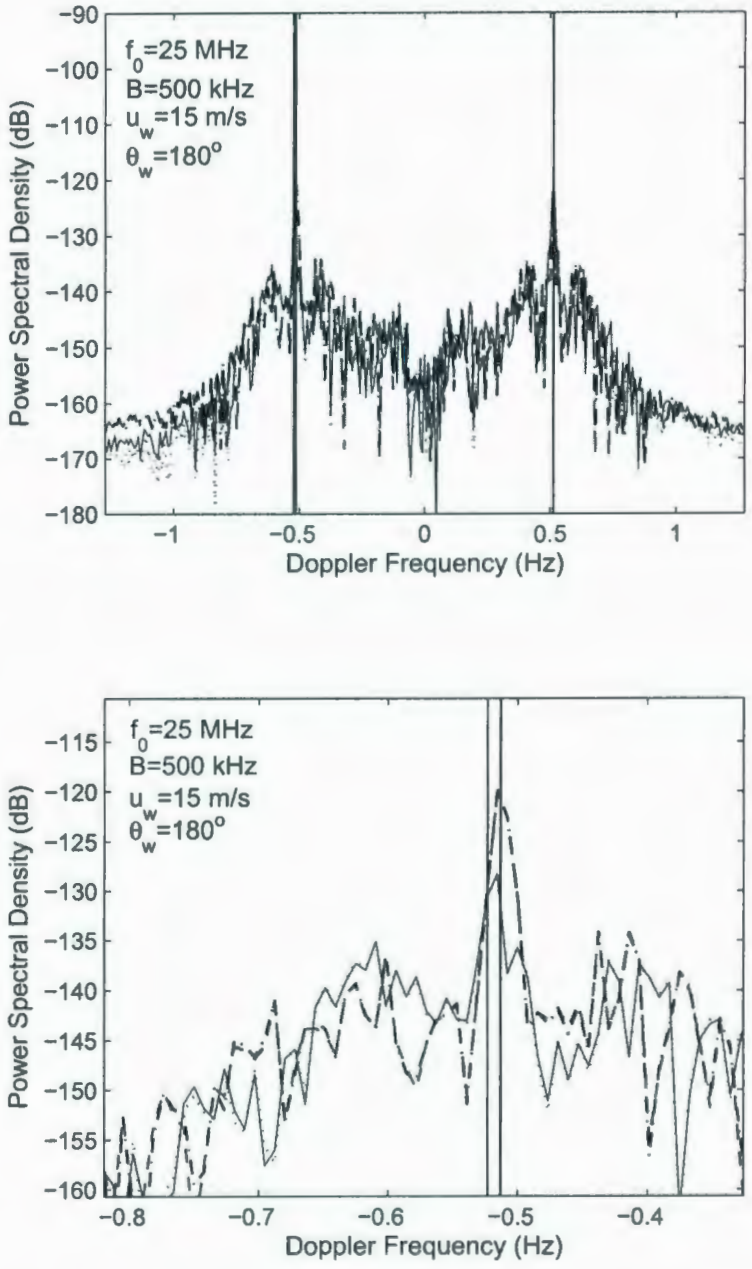

Figure 4.13: Fluctuations of the centroid positions for $f_0 = 25$ MHz and $B = 500$ kHz. Figure in the bottom is a closer look around the left-hand side peak region. The centroid positions are indicated as solid lines from top to bottom.

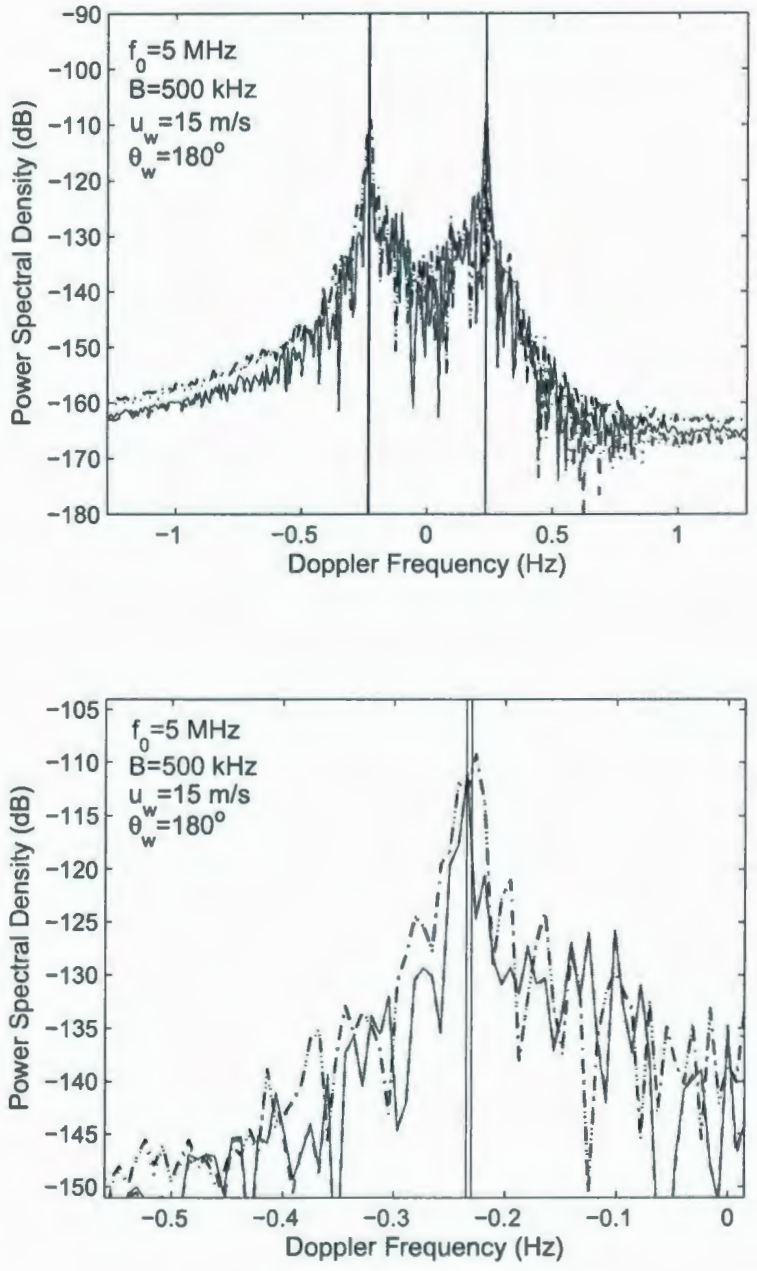

Figure 4.14: Fluctuations of the centroid positions for $f_0 = 5$ MHz and $B = 500$ kHz. Figure in the bottom is a closer look around the left-hand side peak region. The centroid positions are indicated as solid lines from top to bottom.

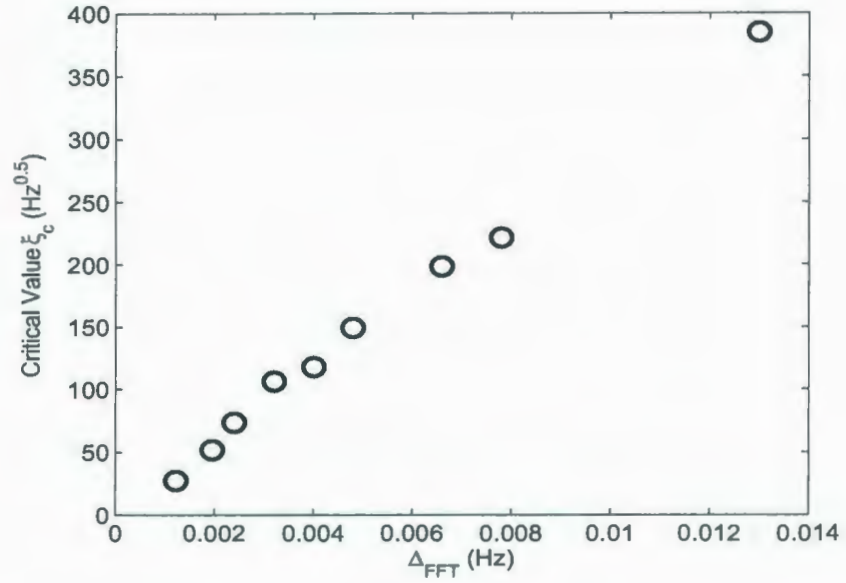

Figure 4.15: Critical value ξ_c as a function of Δ_{FFT}.

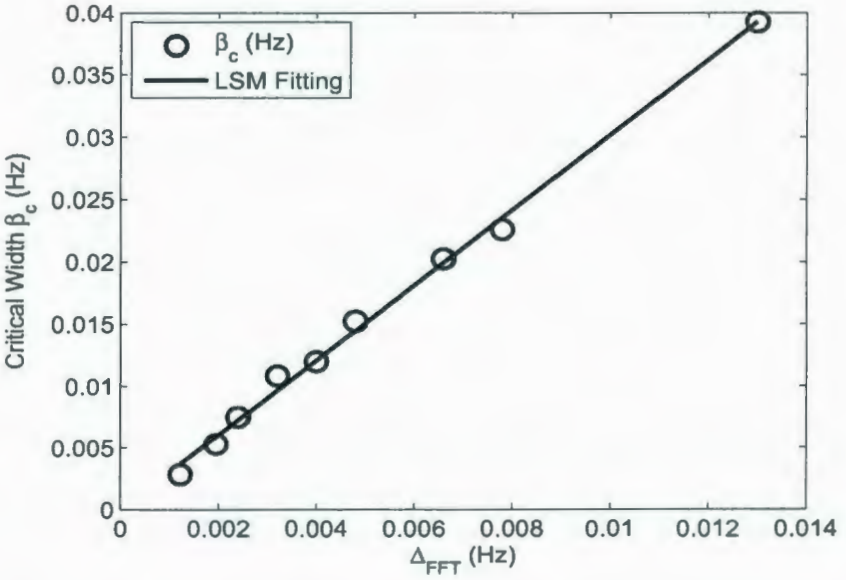

Figure 4.16: Critical width β_c as a function of Δ_{FFT} to determine N_c.

Table 4.1: Estimation of the critical values for different Δ_{FFT}s.

Δ_{FFT} (Hz)	ξ_c	β_c (Hz)	N_c
0.0130	384.52	0.0392	3.01
0.0078	221.30	0.0226	2.89
0.0066	198.22	0.0202	3.11
0.0048	149.33	0.0152	3.12
0.0040	117.38	0.0120	3.07
0.0032	106.13	0.0108	3.33
0.0024	73.430	0.0075	3.07
0.0020	51.76	0.0053	2.73
0.0012	27.57	0.0028	2.33

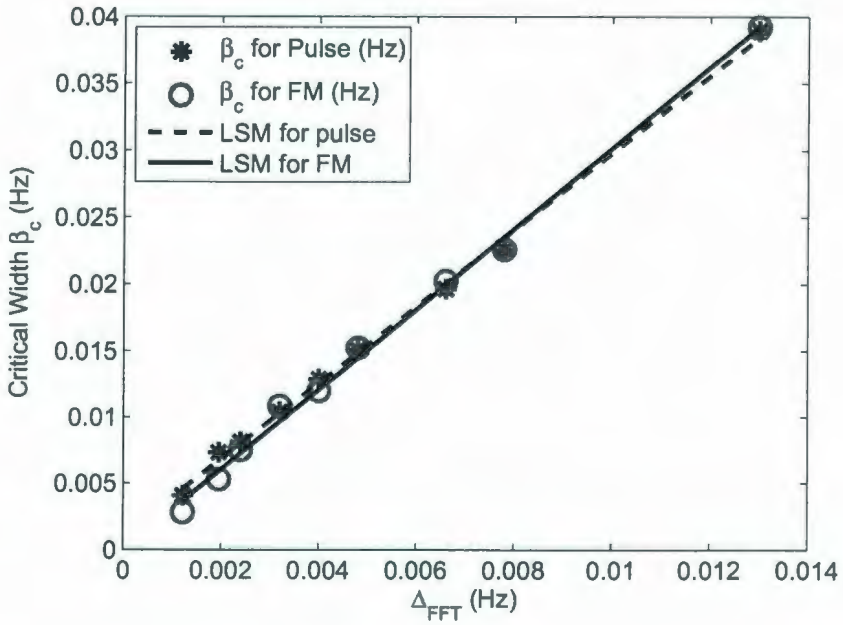

Figure 4.17: Comparison of Figures 2.35 and 4.16.

the University of Hamburg, Germany, and manufactured by Helzel Messtechnik GmbH. The radar receive antenna was a 16-element linear array. For the experiment considered here, the radar parameters include an operating frequency of $f_0 = 27.65$ MHz, a sweep bandwidth of $B = 500$ kHz, a sweep interval of $T_r = 0.26$ s, and, for the purposes of this work, we consider time series lengths of approximately 9 min, corresponding to 2048 sweep intervals for an ocean scattering patch width of 300 m. Figure 4.18 depicts the PSDs of the WERA data calculated using the periodogram method for (a) 512-point time series and (b) 13 averages of 512-point FFTs implemented with a 75% overlap. In Figure 4.18, the half Δ_{FFT} is 0.0038 Hz. The vertical dashed lines indicate the theoretical Bragg frequencies. The amplitude of the PSD has been normalized with respect to the maximum value of the spectrum. A rectangular window is used in creating the PSDs.

From Figure 4.18 we can see that during the radar measuring period for a specific scattering patch, the wind speed is strong enough to give a visibly clear second-order spectrum. The wind direction is approximately perpendicular to the radar look direction, making approximately the same amplitude for the left- and right-hand side Bragg peaks. There exists an apparent radial current underlying the wind wave moving away from the radar. Judging from the Doppler shifts of the Bragg peaks from their theoretical values, the radial current is approximately 11.9 cm/s [45].

Based on the parameters of the WERA data (operating frequency of 27.65 MHz, sweep bandwidth of 500 kHz, sweep interval of 0.26 s, and *median* value of external *noise figure* of $F_{am} = 21$ dB [79] in the radar location), time series with Gaussian white noise are simulated in a manner similar to those which gave rise to the plots in Figures 4.11 and 4.12. The resulting PSDs are calculated as for Figure 4.18 and the results are depicted in Figure 4.19. The significant similarity between simulated data and real data shown in Figure 4.19 gives a solid confirmation not only of the backscattering cross sections developed for the FMCW waveform in Chapter 3 in this thesis, but also of the simulation algorithm of the radar received signal developed by Pierson [7], and successfully used by Gill and Walsh [42] and Zhang and Gill [41].

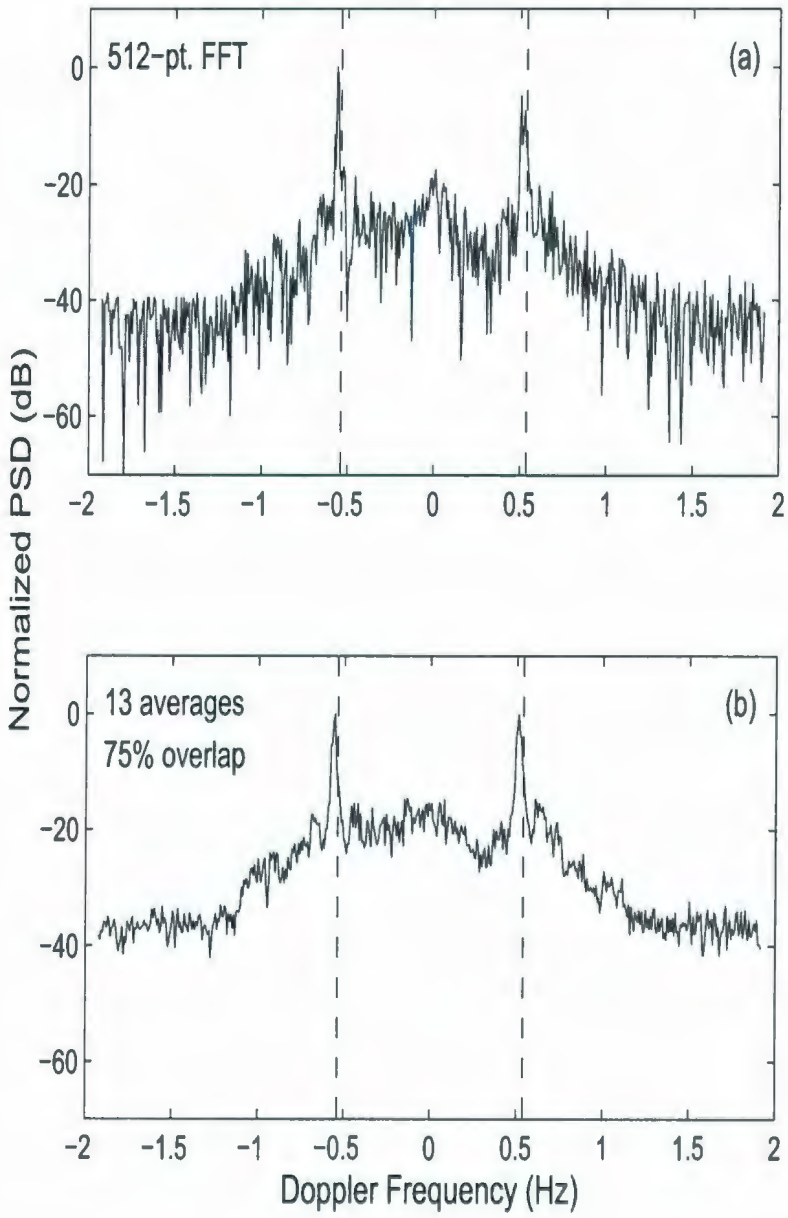

Figure 4.18: PSD calculated from WERA radar data for the FMCW waveform with $f_0 = 27.65$ MHz. The vertical dashed lines indicate the theoretical Bragg frequencies.

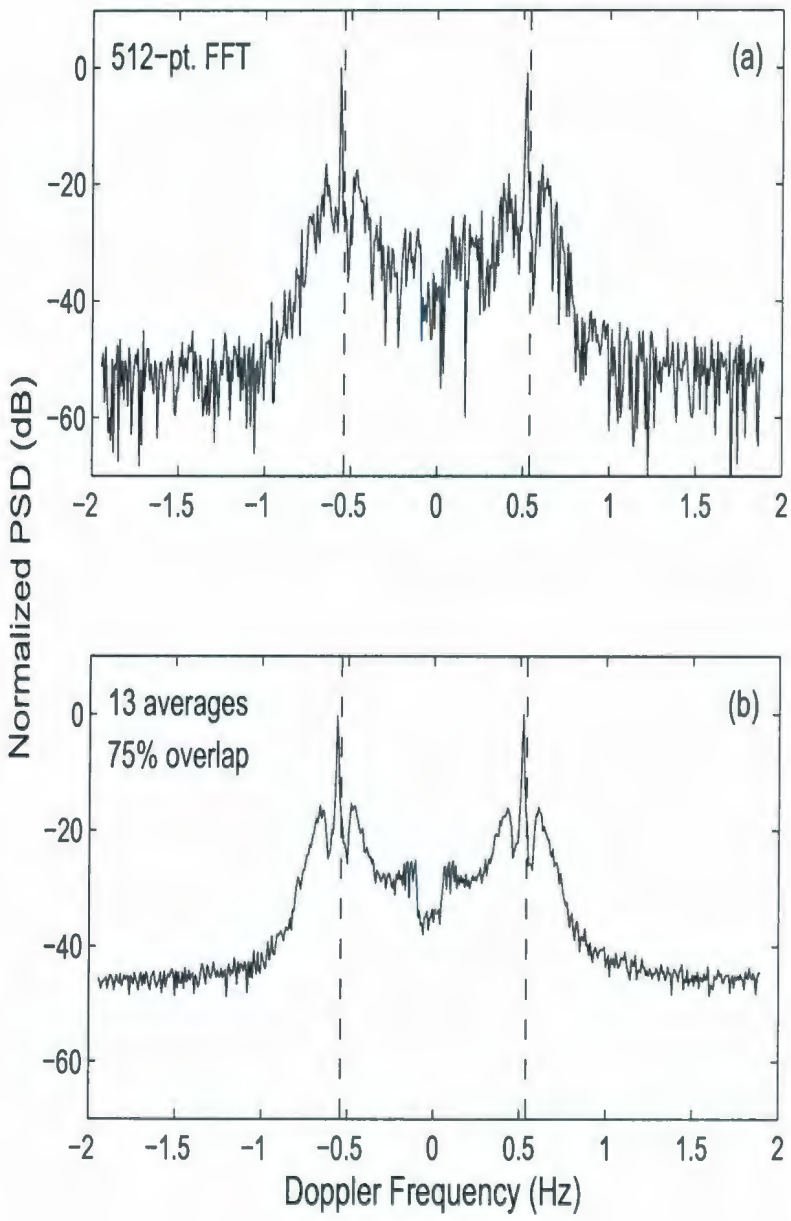

Figure 4.19: PSD calculated from simulated noisy data for the FMCW waveform with $f_0 = 27.65$ MHz. The vertical dashed lines indicate the theoretical Bragg frequencies.

In Figure 4.20, Figures 4.18(a) and 4.19(a) are depicted together for further comparison. In this figure, the underlying current in the real and simulated spectra has been removed. Two points need to be highlighted. Firstly, the amplitudes of the high-frequency tails are significantly different between two spectra. Specifically, the amplitude of the high-frequency tail is about 10 dB higher for the WERA field data as compared to the simulated spectrum. This amplitude difference may be accounted for in at least two ways. First, in the simulation, a *median* value of $F_{am} = 21$ dB is used for the external *noise figure*. However, in practice, the external noise will consist of atmospheric, galactic, and man-made noise components. Each type of noise may vary according to the location, operating frequency, and the time of day or the season of year. The galactic noise will even have an 11-year period depending on the solar activity. These practical conditions may not be specified exactly in data simulation. Another factor which could easily account for a difference between the simulated and actual noise floors, is that for the simulation only external Gaussian white noise is considered, while the real radar received signal may contain other types of noise, such as, but not limited to, system noise.

Another difference between the simulated and field spectra as seen from Figure 4.20 are the respective widths of the Bragg regions. This point is particularly interesting because it will influence the accuracy of current measurement. In Figure 4.20(b), we provide a closer look at the left-hand side Bragg region to detail the comparison. In accordance with the previous theoretical analysis, the width of the Bragg peaks will be determined sufficiently by operating frequency and sweep bandwidth (see equation (2.65) in Chapter 2). From equation (2.65), the theoretical width of the Bragg peaks in this case will be 0.0097 Hz. However, in Figure 4.20 for the simulated noisy spectrum, the width of the Bragg peaks is actually wider than the theoretical value due to contaminations of random noise. In this example, the widths of the Bragg peaks are estimated as 0.0300 Hz and 0.0526 Hz for the left and right regions, respectively. Also from Figure 4.20(b) we can see that the Bragg peak for the real Doppler spectrum is much wider (approximately double) than that for the simulated spectrum. A numerical estimation shows that the widths of the Bragg peaks

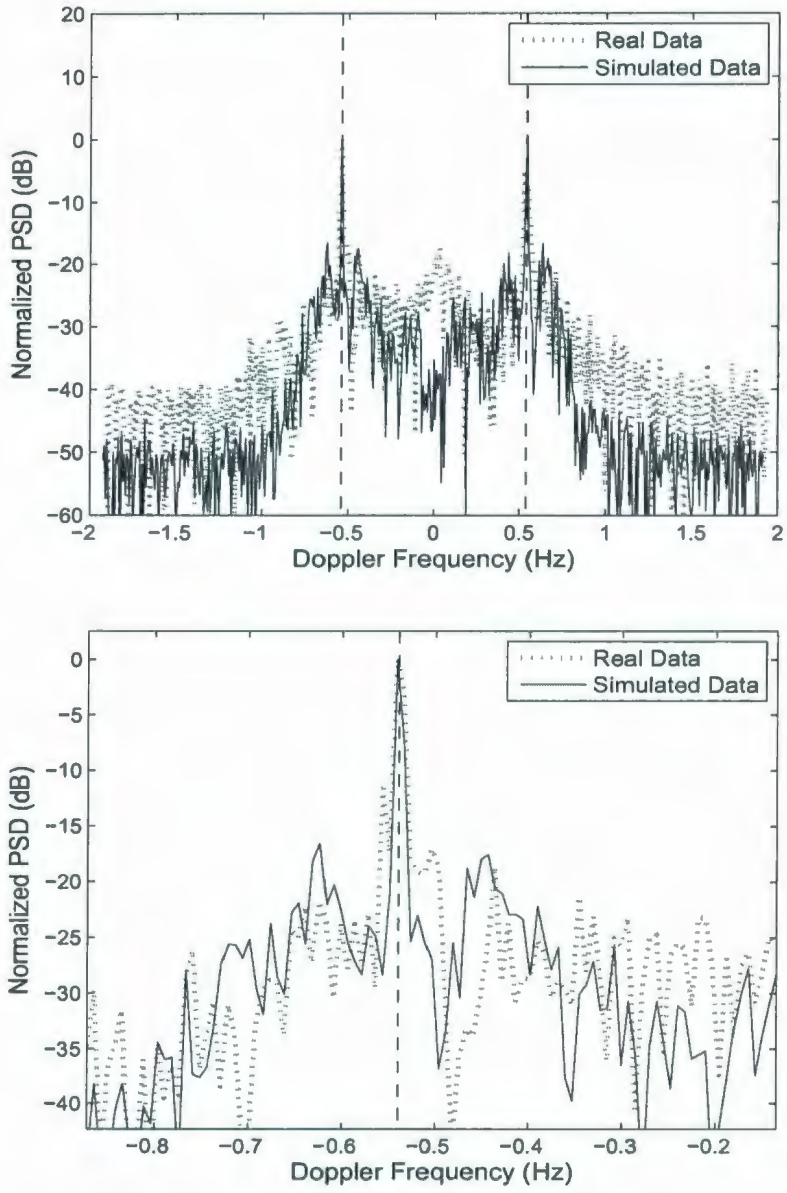

Figure 4.20: Comparison of the PSDs between the simulated noisy data (solid) and WERA (dotted) data. (b) is a closer look at the left-hand Bragg region of Figure (a). The vertical dashed lines indicate the theoretical Bragg frequencies

for the field data are 0.0751 Hz and 0.0826 Hz for the left and right regions, respectively. This phenomenon implies that in practice, there will be some other reasons that enlarge and/or disturb the Bragg region, such as current fluctuations on the scattering patch, which is a good topic for future work. Since we have shown by the simulated data for the pulsed and FM waveforms, roughly speaking, the wider Bragg region will result in more opportunity for the significant fluctuations to occur, it is reasonable to expect that in practical current measurement significant fluctuations are more likely to be observed than when using simulated data.

Figure 4.21 is an example plot of the fluctuations of the Bragg peaks for the WERA radar data used in Figure 4.18. In this figure, PSDs for the four consecutive 512-point time sequences are calculated and depicted. The respective centroid positions are obtained and are indicated by the vertical lines. In Figure 4.21(b) a closer look at the left-hand side Bragg region is depicted. This figure clearly shows the fluctuations of the Bragg peaks.

We are now in a position to quantitatively examine the significance of the Bragg fluctuations in the WERA field data. In order to evaluate the standard deviation of these fluctuations, a large number of events (512-point time series) is collected from WERA radar data that were obtained from six successive scattering patches. Since each scattering patch is 300 m in radial extent, six successive patches correspond to a 1800 m patch width over the ocean surface. We assume that in this big patch the ocean surface is statistically homogeneous spatially and stationary temporally (within 9 min). Figure 4.22 depicts the PSDs of the six successive patches. It is evident that the radial current is approximately fixed from subfigures (a) to (f), which are associated with the six scattering patches, arranged near to far, for one WERA look direction. In the investigation of the statistical properties of the fluctuations of the Bragg peaks, we may remove the radial currents from each spectrum since we are considering the random ocean phases that cause the fluctuations – not the currents.

The standard deviations for the 512-point time series segmented with different overlap percentages are tabulated in Table 4.2. From Table 4.2 we can see that despite the different

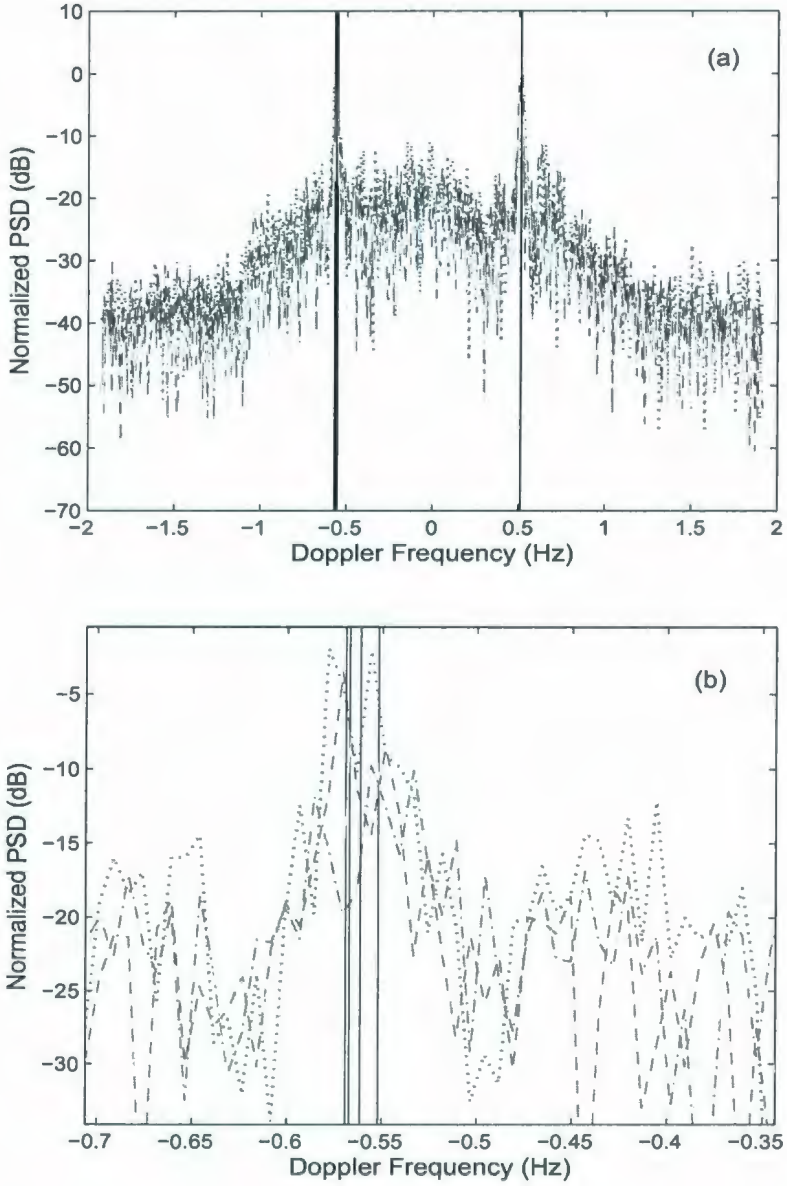

Figure 4.21: Fluctuations of the PSDs for WERA (dotted) data. (b) is a closer look at the left-hand Bragg region of Figure (a). The vertical lines indicate the centroid frequencies.

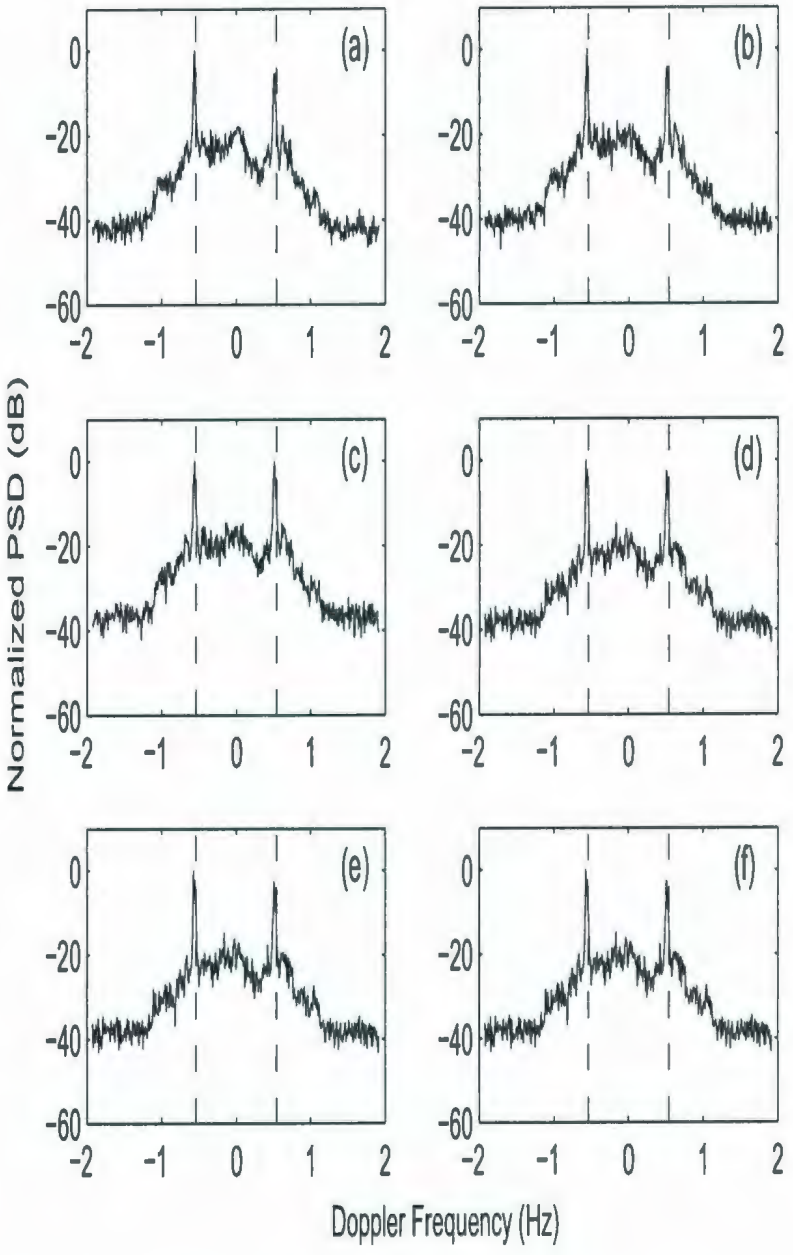

Figure 4.22: PSDs of WERA data for six successive scattering patches near to far from WERA radar. The vertical dashed lines indicate the theoretical Bragg frequencies.

Table 4.2: Standard deviations calculated from WERA data for different overlap percentages. N_{event} is number of statistical events. The definitions of "STDL" and "STDR", and V_L and V_R have been given in Table 2.1 in Chapter 2.

Overlap (%)	N_{event}	STDL (Hz)	V_L (cm/s)	STDR (Hz)	V_R (cm/s)
0	24	0.0053	5.8	0.0052	5.6
25	30	0.0049	5.3	0.0055	6.0
50	42	0.0048	5.2	0.0053	5.8
75	78	0.0050	5.4	0.0046	5.0
87.5	150	0.0056	6.1	0.0048	5.2

overlap percentages, the values of the standard deviations do not vary appreciably. It is evident that the standard deviations of the fluctuations of the Bragg peaks, left- and right-hand sides, are greater than the half Δ_{FFT}. Therefore, there are significant fluctuations of the Bragg peaks, which should be considered when developing error bars for surface currents derived from the field data. As an example, Figure 4.23 depicts the 75% overlap case. From Table 4.2, for this case the standard deviations of the Bragg centroids are seen to be 0.0050 Hz and 0.0046 Hz for the left and right Bragg peaks, respectively. These values correspond to a speed fluctuation of about 5 cm/s. However, the half Δ_{FFT} of 0.0038 Hz represents only a 4.2 cm/s resolution error. This difference is indicated by the widths between the two sets of dashed vertical lines in Figure 4.23. In Figure 4.23, standard deviations of the centroid positions to the left- (top) and right-hand (bottom) sides are depicted. The half Δ_{FFT}, 0.0038 Hz, corresponding to 4.2 cm/s in speed, is also plotted as a dotted line for illustration of significant fluctuations of the Bragg peaks.

4.5 Chapter Summary

In this chapter, the first- and second-order cross sections for the FM waveforms developed in Chapter 3 have been depicted and compared to cross sections for the pulsed waveform. Based on the cross section equations, PSDs for the radar received clutter have been

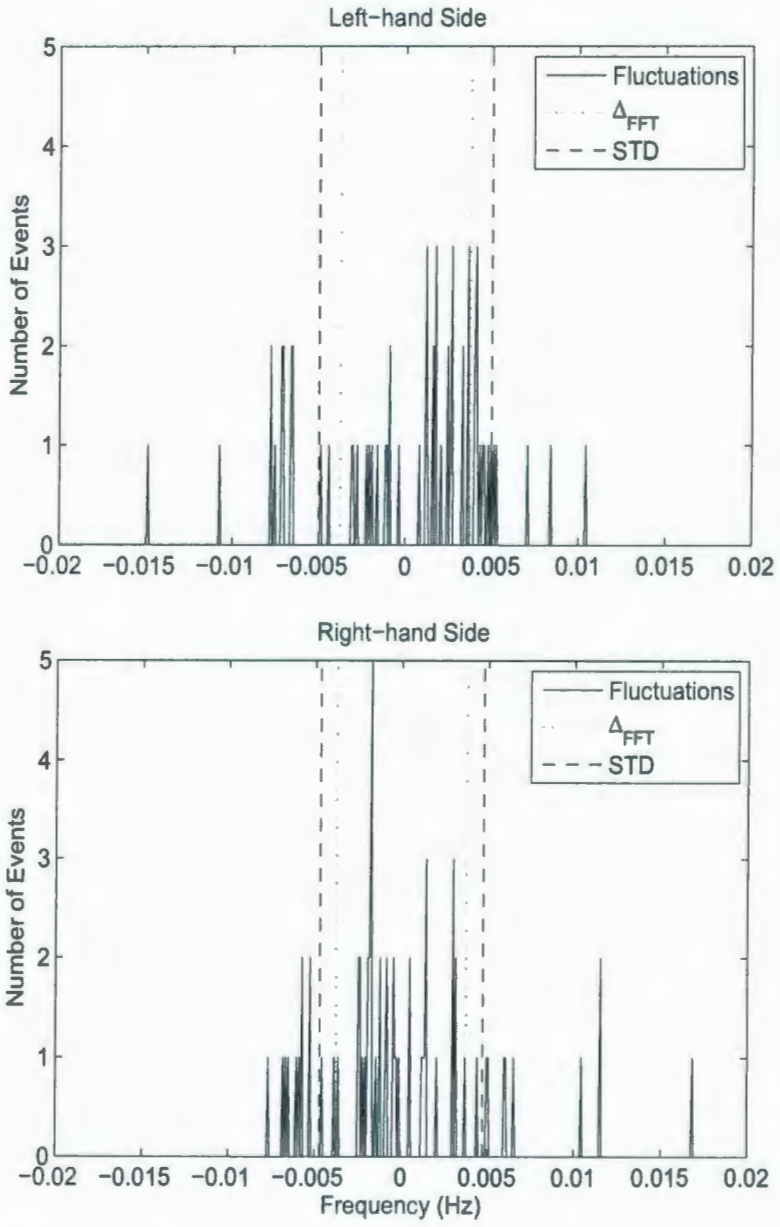

Figure 4.23: Histogram plot of the distribution of the centroid positions to (top) left- and (bottom) right-hand side Bragg peaks. Dashed lines are the standard deviations of the Bragg peaks. The Δ_{FFT} (dotted) is also plotted for comparison.

simulated and the Bragg fluctuation features have been investigated.

In the development of the second-order cross sections for the FM waveforms, only the hydrodynamic coupling effect has been considered. As for the pulsed waveform, the calculation of the Jacobian transformation will introduce a pair of singularities at $\pm\sqrt{2}\omega_{\mathrm{B}}^{m}$, where ω_{B}^{m} is the theoretical Bragg frequency for the FM waveforms. A comparison between the second-order cross sections for the pulsed and FM waveforms has shown that their singularities occur at the same positions.

The Bragg fluctuations for the FM waveforms have been examined following the same procedure as for the pulsed waveform in Chapter 2. A numerical scheme has been used to determine the critical frequency number, N_c, within the Bragg region for the FM waveforms, which can be used to examine whether the significant fluctuations of the Bragg peaks will occur or not. The results have shown that this critical number is approximately equal to that for the pulsed waveform. This result may lead to a postulate that the critical number for the occurrence of significant fluctuations is independent of the transmitting waveform.

Power spectral densities for the WERA field data have been calculated and depicted. Favourable comparisons between the field data and the simulations provide additional verification of the integrity of the cross section models developed here.

Additionally, the fluctuations of the Bragg peaks for the WERA field data has been examined and the occurrence of the significance has been observed. Since field data contain additional variability from the environment and system, relatively wider Bragg regions than those seen in simulated data would be obtained, and more significant fluctuations would likely be observed. A well design field experiment is desired to quantify the details.

Chapter 5

Summary and Suggestions

5.1 Summary

The whole research work consists of two major parts. The first is an investigation of the Bragg fluctuations when pulsed HF radar is employed to measure the ocean surface, which is assumed to be a Gaussian process. The second part includes a development of HF radar backscatter cross sections and an investigation of the Bragg fluctuation properties for the frequency modulated (FM) waveforms. Both of these initiatives have been accomplished and are intended to improve models which presently exist for the application of HF radar to ocean surface current measurements and for related development, including the measurement of wave and wind parameters and the detection of hard targets.

To tackle the first problem, lengthy time series of the radar received electric field for various radar operating frequencies and pulse widths are simulated based on existing cross section expressions. These time series are segmented into equal length consecutive subsequences and the power spectral densities (PSDs) for these subsequences are calculated as periodograms. The centroids of the Bragg peaks are located and histogram plots are used to depict the distributions of these centroids and their standard deviations are compared to the corresponding FFT resolutions (Δ_{FFT}s). This procedure is undertaken to show that the analysis adequately models the existence of fluctuations in the first-order return

that is commonly observed in field data. It has been shown that the standard deviations of the Bragg fluctuations vary with operating frequency and pulse width and in some cases these fluctuations are more significant than the corresponding Δ_{FFT}s. Equivalently, the fluctuations are a function of the width of the Bragg region in the Doppler spectra.

After reviewing the electric field equation of the radar return, it has been determined that the Bragg fluctuations are a consequence of the randomness of the ocean surface. The sources of randomness are the random phases, which are uniformly distributed between 0 to 2π (e.g. Pierson [7]) and which are associated with each Fourier component of the surface. The field equation is then developed in such a way that the focus is placed on the behavior of these random phases. As a proof of concept, the original field equation is simplified by taking only two adjacent ocean wave frequency components into consideration. It has been shown that the fluctuations in the resulting signal are the consequence of a cross term incorporating the interactions between the two components. The simplified model has been extended to a general case in which many frequencies are involved and many cross terms with randomness are present. The distribution of the summation of these cross terms has been examined at some specific frequencies and the results have been depicted by histogram plots. Comparison with a chi-square distribution with two degrees of freedom has shown that there are distinct similarities.

Extending the previous deliberations, the next step of the first research portion has been carried out to describe the distribution of the Bragg fluctuations. Barrick and Snider [8] achieved a Gaussian distribution with the assumption that there are many frequency points within the Bragg region. This method has been checked and the result is negative. The reason has been recognized that the assumptions of large scattering patch (several tens of kilometres) used by Barrick and Snider does not apply in this research. However, a numerical scheme has been used to check the dependence of the standard deviation of the Bragg fluctuations with respect to the width of the Bragg region. A linear connection between them has been observed for a fixed Δ_{FFT}. Additionally, there are different "critical values ξ_c" associated with different Δ_{FFT}s. These ξ_c values are the thresholds that when

the combination of radar frequency and pulse width exceeds them, or $\xi = \tau_0^{-1} f_0^{-\frac{1}{2}} \geq \xi_c$, the Bragg fluctuations will be significant. The critical value ξ_c has been recognized to be linearly proportional to the Δ_{FFT}. This conclusion implies that if the radar operating frequency and the transmitted pulse width are known, an optimal choice of Δ_{FFT} will avoid significance of the Bragg fluctuations, and *vice versa*. When ξ_c is multiplied by a factor $\sqrt{\frac{4\pi g}{c}}$, the product will be the "critical width" of the Bragg region β_c. β_c is also linearly proportional to the Δ_{FFT}, which means that when β_c is divided by the corresponding Δ_{FFT}, the ratio will be a constant, which is denoted as N_c. N_c is actually the critical number of the frequency points within the Bragg region. A physical explanation of N_c is that no matter how the radar parameters and the Δ_{FFT} are chosen, if the number of the frequency points within the Bragg region exceeds N_c, significant Bragg fluctuations will always occur. N_c has been obtained as 3.0 based on a numerical examination.

In the second part of this research, the radar cross sections have been developed under the condition that the radar transmitting waveforms are linear FM waveforms, i.e. frequency modulated continuous wave (FMCW) and frequency modulated interrupted continuous wave (FMICW). The waveform equations have been inserted into the electric field equations to obtain the temporal field expressions. In this case, the radar operating frequency is no longer time independent as for the pulsed waveform, but a function of time within a frequency sweep interval. The resulting electric field equations therefore have been modified by a time-varying term. The first-order radar backscatter cross sections for the FM waveforms show that after appropriate approximation, Bragg peaks appear at the same Doppler frequency positions as that for the pulsed waveform with the same operating frequency. In addition to these first-order results, the second-order cross sections for the FM waveforms have been developed, but for the hydrodynamic coupling condition only. The reason is that the electromagnetic portion of the second-order scatter is significantly smaller than the hydrodynamic portion in the vicinity of the Bragg peak regions, and will not influence the result of the Bragg fluctuations. As an intermediate result, the range spectra for the FM waveforms have also been extracted. For an individ-

ual scattering patch over the ocean surface, ambiguity peaks have been observed in the range spectrum for the FMICW waveform. Mathematically, this is due to the fact that the range is indicated by the peaks that are defined by a $\frac{\sin}{\sin}$ function, which inherently has multiple peaks at repeating deterministic positions.

All the cross sections for the FM waveforms have been depicted in Chapter 4. The properties of the cross sections, such as the positions of the Bragg peaks for the first-order cross sections and singularities that occur in the second-order cross sections, have been explored.

The behavior and properties of the Bragg fluctuations for the FM waveforms have been examined. The critical value ξ_c and critical number N_c for the FM waveforms have been obtained by a numerical method analogous to that for the pulsed waveform. The critical number has been shown to be approximately equal to that for the pulsed waveform. A conclusion that the critical number is essentially independent of the choice of waveform has been achieved.

The objectives of obtaining an appropriate model to describe the fluctuations of the Bragg peaks of the received Doppler spectrum for monostatic HF ground wave radar with pulsed and frequency modulated transmitted signals have been accomplished. The simulations for the FMCW waveform have shown favorable agreement with field data obtained using a high bandwidth WERA radar operating in the upper HF band. It is expected that the model developed here will provide a fundamental starting point for investigating the statistical properties of the HF radar received signals. Furthermore, when the results for pulsed and FMICW are similarly verified with field data, the outputs of this thesis will help enhance the capabilities of HF radar as a powerful remote sensing tool, especially from the perspective of properly constructing error bars for the various measurements. It is expected that the results will also help to improve clutter suppression algorithms for hard-target detection when HF radar is deployed along the coastline to monitor a nation's exclusive economic zone.

5.2 Suggestions for Future Work

Based on the analyses in this thesis, several points may be suggested for future experimental and research work.

First, although the algorithm shows reasonable and encouraging results, it still needs to be checked more extensively against real data. For example, the critical value ξ_c may be obtained from a well designed experiment with several combinations of radar frequencies and pulse widths. It should be pointed out that the values obtained from real data may be variable due to other phenomena that cause broadening of the Bragg region (such as external noise, current variability, and ionospheric instabilities), and in a real Doppler spectrum, the width of the Bragg peaks may, for these reasons, be larger than the theoretical width indicated by the squared sinc function appearing in the derived cross sections. Gill and Walsh [42] (see also [65]) provides a model of external noise for the pulsed radar waveform as a zero-mean Gaussian process. Examples of time series have been simulated and PSDs have been depicted in Chapter 4. However, high bandwidth field data for the pulsed waveform are desired to check the results.

As noted, for the case of the FMCW waveform, a comparison of simulated spectra with WERA field data has provided partial but encouraging results. However, experimentation dedicated to further verification of the models should be conducted. Such investigations should incorporate a variety of waveform and operating parameters.

In our cross section development for the FM waveforms, the second-order backscatter cross section arising from double scattering (the so-called electromagnetic second-order) has been ignored for the sake of simplicity and because it would not significantly influence the problem addressed here. However, it should be worked out because it may reveal important physical processes appearing in the Doppler spectra at positions appreciably removed from the Bragg region. For example, there is no doubt that the e-m coupling process will introduce singularities, such as the well known "corner reflector" condition discussed by Barrick [19] and Srivastava [5] for monostatic operation. This effect might

significantly influence hard-target detection if HF radar were deployed for the purpose of surveillance.

Due to the widespread deployment of HF radar systems with FM waveforms, it is desirable to develop the bistatic cross sections for these waveforms. This process should be facilitated by the fact that similar work has been already done for the pulsed HF radar waveforms (e.g. Walsh and Dawe [34], Gill and Walsh [35]). Furthermore, with availability of the cross sections for the FM waveforms, an algorithm to extract the ocean surface wave spectrum can be developed following the methods that have already been developed by previous investigators (e.g. Gill and Walsh [39], Howell and Walsh [40], Zhang and Gill [41]).

With the further modeling and experimentation suggested here it is to be expected that HF radar, as a marine remote sensing tool, will become increasingly important.

Bibliography

[1] K. Hasselmann, "Determination of ocean wave spectra from Doppler return from sea surface," *Nature Physical Science*, vol. 229, pp. 16–17, 1971.

[2] D. Crombie, "Doppler spectrum of sea echo at 13.56 Mc./s.," *Nature*, vol. 175, pp. 681–682, 1955.

[3] B. Kinsman, *Wind Waves.* New York: Dover Publications Inc., 1984.

[4] D. Barrick, "First-order theory and analysis of MF/HF/VHF scatter from the sea," *IEEE Transactions on Antennas and Propagation*, vol. 20, pp. 2–10, 1972.

[5] S. Srivastava, *Analysis of HF scattering from an ocean surface: An alternative approach incorporating a dipole source.* PhD thesis, Memorial University of Newfoundland, St. John's, Newfoundland, 1984.

[6] J. Walsh, R. Howell, and B. Dawe, "Model development for evaluation studies of ground wave radar," Contract Report 90-C14, Centre for Cold Ocean Resources Engineering, 1990. (Prepared for Department of National Defence, Government of Canada, DSS Contract Number W7714-8-5655/01-SS).

[7] W. Pierson, "Wind generated gravity waves," *Advances in Geophysics*, vol. 2, pp. 93–178, 1955.

[8] D. Barrick and J. Snider, "The statistics of HF sea-echo Doppler spectra," *IEEE Transactions on Antennas and Propagation*, vol. 25, pp. 19–28, 1977.

[9] D. Barrick, "Extraction of wave parameters from measured HF radar sea-echo Doppler spectrum," *Radio Science*, vol. 12, no. 3, pp. 415–424, 1977.

[10] J. Zhang, E. Gill, D. Green, and J. Walsh, "Examination of fluctuations in the Bragg peaks under the assumption of a stationary Gaussian process and other recent developments," in *Presented at The 5th International Radiowave Oceanography Workshop, Costanoa, California*, vol. 1, pp. 153–158, 2005.

[11] J. Walsh and E. Gill, "An analysis of the scattering of high frequency electromagnetic radiation from rough surfaces with application to pulse radar operating in backscatter mode," *Radio Science*, vol. 35, no. 06, pp. 1337–1359, 2000.

[12] L. R. Wyatt, J. J. Green, K. W. Gurgel, J. C. N. Borge, K. Reichert, K. Hessner, H. Gnther, W. Rosenthal, O. Saetra, and M. Reistad, "Validation and intercomparisons of wave measurements and models during the eurorose experiments," *Coastal Engineering*, vol. 48, pp. 1–28, 2003.

[13] J. W. Strutt, *The Theory of Sound*, vol. 2. New York: Macmillan, 1945.

[14] Antenna Standards Committee of the IEEE Antennas and Propagation Society, The Institute of Electrical and Electronics Engineers Inc., New York, *IEEE Standard Definitions of Terms for Antennas*, 145-1983 ed., 1983.

[15] S. Rice, "Reflection of electromagnetic waves from a slightly rough surface," in *Theory of Electromagnetic Waves* (K. Kline, ed.), pp. 351–378, New York: Interscience, 1951.

[16] W. Peake, "Theory of radar return from terrain," in *IRE National Convention Record*, vol. 7, pp. 27–41, 1959.

[17] G. Valenzuela, "Depolarization of EM waves from slightly rough surfaces," *IEEE Transactions on Antennas and Propagation*, vol. 15, pp. 552–557, 1967.

[18] D. Barrick, "Theory of HF and VHF propagation across the rough sea, 1 and 2," *Radio Science*, vol. 6, no. 5, pp. 517–533, 1971.

[19] D. Barrick, "Remote sensing of sea state by radar," in *Remote Sensing of the Troposphere* (V. Derr, ed.), ch. 12, pp. 1–46, Washington, DC: U.S. Government Printing Office, 1972.

[20] R. Kodis, "A note on the theory of scattering from an irregular surface," *IEEE Transactions on Antennas and Propagation*, vol. 14, no. 1, pp. 77–82, 1966.

[21] D. Barrick and E. Bahar, "Rough surface scattering using specular point theory," *IEEE Transactions on Antennas and Propagation*, vol. 29, no. 1, pp. 798–800, 1981.

[22] G. Brown, "Backscattering from a Gaussian-distributed perfectly conducting rough surface," *IEEE Transactions on Antennas and Propagation*, vol. 26, no. 1, pp. 472–482, 1978.

[23] G. Brown, "Application of the integral equation method of smoothing to random surface scattering," *IEEE Transactions on Antennas and Propagation*, vol. 32, no. 1, pp. 1308–1312, 1984.

[24] E. Bahar, "Radio wave propagation in stratified media with nonuniform boundaries and varying electromagnetic parameters — full-wave analysis," *Canadian Journal of Physics*, vol. 50, no. 24, pp. 3132–3142, 1972.

[25] E. Bahar and G. Rajan, "Depolarization and scattering of electromagnetic waves by irregular boundaries for arbitrary incident and scatter angles — full-wave solutions," *IEEE Transactions on Antennas and Propagation*, vol. 27, no. 2, pp. 214–225, 1979.

[26] D. Barrick, J. Headrick, R. Bogle, and D. Crombie, "Sea backscatter at HF: Interpretation and utilization of the echo," in *Proceedings of the IEEE*, vol. 62, pp. 673–680, 1974.

[27] B. Lipa and D. Barrick, "Analysis methods for narrow-beam high-frequency radar sea echo," Technical Report ERL 420-WPL 56, National Oceanic and Atmospheric Administration, U.S. Department of Commerce, 1982.

[28] B. Lipa and D. Barrick, "Extraction of sea state from HF radar sea echo: Mathematical theory and modeling," *Radio Science*, vol. 21, no. 1, pp. 81–100, 1986.

[29] L. R. Wyatt, "The measurement of the ocean wave directional spectrum from HF radar Doppler spectra," *Radio Science*, vol. 21, no. 3, pp. 478–485, 1986.

[30] B. Lipa, "Derivation of directional ocean-wave spectra by integral inversion of second-order radar echoes," *Radio Science*, vol. 12, no. 3, pp. 425–434, 1977.

[31] D. Barrick and B. Lipa, "A compact transportable HF radar system for directional coastal wavefield measurements," in *Ocean Wave Climate* (M. D. Earle and A. Malahoff, eds.), pp. 129–152, New York: Plenum, 1979.

[32] D. Barrick and B. Lipa, "The second-order shallow water hydrodynamic coupling coefficient in interpretation of HF radar sea echo," *IEEE Journal of Oceanic Engineering*, vol. 11, no. 2, pp. 310–315, 1986.

[33] J. Walsh, "On the theory of electromagnetic propagation across a rough surface and calculations in the VHF region," OEIC Report N00232, Memorial University of Newfoundland, St. John's, Newfoundland, 1980.

[34] J. Walsh and B. Dawe, "Development of a model for the first-order bistatic ocean clutter radar cross section for ground wave radars," contract report, Northern Radar Systems Limited, 1994. (Prepared for the Defence Research Establishment Ottawa, Department of National Defence, Government of Canada, DSS Contract Number W7714-1-9565/01-ST).

[35] E. Gill and J. Walsh, "High-frequency bistatic cross sections of the ocean surface," *Radio Science*, vol. 36, no. 06, pp. 1459–1475, 2001.

[36] E. Gill, W. Huang, and J. Walsh, "On the development of a second-order bistatic radar cross section of the ocean surface: A high frequency result for a finite scattering patch," *IEEE Journal of Oceanic Engineering*, vol. 31, no. 4, pp. 740–750, 2006.

[37] P. Bobby, "Estimation of vector surface currents beyond the region of overlap of dual-site HF radar: An implementation of the continuity equation," Master's thesis, Memorial University of Newfoundland, St. John's, Newfoundland, 2003.

[38] Q. Jin, "An algorithm for the extraction of ocean surface current velocity from bistatic HF groundwave radar data — A simulation," Master's thesis, Memorial University of Newfoundland, St. John's, Newfoundland, 2007.

[39] E. Gill and J. Walsh, "Extraction of ocean wave parameters from HF backscatter received by a four-element array: Analysis and application," *IEEE Journal of Oceanic Engineering*, vol. 17, no. 4, pp. 376–386, 1992.

[40] R. Howell and J. Walsh, "Measurement of ocean wave spectra using narrow beam HF radar," *IEEE Journal of Oceanic Engineering*, vol. 18, no. 3, pp. 296–305, 1993.

[41] J. Zhang and E. Gill, "Extraction of ocean wave spectra from simulated noisy bistatic high frequency radar data," *IEEE Journal of Oceanic Engineering*, vol. 31, no. 4, pp. 779–796, 2006.

[42] E. Gill and J. Walsh, "A combined clutter and noise model appropriate to the operation of high frequency pulsed doppler radar in regions constrained by external noise limitations," *Radio Science, in press.*

[43] R. Stewart, *Introduction to Physical Oceanography.* Texas: Texas A&M University, 2002.

[44] D. Crombie, "Resonant backscatter from the sea and its application to physical oceanography," in *Oceans'72 Conf. Rec.*, (IEEE Publ. No. 72CHO 660-1 OCC), pp. 173–179, 1972.

[45] R. Stewart and J. Joy, "HF radio measurements of surface currents," *Deep-Sea Research*, vol. 21, pp. 1039–1049, 1974.

[46] D. M. Fernandez, *High-frequency radar measurements of coastal ocean surface currents.* PhD thesis, Stanford University, California, USA, 1993.

[47] J. G. Proakis, *Algorithms for Statistical Signal Processing.* New Jersey: Prentice-Hall, 2002.

[48] D. Barrick, "Accuracy of parameter extraction from sample-averaged sea-echo Doppler spectra," *IEEE Transactions on Antennas and Propagation*, vol. AP-28, no. 1, pp. 1–11, 1980.

[49] K. Hickey, "Ocean surface current estimation using a long-range, single-station, high-frequency ground wave radar," Master's thesis, Memorial University of Newfoundland, St. John's, Newfoundland, 1999.

[50] D. Barrick, "FM/CW radar signal and digital processing," Technical Report ERL 283-WPL 26, National Oceanic and Atmospheric Administration, U.S. Department of Commerce, 1973.

[51] R. H. Khan and D. K. Mitchell, "Waveform analysis for high-frequency FMICW radar," in *IEE Proceedings-F*, vol. 138, pp. 411–419, 1991.

[52] R. Khan, B. Gamberg, D. Power, J. Walsh, B. Dawe, W. Pearson, and D. Millan, "Target detection and tracking with a high frequency ground wave radar," *IEEE Journal of Oceanic Engineering*, vol. 19, no. 4, pp. 540–548, 1994.

[53] D. Barrick, "Ocean surface current mapped by radar," *Science*, vol. 198, pp. 138–144, 1977.

[54] M. Heron, P. Dexter, and B. McGann, "Parameters of the air-sea interface by high frequency ground wave HF Doppler radar," *Aust. J. Mar. Freshwater Res.*, vol. 36, pp. 655–670, 1985.

[55] H. Takeoka, Y. Tanaka, Y. Ohno, Y. Hisaki, A. Nadai, and H. Kuroiwa, "Observation of the kyucho in the Bungo Channel by HF radar," *J. Oceanogr.*, vol. 51, pp. 699–711, 1995.

[56] Z. Yang, S. Wu, J. Hou, B. Wen, and Z. Shi, "Some problems in the general scheme for HF ground wave radar engineering," *Journal of Wuhan University (Natural Science Ed.)*, vol. 47, no. 5, pp. 513–518, 2001.

[57] D. Prandle, S. Loch, and R. Player, "Tidal flow through the straits of Dover," *J. Phys. Oceanogr.*, vol. 23, pp. 23–37, 1992.

[58] E. Shearman and M. Moorhead, "PISCES: a coastal ground wave HF radar for current, wind and wave mapping to 200 km ranges," in *IEEE International Geoscience and Remote Sensing Symposium 1988 (IGARSS'88)*, pp. 773–776, 1988.

[59] D. Paduan and L. Rosenfeld, "Remotely sensed surface currents in Monterey Bay from shore-based HF radar (Coastal Ocean Dynamics Applications Radar)," *J. Geophys. Res.*, vol. 101, pp. 20669–20686, 1996.

[60] K. Gurgel, G. Antonischki, H. Essen, and T. Schlick, "Wellen radar (WERA), a new ground wave based HF radar for ocean remote sensing," *Coastal Engineering*, vol. 37, pp. 219–234, 1999.

[61] C. Teague, "Multifrequency HF radar observations of currents and current shears," *IEEE Journal of Oceanic Engineering*, vol. 11, no. 2, pp. 258–269, 1986.

[62] C. Teague, J. Vesecky, and P. Hansen, "Multifrequency coastal radar system overview," in *Presented at the 1st International Radiowave Oceanography Workshop, Miami, FL*, pp. 36–41, 2003.

[63] M. Six, J. Parent, A. Bourdillon, and J. Delloue, "A new multibeam receiving equipment for the Valensole skywave HF radar: description and applications," *IEEE Transactions on Geoscience and Remote Sensing*, vol. 34, no. 3, pp. 708–719, 1996.

[64] J. Walsh, B. Dawe, and S. Srivastava, "Remote sensing of icebergs by ground wave Doppler radar," *IEEE Journal of Oceanic Engineering*, no. 11, pp. 276–284, 1986.

[65] E. Gill, *The scattering of high frequency electromagnetic radiation from the ocean surface: An analysis based on a bistatic ground wave radar configuration.* PhD thesis, Memorial University of Newfoundland, St. John's, Newfoundland, 1999.

[66] M. Tucker, *Waves in Ocean Engineering.* New York: Ellis Horwood, 1991.

[67] W. Pierson and L. Moskowitz, "A proposed spectral form for fully developed seas based upon the similarity theory of S.A. Kitaigorodskii," *J. Geophys. Res.*, vol. 69, no. 24, pp. 5181–5190, 1964.

[68] R. Howell, "An algorithm for the extraction of ocean wave spectra from narrow beam HF radar backscatter," Master's thesis, Memorial University of Newfoundland, St. John's, Newfoundland, 1990.

[69] E. Gill, "An algorithm for the extraction of ocean wave parameters from wide beam HF radar (CODAR) backscatter," Master's thesis, Memorial University of Newfoundland, St. John's, Newfoundland, 1990.

[70] B. Lathi, *Random Signals and Communication Theory.* Scranton, Penn.: International Textbook Company, 1968.

[71] J. Walsh, "Ocean spectra of surface description," *Private correspondence*, 2004.

[72] D. Barton, *Radar System Analysis and Modeling.* Norwood, MA: Artech House, Inc., 2005.

[73] B. Dawe, "Radio wave propagation over Earth: Field calculations and an implementation of the roughness effect," Master's thesis, Memorial University of Newfoundland, St. John's, Newfoundland, 1988.

[74] M. Skolnik (Editor in Chief), *Radar Handbook (Second Edition)*. New York: McGraw-Hill, 1990.

[75] C. E. Cook and M. Bernfeld, *Radar Signals: An Introduction to Theory and Application*. 685 Canton Street, Norwood, MA: Artech House, Inc., 1993.

[76] K. Gurgel, H. Essen, and S. Kingsley, "High frequency radars: physical limitations and recent developments," *Coastal Engineering*, vol. 37, pp. 201 218, 1999.

[77] A. Papoulis, *Probability, Random Variables, and Stochastic Processes*. New York: McGraw-Hill, 1965.

[78] R. Collin, *Antennas and Radio Wave Propagation*. New York: McGraw-Hill Book Company, 1985.

[79] International Telecommunications Union, Geneva, *Propagation in Ionized Media (ITU-R Recommendations, 1994 PI Series Volume)*, 1994.

Appendix A

Derivation Pertinent to the Cross Sections for the FM Waveforms

A.1 Processing of the Demodulation

In the development of the range spectra for the FM waveforms, the radar received signal should be demodulated by multiplying it with an ungated version of the transmitted signal followed by a low-pass filter (e.g. [50, 52]). In our analysis, the ungated transmitted FM signal equation (3.3) is rewritten here as

$$i(t) = I_0 e^{j\left(\omega_0 t_r + \alpha\pi t_r^2\right)} , \quad -\frac{T_r}{2} \leq t_r < \frac{T_r}{2} , \tag{A.1}$$

or with its real part as

$$i(t_r) = I_0 \cos\left(\omega_0 t_r + \alpha\pi t_r^2\right) , \quad -\frac{T_r}{2} \leq t_r < \frac{T_r}{2} , \tag{A.2}$$

where t is replaced by t_r as the time variable within the period T_r. All the other parameters are defined in Chapter 3. The first- and second-order received signals for the FMCW and

FMICW waveforms, may have a common form as

$$E\left(t_r\right) = E_c e^{-j\pi/4} e^{j\left(\omega_0 t_r + \alpha\pi t_r^2\right)} e^{j\rho_s\left(K - 2k_0 - \frac{4\pi\alpha t_r}{c}\right)}$$
$$\mathrm{Sa}\left[\frac{\Delta\rho_s}{2}\left(K - 2k_0 - \frac{4\pi\alpha t_r}{c}\right)\right] , \tag{A.3}$$

where E_c is a collection of unused factors. It can be written as

$$E(t_r) = E_c \cos\left[\omega_0 t_r + \alpha\pi t_r^2 + \Theta(t_r)\right] , \quad -\frac{T_r}{2} \leq t_r < \frac{T_r}{2} , \tag{A.4}$$

where $\Theta(t_r)$ is summation of all the other phase terms with assumptions that $\frac{d\Theta(t_r)}{dt_r} << \omega_0 + 2\alpha\pi t_r$. After absorbing I_0 into E_c, the demodulation of $E(t_r)$ gives,

$$\begin{aligned} E^D(t_r) &= \mathrm{LPF}\left\{i(t_r)E\left(t_r\right)\right\} \\ &= \mathrm{LPF}\left\{E_c \cos\left(\omega_0 t_r + \alpha\pi t_r^2\right) \cos\left[\omega_0 t_r + \alpha\pi t_r^2 + \Theta(t_r)\right]\right\} \\ &= \mathrm{LPF}\left\{\frac{E_c}{2}\cos\left[2\omega_0 t_r + 2\alpha\pi t_r^2 + \Theta(t_r)\right] + \frac{E_c}{2}\cos\left[-\Theta(t_r)\right]\right\} = \frac{E_c}{2}\cos\left\{-\Theta(t_r)\right\} , \end{aligned} \tag{A.5}$$

where $E^D(t_r)$ represents the demodulation with respect to $E(t_r)$ and $\mathrm{LPF}\{\cdot\}$ refers to the operation of an ideal low-pass filtering. Equation (A.5) may be written in a concise form as

$$E^D(t_r) = i(t_r)E^*(t_r) , \tag{A.6}$$

where $E^*(t_r)$ is complex conjugation of $E(t_r)$. Therefore, the demodulation of equation (A.3) can be expressed as

$$E^D\left(t_r\right) = E_c e^{j\pi/4} e^{-j\rho_s\left(K - 2k_0 - \frac{4\pi\alpha t_r}{c}\right)} \mathrm{Sa}\left[\frac{\Delta\rho_s}{2}\left(K - 2k_0 - \frac{4\pi\alpha t_r}{c}\right)\right] . \tag{A.7}$$

This demodulation process will be used in our analysis in Chapter 3 for the cross section derivation with FMCW and FMICW waveforms.

A.2 Range Spectra for the Second-order Field Equations

A.2.1 For the FMCW Waveform

The derivation is from the first-order field equation (3.33). The exponential factor $e^{j\left(\omega_0 t_r+\alpha\pi t_r^2\right)}$ has been eliminated by means of demodulation, which gives

$$\left(E_0^+\right)_{12}^D(t_r) = E_0 e^{-j\rho_s\left(K-2k_0-\frac{4\pi\alpha t_r}{c}\right)}\mathrm{Sa}\left[\frac{\Delta\rho_s}{2}\left(K-2k_0-\frac{4\pi\alpha t_r}{c}\right)\right], \tag{A.8}$$

where

$$E_0 = \frac{-jI_0\eta_0\Delta l k_0^2 F^2\left(\rho_s\right)\Delta\rho_s}{(2\pi\rho_s)^{3/2}}\sum_{\vec{K}_1,\omega_1}\sum_{\vec{K}_2,\omega_2} {}_H\Gamma_P\,{}_1P_{\vec{K}_1,\omega_1}\,{}_1P_{\vec{K}_2,\omega_2}\sqrt{K}e^{-j\pi/4}. \tag{A.9}$$

The sinc function in equation (A.8) has a form of $\frac{\sin x}{x}$, and the $\sin x$ can be expressed in exponential form so that

$$\begin{aligned}\mathrm{Sa}\left[\frac{\Delta\rho_s}{2}\left(K-2k_0-\frac{4\pi\alpha t_r}{c}\right)\right] &= \left[2j\frac{\Delta\rho_s}{2}\left(K-2k_0-\frac{4\pi\alpha t_r}{c}\right)\right]^{-1}\\ &\left[e^{j\frac{\Delta\rho_s}{2}\left(K-2k_0-\frac{4\pi\alpha t_r}{c}\right)} - e^{-j\frac{\Delta\rho_s}{2}\left(K-2k_0-\frac{4\pi\alpha t_r}{c}\right)}\right].\end{aligned} \tag{A.10}$$

The magnitude factor can be simplified by applying a binomial expansion to get

$$\left[2j\frac{\Delta\rho_s}{2}\left(K-2k_0-\frac{4\pi\alpha t_r}{c}\right)\right]^{-1} \approx \frac{1}{j\Delta\rho_s\left(K-2k_0\right)} \tag{A.11}$$

since, compared with K and $2k_0$, the $\frac{4\pi\alpha t_r}{c}$ term is much smaller and can be neglected. Therefore, equation (A.8) becomes

$$\begin{aligned}
&\left(E_0^+\right)_{12}^D(t_r) = \frac{E_0}{j\Delta\rho_s\left(K-2k_0\right)} \\
&\left[e^{-j(K-2k_0)\left(\rho_s-\frac{\Delta\rho_s}{2}\right)}e^{j\frac{4\pi\alpha}{c}\left(\rho_s-\frac{\Delta\rho_s}{2}\right)t_r} - e^{-j(K-2k_0)\left(\rho_s+\frac{\Delta\rho_s}{2}\right)}e^{j\frac{4\pi\alpha}{c}\left(\rho_s+\frac{\Delta\rho_s}{2}\right)t_r}\right] \\
&= E_0^A e^{j\frac{4\pi\alpha}{c}\left(\rho_s-\frac{\Delta\rho_s}{2}\right)t_r} - E_0^B e^{j\frac{4\pi\alpha}{c}\left(\rho_s+\frac{\Delta\rho_s}{2}\right)t_r} \\
&= E^A - E^B \ , \qquad \text{(A.12)}
\end{aligned}$$

where

$$E_0^A = \frac{E_0}{j\Delta\rho_s\left(K-2k_0\right)}e^{-j(K-2k_0)\left(\rho_s-\frac{\Delta\rho_s}{2}\right)} \ , \qquad \text{(A.13)}$$

and

$$E_0^B = \frac{E_0}{j\Delta\rho_s\left(K-2k_0\right)}e^{-j(K-2k_0)\left(\rho_s+\frac{\Delta\rho_s}{2}\right)} \ . \qquad \text{(A.14)}$$

The second-order range spectrum $\Phi_2^r(\omega_r)$ will be obtained by the Fourier transform of equation (A.12) with respect to t_r following the process for the development of the first-order range spectrum (equations (3.52) to (3.57)), since the only difference is within the factor E_0. With the same assumption and approximations as for the first-order case, the second-order range spectrum will be obtained as equation (3.58) in Section 3.3.1.

A.2.2 For the FMICW Waveform

The development of the second-order range spectrum for the FMICW waveform starts from equation (3.44). With the experience of derivation of the first-order range spectrum for the FMICW waveform and the second-order range spectrum for the FMCW waveform, we may find that the only difference to the first-order case is the definition of the factor

E_{0g}, which is

$$E_0 = \frac{-jI_0\eta_0\Delta l k_0^2 F^2(\rho_s)\Delta\rho_s}{(2\pi\rho_s)^{3/2}} \sum_{\vec{K}_1,\omega_1} \sum_{\vec{K}_2,\omega_2} {}_H\Gamma_P \, {}_1P_{\vec{K}_1,\omega_1} \, {}_1P_{\vec{K}_2,\omega_2} \sqrt{K} e^{-j\pi/4} \,. \tag{A.15}$$

Then, the received field equation (3.44), after the demodulation, will be

$$\begin{aligned} \left(E_{0g}^{+}\right)_{12}^{D}(t_r) &= E_0 \sum_{n=0}^{N-1} \mathrm{Rect}\left(\frac{t_r - \frac{2\rho_s}{c} - nT_g - \frac{\tau_g}{2} + \frac{T_r}{2}}{\tau_g}\right) e^{-j\rho_s\left(K-2k_0-\frac{4\pi\alpha t_r}{c}\right)} \\ &\quad \mathrm{Sa}\left[\frac{\Delta\rho_s}{2}\left(K - 2k_0 - \frac{4\pi\alpha t_r}{c}\right)\right] \,, \end{aligned} \tag{A.16}$$

or, with the sinc function being expanded,

$$\begin{aligned} \left(E_{0g}^{+}\right)_{12}^{D}(t_r) &= E_g^A - E_g^B \\ &= E_{0g}^A \sum_{n=0}^{N-1} \mathrm{Rect}\left(\frac{t_r - \frac{2\rho_s}{c} - nT_g - \frac{\tau_g}{2} + \frac{T_r}{2}}{\tau_g}\right) e^{j\frac{4\pi\alpha}{c}\left(\rho_s - \frac{\Delta\rho_s}{2}\right)t_r} \\ &\quad - E_{0g}^B \sum_{n=0}^{N-1} \mathrm{Rect}\left(\frac{t_r - \frac{2\rho_s}{c} - nT_g - \frac{\tau_g}{2} + \frac{T_r}{2}}{\tau_g}\right) e^{j\frac{4\pi\alpha}{c}\left(\rho_s + \frac{\Delta\rho_s}{2}\right)t_r} \,, \end{aligned} \tag{A.17}$$

where

$$E_{0g}^A = \frac{E_0}{j\Delta\rho_s(K-2k_0)} e^{-j(K-2k_0)\left(\rho_s - \frac{\Delta\rho_s}{2}\right)} \tag{A.18}$$

and

$$E_{0g}^B = \frac{E_0}{j\Delta\rho_s(K-2k_0)} e^{-j(K-2k_0)\left(\rho_s + \frac{\Delta\rho_s}{2}\right)} \,. \tag{A.19}$$

The range spectrum $\Phi_{2g}^r(\omega_r)$ will be obtained by the Fourier transform of equation (A.17) with respect to t_r. The resulting expression is equation (3.91) in Section 3.3.2.

Appendix B

Critical Value Estimation for the FM Waveforms

Here, the critical values for different FFT resolutions (Δ_{FFT}s) are determined for the FM waveforms using the same numerical scheme as was used for the pulsed radar waveform in Chapter 2. The process of the LSM fitting is depicted in Figure B.1 to Figure B.9. The resulting critical values, as well as values of "critical width (β_c)" for the Bragg region, and the "critical number (N_c)" of frequency points within the Bragg region are tabulated in Table 4.1 in Section 4.3.4. The corresponding analysis is also given associated with Table 4.1.

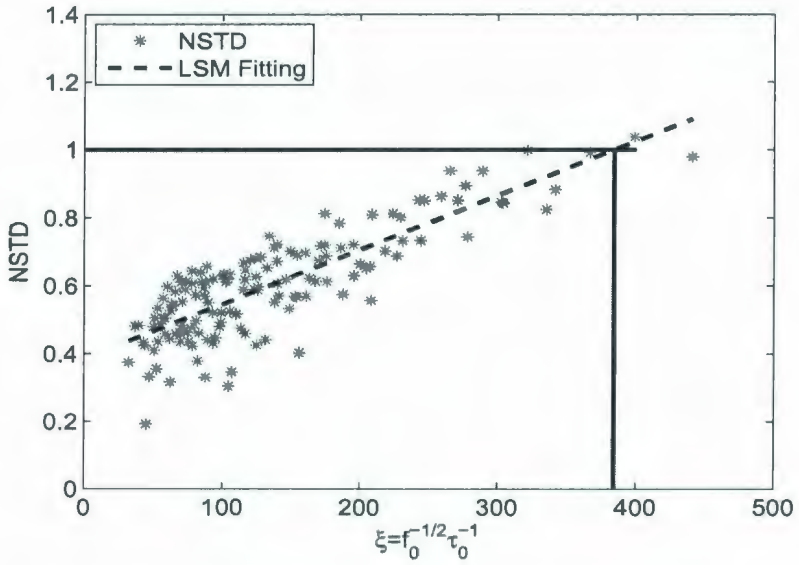

Figure B.1: Plot of ξ as a function of NSTD for the Δ_{FFT} of 0.0130 Hz. The critical value is determined as $\xi_c = 384.5$.

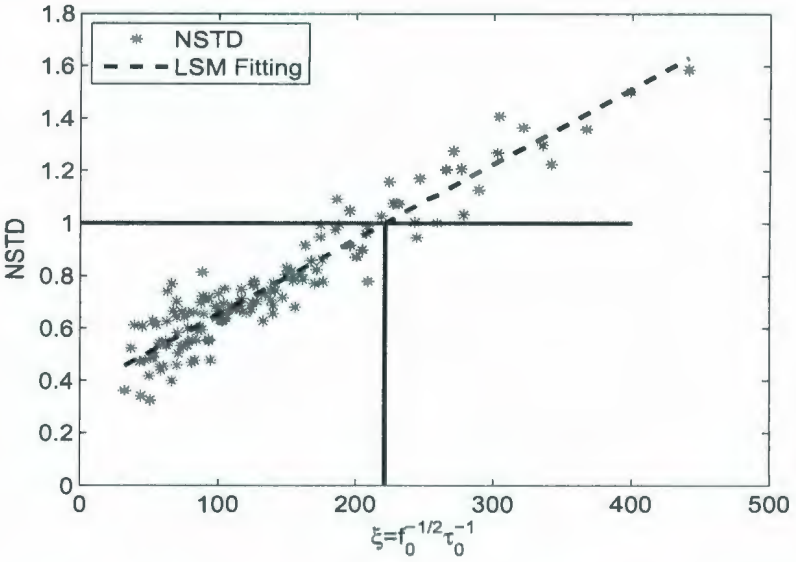

Figure B.2: Plot of ξ as a function of NSTD for the Δ_{FFT} of 0.0078 Hz. The critical value is determined as $\xi_c = 221.3$.

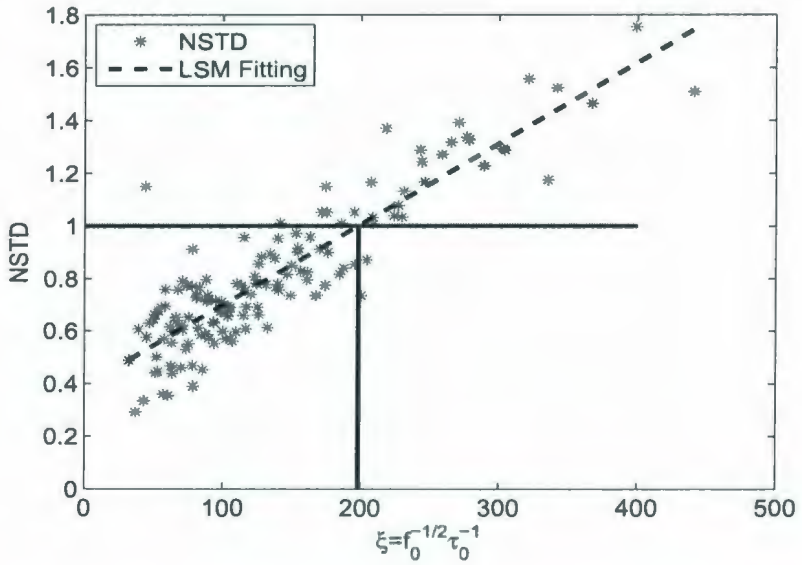

Figure B.3: Plot of ξ as a function of NSTD for the Δ_{FFT} of 0.0066 Hz. The critical value is determined as $\xi_c = 198.2$.

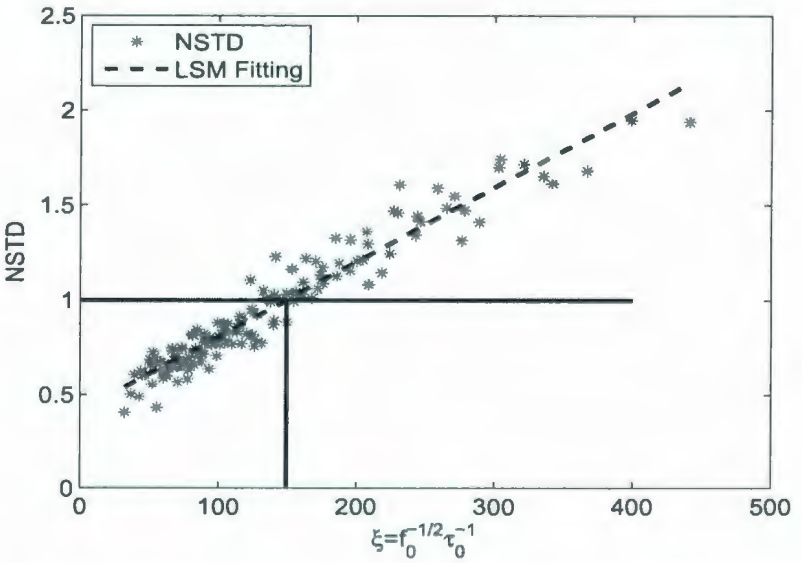

Figure B.4: Plot of ξ as a function of NSTD for the Δ_{FFT} of 0.0048 Hz. The critical value is determined as $\xi_c = 149.3$.

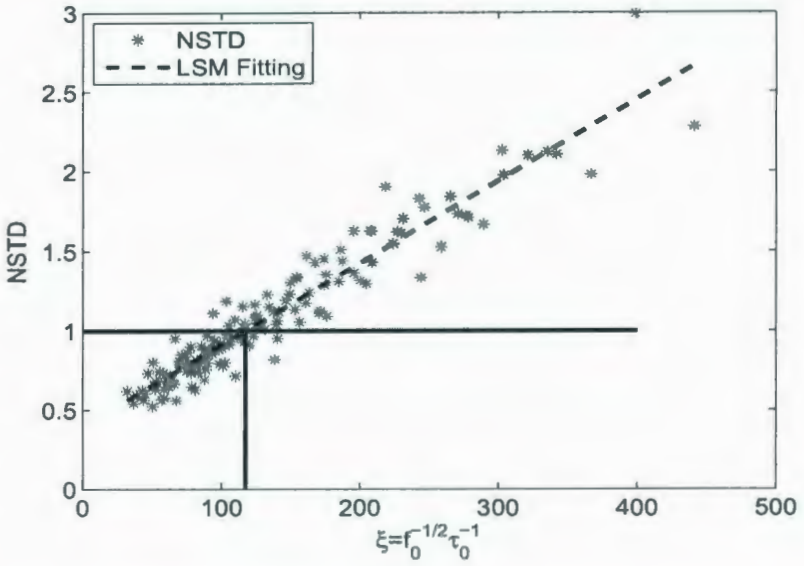

Figure B.5: Plot of ξ as a function of NSTD for the Δ_{FFT} of 0.0040 Hz. The critical value is determined as $\xi_c = 117.4$.

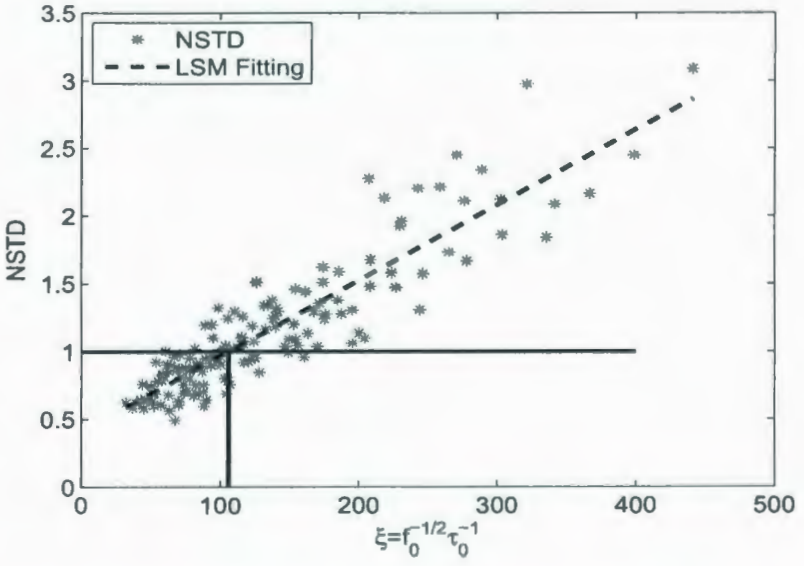

Figure B.6: Plot of ξ as a function of NSTD for the Δ_{FFT} of 0.0032 Hz. The critical value is determined as $\xi_c = 106.1$.

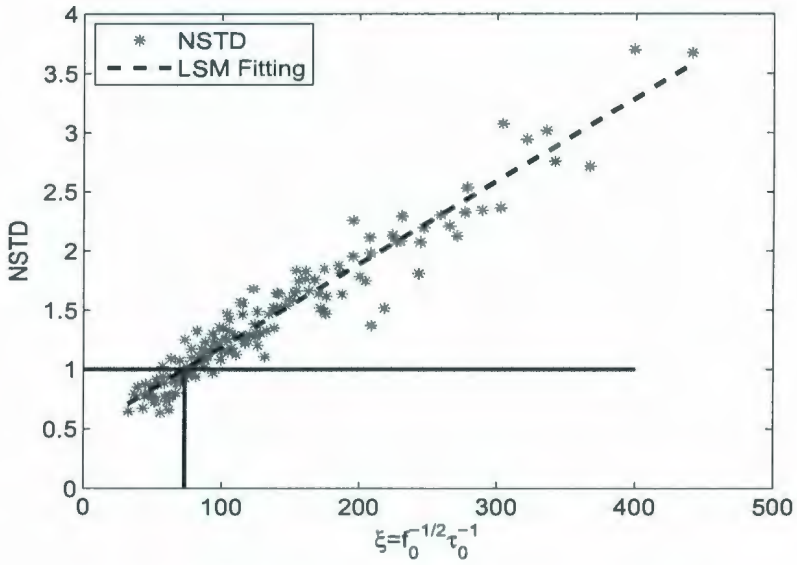

Figure B.7: Plot of ξ as a function of NSTD for the Δ_{FFT} of 0.0024 Hz. The critical value is determined as $\xi_c = 73.4$.

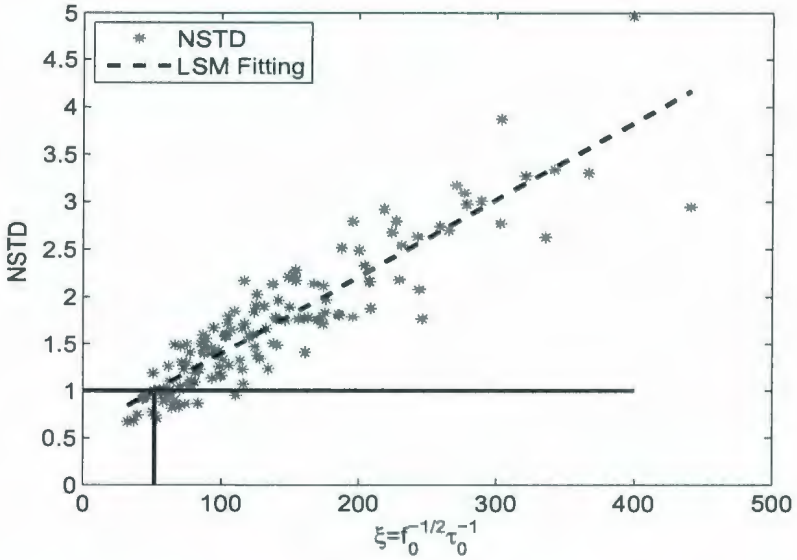

Figure B.8: Plot of ξ as a function of NSTD for the Δ_{FFT} of 0.0020 Hz. The critical value is determined as $\xi_c = 51.8$.

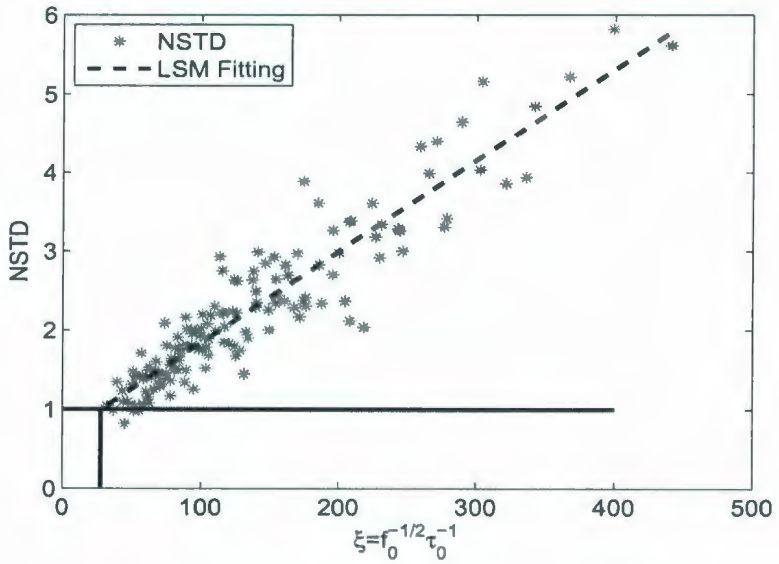

Figure B.9: Plot of ξ as a function of NSTD for the Δ_{FFT} of 0.0012 Hz. The critical value is determined as $\xi_c = 27.6$.